# Optimization of electromagnetic and acoustic performances of power transformers

Mingyong Liu

NNT : 2017 SACLS 256

# Thèse de doctorat de l'Université Paris–Saclay préparée à l'Université Paris-Sud

Ecole doctorale n°579
Sciences mécaniques et énergétiques, matériaux et géosciences - SMEMAG
Spécialité de doctorat : mécanique des solides

par

M. Mingyong LIU

## Optimization of electromagnetic and acoustic performances of power transformers

Thèse présentée et soutenue à l'École Normale Supérieure à Cachan, le 25 10 2017.

Composition du Jury :

| | | | |
|---|---|---|---|
| M. | Anouar BELAHCEN | Professeur<br>Aalto University | (Rapporteur) |
| M. | Fausto FIORILLO | Professeur<br>INRIM | (Rapporteur) |
| M. | Nicolas TRIANTAFYLLIDIS | Professeur<br>Ecole Polytechnique | (Examinateur) |
| M. | Vincent LANFRANCHI | Professeur<br>UTC | (Président) |
| M. | Gérard MEUNIER | Professeur<br>CNRS | (Examinateur) |
| M. | Frédéric BOUILLAULT | Professeur<br>Université Paris-Sud | (Co-directeur de thèse) |
| M. | Xavier MININGER | Professeur<br>Université Paris-Sud | (Co-directeur de thèse) |
| M. | Olivier HUBERT | Professeur<br>ENS Paris-Saclay | (Directeur de thèse) |

# Résumé

Dans le contexte 'Plus Electrique' ou 'Tout Electrique', les fabricants de véhicules terrestres et aériens cherchent à augmenter la puissance embarquée à masse égale. Une des solutions envisagées est d'augmenter la densité de flux magnétique dans les matériaux magnétiques constitutifs des machines électriques. Cependant, les matériaux présentant les densités de flux les plus élevées ont le désavantage de se déformer sous l'effet du champ magnétique. Cette déformation conduit à une augmentation significative des vibrations, ce qui provoque un bruit acoustique indésirable. L'origine principale de ces déformations est le phénomène de magnétostriction. La magnétostriction provient du réarrangement sous champ magnétique de la microstructure en domaines magnétiques constitutifs de tout matériau magnétique. Les voies explorées pour réduire ce bruit sans nuire aux performances des systèmes sont multiples. Nous nous intéressons ici au développement d'une chaîne de modélisation complète, du comportement local du matériau au calcul de la déformation totale de la structure, à l'aide d'une approche multi-échelle mêlant une loi de comportement locale, une homogénéisation analytique pour la description du milieu multicouche et une modélisation éléments finis pour la résolution du problème de structure mécanique et magnétique.

1. Stratégies de modélisation

Il s'agit de résoudre un problème magnéto-mécanique couplé (un modèle numérique 2D est privilégié). Une approche séquentielle et quasi-statique est d'abord appliquée: nous débutons par la résolution du problème magnétique. La résolution du problème mécanique vient ensuite. Les contraintes induites dans la structure de transformateur sont généralement faibles ; elles influencent néanmoins le comportement magnétique et magnétostrictif du matériau. Un couplage fort est mis en œuvre au sein du modèle multicouche. Ce mode de calcul est adapté pour les matériaux dont le comportement est réputé sensible aux contraintes.

Deux méthodes de résolution itérative (point-fixe modifié et Newton-Raphson) sont implantées pour résoudre le problème magnétique non-linéaire. En envoyant un courant sinusoïdal dans les bobinages (ou un flux magnétique dans le noyau) discrétisé en temps, à la convergence, on obtient une série de solutions constituées par des champs magnétiques (champ, induction, flux, aimantation) et le champ de déformations de magnétostriction libre. L'opération suivante consiste à définir une force volumique équivalente à la déformation de magnétostriction à partir de l'équation d'équilibre mécanique. Le calcul est réalisé à chaque pas de temps sur une période d'excitation puis décomposée en séries de Fourrier. Chaque harmonique est considéré comme l'excitation du problème mécanique pour différentes fréquences. Le déplacement total de la structure en fonction du temps est obtenu en sommant les harmoniques de déplacements (principe de superposition). Le problème mécanique est résolu dans le domaine fréquentiel pour éviter les calculs transitoires et ainsi gagner du temps. Un bloc acoustique de post-traitement est développé, ce qui donne la puissance du bruit. Il est considéré comme un indicateur global du comportement acoustique des transformateurs.

Une phase d'optimisation de la géométrie à masse égale est réalisée, avec flux magnétique triphasé directement imposé dans le noyau du transformateur. Une optimisation de la géométrie afin de réduire le bruit et les pertes à puissance donnée est ainsi rendue possible. Cette procédure

est appliquée pour identifier le facteur de forme idéal d'un transformateur triphasé en fer-silicium à grains orientés à puissance donnée.

2. Développement de lois de comportement

Compte tenu de la complexité du comportement magnétique et magnétostrictif des matériaux (non linéarité, anisotropie, sensibilité à la contrainte, hystérésis…), un modèle multi-échelle simplifié est intégré à la chaîne de calcul éléments finis. Dans ce modèle, le comportement macroscopique du matériau magnétique est représenté par un mono-cristal équivalent. On cherche la probabilité de présence d'un domaine magnétique dans différentes directions à partir de son énergie locale, somme de différents contributions: l'énergie de champ, d'anisotropie magnétocristalline, élastique (magnéto-mécanique), et de configuration. Plusieurs extensions et améliorations de ce modèle sont proposées pour l'adapter à différents matériaux, en particulier, le fer-silicium à grains-orientés fortement anisotrope, le fer-silicium à grains non orientés, le fer-cobalt afk1, et le fer-nickel supra50.

Un modèle multi-échelle complet avec hystérésis est ensuite proposé. Ce modèle est capable de tenir compte du chargement en champ magnétique tournant, et d'estimer les pertes fer associées. Le chargement en champ magnétique tournant est en effet souvent présent dans les machines électriques et au niveau des T-joints des transformateurs de puissance. Disposer d'un modèle d'hystérésis en champ tournant est une point-clé pour réaliser des calculs précis de pertes et accéder aux vibrations des dispositifs. A noter que ce modèle multi-échelle n'a pas encore été proposé dans une version simplifiée et est n'est donc pas implémenté dans la chaîne de calcul éléments finis. Tous les calculs présentés dans cette thèse sont réalisés sans tenir compte de l'effet d'hystérésis.

Un transformateur est généralement constitué d'un empilement de tôles taillées sous forme de E et de I (de manière à refermer le circuit magnétique). Celles-ci sont empilées tête-bêche ce qui conduit à un mélange des comportements de chaque tôle. La résolution 2D nécessite de définir le comportement moyen de l'empilement de tôles. Une loi des mélanges est appliquée: elle utilise une hypothèse de champ magnétique et de déformation totale homogène dans les différentes couches compte tenu des conditions classiques de continuité tangentielle du champ magnétique d'une part et du déplacement d'autre part.

3. Identification et validation expérimentale

Une première série d'expérience doit permettre une identification de la loi de comportement anhystérétique des matériaux. Les éprouvettes sont prélevées suivantes la direction du laminage, transversale et à 45° par rapport à la direction du laminage. Elles sont caractérisées dans un banc de mesure magnétique et magnétostrictif, développé au LMT-Cachan. Les paramètres du modèle multi-échelle simplifié sont identifiés à partir des comportements mesurés.

La validation de l'ensemble matériau-structure utilise un transformateur tri-couches (par raison de simplicité) sous forme de '8' constitué des différents matériaux. Sur certaines structures, des jauges de déformation sont collées en différents points caractéristiques du transformateur ainsi formé. La même procédure de caractérisation du comportement anhystérétique est appliquée. Les simulations numériques sont lancées en utilisant les mêmes conditions de chargement et de conditions limites que les mesures pour tous les matériaux. Les résultats numériques sont en global accord avec les mesures expérimentales ce qui permet une première validation du modèle complet.

Une deuxième série d'expériences réalisées sur transformateurs permet une mesure de la vibration du transformateur et de faire une estimation du bruit émis. Plusieurs transformateurs 'EI' tri-couches sont constitués en différents matériaux. Ils sont suspendus pour éliminer les efforts parasites. Un courant (ou tension) d'excitation sinusoïdale alimente le bobinage central. Des accéléromètres placés en différents points de la tôle doivent permettent une mesure du déplacement local par intégration. Les points de mesure sont choisis de manière à identifier et éliminer les composantes de déplacement de corps solide. Le déplacement du point de mesure en fonction du temps est obtenu à l'aide d'un post-traitement. Les vibrations du transformateur et le bruit émis sont également comparés aux estimations du modèle. Le modèle permet de restituer les grandes tendances du comportement mesuré. Les écarts qui subsistent sont discutés.

Les travaux de thèse ont été réalisés en collaboration avec deux industriels : Aperam-Imphy-Alloys et Thales-AES.

# Contents

# List of Figures

# List of Tables

# Introduction

The world of transport, particularly in the aerospace industry, is undergoing deep changes. On one hand, the number of electrical comfort equipment, electronic control systems and navigation systems increases significantly. On the other hand, with the desire to reduce CO2 gas emission, "all electric aircrafts" (so-called carbon-free aircrafts) are developed. The electrical power supplied by the generators plugged to the turbojet has to be increased to feed these systems. Depending on the application, this electrical revolution is spreading to all parts of the energy transmission system, going from the power supply to the actuator through the electrical power chain. The electrical power is commonly transformed through power electronic devices and power transformers to adapt voltage, current and frequency to the final on board user. Therefore the increase of the electrical power leads to an increase of the size and mass of these devices at constant power to mass ratio (Fig.1).

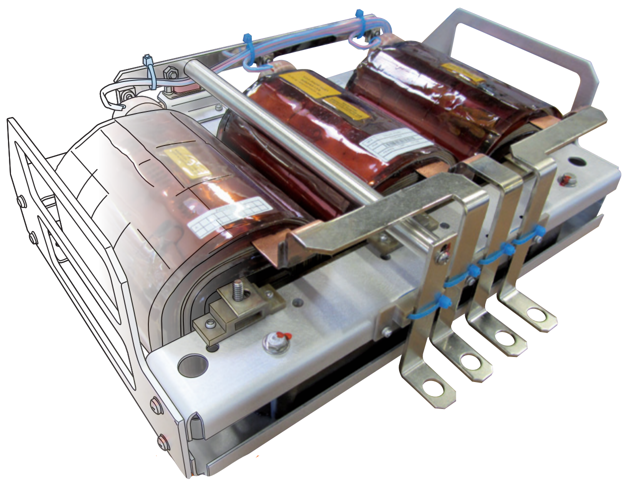

**Figure 1:** Thales Auto Transformer Unit (source figure from the internet [Thales, ])

In order to make the switch to a viable solution, many scientific studies focus on optimizing the geometry of the electrical devices, but this single approach seems today not enough innovative to increase the power to mass ratio. The best way to solve this problem is to work on an evolution of both the core structrues and magnetic materials. Ferromagnetic materials have evolved little for several decades. However, research in metallurgical industries has continued all over the world (and particularly in France at APERAM). Some products currently under development in the laboratories are close to being industrialized and adapted to the various functions mentioned above.

The newly developed ferromagnetic materials presenting a higher power density are often made of iron and cobalt. Power transformers made with these materials generate unfortunately a loud noise in operation. This noise is usually separated into load noise [Ertl et Landes, 2007] [Wang *et al.*, 2011] and no-load noise. The former is due to magnetic interactions (especially Lorentz forces) between the current carrying windings and transformer magnetic stray field. The latter is caused by periodic deformations of sheets linked with the structure of the transformer core [Chang *et al.*, 2011] [Hsu *et al.*, 2012]. This sheet deformation is believed resulting from many phenomena. Up to now, several factors have been claimed to have relevant effects on flux distribution and core vibrations, such as bolt holes [Balehosur *et al.*, 2010], core clamping [Penin *et al.*, 2014b] and core structures [Chang *et al.*, 2011].

Sheet deformation has two origins: i) elastic strain associated with magneto-static forces appearing on the free surfaces and in the volume; ii) magnetostriction depending on the local magnetic state of the material [Du Trémolet de Lacheisserie, 1993a]. Magnetic forces are induced when the medium exhibits inhomogeneous permeability. Magnetostrictive strain is associated with the re-organization of magnetic domains. The domains are characterized by a magnetization vector whose magnitude equals the saturation magnetization of the material, and free magnetostriction strain depending on the magnetostriction constants and magnetization direction. When a magnetic field $\vec{H}$ is applied, the domain wall moves and then magnetization vectors rotate toward the direction of the applied field at high magnetic field leading to a displacement of domain walls that separate the magnetic domains, increasing the volume fraction of domains aligned with the field. Thus a deformation appears at the macroscopic scale induced by the free strain $\epsilon_{\mu}$ of the considered domains. The crystallographic texture has a strong impact on the magnetostrictive behavior [Hubert et Daniel, 2008]. It leads to both magnetic and magnetostrictive anisotropies (coupled magneto-mechanical phenomena with isotropic magnetic and magnetostrictive behavior are studied in [Fonteyn *et al.*, 2010] [Belahcen, 2005]).

Modeling and optimization of the power transformer, in order to reduce the noise emission, involves a multi-physical approach including electromagnetic, mechanical and acoustic aspects. It is so complex that, despite strong recent efforts in this field, there is currently no robust and reliable commercial software nor academic code yet available to estimate and optimize the global deformation and the noise level in laminated transformer cores, with the consideration of material anisotropy, nonlinearity of the magneto-mechanical behavior and stress dependency. Such a tool is however essential for optimization. The goal of this thesis work is to propose a complete numerical modeling of this noise generation to allow an optimization of the transformer with respect to the mass, noise, inrush, efficiency, thermal, cost constraints thanks to the simulation and optimization of **material** and **design** of the devices. It should also be noted that in the context of noise generation, the magnetic circuit can not be considered independently to its environment. It will thus be important to be able to evaluate the magnitudes of the induced forces injected into the structure at the fixing points of the transformer. This aspect of the simulation could ultimately make it possible to optimize the fixations (number, arrangement) by minimizing the transmitted vibrations, and/or by reducing the stresses in the material which can lead to a reduction in the magnetic permeability of the material or to an undesirable modification of its magnetostrictive behavior and the global performance.

This dissertation is divided into four chapters. Chapter 1 introduces the basic concepts of the noise generation in power transformers, existing studies in this area and presents the strategy to solve the problems. Chapter 2 is dedicated to the modeling of magneto-mechanical behavior, including a full multi-scale model with and without hysteresis extension, a simplified multi-scale model adapted to the finite element modeling chain. Chapter 3 addresses the fully coupled modeling chain of power transformer core vibration and noise emission, using finite element method. Chapter 4 and 5 present the measurements on power transformer prototype and its comparison with simulation. A numerical optimization procedure of geometry is finally proposed, allowing better acoustic and electromagnetic performances to be reached.

# Chapter 1

# Introduction to Transformer Noise

## Contents

# 1.1 Introduction to power transformer

## 1.1.1 Working principle

A power transformer is an electrical device that transfers electrical energy between two or more circuits through electromagnetic induction. It is used to increase or decrease the alternating voltages in the electrical system. The power transformer is typically composed of a ferromagnetic core, several current carrying windings, holding structures and accessories such as the cooling system, illustrated in Fig.1.1.

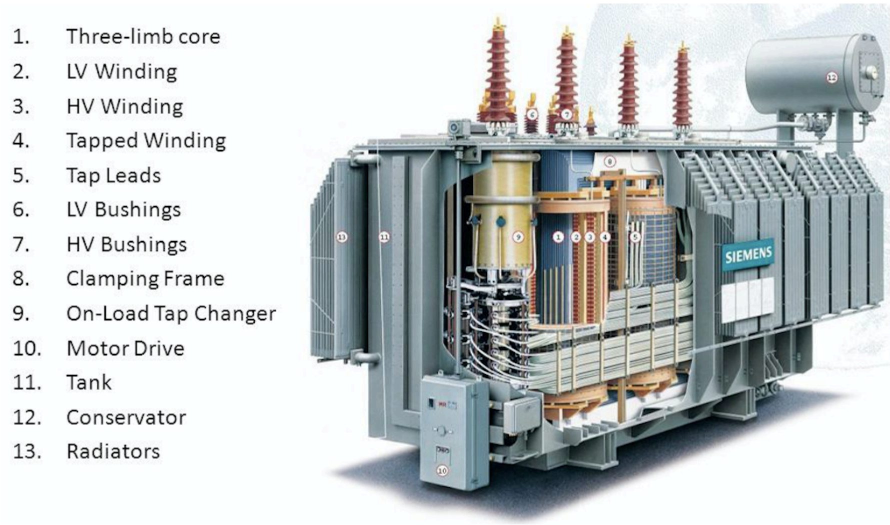


**Figure 1.1:** Illustration of the power transformer parts (source figure from the website [Siemens, ]).

The basic theory of the power transformer is simple. The primary windings that carry varying current creates a varying magnetic flux in the transformer core. The transformer core made of ferromagnetic material guides and keeps the magnetic flux inside the core. Secondary windings get back the corresponding voltage and current by means of electromagnetic flux density. The proportion of the input and output voltage can be easily adjusted by the number of winding turns.

The power transformer comes with various types, from the largest ones used for power grid with thousands of tons to the smallest ones integrated into electronic cards. The classification of power transformers can be carried out from different angles. It could be monophase or polyphase for different electric systems. In terms of cooling type, large transformers used in power distribution are often cooled by oil for better efficiency, while medium and small transformers are normally cooled by air for simplicity. Power transformers that amplify the voltage are called step-up transformers, otherwise, they are called step-down transformers. The autotransformer has one winding that is tapped at some point along the winding (without Galvanic insulation), making it possible to modify the ratio between the input and output voltage.

### 1.1.2 Transformer core

The transformer core is usually made of very soft ferromagnetic materials for high efficiency. It comes with different types, such as bulk cores and laminated steel cores. Bulk cores are often made of ferrite, a ferromagnetic ceramic material. It is usually used for high-frequency applications, because of its non-conductivity. This prevents the eddy currents and leads to a low no-load loss for the power transformer. However, the magnetization saturation of the ferrite is about $0.3T$, which is low compared to the iron based ferromagnetic laminations. Meanwhile, in the industry of power transmission, the most widely used is the laminated steel core, which is the studying object of this thesis.

The laminated steel core is made of an assembly of hundreds of thin sheets to ensure a homogeneous magnetic field through the thickness and more importantly to limit the eddy currents. Eddy currents losses in a magnetic core can be greatly reduced by reducing the thickness of the electrical sheet. Instead of having one big solid piece of magnetic material, it is splited into hundreds of thin sheets of $0.2-0.5mm$ thickness (Fig.1.2). These sheets are insulated from each other by specific coatings or papers, to increase the surface resistance and prevent the flow of eddy currents between electrical sheets.

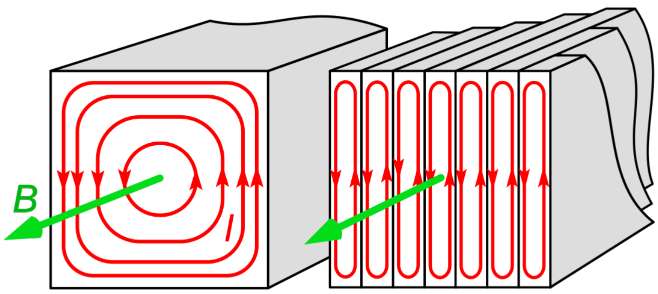


**Figure 1.2:** Eddy currents within a solid iron transformer core (left) and a laminated transformer core composed of insulated sheets (right).

Associated to the forming process (hot/cold rolling, heat treatments), transformer sheets usually exhibit anisotropic magnetic and mechanical behaviors. Classical on-board electrical transformers are for example made of Non-Oriented FeSi or FeCo alloys. These sheets exhibit the highest induction (and permeability) at a given magnetic field level along the rolling direction (RD). The transformer core is consequently designed to increase the volume of material offering improved permeability in the direction of magnetic field.

One common design of laminated core is made from interleaved stacks of 'E-shaped' steel sheets capped with 'I-shaped' pieces, named 'E-I' core. This solution can reduce the manufacturing cost and facilitate the winding fabrication. 'E-shaped' and 'I-shaped' sheets are cut along the rolling direction of the lamination as shown in Fig.1.3. They are positioned alternatively on top or on bottom of the transformer in order to dilute parasitic air-gaps and limit their effects [Weiser et Pfützner, 1998].

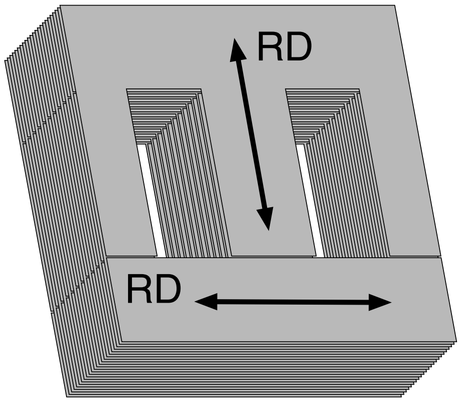


**Figure 1.3:** Example of an E-I stacked core (RD indicates the rolling direction)

### 1.1.3 Electrical steel sheet

The electrical steel sheet is an essential component for the fabrication of power transformers and electrical motors. The electrical steel sheet is usually manufactured by a process called rolling, in which metal block is passed through a pair of rolls to reduce the thickness. This process is repeated several times to obtain an electrical steel sheet with a thickness of $0.2 - 2mm$. Fig.1.4 gives an illustration of the rolling process, with an indication of rolling direction (RD), transverse direction (TD), and normal direction (ND). These sheets are then cut to their final shape by punching, laser, or water jet cutting.

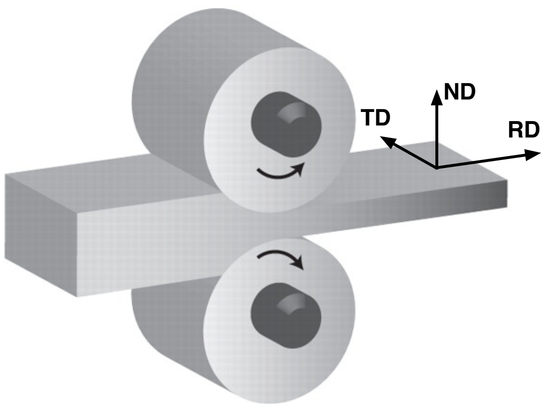


**Figure 1.4:** Rolling process schematic view with indication of rolling direction (RD), transverse direction (TD), and normal direction (ND).

Electrical steel is usually tailored to produce specific magnetic properties: low hysteresis loss, small magnetostriction, and high magnetic permeability. Looking for a low magnetostriction is a more recent issue. Electrical steels usually indicate iron based materials that contain a small amount of silicon (up to 6.5%). They are often called FeSi alloy for simplicity reasons. A special process allows crystal size and orientation to be controlled allowing to orient all magnetic domains along RD (grain-oriented (GO) FeSi). This strong anisotropy favors the magnetic and magnetostrictive performances along RD making this material widely used in the large distribution power transformers, where the direction of magnetic flux is constant in most of the parts. Most of the FeSi sheets are processed to develop an isotropic (compared to GO FeSi) behavior. These materials, called Non-Oriented (NO) FeSi, are often used inside rotating machines where the direction of the magnetic flux at a given point changes all the time. For the application of low-noise power transformer, other high-end materials are also good candidates, such as FeNi Supra50 and FeCo Afk1. FeNi Supra50 is composed of 50% Iron and 50% Nickel, forming a quasi-single-crystal cubic texture. This creates two easy axes along RD and TD and leads to a low magnetostriction in these directions. FeCo Afk1 develops a low magnetostriction under special (confidential) heat treatment, which is still under development, in order to obtain the optimized performance. These materials will be presented more extensively in the next chapters.

## 1.2 Noise source

The noise of the power transformer, or transformer 'humming', has been known as a big issue for several decades. A common solution, perhaps the easiest one, to reduce noise emission is to stop it from the transmission. For example, a solution is to place sound barriers or to use a full enclosure [Yang et Zhang, 2006]. However, any additional mass is strictly limited for aeronautic power transformers, making it necessary to reduce the noise source itself. The noise source can be sorted into three main categories: core noise, load noise and noise from cooling systems (Fig.1.5).

### 1.2.1 Core noise

Noise from the transformer core is considered as the dominant source of the noise. It is caused by the periodic deformation/movement of the electric sheets, under the alternative magnetic field [Chang *et al.*, 2011, Hsu *et al.*, 2012]. This deformation is produced by the combination effects of magnetostriction and magnetic forces (or Maxwell forces).

#### Magnetostriction

Magnetostriction is an intrinsic property for all ferromagnetic materials. When a piece of magnetic material is magnetized, it undergoes a small deformation, called magnetostriction. It has been first discovered in 1842 by Joule, that the ferromagnetic magnetic mate-

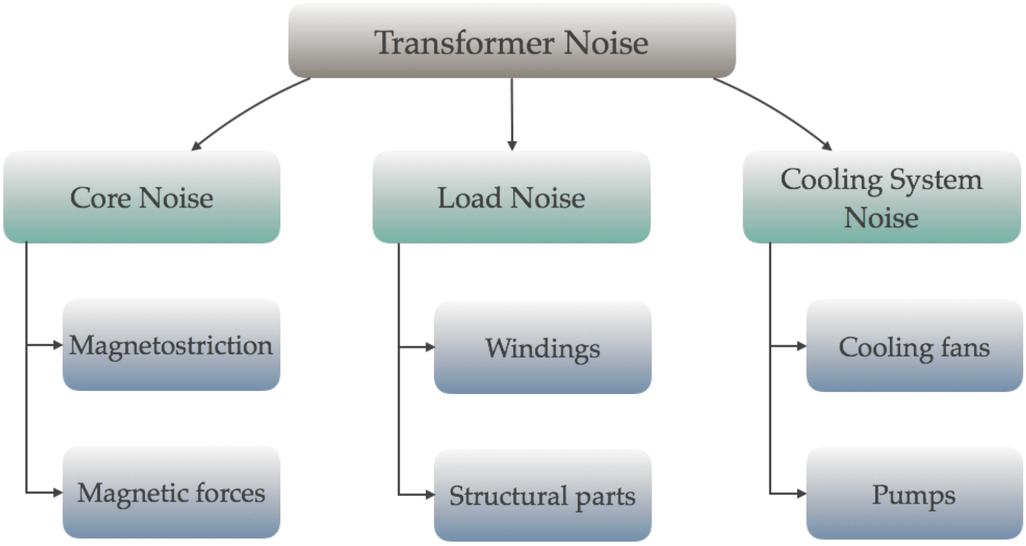


**Figure 1.5:** Sources of power transformer noise.

rial changes the shape under magnetic field [Williams et Shockley, 1949]. The mechanism of the magnetostriction can be explained by magnetic domain theory. Under external magnetic field, the magnetic domains tend to rotate and reorient to the direction of the magnetic field, in order to minimize the local energy, thus creates deformation. Since the deformation is isochoric, there is an opposite dimensional change in the orthogonal direction.

For applications such as power transformers, magnetostriction creates undesirable vibrations. For electrical sheets used in electrical motors and power transformers, often made of FeSi, the magnetostrictive strain is normally lower than $10ppm$. However, some alloys come with huge magnetostriction under relatively small magnetic fields. One of the most famous 'giant' magnetostriction material is Terfenol-D, which reaches about $2000ppm$ at room temperature. Applications based on these 'giant' magnetostriction materials are sensors and actuators [Anjanappa et Bi, 1917].

Magnetostriction depends on the applied field, mechanical stress, material type, and even temperature. It is important to notice that the magnetostriction is independent of the sign of the magnetic field. This results in a double frequency of magnetostriction compared to its magnetic excitation. Because of its non-linearity, higher harmonics also appear, which may trigger mechanical resonances of the whole transformer structure.

### Magnetic forces

Magnetic forces appear when magnetic field goes from one medium to another. In the core power transformer, magnetic forces are generally concentrated at the joints [Liu *et al.*, 2016], where magnetic field meets the air-gap. This makes the noise emission of the power transformer highly depended on the fabrication process, such as the flatness of the electric sheets, electric sheets cutting method and assembling precision. Admittedly, the core vibration induced by magnetic forces can not be easily reduced, because the transformer core is always assembled by hundreds of electric sheet and there are always parasite air-gaps.

### 1.2.2 Winding noise

Winding noise, also called load noise or coil noise, is due to the Lorentz forces resulting from the interaction of magnetic leakage fields and the load currents [Ertl et Landes, 2007, Wang *et al.*, 2011]. Forces acting on the windings can cause vibration. The frequency of the winding vibration is twice the current frequency [Rausch *et al.*, 2002, Shao *et al.*, 2012]. If it falls within the resonance frequency of the windings, large audible noise will be generated. In general, winding noise makes a limited contribution to the total transformer noise. The difference between no load and full load noise is usually no greater than 1 or 2dB, if the coil is well secured to the circuit board or is well damped. An example of the vibration of the windings on power transformer is given in Fig.1.6.

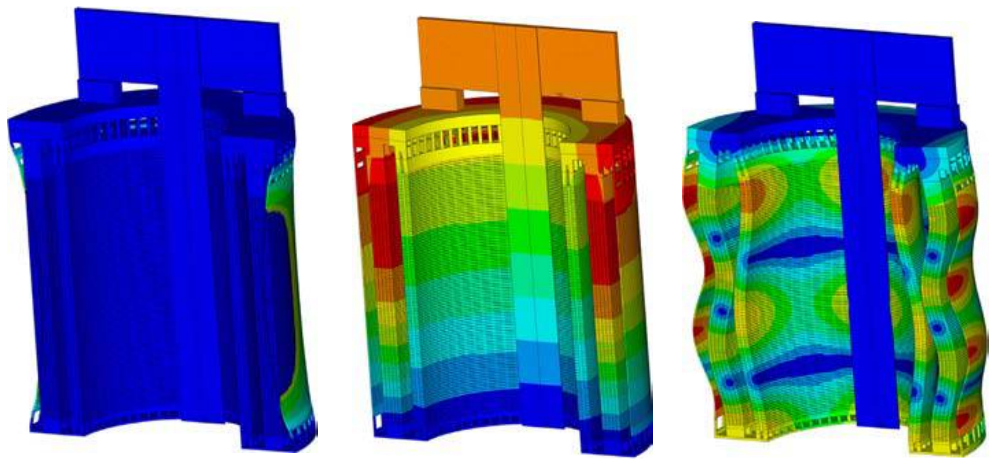

(a) 28 Hz (b) 46 Hz (c) 119 Hz

**Figure 1.6:** Example of the winding vibration in power transformers [Ertl et Landes, 2007].

In order to reduce the winding noise, good damping is often the key point. However, the progressive degradation of damping material (damage, oxidation...) may lead to more noise generation. Studies are also carried out to develop low noise windings, with a resonance frequency far from the current frequency.

### 1.2.3 Cooling system noise

Power transformers produce a huge amount of energy losses, such as iron losses in electrical sheets and joule losses in the windings. These losses act as heat sources, that have to be removed by the cooling system. Fans and pump are widely used for creating air flow and oil flow to cool the power transformer. As part of the power transformer, the cooling system usually adds a non-negligible contribution to the noise emission. This aspect is rarely studied in the literature. In this thesis, only the core noise is considered.

## 1.3 State of the art

### 1.3.1 Factors related to core noise

The noise generated by power transformers and inductors [Krell *et al.*, 2000, Valkovic, 1998, Rossi et Le Besnerais, 2015] has been studied for several decades and the related literature is abundant. Up to now, several factors have been claimed to have relevance to the flux distribution and core vibrations, such as material core nature, core joints, clamping stress, and electrical excitation.

- Core shape: Power transformers made of the same material can have totally different performance, depending on the core shapes [Chang *et al.*, 2011]. Not only does the core shape influence the noise emission, but also has an impact on the winding section, copper fill factor, efficiency, power density, and thermal performances. Shuai *et al.* [Shuai et Biela, 2015] compares the performances of four power transformer cores with different shapes, including rectangular, square, oval and ring shape, illustrated in Fig.1.7. Both numerical simulations and experimental measurements are carried out in this work. Compared to the conventional rectangular core, the oval core leads to lower vibration and noise emission and further reduction can be achieved by using a ring core. However, the ring core leads to a much lower power density than the other core shapes. There is always a trade-off between different performances of the power transformer, when it comes to a certain application.

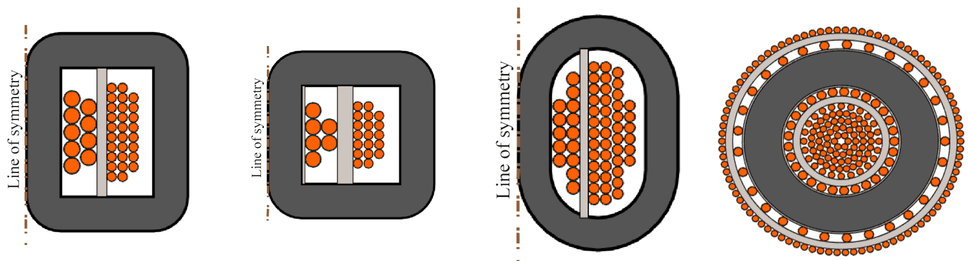


(a) Rectangular core (b) Square core (c) Oval core (d) Ring core

**Figure 1.7:** Studied core shapes in [Shuai et Biela, 2015].

- Core joints: Stacked cores are built up from a stack of electrical sheets, usually cut in form of 'E', 'I' or 'C'. To stack these laminations together, an overlap is often needed to reduce the core noise. The joint with only one step overlap is called single step lap (SSL). The joint with multi-step overlap is called multi step lap (MSL), shown in Fig.1.8. The MSL is widely used in distribution power transformer, in order to allow a better distribution of the magnetic flux at the joints, and thus reduce the core loss and the noise emission [Mechler et Girgis, 2000]. Zhu *et al.* [Zhu *et al.*, 2013] find that filling the multi-joint gaps with nanocrystalline soft magnetic composite material decreases magnetostriction and vibrations of the core because of an improved distribution of magnetic flux. Hsu *et al.* [Hsu *et al.*, 2014] propose a new method to reduce the transformer core noise by re-arranging the step-lapped joint structure. They also found that an increasing number of step laps increases the core losses and vibrations.

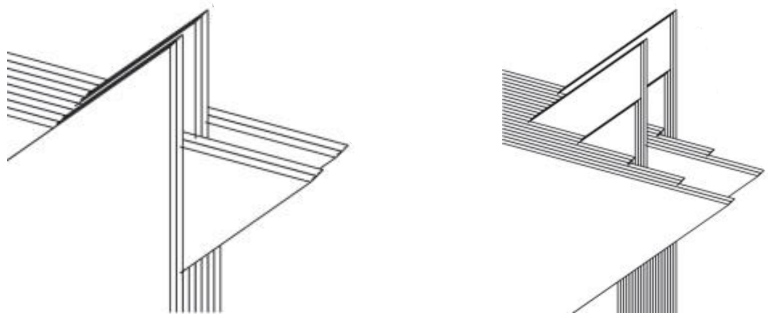

**Figure 1.8:** Single step lap joints (left); Multi step lap joints (right) [Phophongviwat, 2013].

- Clamping stress: The clamping of the power transformer core allows the sheets to be stacked together and provides an additional mechanical rigidity of the structure. Stress reduces the air-gaps between the electrical sheets on the overlap region, and finally has an impact on the core losses and core noise. There are two types of clampings: One in the rolling direction or transverse direction of the electrical sheets, holding the yokes and limbs together. The other, called C-clamp, compresses the sheets together from their upper and lower surface (normal direction). Mizokami *et al.* [Mizokami et Kurosaki, 2015] experimentally demonstrates that the compression clamping stress along rolling direction of the electrical steel increases magnetostriction and noise level. The schematic of the mechanism for applying compression to a limb is shown in Fig.1.9. Meanwhile, Penin *et al.* [Penin *et al.*, 2014b] finds that the C-clamping helps to reduce core noise. The optimized pressure is around $0.8MPa$. A lack of C-clamping or a non-uniform one has a direct and unwanted influence on the core losses and vibrations. However, the clamping of the power transformer is complex and can be difficult to adjust in massive production.

- Current DC bias: Although power transformers are normally designed to operate under sinusoidal excitation, in some particular cases, a direct current (DC) component may be superimposed in primary or secondary windings. This is caused by

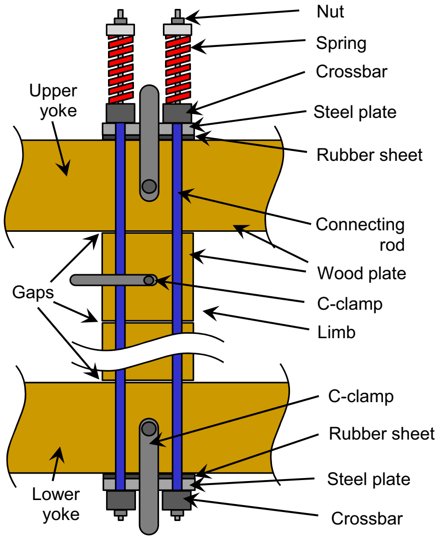


**Figure 1.9:** Schematic of the mechanism for applying compression to a limb of the model core [Mizokami et Kurosaki, 2015].

strong solar flares hitting the Earth's atmosphere, which create induced voltage in the long distance transmission lines. The DC component may lead to the saturation of a half-cycle, which increases the losses, creates more harmonics, and generates more vibrations and noise [Li *et al.*, 2013, Wang *et al.*, 2015]. These effects need to be taken into consideration for the power transformer design. Therefore, a good comprehension of power transformer behavior under DC bias becomes crucial for its optimized design.

- Voltage harmonics: Power transformers are normally connected to the power grid, where the voltage is never purely sinusoidal and contains harmonics. These harmonics of voltage result in harmonics of magnetostriction and magnetic forces, which have a direct impact on the transformer noise. Ghalamestani *et al.* [Ghalamestani *et al.*, 2014] measured the core vibration under voltage harmonics using laser vibrometer. Measurements are carried out at different points of the core, using the third harmonic component with 6%, 8%, 10% amplitude ratios and 0°, 90°, 180° phase delays. Compared to purely sinusoidal voltage excitation, voltage harmonics result in a more complex core deformation, not only in terms of amplitude but also in terms of phase delay.

### 1.3.2 Research approaches

The mechanism of the noise emission of the power transformer core is a complex problem that needs both numerical simulation and experimental measurement to be better understood. Numerical simulations give scientists a global vision of the core distortion. various parameter configurations are able to be easily tested at a very low cost, without fabricating a series of transformer prototypes. However, numerical simulations always come with assumptions and simplifications. This may be the source of discrepancies, which strongly limits its use. On the other hand, experimental setups may not be representative of the real problems: they suffer from the defective material, inaccurate assembling, and other specificities of the fabrication process that are very difficult to reproduce. Due to these factors, transformer prototypes fabricated with the same process may exhibit different noise levels comparing to a real transformer. It is therefore important to develop experiment and modeling at the same time and model the exact experimental setup using the same boundary conditions, even if the setup is not exactly representative of a real transformer. The measured data serves as the fundamental knowledge to correct and guide the numerical simulations. After that, the numerical simulations may easily eliminate bad designs and optimize the performance at an early development stage, in order to accelerate the development of the devices.

Both numerical simulation and experimental measurements face some difficulties. A reliable material model of magnetic and magnetostrictive behavior is the fundamental element in the numerical simulation. It has to be nonlinear and anisotropic, and most importantly be compatible with the finite element resolution. Several key points of the modeling chain need to be carefully considered in order to achieve the balance between the efficiency and accuracy, for example the size of the mesh, strong/weak coupling strategy, and nonlinear system resolution. In terms of experimental measurement, it's never easy to measure the vibration at a precision lower than $0.1\mu m$, so that the equipment needs to be well selected and signals need to be carefully processed.

### Numerical simulation

In terms of modeling, efforts have been made to estimate the magnetostriction induced deformation, vibration and noise emission of the power transformer cores.

Hilgert *et al.* [Hilgert *et al.*, 2008] focus on the vibrations modeling of magnetic cores of power transformer due to magnetostriction. A neural network based model is used to describe the hysteresis effect of the magnetostriction. The parameters of this model are first adjusted by a series of magnetostriction measurement. It is then implemented to the modeling chain for the vibration computation. This method is used to calculate the vibration of a three-phase power transformer (50kVA). However, this neural network must be trained in order to produce the correct results. This training requires a lot of measurements.

Yang *et al.* [Yang *et al.*, 2016] give a complete finite element analysis modeling chain from current injection to the noise emission. Vibration and noise generated from both windings and core of a 110 kV oil-immersed transformer are studied. The electromagnetic analysis is carried out with transient state analysis using commercial software ANSYS, including Lorentz forces, magnetic forces, and magnetostriction. Harmonic analysis is then performed for the mechanical computation. The surface vibration of the windings and core is then considered as the source term in the acoustic analysis. The authors claimed to obtain good agreements between the simulated and measured noise level. However, in terms of magnetic material properties, little information is provided in this paper. The magnetic and magnetostrictive behavior laws used in this modeling chain is isotropic and stress independent, which might lead to some additional discrepancies between the experiment and modeling.

Shuai *et al.* [Shuai et Biela, 2015] push it even further to the optimization step, taking efficiency and vibration as criterions. Studies are carried out on medium frequency transformers, which are smaller in size and weight compared to conventional low frequency (50 Hz) transformer. However, the increase of frequency adds some drawbacks, such as losses and vibration. The numeric modeling process is divided into four sections, electromagnetic model, magnetic force and magnetostriction computation model, mechanical model, and acoustic model (Fig.1.10). Based on a sectional weakly coupled modeling chain, an optimization procedure is applied to optimize both magnetic materials and core shapes. The core made of nanocrystalline material is predicted to be ideal for low noise transformer design, and that is confirmed by measurements. In terms of core shape, the ring core tends to have the lowest noise emission, but is higher in volume. However, the magnetic and magnetostrictive model used in this work is too simple to reproduce the real material property.

Similar studies [Belahcen *et al.*, 2015, Mbengue *et al.*, 2016, Vanoost *et al.*, 2015] have been made by implementing an anisotropic, nonlinear and stress-dependent material model to simulate the vibration due to magnetostriction. However, the magnetic circuits they worked on are generally simple, and seem to be far from a laminated three-phase transformer core.

### Experimental measurements

Experimental measurements are also an important way to understand the vibration and noise emission of the power transformer. Unfortunately, no international standard exists for power transformer vibration characterization. Large industry groups such as ABB are rarely associated to publications where the vibration of thier transformers is considered. Researchers and scientists mainly from Austria, England, France, and China have developed various systems and methods to make measurements of the core vibration and noise.

Shuai *et al.* [Shuai et Biela, 2014, Shuai et Biela, 2015] fixed the core to a metal plate with relative large weight for stability. Soft foam materials are used between the core and the metal parts in order to reduce the mechanical influence of the setup. Fig. 1.11 gives the schematic of the measurement setup, including the command, power, sensors, and the transformer core. A signal generator works together with a power amplifier to generate sinusoidal voltage excitation in the windings. Laser vibrometer is used to scan the core surface and record the speed, leading to a 3D surface speed field. A microphone connected to the acoustic data acquisition system is also provided, in order to record the noise emission of the core. Wang *et al.* [Wang *et al.*, 2015] established a test platform

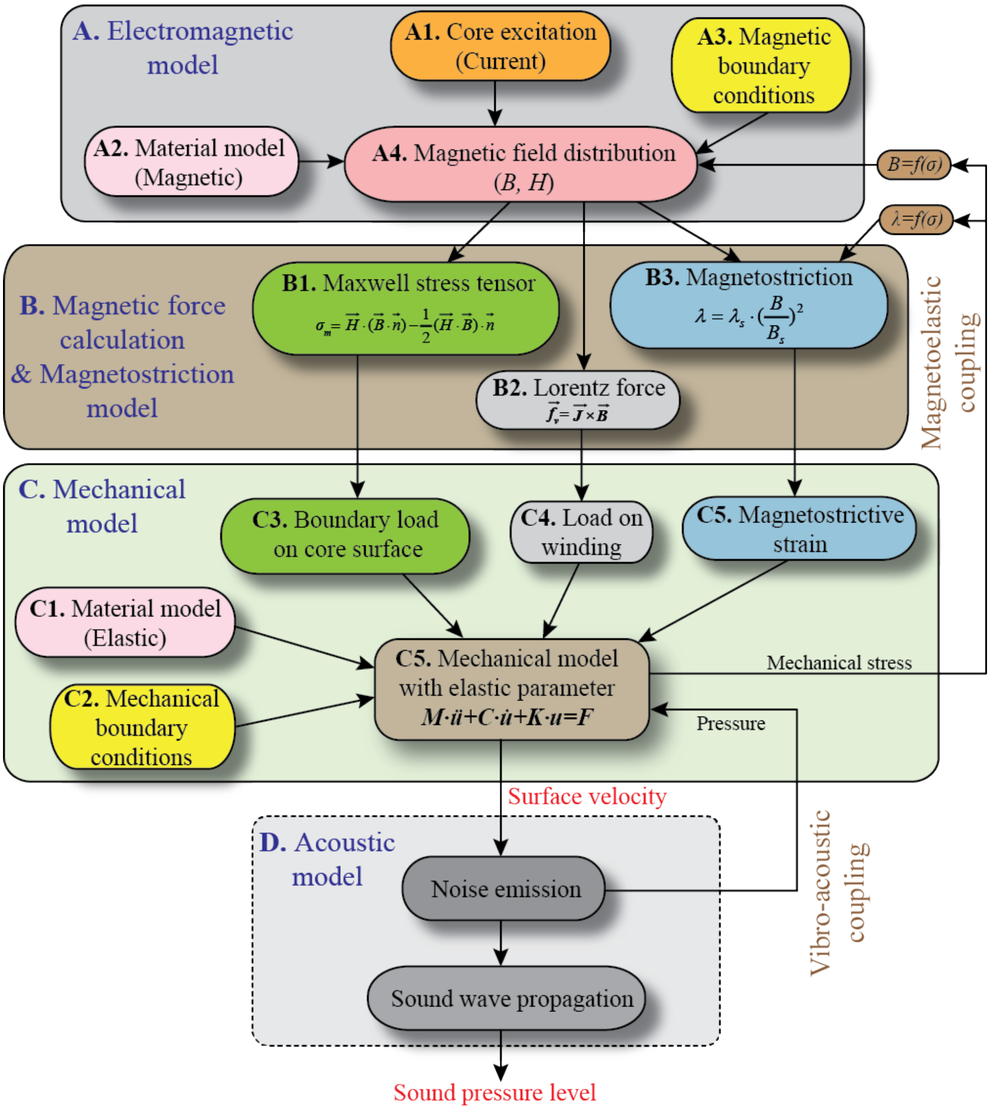


**Figure 1.10:** Modeling process of core vibration [Shuai et Biela, 2015].

using acceleration sensors, signal conditioners, and data acquisition cards. Compared to laser vibrometer, the acceleration sensor is relatively of low cost and easier to install. Hsu *et al.* [Hsu *et al.*, 2015a, Hsu *et al.*, 2015c] make the comparison of the noise emitted by different transformer cores, using a direct measurement of sound pressure. By varying the physical parameters of the power transformers, an experience-based noise computation equation is finally deduced.

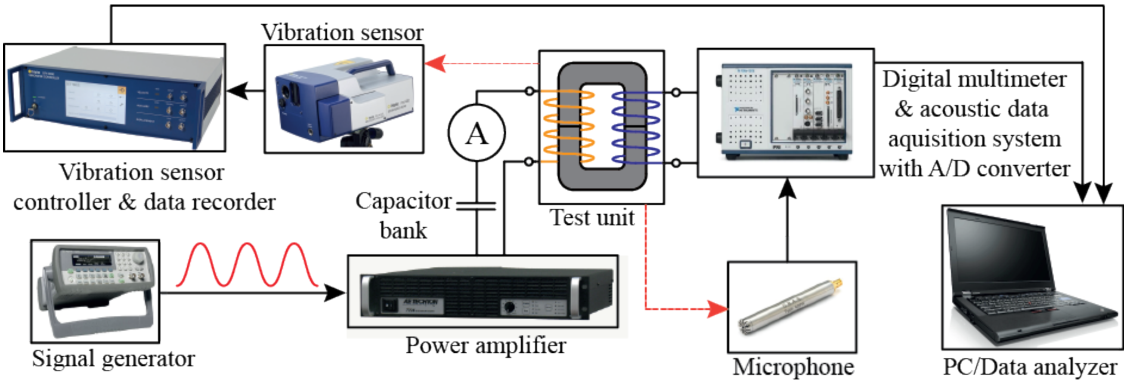


**Figure 1.11:** Schematic of measurement setup [Shuai et Biela, 2014].

## 1.3.3 Research scale

Although power transformer is treated as a component of the electrical system, it may be a complex system itself. To study the power transformers properly, investigations need to be carried out at different scales. At the lowest scale, is the electrical steel sheet. These materials are famous for the complex magnetic and magnetostrictive behavior such as non-linearity, saturation, anisotropy, hysteresis, and stress dependency. A good understanding of the electrical steel sheet behavior is fundamental. Power transformer cores are assembled with hundreds of electrical steel sheets, creating air-gaps between sheets and layers. Techniques are developed to reduce the influence of the air-gaps. At the largest scale is the power transformer. A real transformer is studied with electrical excitation. A series of analysis is able to be carried out in both time and frequency domains.

### Electrical steel sheet scale

The electrical steel sheet is regarded as the basic component of a power transformer core. Having an accurate measurement and model of the electrical sheet behavior is fundamental to the design and model the power transformer.

Pfutzner *et al.* [Pfützner *et al.*, 2011, Shilyashki *et al.*, 2014a] have worked on the characterization of the electrical sheet submitted to a rotational magnetization. Rotational magnetization is particularly important when rotating machine cores are considered and at the T joint of power transformer cores. As the demand of high-precision modeling of these devices grows, measurement of the losses and magnetostriction under rotational magnetization become an important issue. A system named rotational single sheet tester has been developed Pfutzner *et al.* with a 3-phase excited system, creating rotational magnetization (Fig.1.12). The magnetic field pattern can be detected by means of a pair of tangential field coils, shown as in Fig.1.12(b). The induction pattern is obtained by the well-known needle method. Losses are then computed from the measured magnetic field and magnetic flux density. The effective evaluation of magnetostriction is possible by a set of strain gauges. Based on this system, various measurements can be carried out by varying the angular velocity, induction amplitude, and the axis ratio (the ratio between the magnetic flux density along RD and TD, defined as $\alpha$). Some of the conclusions are listed below:

- Losses increase with the rising of axis ratio $\alpha$ and velocity of the induction vector
- Compared to alternative magnetization, rotational magnetization causes much more magnetostrictive strain.
- The maximum magnetostriction along RD increases as axis ratio rises.

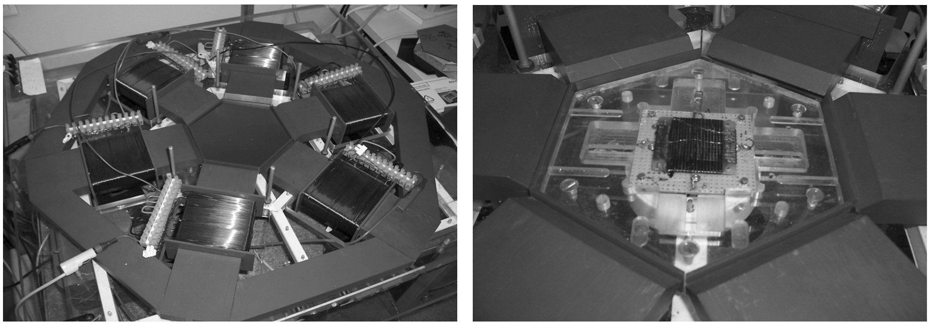

(a) Total view with sample (b) Detail without sample

**Figure 1.12:** Rotational single sheet tester [Pfützner *et al.*, 2011].

Lundgren *et al.* [Lundgren, 1999] have introduced a mathematical model to describe the magnetostriction under rotational magnetization. This model uses an analogy with the mechanical elasticity expressed as in eq.1.1.

$$\begin{pmatrix} \varepsilon_x^M \\ \varepsilon_y^M \\ \gamma_{xy}^M \end{pmatrix} = \begin{bmatrix} \frac{1}{P} & -\frac{\xi}{P} & 0 \\ -\frac{\xi}{P} & \frac{1}{P} & 0 \\ 0 & 0 & \frac{2(1+\xi)}{P} \end{bmatrix} \frac{1}{\mu_0} \begin{pmatrix} B_x^2 \\ B_y^2 \\ B_x B_y \end{pmatrix} \tag{1.1}$$

where $B_x$ and $B_y$ are the components of the magnetic flux density in the X-Y plane. Considering that the magnetostriction depends on the square of the magnetic flux density, so $\frac{B_x^2}{\mu_0}$, $\frac{B_y^2}{\mu_0}$, and $\frac{B_x B_y}{\mu_0}$ are considered as magnetic stresses. $P$ and $\xi$ are respectively the 'magnetic' Young's modulus and 'magnetic' Poisson's ratio. This model can be extended to the anisotropic and angular velocity dependent cases. Somkun *et al.* [Somkun *et al.*, 2010] observed a good agreement between the modeled and measured magnetostriction in NO FeSi steel sheet. However, due to the quadratic relation between the magnetostriction and the magnetic induction, the application of this model is restricted to 'traditional' materials.

Modeling of magnetostriction hysteresis loop with or without applied stress is reported in [Daniel *et al.*, 2015] and [Baghel *et al.*, 2015]. These works bring fundamental approaches for a precise modeling of the transformers dynamic behavior.

### Lamination structure scale

Difficulties arise when electrical sheets are assembled together, forming the laminated structure. In this case, magnetic flux may go from layer to layer and causes inhomogeneity through the layers. At the joints of the sheets, often called overlap region, the presence of the air-gaps creats magnetic forces, which then leads to in-plane vibration.

Ebrahimi *et al.* [Ebrahimi et Moses, 1991] have worked on the normal flux transfer from layer to layer during the magnetization process. Pairs of 0.27-mm-thick GO FeSi are magnetized at frequencies of 50 and 60 $Hz$. Search coils are glued in several test points between the two layers, in order to capture the normal magnetic flux. Conclusions are that the normal magnetic flux increases with the frequency. Moreover, when small and misoriented grains are in contact in the plane, an increase of normal flux is observed. From these conclusions, the authors made predictions that the normal flux will be lower in large grain, well-oriented materials such as domain refined steels. It is also believed that a normal flux greater than $1mT$ causes an increase in surface eddy current losses. This point needs further investigation to be confirmed.

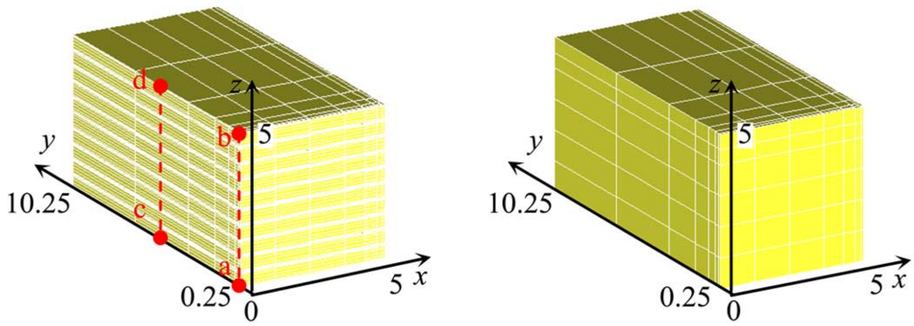


(a) Laminated core (b) Solid and homogeneous core

**Figure 1.13:** Meshes of the laminated and solid homogeneous core [Gao *et al.*, 2011a].

Gao *et al.* [Gao *et al.*, 2011a] developed a homogenization law for laminated cores, in terms of both magnetic and mechanical properties. By applying this homogenization technique, a laminated core is represented by a homogeneous core model, as shown in

Fig.1.13. Homogenized magnetic behavior is obtained by averaging the permeabilities in air $\mu_0$ and iron $\mu_i$ with the consideration of space factor $F$. Space factor $F$ is defined as the ratio between the sectional surface of the iron and the total sectional surface of the laminated core.

$$\mu_{||} = F\mu_i + (1-F)\mu_0 \tag{1.2}$$

$$\mu_{\perp} = \frac{1}{F/\mu_i + (1-F)/\mu_0} \tag{1.3}$$

where $\mu_{||}$ and $\mu_{\perp}$ are respectively the homogenized in-plane and out-of-plane permeability. According to the numerical simulation, the solid homogenized model gives an accurate prediction of the distribution of the magnetic flux, while keeping the computation cost relatively low. The similar idea is applied to the mechanical properties of the laminated core. The magnetic forces and the displacement fields are then computed. Good agreements are observed between the laminated core model and the bulk homogeneous model. Similar works can be found in [Hihat *et al.*, 2011], where the authors focus on the homogenization technique for the overlap joints of the laminated core. This leads to a precise 2D description of a complex 3D overlap joint. Validation of the model is carried out by both 3D simulation and experimental measurements.

Some studies about in-plane and out-of-plane vibration of a laminated structure have been recently addressed by Javorski et al. [Javorski *et al.*, 2013]. An analytical model is used to describ the magnetostrictive strain in the three directions. A model of dry friction between the lamination and at the interlaminar contact is applied to compute the mechanical behavior of this laminated structure. Experimental measurements are also carried out. They are in accordance with the vibration predicted by the numerical model. This work reveals the importance of research on the cross-axis transmission of vibrations.

### Power transformer scale

At the scale of the entire power transformer, studies revealed the role of magnetostriction and magnetostatic forces in the generation of vibration and noise in transformer cores. The noise of the transformer core can be roughly separated into two parts. The first one is due to the magnetostriction along the bulk parts of the core (yokes and limbs), which depends largely on the magnetic material. The second one comes from core joints between the limbs and yokes, due to the interaction of the sheet ends. The latter can be largely reduced by effective clamping and by the use of multi-step-lap joints. However, the mechanism of noise generation at the core joint remains poorly understood.

Weiser *et al.* [Weiser et Pfützner, 1998, Krell *et al.*, 2000, Weiser *et al.*, 2000] are the first who developed some systems to study the vibration of the transformer cores, and give detailed explanations of the noise generation mechanism at the core joints. Different core prototypes are built with different design parameters, such as overlap length, number of the overlap steps, and mean air-gap length. Measurements of the core noise and acceleration of the core surface are carried out. An example of measured surface displacement of a core is given in Fig.1.14. Mechanisms of the noise generation at the core joints are explained, including (a) interlaminar repulsive forces between sheets due to in-plane magnetic flux; (b) in plane attractive forces between sheets ends; (c) interlaminar attractive forces between sheet ends in the core joints. A schematic outline of these three possible mechanisms of the orgin of the noise generation is given in Fig.1.15

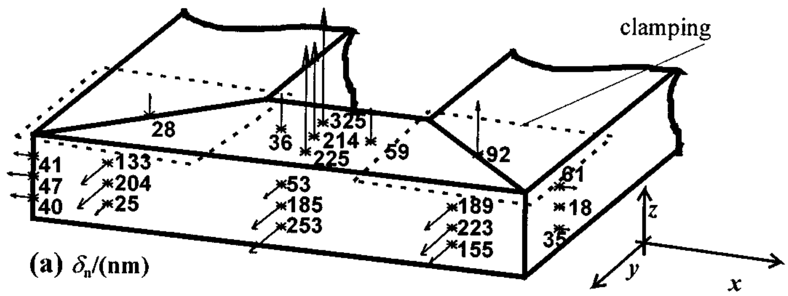


**Figure 1.14:** Typical surface displacements $\delta_n$ of a core with well compressed MSL corner regions (Magnetic induction equals $1.6T$, Number of overlap steps equals 2, number of lamination equals 110, outside core dimension equals $400 \times 210mm$) [Weiser et Pfützner, 1998, Weiser *et al.*, 2000].

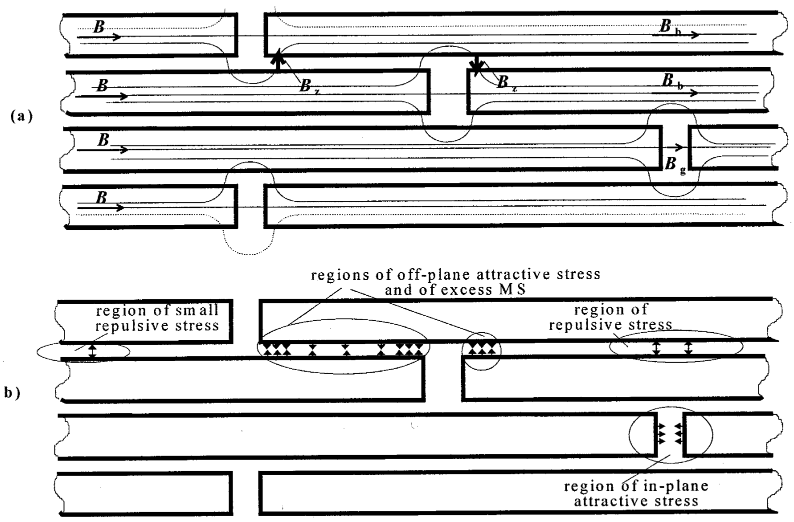


**Figure 1.15:** Schematic outline of these three possible mechanisms of the noise generation (a) magnetic flux distribution; (b) forces. [Weiser *et al.*, 2000].

## 1.4 Objective and strategy

This work proposes a complete modeling chain of a multilayered transformer, from material characterization to the estimation of core vibrations. A complete chain from the material and external loading to the prediction of the transformer deformation is presented, leading to the possibility of a global optimization including the design, assembly, and magnetic material behavior. It involves magnetic material characterization and modeling, finite element modeling chain, validation simulation and measurement, and finally optimization. The global strategy and achievement can be summarized and divided into four parts:

- A powerful material model is necessary, considering magnetic and magnetostrictive nonlinearity, anisotropy, and stress dependency.
- A homogenization procedure (rule) is needed, in order to consider the laminated structure in a 2D simulation.
- A strongly coupled finite element modeling chain is essential, from electrical excitation to core vibration and finally acoustic power estimation. Electromagnetic and acoustic optimization of the power transformer is made possible thanks to this modeling chain.
- Measurements on transformer prototype have to be finally carried out, validating (or invalidating) the numeric simulation.

### 1.4.1 Material model

It involves a simplified multi-scale model, based on the energetic description of the equivalent single crystal, in order to deal with the magnetic and magnetostrictive nonlinearity, anisotropy, and stress dependency. This model is applied to various magnetic materials such as Non-Oriented FeSi, Grain Oriented FeSi, FeNi Supra50, and FeCo Afk1. This model is the simplified version of this multi-scale model, which makes the best compromise of the precision and computation speed and is fully implemented in the finite element modeling chain for 2D simulation. A hysteresis extension of the full multi-scale model under the rotational field is also proposed. Accurate predictions of hysteresis loss under rotational field are achieved by a multi-scale model for the first time. Further simplification and finite element implementation of this formulation are still in process.

### 1.4.2 Homogenization procedure

As the studied power transformer is equipped with a laminated 'E-I' core, the magneto-elastic and magnetic behavior may not be homogeneous throughout the thickness. We have developed a magnetic and a mechanical mixing rule, in order to consider the laminated structure of the E-I stacked core in a 2D simulation. Other mechanisms coming from assembly precision and air gaps that may have also an influence on the sound emission are not considered in this modeling chain.

### 1.4.3 Finite element modeling chain

It proposes a **strongly** coupled finite element modeling chain, including magnetic resolution, force computation, mechanical feedback loop, harmonic mechanical resolution, and acoustic power estimation. This works with both the magnetic flux and winding current as the source term (excitation), together with circuit coupling. The core analysis and comparison at the same power level are facilitated. By imposing directly the magnetic flux in limbs, or coil current in each phase, displacement fields and acoustic power estimation of the transformer core are finally obtained. An optimization process is finally carried out to optimize the core dimensions, offering optimized electromagnetic and vibrational performances. Parallel computing and fast convergence method (such as the Newton-Raphson method) are also achieved to accelerate the numerical simulation.

### 1.4.4 Validation model/measurement

A benchmark is developed to measure the core distortion and noise emission on core prototypes. Comparisons between simulations and measurements allow the modeling chain to be validated for various cases, using different materials and core structures. Some important conclusions are made thanks to the measurements.

## 1.5 Conclusion

As shown in this state of the art, the noise of the power transformer has been studied for several decades. Numerous relative literature is found focusing on different aspects of the noise generation. Despite strong recent efforts in this field, no commercial software nor academic code is yet available to estimate and optimize the global deformation or noise level of a laminated transformer core, with the consideration of material anisotropy, nonlinearity of the magneto-mechanical behavior, and stress dependency. More importantly, numerical simulations proposed in the literature are rarely validated by experimental measurements carried out on a real structure.

This state of the art allows on the other hand to identify several key points and possible improvements. First, a complete modeling chain needs to be proposed, from the excitation (coil current or magnetic flux in the limbs) to the noise emission. Such a modeling chain needs a strong coupling to be established between the magnetic and mechanical aspects. Second, the material model is usually poor and needs to be improved. The magnetic and magnetostrictive anisotropy and stress dependency have to be considered. Ideally, this model must be able to adapt to various materials with different behaviors. Third, a homogenization strategy has to be considered to model the laminated structure of the stacked power transformer. Last, the numerical modeling has to be compared to experimental measurements obtained in the same condition to ensure a complete validation. Ideally, the validation is carried out under various materials, structures, and test conditions.

# Chapter 2

# Constitutive Law by Multiscale Modeling

## Contents

# 2.1 Introduction: basic ferromagnetism

## 2.1.1 Free energy of magnetic materials

### Free energy (internal energy) of a magnetic domain

At the atomic grouping scale, the magnetic equilibrium state can be described by different energy terms [Hubert et Schäfer, 1998]. The free energy is defined as:

$$W = W_{ex} + W_{mag} + W_{an} + W_{el} \tag{2.1}$$

- $W_{ex}$ refers to the exchange energy.
- $W_{mag}$ refers to the magnetostatic energy.
- $W_{an}$ refers to the magneto-crystalline anisotropy energy.
- $W_{el}$ refers to the elastic energy.

Each magnetic domain is characterized by its magnetization $\vec{M}$ oriented along direction $\vec{\gamma}$ and its magnetostriction strain $\epsilon_\mu$.

$$\vec{M} = M_s\vec{\gamma} = M_s[\gamma_1\,\gamma_2\,\gamma_3]^t \tag{2.2}$$

$M_s$ is the saturation magnetisation. $\gamma_1$, $\gamma_2$ and $\gamma_3$ are the direction cosine of magnetization direction $\vec{\gamma}$ in the crystal frame (CF). For typical cubic crystallographic symmetry, it is usual to define the free magnetostriction strain $\epsilon_\mu$ as:

$$\epsilon_\mu = \frac{3}{2}\begin{pmatrix} \lambda_{100}(\gamma_1^2 - \frac{1}{3}) & \lambda_{111}\gamma_1\gamma_2 & \lambda_{111}\gamma_1\gamma_3 \\ \lambda_{111}\gamma_1\gamma_2 & \lambda_{100}(\gamma_2^2 - \frac{1}{3}) & \lambda_{111}\gamma_2\gamma_3 \\ \lambda_{111}\gamma_1\gamma_3 & \lambda_{111}\gamma_2\gamma_3 & \lambda_{100}(\gamma_3^2 - \frac{1}{3}) \end{pmatrix}_{CF} \tag{2.3}$$

where $\lambda_{100}$ (resp. $\lambda_{111}$) is the saturation magnetostriction strain along the $< 100 >$ (resp. $< 111 >$) direction of the single crystal.

### Exchange energy

The exchange energy corresponds to the electromagnetic coupling between the neighbor magnetization vectors, which tends to unify the magnetization direction. It is defined as follows:

$$W_{ex} = A \cdot (\nabla\vec{\gamma})^2 \tag{2.4}$$

$A$ is a constant parameter depending on the material. The exchange energy is null when the spatial variation of the magnetization direction is null.

### Magnetostatic energy

$W_{mag}$ (equation (2.5) - where $\mu_0$ is the vacuum permeability) tends to align the local magnetization $\vec{M}$ along the magnetic field $\vec{H}$. This energy reaches its minimum when the magnetization lines up with the magnetic field.

$$W_{mag} = -\mu_0\vec{M}\cdot\vec{H} \tag{2.5}$$

### Magneto-crystalline anisotropy energy

$W_{an}$ (equation (2.26)) tends to align the magnetization direction along the easy axes. In the form of cubic crystallographic symmetry proposed hereafter, $K_1$ is the so-called magneto crystalline energy constant and $K_2$ the second order terms.

$$W_{an} = K_1 \left(\gamma_1^2\gamma_2^2 + \gamma_2^2\gamma_3^2 + \gamma_3^2\gamma_1^2\right) + K_2 \left(\gamma_1^2\gamma_2^2\gamma_3^2\right) \tag{2.6}$$

### Elastic energy

$W_{el}$ (equation (2.7)) is the elastic energy, expressed as a function of the local stress.

$$W_{el} = \frac{1}{2}\boldsymbol{\sigma} : \mathbb{C}^{-1} : \boldsymbol{\sigma} \tag{2.7}$$

where $\mathbb{C}$ is the local elasticity tensor. This local stress can be expressed as a function of the free magnetostriction strain depending on the assumptions, leading to the so-called elastic energy equations.

## 2.1.2 Magneto-mechanical coupling

The magneto-mechanical coupling phenomena in ferromagnetic materials have two main manifestations: magnetostriction strain and the effect of stresses on magnetization.

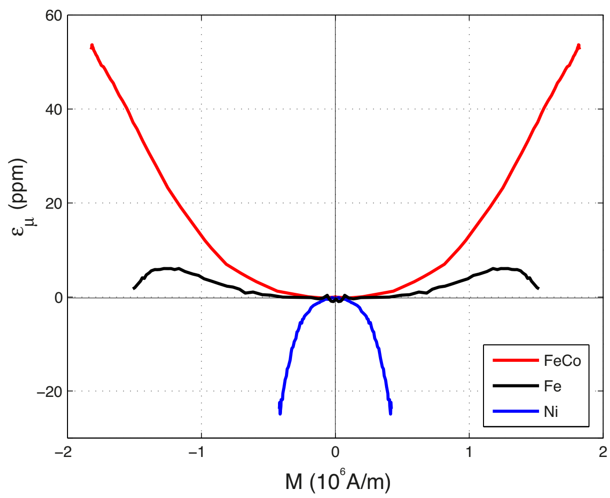


**Figure 2.1:** Longitudinal anhysteretic magnetostrictions of three ferromagnetic materials - measurements carried out at LMT [Fall, 2017].

### Magnetostriction

When a ferromagnetic material is submitted to a magnetic field, it deforms. This strain is associated with two distinct phenomena (already introduced):

- The magnetic forces, associated with the magnetization gradients, cause a purely elastic strain. This is a structural effect not considered in a constitutive behavior law.

- A 'spontaneous' strain, intrinsic to the material, also appears (Joule's strain). This strain is related to the re-arrangement of the domains and/or the modifications of the lattice parameters that are a function of the local magnetization.

Only the second phenomenon is called magnetostriction and noted in the tensor form $\epsilon_\mu$. Similar to the magnetic behavior, the magnetostrictive behavior $\epsilon_\mu(\vec{M})$ is strongly nonlinear (see magnetostrictive behavior for three different materials measured at LMT - 2.1). This nonlinearity is associated with the existence of a maximum strain, called saturation strain (scalar value usually noted as $\lambda_s$). The main features of magnetostriction are its sign ($\lambda_s$ can be positive or negative), its amplitude ($\lambda_s$ varies typically from 0 to $10^{-3}$ depending on materials), and this strain is volume-conservative (isochoric) ($tr(\epsilon_\mu) = 0$) for magnetic materials [Du Trémolet de Lacheisserie, 1993b, Du Trémolet de Lacheisserie, 2002] (It is true up to certain values of magnetization after which there volume magnetostriction starts to appear).

### Magnetic behavior under stress

The application of a stress modifies considerably the magnetic behavior. This effect is documented from the 19th century. In the case of nickel, a uniaxial compression stress of $-70MPa$ doubles the initial permeability; A uniaxial tensile stress of the same amplitude divides it by 10.

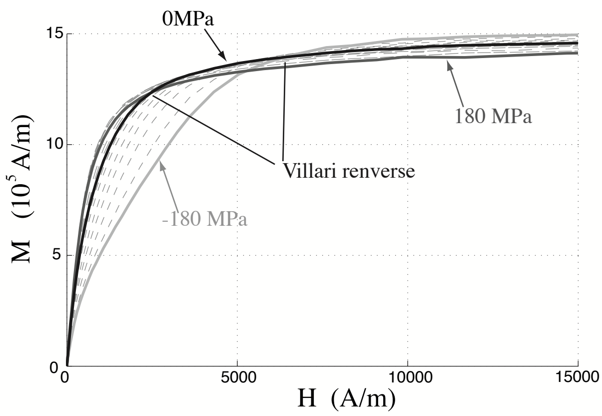


**Figure 2.2:** Stress effect on the magnetization of a low-carbon steel (0,18wt%) [Lollioz *et al.*, 2006].

The behavior of iron is more complex (figure 2.2): a tensile stress causes an increase in permeability at low magnetic fields but a decrease at high magnetic field. This phenomenon is called 'Villari effect' or 'Villari reversal'. On the other hand, a compression stress generally leads to a drop in the permeability. In all other cases, the influence on the magnetic behavior of the applied stress is not symmetric under tensile and compression stress. This mechanism, can be explained in the following way: Locally, the strain $\epsilon$ is the sum of two strains, the elastic strain $\epsilon_{el}$ of mechanical origin and the magnetostriction strain $\epsilon_{\mu}$ (equation 2.8). The stress is linearly associated to the elastic strain via the local Hooke's law. $\epsilon_{\mu}$ denotes the 'free' magnetostriction strain, in other words, the magnetostriction strain we observed if the material could deform freely. In reality, deformation incompatibilities appear. The elastic energy can thus increase or decrease as a function of the magnetostriction (arrangement of the microstructure). The magnetic behavior becomes consequently a function of the applied stresses. The stress causes a re-arrangement of the microstructure.

$$\epsilon = \epsilon_e + \epsilon_{\mu} \tag{2.8}$$

### 2.1.3 Magnetic material composition

#### Crystal and Polycrystal

In terms of magnetic structure, all magnetic materials are heterogeneous. These materials, often polycrystals, are composed of small crystals called grains. Depending on the so-called magnetocrystalline energy, each grain defines different easy axes of magnetization. The size and orientations of these grains, known as texture, depends on the chemical composition and the forming process. The area separating two grains is the grain boundary.

#### Magnetic domain

Magnetic domains are observed as a sub-structure of the grain. They correspond to regions where magnetization is uniform and equals to $M_s$. They can be observed through the use of microscopes [Bitter, 1932, Landau et Lifshitz, 1935] (Fig.2.3 illustrates some domains observed by Kerr effect). Each magnetic domain possesses a uniform magnetization, whose norm is $M_s$. From one magnetic domain to another, the magnetization norm remains the same, while its direction varies. A grain is divided into several magnetic domains oriented in different directions to minimize its internal energy. If the grain remains undivided with a constant magnetization all over the grain, strong magnetic poles are created. This requires huge magnetostatic energy stored in the magnetic field. To reduce this energy, grain can split into two domains exhibiting opposite magnetization directions. This allows the magnetic field to go from one magnetic domain into the other, reducing the magnetic field in the outer space, thus reducing the internal energy. This splitting procedure is repeated in each magnetic domain, until the lowest internal energy is achieved, resulting in smaller parallel domains with magnetizations in alternating directions.

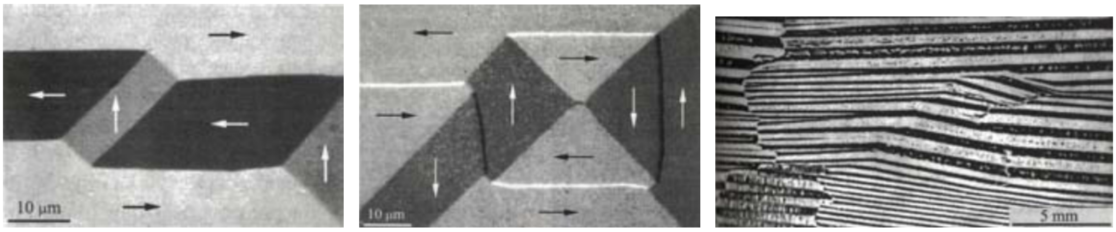


(a) (b) (c)

**Figure 2.3:** Observation of magnetic domains in FeSi [Hubert et Schäfer, 2008].

### Domain wall

The interface between two magnetic domains, where the magnetization direction varies progressively, is called domain wall. This transition usually undergoes an angular variation 90° or 180°. Applied magnetic field causes the movement of the domain walls, leading to the change of the domain volume fraction. Ideally, the domain wall is free to move and depends on the applied magnetic field, but a material contains some defects. The defects reduce the local magnetic energy of the wall itself, leading to the 'pinning' effect. The displacement of domain walls is brake by this effect. Thus the application of a greater magnetic field is required to pass over these defects. This procedure is often called unpinning, and is illustrated in Fig.2.4.

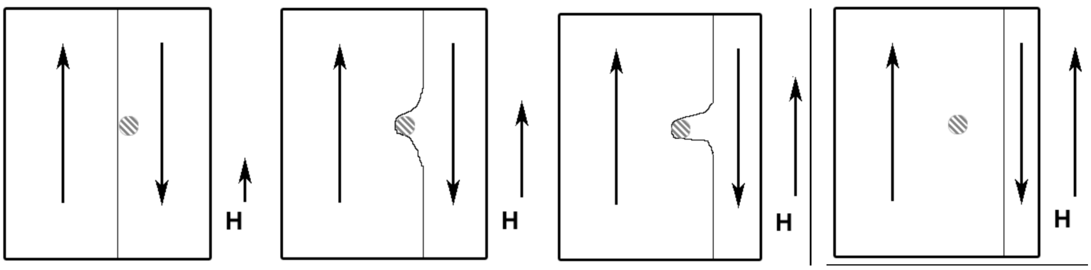


(a) (b) (c) (d)

**Figure 2.4:** The pinning/unpinning procedure of the domain wall.

## 2.1.4 Ideal magnetization process: anhysteretic behavior

The ideal magnetization process is achieved when the magnetic material is considered perfect, meaning defects free. In this case, domain walls are free to move, and no pinning nor unpinning is considered. In the absence of the magnetic field, the magnetization of each domain tends to align spontaneously in the directions of 'easy' magnetization, leading to the domain structure. When a magnetic field is applied, two distinct magnetization mechanisms appear that modify the magnetic equilibrium:

- movement of magnetic domain walls, modifying the size of the magnetic domains.
- rotation of the magnetic moments, modifying the average direction of magnetic domains and the magnetization direction.

In the case of materials with high magnetocrystalline anisotropy, the wall movements mechanism is dominant at the weak magnetic fields and rotation occurs at more intense magnetic fields. The ideal magnetization process of such materials is shown in Fig.2.5 from the demagnetized state to the saturated state. This is combined with an illustration of magnetic domains evolution. Fig.2.5(a) refers to the demagnetized state without applied field. When the external magnetic field is applied, concomitant mechanisms of movement of the domain wall and rotation appear. At small applied field, where magnetization curve is almost linear, the mechanism of domain wall movement is dominant, as shown in Fig.2.5(b). The 'knee' of the magnetization curve indicates that the magnetic domain rotation starts as shown in Fig.2.5(c). The modeling of this zone, where both two magnetization mechanisms occur, is key for magnetic cores of the transformer application. At the extremely high field, the magnetic material reaches the saturation and the rotation mechanism dominates, as shown in Fig.2.5(d).

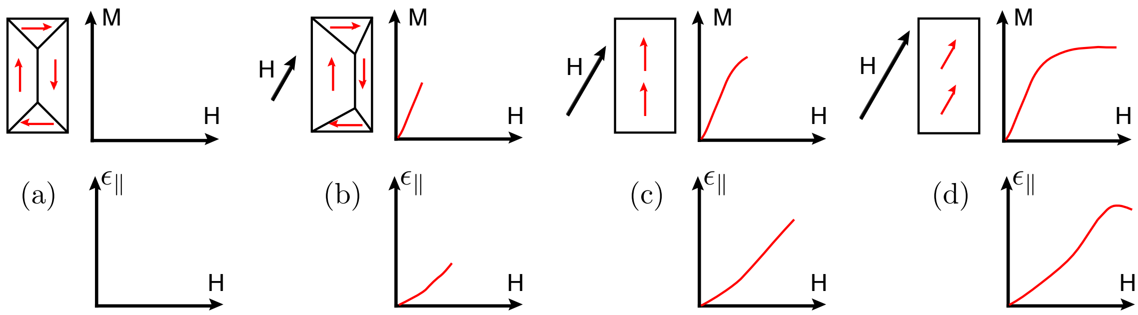


**Figure 2.5:** Ideal magnetization process: magnetization curve [Daniel, 2003] and magnetostriction curve.

### 2.1.5 Real magnetization process: hysteretic behavior

In a real magnetization process, the domain walls need to cross over the crystallographic defects and consume extra energy, associated to pinning and unpinning process. Theses effects lead to an irreversible magnetization process, known as magnetic hysteresis.

Hysteresis is the dependence of the state of a system on its history. For example, magnetic materials may have more than one possible magnetization state at a given magnetic field, depending on the loading history. It is, in fact, a lag between the applied magnetic field and the magnetization of the material. Plots of magnetic induction as a function of a periodically applied field often forms a loop, known as the hysteresis loop. The surface of this loop gives the magnetic losses. It is one of the most important sources of the losses in electrical devices. (Other losses include: eddy current and excess in sheets and joules losses in windings)

Fig.2.6 gives a general illustration of a hysteretic magnetization process for a 2D single crystal. Similar to the ideal magnetization process, real magnetization process starts from the demagnetized state with zero external magnetic field. Then domain walls begin to move under the action of the external field until they meet the crystallographic defects. The pinning and unpinning process follows as external magnetic field continues to increase. Because of the existence of crystallographic defects, the displacement of domain walls is smaller than the expected ideal magnetization process. In other words, for the first magnetization, the pinning and unpinning process slows down the magnetization process, and the level of magnetization reached is actually lower than it would be in the ideal case. Rotation of the magnetic moments appears and becomes dominant at higher external magnetic field. When the material is highly saturated, domain walls disappear. Grains theoretically become domains.

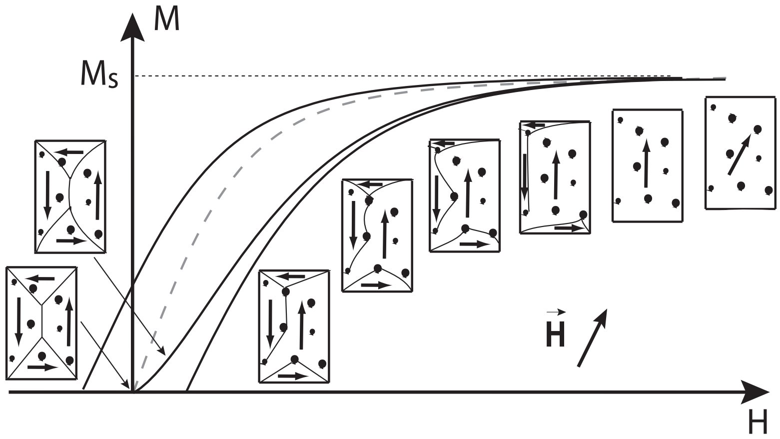


**Figure 2.6:** Real magnetization process [Rekik, 2014]

The grain then splits into small domains when the magnetic field decreases, leading to new walls. As the external magnetic field continues to decrease, domain walls move to meet back the crystallographic defects, and cross back these defects. This time, the crystallographic defects prevent the domain wall from turning back, so that the actual magnetization is higher compared to the magnetization of a perfect magnetic material. Even if the external magnetic field is decreased to zero, the magnetization remains positive, leading to the remanent magnetization. The remanence level depends on the type of material, textures, fabrication process, and maximum applied magnetic field.

## 2.2 Multiscale magneto-mechanical modeling of anhysteretic behavior

### 2.2.1 State of the art: anhysteretic model

There are many models for magnetic materials. They are not distinguished by their characteristic scales, the consideration of certain phenomena (hysteresis, eddy currents, coupling to mechanics...) nor the resolution methods.

#### Micro-magnetic approaches

Micromagnetism is a theoretical approach to describe the magnetization process at $\mu m^3$ scale. This scale is broad enough so that the discrete character of atomic magnetic moments can be replaced by continuous functions and sufficiently fine to consider the transition zones between the domains. The numerical resolution is in charge of minimizing the energetic function containing nonconvex terms (magnetocrystalline anisotropy energy) and interface terms (exchange energy). The solution of the problem is not unique and depends on the initial domain configuration and steps (numerical discretizations) of the calculation. Magneto-mechanical coupling is achieved by the introduction of elastic energy and the free magnetostriction [Mballa-Mballa *et al.*, 2014]. This method is mainly used to model fine structures at the magnetic domain scale. It is not suitable for the resolution of a polycrystalline REV (Representative Elementary Volume) problem or would lead to prohibitive calculation times otherwise.

#### Macro-magnetic approaches

Among the macroscopic models, anhysteretic and/or hysteretic thermodynamic models, or loss models that do not predict the behavior properly, should be distinguished. Thermodynamic models usually use a separation between nondissipative reversible mechanisms (often associated with Langevin functions) and dissipative mechanisms associated with first or second order differential equations. One of the most famous models is probably the Jiles-Atherton-Sablik model [Jiles et Atherton, 1986a]. It is used by many authors, and implemented in some computational codes. It has been extended to situations as diverse as dynamic behavior, elastic coupling [Sablik et Jiles, 1993] and plasticity. A variant model of this kind has been developed at LMT-Cachan by Gourdin [Gourdin *et al.*, 1998]. The thermodynamic potential formulation makes the elementary macroscopic magnetization (and magnetostriction) accessible, making it possible to describe the minor cycles in particular. The Preisach model [Preisach, 1935] falls into the category of hysteresis models. It involves a series of functions depending on parameters whose physical sense are sometimes difficult to identify. The simplified multiscale model [Daniel *et al.*, 2015] is included in the category of macroscopic models. This results from the work carried out at the GeePs, in continuation with the multi-scale model developed at LMT or the multi-domain model [Lazreg et Hubert, 2011]. Its main characteristic is the use of an equivalent single crystal: a polycrystalline REV can be modeled at a lower cost by the use of an equivalent single crystal whose domain equilibrium is ensured by the use of a Boltzmann function. A coupling of these codes to the Hauser model allows considering the static hysteresis.

#### Multiscale approaches

The main elements of this model will be included in the next subsection of this thesis. We will not, therefore, give a detailed description of this model in this paragraph. Let us simply note that the multi-scale model (MSM), developed over the last twenty years at the LMT [Buiron *et al.*, 1999, Daniel *et al.*, 2008], is based on three different scales and the interactions between them. Given the magnetocrystalline energy, it is possible to divide the crystal into a finite number of magnetic domains families. Each family corresponds to a volume fraction that is a function of its free energy. At the grain scale, the anhysteretic equilibrium corresponds to a certain energetic minimum. This minimum is achieved by combining a Boltzmann-like function to compute the volume fractions of the domain families and the minimization of the total energy to calculate the orientation of the magnetization of the domains. A change of scale (localization and homogenization under certain hypotheses) makes it possible to define the magnetic, elastic and magnetoelastic behavior at the scale of the single crystal (or grain). The second change of scale (localization and homogenization under certain hypotheses) makes it possible to define the behavior of a RVE. The notion of macroscopic anisotropy factors (surface effect, configuration) has been introduced in order to consider the initial anisotropic distribution of the domains.

### 2.2.2 Introduction of the multi-scale model (MSM)

The anhysteretic multiscale elastic coupled model described hereafter [Daniel *et al.*, 2008] is used as the basis of material modeling. First the energetic description of the constitutive law of single crystal is recalled. Then polycrystalline medium behavior is obtained by averaging the single crystal behavior.

#### Behavior of magnetic domain

A single crystal $g$ is considered composed of a series of magnetic domains with random orientations. A magnetic domain family $\alpha$ is defined as a set of magnetic domains oriented to certain direction $\vec{\gamma}^{\alpha}$. The definition of the corresponding magnetization $\vec{M}^{\alpha}$ and magnetostriction strain $\epsilon_{\mu}^{\alpha}$ is recalled here after:

$$\vec{M}^{\alpha} = M_s \vec{\gamma}^{\alpha} = M_s [\gamma_1^{\alpha} \gamma_2^{\alpha} \gamma_3^{\alpha}]^t \tag{2.9}$$

$$\epsilon_{\mu}^{\alpha} = \frac{3}{2} \begin{pmatrix} \lambda_{100}((\gamma_1^{\alpha})^2 - \frac{1}{3}) & \lambda_{111}\gamma_1^{\alpha}\gamma_2^{\alpha} & \lambda_{111}\gamma_1^{\alpha}\gamma_3^{\alpha} \\ \lambda_{111}\gamma_1^{\alpha}\gamma_2^{\alpha} & \lambda_{100}((\gamma_2^{\alpha})^2 - \frac{1}{3}) & \lambda_{111}\gamma_2^{\alpha}\gamma_3^{\alpha} \\ \lambda_{111}\gamma_1^{\alpha}\gamma_3^{\alpha} & \lambda_{111}\gamma_2^{\alpha}\gamma_3^{\alpha} & \lambda_{100}((\gamma_3^{\alpha})^2 - \frac{1}{3}) \end{pmatrix}_{CF} \tag{2.10}$$

where $\gamma_1^\alpha$, $\gamma_2^\alpha$, and $\gamma_3^\alpha$ are the direction cosine of the magnetization $\vec{\gamma}^\alpha$ in the crystallographic frame (CF).

The magnetization and the magnetostriction strain in a magnetic domain are supposed uniform, so that the exchange energy $W_{ex}^\alpha$ in domain family $\alpha$ is null.

$$W_{ex}^\alpha = 0 \tag{2.11}$$

We suppose that the local magnetic field in the magnetic domain is equal to the magnetic field applied to the single crystal ($\vec{H}^\alpha = \vec{H}^g$). With this hypothesis, the magnetostatic energy in magnetic domain family $\alpha$ is expressed as:

$$W_{mag}^\alpha = -\mu_0 \vec{M}^\alpha \cdot \vec{H}^g \tag{2.12}$$

The definition of magneto-crystalline anisotropy energy in magnetic domain remains unchanged. It is recalled hereafter:

$$W_{an}^\alpha = K_1 \left( (\gamma_1^\alpha \gamma_2^\alpha)^2 + (\gamma_2^\alpha \gamma_3^\alpha)^2 + (\gamma_3^\alpha \gamma_1^\alpha)^2 \right) + K_2 (\gamma_1^\alpha \gamma_2^\alpha \gamma_3^\alpha)^2 \tag{2.13}$$

The stress in the magnetic domain $\boldsymbol{\sigma}^\alpha$ is a complex function of the stress applied to the grain $\boldsymbol{\sigma}^g$ and the magnetostriction tensor $\boldsymbol{\epsilon}_\mu^\alpha$. Daniel *et al.* [Daniel *et al.*, 2008] have demonstrated that, with the hypothesis of homogeneous strain in the single crystal, the expression of elastic energy is expressed as:

$$W_{el}^\alpha = \frac{1}{2} \boldsymbol{\sigma}^\alpha : \mathbb{C}^{-1} : \boldsymbol{\sigma}^\alpha \tag{2.14}$$

In order to consider the shape of the material (thin sheet or long bar), a configuration energy $W_{conf}^\alpha$ (equation (2.34)) is considered. This term allows the non-randomness of the configuration of the initial domains to be taken into account (in the absence of applied magneto-mechanical loading) due to plastic deformation [Hubert et Daniel, 2006] or to surface (demagnetizing) effects [Hubert et Daniel, 2008]. This configuration energy can be described by a fictitious residual stress $\Sigma^c$, and is proved to be equivalent to a demagnetizing energy [Daniel *et al.*, 2014], given as:

$$W_{conf}^\alpha = -\boldsymbol{\Sigma}^c : \boldsymbol{\epsilon}_\mu^\alpha \tag{2.15}$$

The local free energy $W^\alpha$ of the magnetic domain family $\alpha$ in a single crystal $g$ is then expressed as:

$$W^\alpha = W_{mag}^\alpha + W_{an}^\alpha + W_{el}^\alpha + W_{conf}^\alpha \tag{2.16}$$

### Grain scale: constitutive law

Once the free energy is known for a given domain family $\alpha$ of direction $\vec{\gamma}^\alpha$, its volume fraction $f^\alpha$ is calculated according to an explicit Boltzmann-type relation (2.17) [Daniel *et al.*, 2008, Buiron *et al.*, 1999]. $A_s$ is an adjusting parameter related to the initial magnetic susceptibility $\chi_0$ of the material in absence of external or configuration loading (2.18).

$$f^{\alpha} = \frac{exp\left(-A_s W^{\alpha}\right)}{\int_{\alpha} exp\left(-A_s W^{\alpha}\right) d\alpha} \tag{2.17}$$

$$A_s = \frac{3\chi_0}{\mu_0 M_s^2} \tag{2.18}$$

Once the volume fractions $f^{\alpha_i}$ of domain family $\alpha_i$ is known for all possible directions (depending on the numerical discretization), the magnetization $\vec{M}^g$ and magnetostriction $\epsilon_{\mu}^g$ of the single grain $g$ are defined as the average values of local quantities (2.23).

$$\vec{M}^g = \int_{\alpha} f^{\alpha} \vec{M}^{\alpha} \quad \text{and} \quad \epsilon_{\mu}^g = \int_{\alpha} f^{\alpha} \epsilon_{\mu}^{\alpha} \tag{2.19}$$

This multi scale model at the grain scale gives finally the average magnetostriction strain and magnetization at a given magnetic field $\vec{H}^g$ and stress $\boldsymbol{\sigma}^g$. This calculation has to be made for each grain of a polycrystalline aggregate.

### From the grain to the polycrystal scale

The orientation of a grain inside the polycrystalline medium is defined by three Euler angles, which are different from one grain to another. This orientation information of the polycrystal is usually called texture, which can be obtained through Electron Backscatter Diffraction (EBSD), forming a so-called Orientation Data File (ODF). The local magnetization and deformation are different from one grain to another, leading to the demagnetizating field and residual stress effect. This effect makes the local magnetic and mechanical loadings ($\vec{H}^g$ and $\boldsymbol{\sigma}^g$) different from the global loadings ($\vec{H}$ and $\boldsymbol{\sigma}$). Typically the calculation of the local loadings are carried out on each grain through a self-consistent polycrystalline scheme [Daniel *et al.*, 2008], where local loadings ($\vec{H}^g$ and $\boldsymbol{\sigma}^g$) are derived from the macroscopic loadings ($\vec{H}$ and $\boldsymbol{\sigma}$), using eq.2.20 and eq.2.21:

$$\vec{H}^g = \vec{H} + \frac{1}{3+2\chi}\left(\vec{M} - \vec{M}^g\right) \tag{2.20}$$

$$\boldsymbol{\sigma}^g = \mathbb{B} : \boldsymbol{\sigma} + \mathbb{L} : \left(\epsilon_{\mu} - \epsilon_{\mu}^g\right) \tag{2.21}$$

$\chi$ is the magnetic susceptibility, $\mathbb{B}$ is the elastic localization operator, and $\mathbb{L}$ is the elastic incompatibility operator. The incompatibility operator defines the compatibility effects resulting from the different behaviors between an isolated grain and the surrounding environment. These tensors depend on the crystallographic orientation of the considered grain. Once this self-consistent procedure is converged, the local magnetic and mechanical loadings ($\vec{H}^g$ and $\boldsymbol{\sigma}^g$) are determined.

However, computation time of such a self-consistent scheme is too high to introduce it in a structural analysis. By neglecting the fluctuations of magnetic field and stress over the volume (uniform magnetic field and stress assumptions), simplification is made to accelerate calculations on local loadings ($\vec{H}^g$ and $\sigma^g$). Once the full knowledge of magnetization $\vec{M}^g$ and magnetostriction $\epsilon_\mu^g$ of each grain is obtained, the macroscopic responses $\vec{M}$ and $\epsilon_\mu$ of the material are obtained from an averaging operation (2.22).

$$\vec{M} = <\vec{M}^g> \quad \text{and} \quad \epsilon_\mu = <\epsilon_\mu^g> \tag{2.22}$$

### 2.2.3 Introduction of the simplified multi-scale model (SMSM)

The full multi-scale model gives a precise description of magnetic and magnetostrictive behavior, however, the computation time is non-negligible considering the complexity of the model. In order to reduce the computation time, some simplifications of this model are necessary. The simplified version of this full multi-scale model is proposed in [Daniel *et al.*, 2014][Daniel *et al.*, 2008], called simplified multi-scale model (SMSM). It involves a simplification of the description of a polycrystal through an equivalent single crystal that will exhibit approximately the same anisotropies, magnetic and magnetostrictive behavior as the polycrystal. The macroscopic magnetic and magnetostrictive behaviors are obtained directly from the magnetic and magnetostriction response of the grain:

$$\vec{M} = \vec{M}^g = \int_\alpha f^\alpha \vec{M}^\alpha \quad \text{and} \quad \epsilon_\mu = \epsilon_\mu^g = \int_\alpha f^\alpha \epsilon_\mu^\alpha \tag{2.23}$$

This SMSM works well for quasi-single-crystal materials such as GO FeSi and FeNi Supra50, because the macroscopic behavior and the behavior of a single crystal is very similar. For other materials whose macroscopic behavior is close to isotropy, the magneto-crystalline anisotropy energy is set to zero. A slight macroscopic anisotropy is then controlled by the configuration energy. In this case, in order to describe correctly the magnetostrictive behavior, an artificial magnetostrictive constant $\lambda_{100} = \lambda_{111} = \lambda_s$ is considered.

### 2.2.4 Extension of the simplified multi-scale model (SMSM)

To adapt the SMSM to different materials and to make possible some sensitivities to the rolling direction of the sheets, some modifications of the SMSM has been proposed in this thesis. In this new SMSM, the local free energy of a magnetic domain $W_{tot}^\alpha$ is expressed as the sum of five contributions (2.24):

$$W_{tot}^\alpha = W_{mag}^\alpha + W_{an}^\alpha + W_{el}^\alpha + W_{conf}^\alpha + W_{struc}^\alpha \tag{2.24}$$

**Magneto-static energy**

The definition of the magnetostatic energy the same in SMSM and MSM:

$$W_{mag}^\alpha = -\mu_0 \vec{M}^\alpha \cdot \vec{H} \tag{2.25}$$

The magnetic field considered is the global magnetic field.

### Anisotropy energy

$W^{\alpha}_{an}$ varies from material to material. The anisotropy energy is seperated in two terms ($W^{\alpha}_{an} = W^{\alpha}_{an1} + W^{\alpha}_{an2}$), presented as follows:

- $W^{\alpha}_{an1}$ applies for materials possessing a very strong textures close to a quasi-single-crystal texture. In this case, the behavior described at the single crystal scale is able to represent the macroscopic behavior. This will be observed later (see Chap.IV). Both FeNi Supra50 and GO FeSi are such materials. In the form proposed hereafter, $K_1$ is the so-called magneto crystalline energy constant and second order terms (e.g. $K_2$) are not considered. $\mathbb{P}$ is a $4^{th}$ order tensor that describes the magneto-crystalline anisotropy in CF - $(xyz)$. $\boldsymbol{Q}$ is a simple transformation matrix from CF to the Sample Frame (SF - $(XYZ)$). ${}^t\boldsymbol{Q}$ denotes its transposed form. The combination of the transformation matrix with the anisotropy matrix allows the expression of a large variety of anisotropies at the macroscopic scale. Several definitions of $\mathbb{P}$ (using a 6×6 Voigt representation) are given in equation (2.27) for cubic symmetry (2.27a), uniaxial symmetry of axis $x$ (2.27b) and isotropy (2.27c).

$$W^{\alpha}_{an1} = (\vec{\gamma}^{\alpha} \otimes \vec{\gamma}^{\alpha}) : \left(\boldsymbol{Q} \cdot \boldsymbol{Q} \cdot \mathbb{P} \cdot {}^t\boldsymbol{Q} \cdot {}^t\boldsymbol{Q}\right) : (\vec{\gamma}^{\alpha} \otimes \vec{\gamma}^{\alpha}) \tag{2.26}$$

$$\mathbb{P} = \frac{1}{3} K_1 \left(\begin{array}{ccc:ccc} 0 & 1 & 1 & 0 & 0 & 0 \\ 1 & 0 & 1 & 0 & 0 & 0 \\ 1 & 1 & 0 & 0 & 0 & 0 \\ \hdashline 0 & 0 & 0 & 1 & 0 & 0 \\ 0 & 0 & 0 & 0 & 1 & 0 \\ 0 & 0 & 0 & 0 & 0 & 1 \end{array}\right)_{CF} \tag{2.27a}$$

$$\mathbb{P} = \frac{1}{3} K_1 \left(\begin{array}{ccc:ccc} 0 & 1 & 1 & 0 & 0 & 0 \\ 1 & 3 & 2 & 0 & 0 & 0 \\ 1 & 2 & 3 & 0 & 0 & 0 \\ \hdashline 0 & 0 & 0 & 1 & 0 & 0 \\ 0 & 0 & 0 & 0 & 2 & 0 \\ 0 & 0 & 0 & 0 & 0 & 1 \end{array}\right)_{CF} \tag{2.27b}$$

$$\mathbb{P} = \frac{1}{3} K_1 \left(\begin{array}{ccc:ccc} 3 & 2 & 2 & 0 & 0 & 0 \\ 2 & 3 & 2 & 0 & 0 & 0 \\ 2 & 2 & 3 & 0 & 0 & 0 \\ \hdashline 0 & 0 & 0 & 2 & 0 & 0 \\ 0 & 0 & 0 & 0 & 2 & 0 \\ 0 & 0 & 0 & 0 & 0 & 2 \end{array}\right)_{CF} \tag{2.27c}$$

- $W^{\alpha}_{an2}$ is an artificial energy related to a weak texture. This energy term is designed to modify the initial distribution of magnetic domains in order to adapt the macroscopic anisotropy. Indeed, the SMSM is based on an equivalent single crystal description of the material, it is necessary to integrate the texture information into the single crystal, in order to represent the macroscopic anisotropy. In the form proposed in 2.28, $K_{11}$, $K_{12}$ and $K_{13}$ are parameters ajusting magnetic and magnetostrictive anisotropy in SF. $\mathbb{R}$ is a $4^{th}$ order tensor that describes the texture related anisotropy in the SF. $\boldsymbol{S}$ is a simple rotation matrix which permits a flexible positioning of the principal orthotropic axes in the electrical sheet. Definition of $\mathbb{R}$ (using a 6×6 Voigt representation) is given in equation (2.29).

$$W^{\alpha}_{an2} = (\vec{\gamma}^{\alpha} \otimes \vec{\gamma}^{\alpha}) : \left(\boldsymbol{S} \cdot \boldsymbol{S} \cdot \mathbb{R} \cdot {}^{t}\boldsymbol{S} \cdot {}^{t}\boldsymbol{S}\right) : (\vec{\gamma}^{\alpha} \otimes \vec{\gamma}^{\alpha}) \tag{2.28}$$

$$\mathbb{R} = \frac{1}{3}\left(\begin{array}{ccc:ccc} 3K_{11} & K_{11}+K_{12} & K_{11}+K_{13} & 0 & 0 & 0 \\ K_{11}+K_{12} & 3K_{12} & K_{12}+K_{13} & 0 & 0 & 0 \\ K_{11}+K_{13} & K_{12}+K_{13} & 3K_{13} & 0 & 0 & 0 \\ \hdashline 0 & 0 & 0 & K_{11}+K_{12} & 0 & 0 \\ 0 & 0 & 0 & 0 & K_{11}+K_{13} & 0 \\ 0 & 0 & 0 & 0 & 0 & K_{12}+K_{13} \end{array}\right)_{SF} \tag{2.29}$$

### Elastic energy

The definition of elastic energy is unchanged, related to a homogeneous stress condition at the polycrystalline scale:

$$W^{\alpha}_{el} = -\boldsymbol{\sigma} : \boldsymbol{\epsilon}^{\alpha}_{\mu} \tag{2.30}$$

In order to describe the elastic energy in a more general way, the free magnetostriction is re-written in SF:

$$\boldsymbol{\epsilon}^{\alpha}_{\mu} = \boldsymbol{Q} \cdot \boldsymbol{\epsilon}^{\alpha}_{\mu CF} \cdot {}^{t}\boldsymbol{Q} \tag{2.31}$$

In a more general way, eq.2.32 can be expressed in form of:

$$\boldsymbol{\epsilon}^{\alpha}_{\mu} = \boldsymbol{Q} \cdot (\mathbb{T} : (\vec{\gamma}^{\alpha} \otimes \vec{\gamma}^{\alpha})) \cdot {}^{t}\boldsymbol{Q} \tag{2.32}$$

where $\mathbb{T}$ is a $4^{th}$ order tensor that describes the free magnetostriction strain in the CF (eq.2.33).

$$\mathbb{T} = \frac{3}{2}\left(\begin{array}{ccc:ccc} \lambda_{100}-\frac{1}{3} & -\frac{1}{3} & -\frac{1}{3} & 0 & 0 & 0 \\ -\frac{1}{3} & \lambda_{100}-\frac{1}{3} & -\frac{1}{3} & 0 & 0 & 0 \\ -\frac{1}{3} & -\frac{1}{3} & \lambda_{100}-\frac{1}{3} & 0 & 0 & 0 \\ \hdashline 0 & 0 & 0 & \lambda_{111} & 0 & 0 \\ 0 & 0 & 0 & 0 & \lambda_{111} & 0 \\ 0 & 0 & 0 & 0 & 0 & \lambda_{111} \end{array}\right)_{CF} \tag{2.33}$$

### Configuration energy

The definition of the configuration energy is the same in SMSM and MSM:

$$W^{\alpha}_{conf} = -\Sigma^{c} : \epsilon^{\alpha}_{\mu} \tag{2.34}$$

### Structure energy

$W^{\alpha}_{struc}$ (equation 2.35) is a new term related to the structure/form of the electrical sheet. Once the original electrical sheets are cut into strips or 'E-I' sheets, the domain configuration may be influenced. Typically for the FeNi Supra50, single crystals are aligned along the cutting board of the sheet, because of a strong sensitivity to the demagnetizating effects. However, as a material model, SMSM should describe the intrinsic behavior of a material.

For applications such as power transformers, the magnetic field is always the board of the electrical sheet. This makes it possible to get an information about the form of the sheets through the knowledge of the direction of the magnetic field. $\vec{h}$ is the direction of the magnetic field. $C$ sets the maximum level of the structure energy. The following expression can be proposed:

$$W^{\alpha}_{struc} = -C\,|\vec{\gamma}^{\alpha} \cdot \vec{h}| \tag{2.35}$$

### Differential magnetic susceptibility

Once the volume fractions of the magnetic domains are computed with the help of free energy, the differential magnetic susceptibility tensor $\chi_d$ is then computed. It is given by (2.36) and can be derived from the SMSM as proposed in [Bernard et Daniel, 2015]. This output of the model SMSM is essential for the non-linear magnetic resolution using the Newton-Raphson method.

$$\chi_d = \frac{\partial \vec{M}}{\partial \vec{H}} = \mu_0 A_s \left( M_s^2 \sum_{\alpha} f_{\alpha} \vec{\gamma}^{\alpha} \otimes \vec{\gamma}^{\alpha} - \vec{M} \otimes \vec{M} \right) \tag{2.36}$$

## 2.3 Multiscale magneto-mechanical modeling of hysteresis behavior

### 2.3.1 State of the art: hysteresis model

Magnetic hysteresis is perhaps one of the most famous phenomena in magnetic materials. It denotes that the current state of a material depends on its history. Magnetic hysteresis varies from one material to another, and depends on the frequency of external excitation. More importantly, the iron loss is closely related to the hysteresis. It is important to understand and model the magnetic hysteresis, in order to give an accurate prediction of the material behavior and to make reliable structural computations. With great efforts carried out by our pioneers, the source and mechanism of the magnetic hysteresis are well understood. Numerical models of magnetic hysteresis are numerous. Some of the most famous models are listed bellow:

- Preisach Model: The Preisach Model (PM) has been first introduced in 1935 [Preisach, 1935], describing the hysteresis loop as a series of parallel connected independent hysterons. Each hysteron possesses its own 'switch-off' and 'switch-on' threshold, noted as $\alpha$ and $\beta$. With the accurate adjustment of the weight factor for each hysteron, PM is able to achieve good agreement between measured and modeled hysteresis loop. The vectorized PM is constructed as the linear superposition of the scalar PM [Mayergoyz, 2003]. Although PM gives good results within reasonable computation time in a finite element simulation, it is still considered a mathematical tool adapted to ferromagnetism. Application of the PM under complex magnetic and mechanical loadings remains difficult.

- Jiles-Atherton Model: The Jiles-Atherton Model (JAM) has been first introduced in 1984 [Jiles et Atherton, 1986a], based on the phenomenological description of the hysteretic behavior. The original model is able to calculate the minor and major hysteresis loop. However, it is limited to isotropic materials. Extension of JAM was then carried out by Ramesh *et al.* [Ramesh *et al.*, 1996] for anisotropic case. Szymanski *et al.* [Szymański et Waszak, 2004] proposed the vectorized JAM, adapted to the rotational magnetic field. Further developments were proposed, adding new features to this model, considering stress dependency [Sablik et Jiles, 1993] and frequency dependency [Jiles, 1994] of the hysteresis loop. These developments and adjustments, however, have made the JAM a model that is too complicated and far from the microstructure of the material. The use of macroscopic internal variables strongly limits the extension of JAM. We are looking for hysteresis model that is close to the microstructure, and use the local internal variables for the definition of the material hysteresis behavior.

- Hauser's Model: The Hauser's Model (HM) has been first proposed in 1994 [Hauser, 1994], based on the energetic description of the magnetic material. This model gives a prediction of the material state by a minimization of the global energy, which allows considering complex physical phenomena. However, in this model, Hauser supposes that the magnetic material only consists of two magnetic domains, one in the direction of the magnetic field, the other in the opposite direction. The entire model works under this bi-domain assumption, where the magnetic field is always in the direction of the magnetic domain. This strongly simplifies the problem and has its physical explanation, as the magnetic hysteresis is generally created by the displacement of the 180° magnetic domain walls. However, this model only deals with scalar magnetic hysteresis, which strongly limits its use in the finite element resolution.

- Hysteresis extension on MSM: Considering the limitation of the existing hysteresis model and the strength of MSM, hysteresis extensions of MSM and SMSM have already been proposed.

One of the first attempts is made by Rizzo [Rizzo, 2012], who added the irreversible part of Hauser's model [Hauser, 1994] directly in the MSM at the magnetic domain scale. This gives the possibility to model magneto-mechanical coupled problem together with hysteresis effects. However, huge modifications of the original Hauser's model have been carried out, making this model far from the physical description of the material.

Rekik *et al.* [Daniel *et al.*, 2014] extended the multiscale magneto-mechanical coupled model using Hauser's hysteresis model at the grain scale, in order to consider hysteresis effect and external stress. Simplifications of this model have also been carried out [Daniel *et al.*, 2015]. Indeed, the applied magnetic field must be considered as unidirectional. The application of hysteresis SMSM is not relevant in devices such as electrical machines and power transformers, where rotational magnetic appears in certain areas (Fig.2.7).

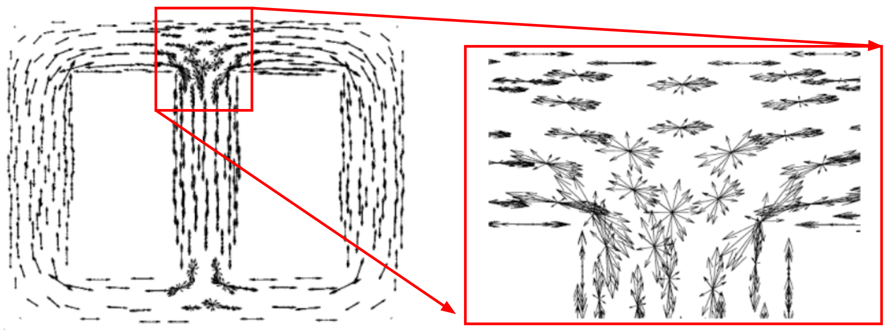

**Figure 2.7:** Direction of the magnetic field in power transformers [Kulkarni et Khaparde, 2016].

Although numerous modifications and improvements of these models are achieved by predecessors, none of them gives an all-in-one solution, handling well both magnetic and magnetostrictive hysteresis, under complex magnetic and mechanical loadings. A magnetic and magnetostrictive hysteresis model adapted to the rotational magnetic field (or 2D magnetic field) is crucial. This new form of model needs to consider the anisotropy and stress dependency for high precision simulation and must be adapted to a various magnetic materials. Ideally, the model requires easy parameter identification process, and must be able to predict material behavior under complex magnetic and mechanical loadings.

### 2.3.2 Irreversible Multiscale model (IMSM)

In this thesis, a new approach is proposed to combine Hauser's model and MSM, called IMSM hereafter. Hysteresis effect is considered by separating the applied magnetic field

$\vec{H}_{eff}$ (so-called effective field) into a reversible field $\vec{H}_{rev}$ and an irreversible field $\vec{H}_{irr}$ (eq.2.37).

$$\vec{H}_{eff} = \vec{H}_{rev} + \vec{H}_{irr} \tag{2.37}$$

The reversible magnetic field $\vec{H}_{rev}$ and applied stress $\boldsymbol{\sigma}$ are inputs of the MSM for the computation of material state. Outputs are magnetization $\vec{M}$ and magnetostrictive strain $\epsilon_\mu$. The irreversible magnetic field $\vec{H}_{irr}$ is computed in parallel with the help of Hauser's model at the magnetic domain scale, depending on the previous magnetization path and external loadings. This decomposition is first applied at the grain scale (eq.2.38), where $\vec{H}^g_{eff}$, $\vec{H}^g_{rev}$, and $\vec{H}^g_{irr}$ are respectively the effective, reversible, and irreversible magnetic field at the grain scale. Averaging operations considering texture information (eq.2.39) allows the magnetic fields to be obtained at the polycrystalline scale.

$$\vec{H}^g_{eff} = \vec{H}^g_{rev} + \vec{H}^g_{irr} \tag{2.38}$$

$$\vec{H}_{irr} = < \vec{H}^g_{irr} > \tag{2.39}$$

Fig.2.8 gives an illustration of the workflow for IMSM. The detailed information is summarized as follows:

- The local energy $W^\alpha$ of the magnetic domain $\alpha$ oriented in all possible directions is first computed, including magnetostatic energy (Zeeman energy), magnetocrystalline energy, elastic energy, and configuration energy.

- Volume fraction $f^\alpha$ of each magnetic domain is then obtained, according to the explicit Boltzmann-type relation.

- Magnetization $\vec{M}^g$ and magnetostrictive strain $\epsilon^g_\mu$ at the grain scale are then obtained through an averaging process.

- Magnetic domains oriented in the opposite directions are combined together, forming bi-domains $\beta$ oriented in a semi-sphere.

- Based on these bi-domains, where the volume fraction of the two opposite magnetic domains is pre-computed, a modified Hauser's model is applied to get the irreversible magnetic field $\vec{H}^\beta_{irr}$ acting on each bi-domain. The direction of this irreversible field is oriented in the direction of the bi-domain.

- The irreversible magnetic field $\vec{H}^g_{irr}$ at the grain scale is then obtained by an averaging process, with the consideration of the volume fraction of each magnetic bi-domain.

- By taking the material texture data into consideration, the macroscopic magnetization $\vec{M}$, magnetostrictive strain $\epsilon_\mu$, and irreversible magnetic field $\vec{H}_{irr}$ are finally computed.

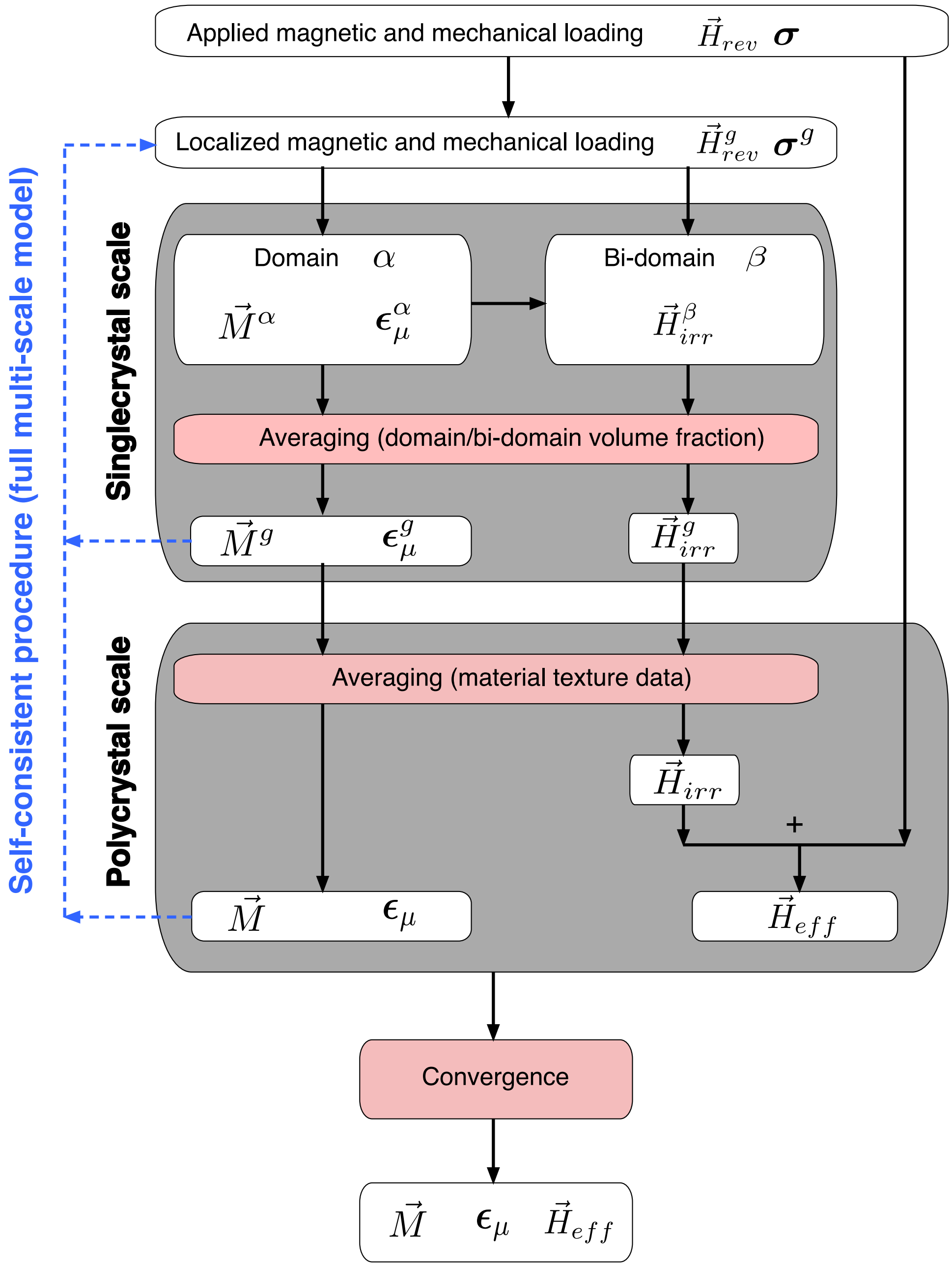


**Figure 2.8:** Modeling stragegy of IMSM.

- The effective magnetic field $\vec{H}_{eff}$ is the sum of the irreversible and reversible magnetic field.

Although the original Hauser's model is based on the energetic description of the local energy and gives a prediction of magnetic hysteresis behavior, this newly proposed IMSM approach has many improvements comparing to the previous propositions. The integration of MSM (with the consideration of crystalline texture) and self-consistent procedure lead to a precise description of the magnetic and magnetostrictive behavior, including anisotropy and stress dependency. Compared to Rekik's extension, the IMSM is constructed on a series of bi-domains, each experiencing the Hauser's model. This new approach allows the quasistatic losses under rotational magnetic excitations to be predicted.

### 2.3.3 Description of the bi-domain in MSM

The MSM already gives the volume fraction of domain family $\alpha$ oriented in all directions. These discrete directions are chosen to be uniformly distributed in a unit sphere, and each direction can find its opposite direction. Each pair of domain families oriented in the opposite direction creates a bi-domain. We consider a bi-domain $\beta$ formed by domain families $\alpha_+$ and $\alpha_-$, with domain family $\alpha_+$ pointing to the direction of the upper semi-sphere. Their volume fractions are respectively $f^{\alpha_+}$ and $f^{\alpha_-}$. The volume fraction of the bi-domain $\beta$ is defined as $f^\beta = f^{\alpha_+} + f^{\alpha_-}$. Thanks to this definition, 180° domain walls are naturally created between the two opposite domains within the same bi-domain. We define the wall positions $n^\beta$ inside the bi-domain $\beta$ (as a new internal variable):

$$n^\beta = \frac{f^{\alpha_+}}{f^{\alpha_+} + f^{\alpha_-}} = \frac{f^{\alpha_+}}{f^\beta} \tag{2.40}$$

$n^\beta$ is varying from 0 to 1. At demagnetising state, $n^\beta = 0.5$, the domain wall is at its initial position. Therefore, the movement of 180° domain wall is represented by the variation of $n^\beta$. The rotation of the bi-domain is represented, on the other hand, by the variation of $f^\beta$. The increase of $f^\beta$ means the rotation of the adjacent bi-domains towards bi-domain $\beta$. The decrease of $f^\beta$ means the rotation of bi-domain $\beta$ towards adjacent bi-domains.

The description of the bi-domain gives complementary information about microscopic behavior at the domain scale, including two main mechanisms of magnetization: wall displacement and magnetization rotation. Considering a rotational field loading, the former mechanism dominates the material behavior at low field, the latter at the high field.

### 2.3.4 Original Hauser's model

Static hysteresis effect, independent of the frequency, is related to the pinning sites. As applied magnetic field increases in certain direction, the domain walls move and meet the pinning sites. The more the domain walls move, the more likely they are to cross the pinning sites, leading to a larger hysteresis loop (larger $\vec{H}_{irr}$). The coercive field meets nevertheless a maximal value for a so-called 'major' loop. Hauser's model is based on this theory that considers magnetic material as a bi-domain structure: one magnetic domain along the direction of applied field, the other magnetic domain in the opposite direction. The hysteresis effect can consequently be described by the movement of the domain wall inside the bi-domain. The domain wall position is defined through the use of macroscopic reduced magnetization $m = M/M_s$. The movement of the domain wall is represented by the variation of the $m$. This leads to the description of irreversible field $H_{irr}$ as follows:

$$H_{irr} = sng(m - m_0)\left(\frac{k_r}{\mu_0 M_s} + c_r H_{rev}\right)\left[1 - \kappa \exp(-\frac{q}{\kappa}|m - m_0|)\right] \tag{2.41}$$

where $q$, $k_r$, $c_r$, and $\kappa$ are material parameters. $m_0$ is the starting value of $m$ at the last field inversion. Term $|m - m_0|$ varies from 0 to 2, describing the wall displacements from a macroscopic scale. $sng(m - m_0)$ is equal to $\pm 1$ depending on the direction of the magnetic loading. The term $\frac{k_r}{\mu_0 M_s}$ controls the coercivity of the hysteresis cycle. $\kappa$ adapts its value each time at the field inversion in order to keep the continuity of irreversible field:

$$\kappa = \kappa_0 \left[1 - exp\left(-\frac{q}{\kappa_0}|m - m_0|\right)\right] \tag{2.42}$$

where $\kappa_0$ is the recorded value of $\kappa$ at the last inversion.

Although this formulation is able to describe the hysteresis effects correctly including remanence, coercivity and static losses, $H_{irr}$ and $H_{rev}$ remain unidirectional. The irreversible field is always in the direction of the reversible magnetic field. This strongly limits the use of the original Hauser's model, especially for rotational field loadings. However, the bi-domain assumption in Hauser's model has a perfect match with the MSM, where a set of bi-domains is considered in each grain.

### 2.3.5 Modified Hauser's model adapted to the MSM

Necessary modifications are made to adapt the Hauser's model to the MSM. Following Hauser's proposition, the contribution of the irreversible field of a bi-domain $\beta$ can be described as follows:

$$\vec{H}^{\beta}_{irr} = sng(n^{\beta} - n^{\beta}_0)\left(\frac{k_r}{\mu_0 M_s} + c_r H^{\beta}_{rev}\right)\left[1 - \kappa^{\beta} \exp(-\frac{q}{\kappa^{\beta}}|n^{\beta} - n^{\beta}_0|)\right]\vec{\gamma}^{\alpha_+} \tag{2.43}$$

where $k_r$, $q$ and $c_r$ are universal parameters throughout the material. $n^{\beta}_0$ is the starting value of $n^{\beta}$ at the last field inversion, representing the last position of the domain wall in the bi-domain $\beta$. $\vec{\gamma}^{\alpha_+}$ is defined as the positive direction of the bi-domain $\beta$, or the direction of domain $\alpha_+$. $H^{\beta}_{rev}$ is the projection of local reversible field $\vec{H}^{g}_{rev}$ on the direction of bi-domain $\beta$ ($H^{\beta}_{rev} = |\vec{H}^{g}_{rev} \cdot \vec{\gamma}^{\alpha_+}|$). An inversion of loading direction is defined as a change of direction of the wall movement. From a practical point of view, this inversion is detected at instant t when $\Delta n_t^{\beta} \cdot \Delta n_{t-1}^{\beta} < 0$. This definition is very strong because it does not depend on the external loading, which can be a magnetic or a mechanical loading. At each inversion, $\kappa^{\beta}$ is updated to keep the continuity of irreversible field of the bi-domain $\beta$, shown in eq.2.44. $\kappa_0^{\beta}$ is the value of $\kappa^{\beta}$ at the last field inversion.

$$\kappa^{\beta} = 2 - \kappa_0^{\beta} \exp\left(-\frac{q}{\kappa_0^{\beta}}|n^{\beta} - n_0^{\beta}|\right) \tag{2.44}$$

The initial value of $\kappa^{\beta}$ is noted $\kappa_{init}^{\beta}$, taking controls of the initial hysteresis curve at the first magnetization. Finally, the irreversible field at the grain scale is obtained by an averaging operation over all bi-domains shown in eq.2.45.

$$\vec{H}_{irr}^{g} = \sum_{\beta} \vec{H}_{irr}^{\beta} f^{\beta} = \int_{\beta} \vec{H}_{irr}^{\beta} \mathrm{d}\beta \tag{2.45}$$

Hysteresis effect in the case of rotational magnetization adds even more complexities, depending on the material texture, 180° domain wall movement, and rotation of the magnetization. Unlike most hysteresis models, the newly proposed IMSM gives a physical description of the local and global hysteresis behavior, possessing numerous advantages. The IMSM uses local internal variable $n^{\beta}$ to describe the 180° domain walls movement, which is supposed to be the main physical source of the hysteresis. The application of modified Hauser's model at each bi-domain forms local hysterons, similar to the idea of Preisach model. The volume fraction of each domain oriented in different directions is given by MSM and material texture data. This also allows the description of material anisotropy and stress dependency. With the application of the external magnetic field, the volume fraction of the domains varies, leading to the computation of the local 180° domain walls movement, and thus hysteresis effect. The illustration of magnetization procedure using IMSM is shown in Fig.2.9.

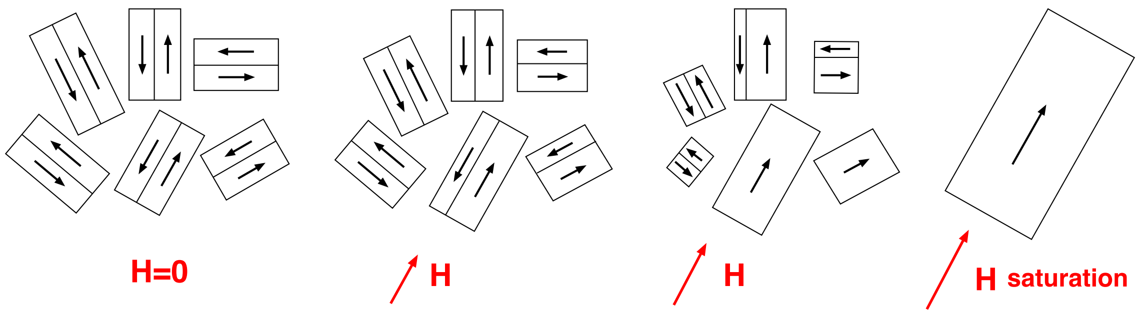


**Figure 2.9:** Illustration of magnetization procedure using IMSM.

Although the irreversible field $\vec{H}_{irr}^{\beta}$ is defined in the direction of reversible field $\vec{H}_{rev}^{\beta}$ and magnetization $\vec{M}^{\beta}$ in each bi-domain, the macroscopic irreversible field $\vec{H}_{irr}$ does not necessarily lie in the direction of reversible field $\vec{H}_{rev}$. This forms an angular offset between the effective field $\vec{H}_{eff}$ and reversible field $\vec{H}_{rev}$. An example of vector diagram is given in Fig.2.10, where the magnetic field is a rotating magnetic field.

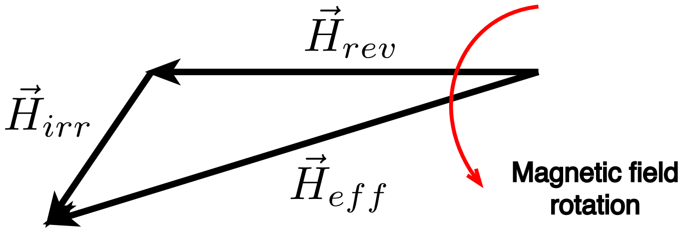


**Figure 2.10:** Vector diagram of effective field, reversible field and irreversible field.

### 2.3.6 Example of application

#### Anhysteretic behavior

The proposed IMSM model is applied to a Non-oriented FeSi (NO50 FeSi) with the thickness of $0.5mm$. The anhysteretic magnetic and magnetostrictive behavior of this material have been measured and modeled (using MSM) at LMT-Cachan by Rekik [Rekik, 2014]. The parameters used for the modeling are recalled in Table 2.1. The crystallographic texture data used for modeling consists of 396 crystallographic orientations, extracted from an EBSD file. The comparison of measured and modeled magnetic and magnetostrictive behaviors are given in Fig.2.11.

| Param. | $M_s$ | $K_1$ | $\lambda_{100}$ ; $\lambda_{111}$ | $A_s$ | $\Sigma^c$ |
|---|---|---|---|---|---|
| Value | $1.61\times10^6$ | 38 | 23.5 ; -4.5 | $20\times10^{-3}$ | 20 |
| Unit | $A/m$ | kJ.m$^{-3}$ | ppm | $m^3/J$ | MPa |

**Table 2.1:** Physical constants used for anhysteretic MSM [Daniel *et al.*, 2014, Rekik, 2014].

It must be noticed that the MSM tends to underestimate the initial magnetic permeability in all directions (RD, 45° and TD) and the magnetization curves predicted by the model reach the saturation more rapidly than the experimental ones. However, the anisotropy of the magnetic behavior is correctly represented by MSM, leading RD as an easy direction and TD as a hard direction. The description of the magnetostrictive behavior of the material is satisfactory. Further optimization of the parameters, such as $A_s$ (or $M_s$ as proposed in [Aydin *et al.*, 2017]), is possible for a better accordance between experimentation and modeling.

#### Hysteretic behavior

Four parameters are used to adjust the hysteretic behavior, according to the IMSM. $k_r$ is proportional to the amplitude of the coercive field. $c_r$ controls the first magnetization behavior. $\kappa_{init}^{\beta}$ and $q$ are related to the width and inclination of the hysteresis cycle. The

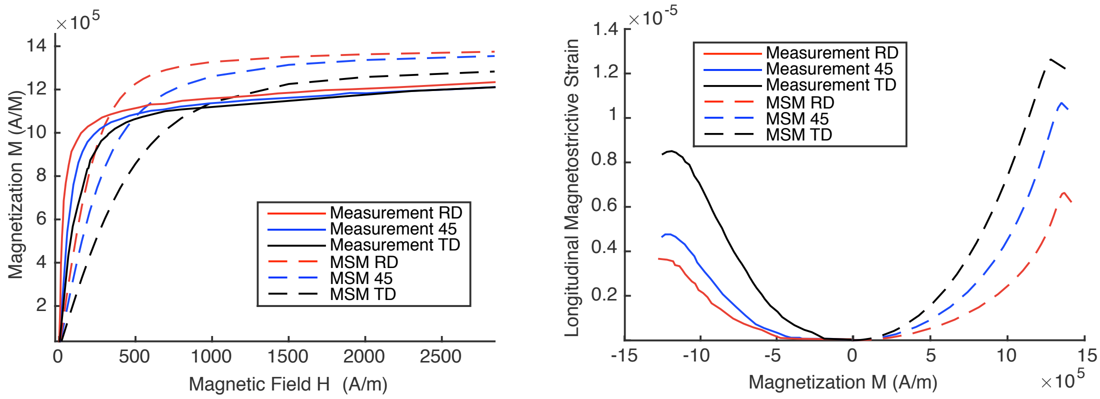


(a) anhysteretic magnetization curve (b) anhysteretic magnetostriction curve

**Figure 2.11:** FeSi NO50: comparison of MSM results (dots) to experimental measurement (lines).

parameters adapted to NO50 FeSi and identified under a major loop are given in Table 2.2.

| Param. | $c_r$ | $\kappa^{\beta}_{init}$ | $k_r$ | $q$ |
|---|---|---|---|---|
| Value | 0.1 | 1 | 150 | 48 |
| Unit | - | - | $J/m^3$ | - |

**Table 2.2:** Numerical parameters used for the irreversible field calculation.

Magnetic hysteresis loop and magnetostrictive butterfly loop under alternative magnetization load are given in Fig.2.12 and Fig.2.13, where the simulated behavior (by IMSM) is compared to the measured behavior obtained at low magnetic field amplitude. The shape of the simulated hysteresis loop is correctly described. As already noticed in Fig.2.11, the predicted anhysteretic magnetization curve exhibits some differences compared to the measured curves. The anhysteretic behavior gives the skeleton of the hysteresis loops. This explains the difference between the simulated and the measured hysteresis loop. Further improvement of the anhysteretic behavior is able to better describe the hysteretic behavior.

Another important difference to notice between the measurement and the simulation is the coercivity. It is observed that the order of the experimental coercivity value in different directions is: TD > 45° > RD. While the IMSM (without any adjustment) gives an opposite prediction: TD < 45° < RD. Indeed the initial distribution of the magnetic domains is anisotropic: more magnetic domains are oriented along RD than along TD. As there are fewer domains initially lying along TD, fewer hysteresis is created by the 180° domain walls movement, resulting in this prediction of coercivity. Making the parameter

$k_r$ as a function of magnetic domain volume fraction may be a good way to adjust the coercivity of IMSM.

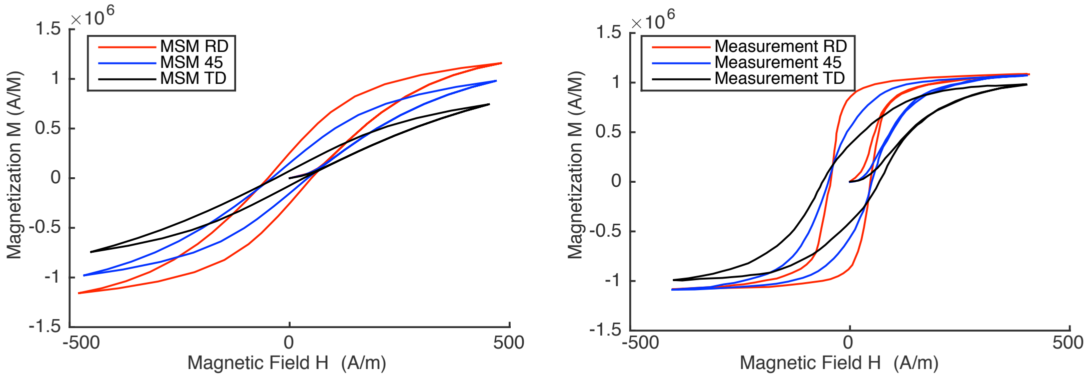


(a) simulation IMSM (b) measurement [Rekik, 2014]

**Figure 2.12:** FeSi NO50: hysteretic magnetization curve.

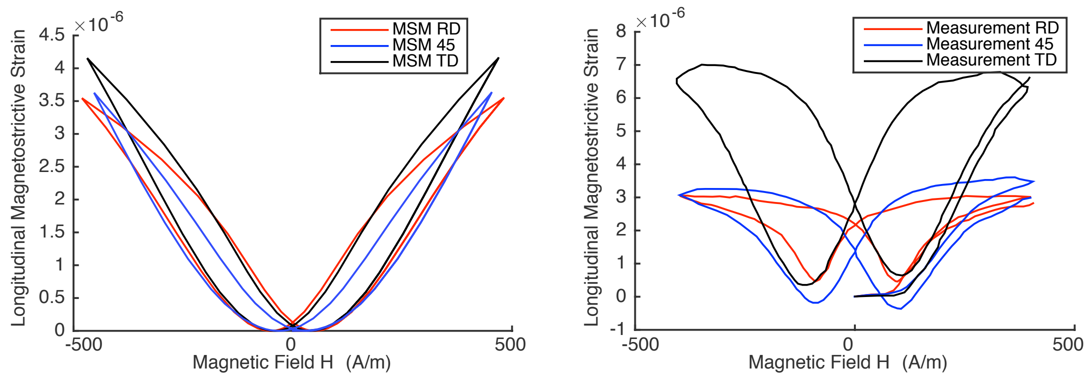


(a) simulation IMSM (b) measurement [Rekik, 2014]

**Figure 2.13:** FeSi NO50: hysteretic magnetostriction curve.

### Hysteresis loss

Despite the fact that the shape and form of the hysteresis loop vary as a function of frequency, the hysteresis loss is restricted as a frequency-independent term of the total core losses. It is often measured with alternative or rotational magnetization at a very low frequency (usually less than $1Hz$). The hysteresis loss $W$ is defined as the integration of the magnetic energy over one stationary cycle, shown in eq.2.46. This hysteresis loss is described as the energy consumed per cycle, with $J/m^3$ as the unit.

$$W = \int_{cycle} \vec{H}\,\mathrm{d}\vec{B} \tag{2.46}$$

In a practical way, the hysteresis loss is computed with a discretized formulation (eq.2.47) for both numerical simulation and experimental measurement. $n$ is the number of simulated/measured data within one hysteresis cycle.

$$W = \sum_{i=2}^{n} \frac{1}{2}\left(\vec{H}_n + \vec{H}_{n-1}\right) \cdot \left(\vec{B}_n - \vec{B}_{n-1}\right) \tag{2.47}$$

In the case of alternative magnetization, the magnetic field is applied in a certain direction with a sinusoidal waveform. The corresponding loss is simply the surface of the hysteresis loop. A series of numerical simulations has been carried out using IMSM under various magnetization levels. The magnetic field is applied along three different directions RD, 45°, and TD. The hysteresis losses as a function of the peak magnetic induction in all three directions are given in Fig.2.14. These simulations are also compared with a recent measurement from the literature [Appino *et al.*, 2016]. The measurement is carried out on a similar $0.35 - thickness$ non-oriented FeSi material under $2Hz$. The comparison between the measurement and the simulation shows good agreement in general: the hysteresis loss rises continuously as the magnetic induction increases.

It must be noticed that the hysteresis loss predicted by IMSM along RD is higher than that along TD. This result is contradictory with former experimental results. This may be due to the wrong estimation of predicted coercivity. We observe on the other hand that the hysteresis loss from experiments rises more rapidly from $1.3T$ to $1.5T$. This point is not addressed by the IMSM. Further investigations are needed to improve the model.

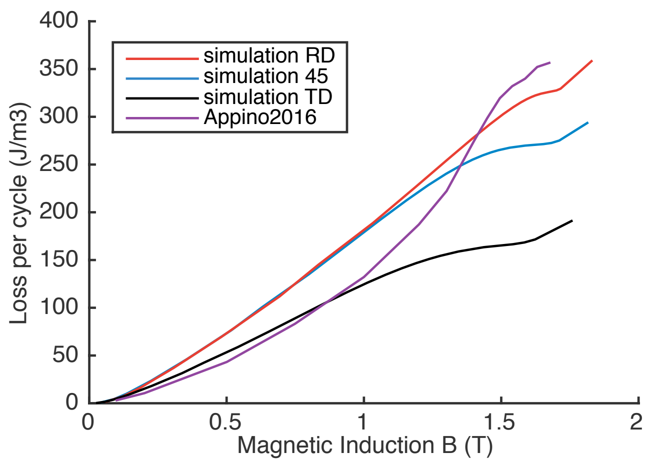


**Figure 2.14:** Hysteresis losses per cycle under alternative magnetization: comparison between IMSM model and literature [Appino *et al.*, 2016].

To obtain a rotational magnetization, a rotating magnetic field is applied: the magnetic field amplitude is progressively increased during the first cycle (transient state) and a constant amplitude is applied for the next cycles (stationary state). An illustration of the applied reversible magnetic field is shown in Fig.2.15 (left), with a maximum amplitude of $3000A/m$. The cumulative loss as a function of magnetic field angle is given in Fig.2.15 (right), where the maximum amplitude of reversible magnetic field varies from 10 to $3000A/m$. Because of the magnetic anisotropy of the material, the amplitude and phase-shift of magnetic induction vary as the magnetic field rotates. The hysteresis loss is based on the phase difference between the magnetic induction and magnetic field and their respective amplitudes. Therefore, the cumulative hysteresis loss increases and decreases according to the direction of the magnetic field. The hysteresis loss per cycle is then computed as a function of the average magnetic induction and given in Fig.2.16. The simulation is compared with four previous measurements in the literature. They are listed below:

- Brailsford *et al.* [Brailsford, 1939] carried out measurements on various of samples under quasi-static condition. The material used for comparison showed in Fig.2.14(b) is called 'ordinary transformer silicon steel' (sample 3) with a thickness of $0.31mm$.

- Fiorillo *et al.* [Fiorillo et Rietto, 1990] gave the rotational hysteresis loss on a $0.35mm$-thickness non-oriented FeSi, with a frequency tending to zero.

- Zhu *et al.* [Zhu et Ramsden, 1998] used a Non-oriented FeSi sheet steel 'lycore 130', with a thickness of $0.35mm$. The frequency of the rotational magnetization field is $1Hz$.

- Appino *et al.* [Appino *et al.*, 2016] worked on a $0.35mm$-thickness non-oriented FeSi disc, with a $2Hz$ rotational magnetic field.

All the selected measurements shown in Fig.2.16 are carried out under similar conditions on similar materials.

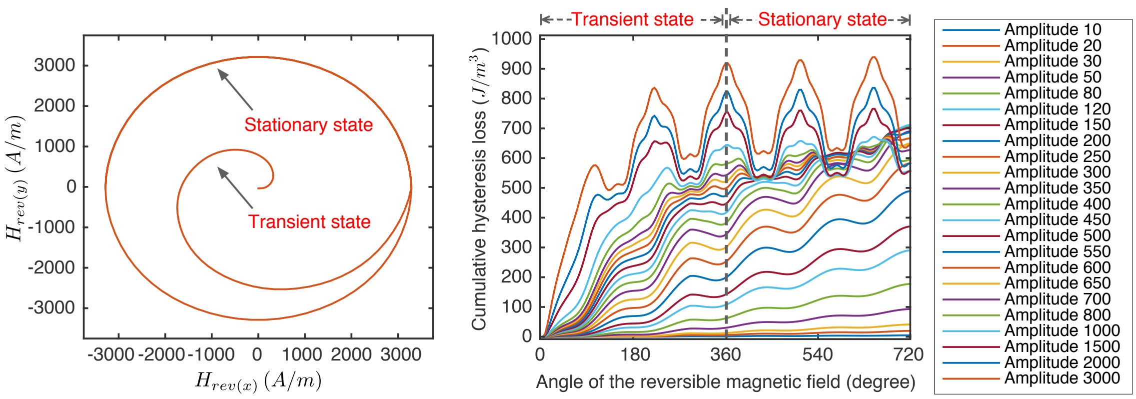


**Figure 2.15:** Illustration of rotational magnetization path (left); Cumulative hysteresis loss for rotational magnetization (right)

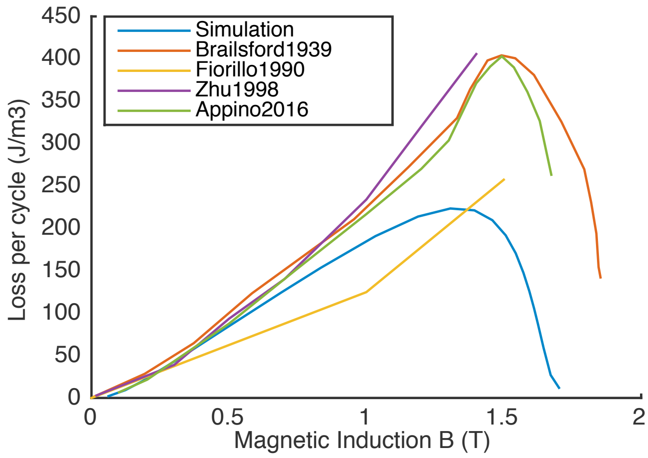


**Figure 2.16:** Hysteresis losses per cycle under rotational magnetization: comparison between IMSM model and literature.

The hysteresis loss, plotted against average magnetic induction, rises slowly before the ’knee’ point and falls rapidly towards zero at saturation. This is a well-known phenomenon for rotational hysteresis loss in accordance with the magnetic domain theory: (i) at low magnetization (before the ’knee’ point), the displacement of the 180° domain walls is dominant. Domain walls have to go across the defects and cause loss. (ii) at high magnetization, the rotation of the magnetization occurs. This is a non-dissipative procedure, so that the rotational hysteresis loss begins to decrease as the magnetization increases. (iii) near saturation, magnetic domain walls disappear. The rotational hysteresis loss goes towards to zero.

The IMSM model perfectly predicts this non-monotonous rotational hysteresis loss curve, and shows general agreement with the previous measurements. This, on the other hand, justifies the choice of combining MSM and Hauser’s model. The introduction of the two mechanisms (domain wall movement and magnetization rotation) is also verified for its efficiency. It is noticed that the peak loss given by IMSM is about 40% lower than the experimental peak losses presented in the literature. More investment and further studies are necessary to improve the IMSM model.

## 2.4 Conclusion

In this chapter, we focused on the multiscale modeling of the magneto-mechanical behavior of the ferromagnetic materials. In terms of the multiscale modeling of magneto-mechanical anhysteretic behavior, extensions of the SMSM have been proposed. This makes the SMSM a generalized model which can be adapted to different materials. More importantly, this extension also allows the rotation of easy axis in a finite element modeling chain to be considered, leading to the simulation of different configurations of power transformers ($8 - shaped$ core, $E - I$ core...). In terms of the multiscale modeling of magneto-mechanical hysteresis behavior, IMSM has been presented. This is a combination of a modified Hauser model and MSM at the grain scale. It must be highlighted that this model is able to predict the magnetic and magnetostrictive hysteresis behavior under a 2D magnetic and mechanical loading. Static hysteresis losses are computed under alternative and rotational magnetic loadings. Good agreements are found between the simulations results of IMSM and the measurements reported in the literature. It should be noted that the IMSM has not been adapted to the finite element modeling presented in the next chapter and in the global comparisons of experiment and modeling carried out on transformers. This remains an unachieved issue.

# Chapter 3

# Finite Element Modeling Chain

## Contents

# 3.1 Modeling of physical phenomena

## 3.1.1 Modeling of magnetic phenomena

The electromagnetic field computation can be solved by partial differential equations derived from Maxwell's equations under certain boundary conditions. Maxwell's equations define relations between the electromagnetic field quantities and the source terms:

$$\vec{\nabla}\times\vec{E} = -\frac{\partial\vec{B}}{\partial t} \tag{3.1}$$

$$\vec{\nabla}\times\vec{H} = \vec{J}+\frac{\partial\vec{D}}{\partial t} \tag{3.2}$$

$$\vec{\nabla}\cdot\vec{D} = \rho_e \tag{3.3}$$

$$\vec{\nabla}\cdot\vec{B} = 0 \tag{3.4}$$

where $\vec{E}$ is the electric field, $\vec{B}$ the magnetic flux density, $\vec{H}$ the magnetic field, $\vec{D}$ the electric induction, $\vec{J}$ the current density, and $\rho_e$ the electric charge density. The first Maxwell's equation (3.1) is the differential form of Faraday's law, which states that the time-varying magnetic field induces the electric field. The second Maxwell's equation (3.2) covers the Ampere's law in differential form, which represents that the current and time-varying electric field generate magnetic fields. These two formulations are strongly coupled and interact with each other, if the eddy current and electromagnetic radiation is considered. The time-varying magnetic field generates electric field leading to eddy current inside the conducting materials. This current creates the magnetic field around and modifies the initial magnetic field. The third Maxwell's equation (3.3) is the Gauss's law for electric fields. The fourth Maxwell's equation (3.4) is the Maxwell-Thomson law, showing that the magnetic field is divergence-free and the magnetic flux lines close upon themselves. Different from the magnetic field, the electric field can be generated from electric charges.

For low-frequency applications, such as synchronous electrical motors and power transformers, the time derirative terms ($-\frac{\partial\vec{B}}{\partial t}$ and $\frac{\partial\vec{D}}{\partial t}$) are negligable. This leads to the approximation of magnetostatic regime, where the eq.3.1-3.4 are reduced to:

$$\vec{\nabla}\times\vec{E} = 0 \qquad \vec{\nabla}\cdot\vec{D} = \rho \tag{3.5}$$

$$\vec{\nabla}\times\vec{H} = \vec{J} \qquad \vec{\nabla}\cdot\vec{B} = 0 \tag{3.6}$$

These expressions can be futher reduced/simplified with the consideration of the constitutive relations between the quantities:

$$\vec{J} = \sigma\vec{E} \qquad \vec{B} = \mu\vec{H} \tag{3.7}$$

The magnetic permeability $\mu$ is a scalar if the material is isotropic, and a tensor if the material is anisotropic. In our case, the magnetic behavior $\vec{B} = \mu\vec{H}$ is given by SMSM.

The magnetic field and magnetic induction can be discontinuous when going from one medium to another. Two medium $\Omega_1$ and $\Omega_2$ are considered, with $\vec{n}$ the normal vector pointing from medium $\Omega_1$ to $\Omega_2$. The boundary between the two media is $\Gamma$. The boundary conditions are given by eq.3.8, where $\vec{J_s}$ is the surface current between two media.

$$\left(\vec{B}_2 - \vec{B}_1\right) \cdot \vec{n} = 0 \quad \text{on} \quad \Gamma \qquad\qquad \left(\vec{H}_2 - \vec{H}_1\right) \times \vec{n} = \vec{J_s} \quad \text{on} \quad \Gamma \tag{3.8}$$

The computation of the static electromagnetic problem comes mainly with two methods: magnetic scalar potential formulation ($T_0 - \varphi$ formulation) and magnetic vector potential formulation ($A$ formulation). Almost all commercial softwares use magnetic vector potential for static electromagnetic solving because of its fast numerical convergence and stable performance. However, for some small projects with limited mesh size, the magnetic scalar potential formulation provides also reliable performance with very low computational cost. A strong advantage of the magnetic scalar potential formulation is its ability of the extension from 2D to 3D resolution. This is important for some scientific researchers who develop their code first in 2D to verify the functionality, and then pass to 3D for more precise computation.

### Magnetic scalar potential ($T_0 - \varphi$) formulation for magnetostatic problems

The magnetic field can be split in two parts, a rotational part $\vec{T_0}$ and a non-rotational part $\vec{H}_m$:

$$\vec{H} = \vec{T_0} + \vec{H}_m \tag{3.9}$$

The rotational part $\vec{T_0}$ is called current vector potential. The curl of this vector potential is related to the source current, discribed as:

$$\vec{\nabla} \times \vec{T_0} = \vec{J} \tag{3.10}$$

The non-rotational part $\vec{H}_m$ can be represented by the gradient of a scalar potential $\varphi$:

$$\vec{H}_m = -\vec{\nabla}\varphi \tag{3.11}$$

because of the identity $\vec{\nabla} \times (\vec{\nabla}\varphi) \equiv 0$ for any scalar function $\varphi$. Therefore, the magnetic field can be re-written as a function of magnetic scalar potential and current vector potential:

$$\vec{H} = \vec{T_0} - \vec{\nabla}\varphi \tag{3.12}$$

Despite the simplicity of the magnetic scalar potential formulation, problems can occur if the magnetic permeability of the material is high. The high permeability leads to a strong decrease of the magnetic field inside the magnetic material, and thus $\vec{T_0} \approx \vec{\nabla}\varphi$. When these two almost equal values are subtracted from each other, it causes cancellation errors. Fortunately, for most applications, this error can be ignored, because the electrical current circulates only in the coils, not inside the magnetic material.

**Magnetic vector potential ($A$) formulation for magnetostatic problems**

Magnetic vector potential formulation is defined in a very similar way compared to magnetic scalar potential formulation. As the magnetic induction is a divergence free quantity, it can be defined by:

$$\vec{B} = \vec{\nabla} \times \vec{A} \tag{3.13}$$

because of the identity $\vec{\nabla} \cdot (\vec{\nabla} \times \vec{v}) \equiv 0$ for any vector function $\vec{v}$. Detailed explanations of the application and source term definition are explained in [Bouillault, 1991]. Typically for FEM, the edge-based magnetic vector potential formulation has more degrees of freedom, that leads to a heavy computational burden. However, this formulation has clear advantages over the magnetic scalar potential formulation for problems with a large number of elements.

In this thesis work, the magnetic scalar formulation is chosen for the magnetic resolution. This makes the integration of the SMSM easier. Magnetic scalar formulation solves the magnetic scalar $\varphi$, leading to the magnetic field $\vec{H}$. The magnetic field is then injected into SMSM as input, in order to update the magnetization $\vec{M}$.

### 3.1.2 Modeling of mechanical phenomena

Within the domain of solid mechanics and approximation of the continuous medium, the local equilibrium equation is defined by:

$$\vec{\nabla} \cdot \boldsymbol{\sigma} + \vec{f} = \rho_m \frac{\partial^2 \vec{u}}{\partial t^2} \tag{3.14}$$

where $\boldsymbol{\sigma}$ is the $2^{nd}$ order mechanical stress tensor, $\vec{f}$ is the volume force, $\rho_m$ is the mass density, and $\vec{u}$ is the displacement field. This equation describes the displacement of all the points in the studied domain under a mechanical excitation, for example, vibration problem. If a mechanical problem is under the static assumption, where no dynamic effect is considered, the eq.3.14 reduces to:

$$\vec{\nabla} \cdot \boldsymbol{\sigma} + \vec{f} = \vec{0} \tag{3.15}$$

In a mechanical system, the displacement and stress fields must be defined under certain boundary conditions, described as:

$$\boldsymbol{\sigma} \cdot \vec{n} = \vec{f_s} \quad \text{on} \quad \Gamma_f \qquad\qquad \vec{u} = \vec{u}_0 \quad \text{on} \quad \Gamma_u \tag{3.16}$$

where $\vec{f_s}$ is the imposed surface force, $\vec{u}_0$ the imposed displacement. $\Gamma_f$ and $\Gamma_u$ are boundaries of the studied object with surface force and displacement boundary conditions.

In this thesis, only the elastic behavior (Hooke's law) is considered in the mechanical system. The general expression for linear constitutive behavior is:

$$\boldsymbol{\sigma} = \mathbb{C} : \boldsymbol{\epsilon}_{el} \tag{3.17}$$

where $\boldsymbol{\epsilon}_{el}$ is $2^{nd}$ order elastic strain tensor. $\mathbb{C}$ is a three-dimensional forth-order stiffness tensor, which contains 81 elements. This is reduced to 21 different elements because of the symmetries of stress and strain tensor and the quadratic form of elastic energy (linear medium). . To reduce the complexity of the expression of eq.3.17, it is useful to express Hooke's law in matrix notation, called Voigt notation. The symmetry of the stress and strain tensors is considered, and these tensors are then expressed in form of six-dimensional vectors:

$$\boldsymbol{\sigma} = \begin{bmatrix} \sigma_{11} \\ \sigma_{22} \\ \sigma_{33} \\ \sigma_{12} \\ \sigma_{13} \\ \sigma_{23} \end{bmatrix} \qquad \boldsymbol{\epsilon}_{el} = \begin{bmatrix} \varepsilon_{el11} \\ \varepsilon_{el22} \\ \varepsilon_{el33} \\ 2\varepsilon_{el12} \\ 2\varepsilon_{el13} \\ 2\varepsilon_{el23} \end{bmatrix} \qquad \mathbb{C} = \begin{bmatrix} C_{11} & C_{12} & C_{13} & C_{14} & C_{15} & C_{16} \\ C_{12} & C_{22} & C_{23} & C_{24} & C_{25} & C_{26} \\ C_{13} & C_{23} & C_{33} & C_{34} & C_{35} & C_{36} \\ C_{14} & C_{24} & C_{34} & C_{44} & C_{45} & C_{46} \\ C_{15} & C_{25} & C_{35} & C_{45} & C_{55} & C_{56} \\ C_{16} & C_{26} & C_{36} & C_{46} & C_{56} & C_{66} \end{bmatrix} \tag{3.18}$$

The stiffness tensor can be further simplified for orthotropic materials that have three orthogonal planes of symmetry:

$$\mathbb{C} = \begin{bmatrix} C_{11} & C_{12} & C_{13} & & & \\ C_{12} & C_{22} & C_{23} & & & \\ C_{13} & C_{23} & C_{33} & & & \\ & & & C_{44} & & \\ & & & & C_{55} & \\ & & & & & C_{66} \end{bmatrix} \tag{3.19}$$

This leads to:

$$\sigma_{11} = C_{11}\varepsilon_{el11} + C_{12}\varepsilon_{el22} + C_{13}\varepsilon_{el33} \tag{3.20}$$

$$\sigma_{22} = C_{12}\varepsilon_{el11} + C_{22}\varepsilon_{el22} + C_{23}\varepsilon_{el33} \tag{3.21}$$

$$\sigma_{33} = C_{13}\varepsilon_{el11} + C_{23}\varepsilon_{el22} + C_{33}\varepsilon_{el33} \tag{3.22}$$

$$\sigma_{12} = 2C_{44}\varepsilon_{el12} \tag{3.23}$$

$$\sigma_{13} = 2C_{55}\varepsilon_{el13} \tag{3.24}$$

$$\sigma_{23} = 2C_{66}\varepsilon_{el23} \tag{3.25}$$

Many problems in elasticity may be treated in 2D. There are generally two types of problems involved in this plane analysis: plane stress or plane strain. These two types will be defined by setting down certain restrictions and assumptions on the stress and displacement fields.

### Plane stress formulation

Plane stress formulation is mainly used for problems such as plates, fillets, or other changes in geometry that are loaded in their plane. It is assumed that the stress in out-of-plane direction is null ($\sigma_{33} = 0$, $\sigma_{13} = 0$, $\sigma_{23} = 0$). Equation (3.20) is then written as follows:

$$\varepsilon_{el33} = -\frac{C_{13}}{C_{33}}\varepsilon_{el11} - \frac{C_{23}}{C_{33}}\varepsilon_{el22} \tag{3.26}$$

as a consequence, the other two equations become:

$$\sigma_{11} = \left(C_{11} - \frac{C_{13}^2}{C_{33}}\right)\varepsilon_{el11} + \left(C_{12} - \frac{C_{13}C_{23}}{C_{33}}\right)\varepsilon_{el22} \tag{3.27}$$

$$\sigma_{22} = \left(C_{12} - \frac{C_{13}C_{23}}{C_{33}}\right)\varepsilon_{el11} + \left(C_{22} - \frac{C_{23}^2}{C_{33}}\right)\varepsilon_{el22} \tag{3.28}$$

Under plane stress assumption, Hooke's law finally reduces to:

$$\begin{bmatrix}\sigma_{11}\\ \sigma_{22}\\ \sigma_{12}\end{bmatrix} = \begin{bmatrix} C_{11} - \frac{C_{13}^2}{C_{33}} & C_{12} - \frac{C_{13}C_{23}}{C_{33}} & 0\\ C_{12} - \frac{C_{13}C_{23}}{C_{33}} & C_{22} - \frac{C_{23}^2}{C_{33}} & 0\\ 0 & 0 & C_{44}\end{bmatrix} \begin{bmatrix}\varepsilon_{el11}\\ \varepsilon_{el22}\\ 2\varepsilon_{el12}\end{bmatrix} \tag{3.29}$$

In the isotropic case, the number of parameters that define the stiffness tensor reduces to two: the Young's modulus $E$ and the Poisson's ratio $\nu$. The isotropic 2D (plane stress) Hooke's law is given by:

$$\begin{bmatrix}\sigma_{11}\\ \sigma_{22}\\ \sigma_{12}\end{bmatrix} = \frac{E}{1-\nu^2}\begin{bmatrix}1 & \nu & 0\\ \nu & 1 & 0\\ 0 & 0 & \frac{1-\nu}{2}\end{bmatrix} \begin{bmatrix}\varepsilon_{el11}\\ \varepsilon_{el22}\\ 2\varepsilon_{el12}\end{bmatrix} \tag{3.30}$$

$$\varepsilon_{el33} = -\frac{\nu}{1-\nu}\left(\varepsilon_{el11} + \varepsilon_{el22}\right) \tag{3.31}$$

**Plane strain formulation**

Plane strain formulation is commonly used to analyze deformation or fracture of materials. It is also used in examination of shape/size changes in two dimensions. It is assumed that the strain in the out-of-plane direction is null ($\varepsilon_{el33} = \varepsilon_{el13} = \varepsilon_{el23} = 0$). Equations (3.20-3.21) are then written as follows:

$$\sigma_{11} = C_{11}\varepsilon_{el11} + C_{12}\varepsilon_{el22} \tag{3.32}$$

$$\sigma_{22} = C_{12}\varepsilon_{el11} + C_{22}\varepsilon_{el22} \tag{3.33}$$

so that:

$$\sigma_{33} = C_{13}\varepsilon_{el11} + C_{23}\varepsilon_{el22} = \frac{C_{13}C_{22} - C_{23}C_{12}}{C_{11}C_{22} - C_{12}^2}\sigma_{11} + \frac{C_{23}C_{11} - C_{12}C_{13}}{C_{11}C_{22} - C_{12}^2}\sigma_{22} \tag{3.34}$$

Under plane strain assumption, the hooke's law finally reduces to:

$$\begin{bmatrix}\sigma_{11}\\ \sigma_{22}\\ \sigma_{12}\end{bmatrix} = \begin{bmatrix}C_{11} & C_{12} & 0\\ C_{12} & C_{22} & 0\\ 0 & 0 & C_{44}\end{bmatrix} \begin{bmatrix}\varepsilon_{el11}\\ \varepsilon_{el22}\\ 2\varepsilon_{el12}\end{bmatrix} \tag{3.35}$$

In the isotropic case, the 2D Hooke's law under plane strain assumption is given by:

$$\begin{bmatrix}\sigma_{11}\\ \sigma_{22}\\ \sigma_{12}\end{bmatrix} = \frac{E}{(1+\nu)(1-2\nu)}\begin{bmatrix}1-\nu & \nu & 0\\ \nu & 1-\nu & 0\\ 0 & 0 & \frac{1-2\nu}{2}\end{bmatrix} \begin{bmatrix}\varepsilon_{el11}\\ \varepsilon_{el22}\\ 2\varepsilon_{el12}\end{bmatrix} \tag{3.36}$$

$$\sigma_{33} = \nu\left(\sigma_{11} + \sigma_{22}\right) \tag{3.37}$$

## 3.2 Overview of modeling chain

The modeling of the power transformer core vibration and noise emission involves several physical phenomena, such as electric, electromagnetism, solid mechanics, and acoustic. These physical phenomena interact more or less with each other. One general modeling strategy for power transformer is to tackle each physical phenomena separately using sectional approach: first magnetic resolution, then mechanical resolution, and finally acoustic power estimation.

The global modeling strategy is summarized in Fig.3.1. As the power transformer works at low frequency, a static assumption is applied for the magnetic resolution. A sequence of current $I$ or magnetic flux $\phi$ in the time domain is considered as excitation of the magnetic problem. Magnetic resolution is carried out in the time domain, with the built in magneto-mechanical coupled SMSM. At each time point, both Maxwell tensor $\boldsymbol{T}$ and magnetostriction free strain $\boldsymbol{\epsilon}_{\mu}$ are obtained, which leads to the computation of the magnetic force density and magnetostriction equivalent force density (detailed in section 3.5). A mechanical feedback loop is designed in parallel with the magnetic resolution loop. This gives the induced stress $\boldsymbol{\sigma}$ in the different layers, that modifies the magnetic and magnetostrictive behavior of the material. Harmonic mechanical resolution is carried out in the frequency domain to avoid the transient state and obtain a better efficiency. The displacement field $\vec{u}$ of the core is finally obtained. Acoustic power estimation $P_{ac}$ is achieved as the last step, which gives a global indicator of noise emission.

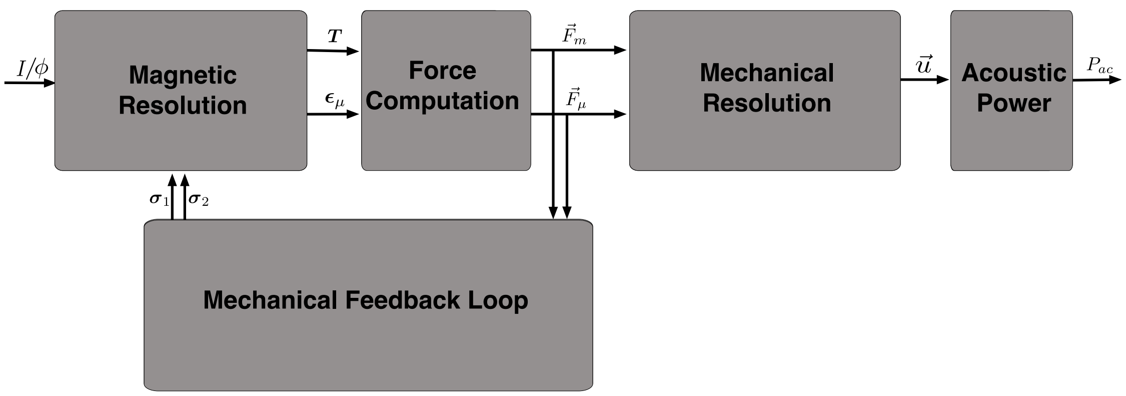


**Figure 3.1:** Global modeling strategy.

## 3.3 Two media homogenization

An E-I stacked core is assembled with hundreds of layers. Typically, a layer is assembled anti-parallel to its neighbor layer, forming two layer families. Each layer consists of an 'E-shaped' sheet and an 'I-shaped' sheet, as illustrated in Fig.3.2. $f_1$ and $f_2$ define the section (or volume) fraction of layer family 1 ('E-shaped' sheet upside and 'I-shaped' sheet downside) and layer family 2 ('E-shaped' sheet downside and 'I-shaped' sheet upside) respectively. Since ferromagnetic materials are often anisotropic, the easy magnetization directions of 'E-shaped' sheets and 'I-shaped' sheets are oriented differently, leading to an inhomogeneous behavior from layer to layer. Considering the complexity of the SMSM, a 2D description of the transformer structure is required in order to save computation time. Fig.3.3 gives the equivalent 2D model of an E-I stacked core, where the material behavior in the 'mixed zone' is different from layer to layer. In order to consider this inhomogeneity in the normal direction for 2D modeling, a homogenization strategy of a heterogeneous problem is required to extract the average behavior (physical notations used hereafter are considered in 2D).

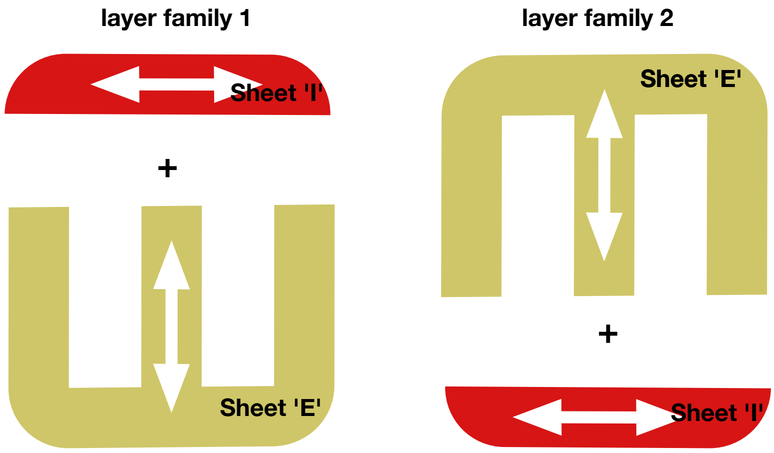


**Figure 3.2:** Transformer core layers: layer family 1 (left) with 'I-shaped' sheet (red region) on top and 'E-shaped' sheet (yellow region) on bottom; layer family 2 (right) with 'E-shaped' sheet on top and 'I-shaped' sheet on bottom. White arrows indicate the easy magnetization direction.

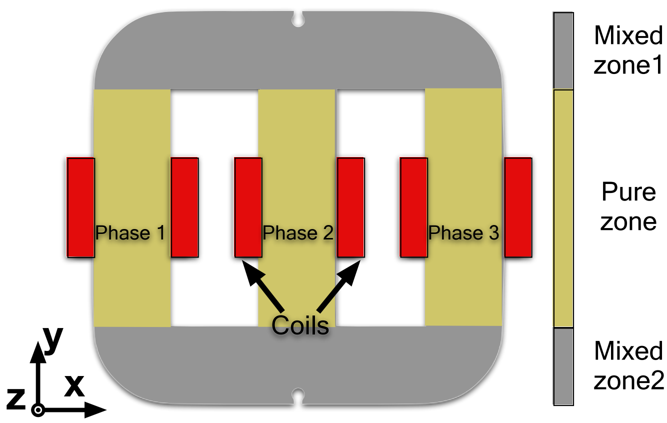


**Figure 3.3:** Equivalent 2D model with coils.

### 3.3.1 Hypotheses

The following assumptions are considered:

- Sheets are normally very thin, allowing to assume a 2D homogeneous magnetic field using the classical tangential magnetic field continuity condition. $\vec{H}_1$ and $\vec{H}_2$ denoting the magnetic field in each family, the following relation is obtained (eq.3.38).

$$\vec{H}_1 = \vec{H}_2 = \vec{H} \tag{3.38}$$

- Sheets are considered perfectly stacked together, allowing to assume a homogeneous displacement field at the interface between two sheets. Homogeneous strain can consequently be considered in the sheet plane. $\boldsymbol{\epsilon}_1$ and $\boldsymbol{\epsilon}_2$ denoting the total strain in each family, the homogeneous strain hypothesis within the sheet plane $(XY)$ leads to:

$$\boldsymbol{\epsilon}_{1XY} = \boldsymbol{\epsilon}_{2XY} = \boldsymbol{\epsilon}_{XY} \tag{3.39}$$

  $\boldsymbol{\epsilon}$ indicates the average deformation (NB: deformation along $Z$-axis is on the contrary not necessarily homogeneous).

- The transformer is supposed mechanically unloaded and thin enough to consider out-of-plane stress free conditions on upper and lower surfaces. This assumption leads to:

$$\boldsymbol{\sigma}_1.\vec{Z} = \boldsymbol{\sigma}_2.\vec{Z} = \boldsymbol{\sigma}.\vec{Z} = \vec{0} \tag{3.40}$$

  $\boldsymbol{\sigma}$ indicates the average stress.

- Elastic and magnetostrictive deformations are considered sufficiently small to allow additive description of total deformation:

$$\boldsymbol{\epsilon} = \boldsymbol{\epsilon}_{\mu} + \boldsymbol{\epsilon}_{el} \tag{3.41}$$

  $\boldsymbol{\epsilon}_{el}$ indicates the elastic strain tensor.

### 3.3.2 Mixing rules

The magnetic flux $\phi$ circulating in the transformer through the surface $S$ of normal $\vec{n}$ belonging to the sheet plane can be expressed as the sum of the flux in families 1 and 2 of sections $S_1$ and $S_2$ of normal $\vec{n}$ (eq.3.42).

$$\phi = \iint_S \vec{B}\cdot\vec{n}ds = \iint_{S_1} \vec{B}_1\cdot\vec{n}ds + \iint_{S_2} \vec{B}_2\cdot\vec{n}ds \tag{3.42}$$

At a given point of the 2D problem, induction is homogeneous through the thickness for each family since magnetic field is homogeneous as well. The flux conservation relation is rewritten in:

$$\vec{B} = f_1\vec{B}_1 + f_2\vec{B}_2 \tag{3.43}$$

with $f_1$ and $f_2$ the section (or volume) fraction of family 1 and 2 respectively $(f_1 + f_2 = 1)$. Homogenized magnetic induction can be defined as $\vec{B} = \mu_0(\vec{H} + \vec{M})$, where $\vec{M}$ is homogenized magnetization. With this mixing rule of magnetic induction (eq.3.43) and the hypothesis of homogeneous magnetic field (eq.3.38), a mixing rule of magnetization is obtained as well:

$$\vec{M} = f_1\vec{M}_1 + f_2\vec{M}_2 \tag{3.44}$$

$\vec{M}_i$ is the magnetization in layer family $i$.

The differential susceptibility in layer family 1 and 2 are respectively defined as $\chi_{d1}$ and $\chi_{d2}$, where

$$\chi_{di} = \frac{d\vec{M}_i}{d\vec{H}} \quad (i = 1,2) \tag{3.45}$$

This leads to a homogenization of differential susceptibility:

$$\chi_d = f_1\chi_{d1} + f_2\chi_{d2} \tag{3.46}$$

The mechanical resultant $\vec{R}$ over a surface $S$ of normal $\vec{n}$ belonging to the sheet plane can be expressed as the sum of the mechanical resultant in families 1 and 2 of sections $S_1$ and $S_2$ of normal $\vec{n}$ as function of the average stress $\boldsymbol{\sigma}$ and the stress in each medium following:

$$\vec{R} = \iint_S \boldsymbol{\sigma} \cdot \vec{n} ds = \iint_{S_1} \boldsymbol{\sigma}_1 \cdot \vec{n} ds + \iint_{S_2} \boldsymbol{\sigma}_2 \cdot \vec{n} ds \tag{3.47}$$

At a given point of the 2D problem, the stress is homogeneous through the thickness for each family since deformation (especially elastic) is homogeneous as well. The resultant conservation relation is rewritten in:

$$\boldsymbol{\sigma} = f_1\boldsymbol{\sigma}_1 + f_2\boldsymbol{\sigma}_2 \tag{3.48}$$

As underlined before, the total strain $\boldsymbol{\epsilon}$ is the sum of elastic strain $\boldsymbol{\epsilon}_e$ and magnetostrictive strain $\boldsymbol{\epsilon}_\mu$. Applying Hooke's law to each family, the following expressions of local stress tensor are obtained:

$$\boldsymbol{\sigma}_1 = \mathbb{C}_1 : \boldsymbol{\epsilon}_{el1} = \mathbb{C}_1 : \left(\boldsymbol{\epsilon}_1 - \boldsymbol{\epsilon}_{\mu 1}\right) \tag{3.49}$$

$$\boldsymbol{\sigma}_2 = \mathbb{C}_2 : \boldsymbol{\epsilon}_{el2} = \mathbb{C}_2 : \left(\boldsymbol{\epsilon}_2 - \boldsymbol{\epsilon}_{\mu 2}\right) \tag{3.50}$$

$\mathbb{C}_1$ and $\mathbb{C}_2$ are the $4^{th}$ order stiffness tensor of families 1 and 2. The average stress is on the other hand related to the average elastic strain using the effective stiffness tensor $\mathbb{C}$.

$$\boldsymbol{\sigma} = \mathbb{C} : \boldsymbol{\epsilon}_e = \mathbb{C} : \left(\boldsymbol{\epsilon} - \boldsymbol{\epsilon}_\mu\right) \tag{3.51}$$

The mixing rule (eq.3.48) is applied and simplified using the homogeneous deformation hypothesis, leading to:

$$\mathbb{C} = f_1\mathbb{C}_1 + f_2\mathbb{C}_2 \tag{3.52}$$

on the one hand (usual averaging operation over the stiffness tensor - Voigt bound), and:

$$\epsilon_\mu = f_1(\mathbb{C}^{-1}\mathbb{C}_1) : \epsilon_{\mu 1} + f_2(\mathbb{C}^{-1}\mathbb{C}_2) : \epsilon_{\mu 2} \tag{3.53}$$

on the other hand. This new mixing rule over the magnetostriction strain allows the calculation of a homogenized magnetostriction deformation depending on the stiffness, volume fraction and magnetostriction strain of each layer. In a real transformer with hundreds of layers $f_1 \approx f_2 \approx 0.5$.

### 3.3.3 Homogenized SMSM

In order to carry out multi-layer power transformer simulation in a 2D description, the combination of the mixing rule and the SMSM is developed. As shown in Fig.3.2, the rolling direction in the 'mixed zone' is different from layer to layer, forming a composite material. The strategy is to apply SMSM to each layer family, with different orientation of rolling direction. Magnetization, differential susceptibility, and free magnetostriction strain in each layer family are first computed. The homogenized behavior is then obtained by applying the mixing rule defined in eq.3.44, 3.46 and 3.53. Fig.3.4 describes the general strategy of the homogenized SMSM.

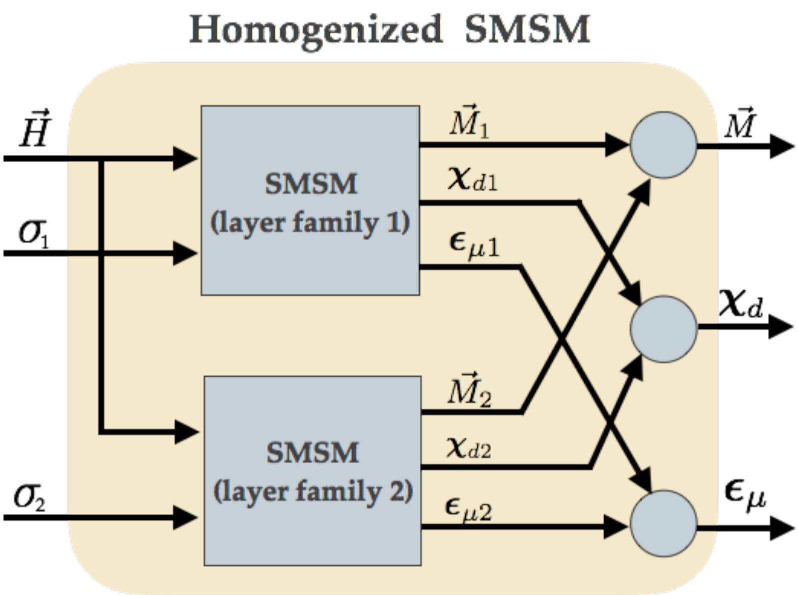


**Figure 3.4:** Homogenized SMSM.

## 3.4 Magnetic resolution

Magnetic resolution is carried out under the magnetic static assumption (induced currents not considered). Since the constitutive model is anhysteretic, magnetic hysteresis and dynamic behavior are not considered. The imposed magnetic flux or coil current is first discretized in the time domain. The magnetic resolution uses an iterative Newton-Raphson method: a magnetic flux $\phi$ or coils current $I$ is imposed; the magnetization $\vec{M}$ is arbitrarily defined at the first loop allowing a first estimation of the magnetic field $\vec{H}$; SMSM is then engaged to take into account anisotropy, nonlinearity and the stress dependency of the material. This SMSM is combined with a homogenization rule, forming a homogenized SMSM, in order to achieve the modeling of the laminated structure in a 2D simulation, which leads to an average behavior through the layers. The homogenized differential magnetic susceptibility $\chi_d$ and magnetization $\vec{M}$ are then updated, using the homogenized SMSM. The procedure is iterated until convergence. At the end of each magnetic iteration, both Maxwell tensor $\boldsymbol{T}$ and magnetostriction free strain $\epsilon_\mu$ are obtained. The block diagram for magnetic resolution is summarized in Fig.3.5.

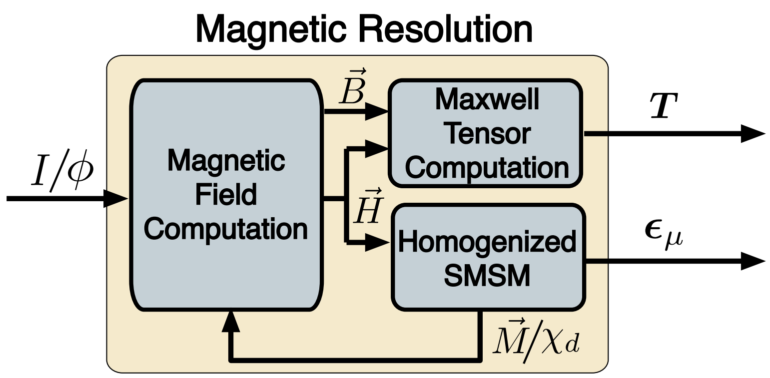


**Figure 3.5:** Block diagram for magnetic resolution.

The creation of magnetic field needs external excitations. For the application of power transformer, this is numerically achieved by injecting current in the coils or 'injecting' the magnetic flux in the ferromagnetic core. According to Faraday's law, the electromotive force is given by the changing rate of the magnetic flux. This means that numerically impose a sinusoidal magnetic flux in the power transformer core is equivalent to apply a sinusoidal voltage on the coils, which is close to the working condition of real power transformers.

The magnetic resolution with imposed current is relatively simple and has advantages such as a low computational cost. However, one important criterion for power transformer design is the power-to-mass ratio (transmitted power per unit mass), which is proportional to the magnetic flux $\phi$ circulating in the transformer core. It i consequently important to compare the core deformation and excitation current of different cores at the same imposed magnetic flux. Besides, transformers are normally driven with voltage, which is proportional to the magnetic flux in each phase. Imposing balanced magnetic flux often leads to unbalanced currents in the coils, because of the unbalanced reluctance in most of the transformer parts. In this section, we are going to introduce magnetic resolution using both methods: current loading and magnetic flux loading.

### 3.4.1 Current injection

**Basic equations and weak formulation**

The following part gives some details on the magnetic field computation for electric current loading. The scalar potential formulation is engaged (eq.3.54), where $\varphi$ is the magnetic scalar potential and $I$ is the current in the coils. A unit current potential vector $\vec{T}_0^n$ is defined to get current density in coils $\vec{j}$ (eq.3.55). Considering the magnetization $\vec{M}$ and vacuum permeability $\mu_0$, the magnetic induction $\vec{B}$ is deduced, based on eq.3.56.

$$\vec{H} = -\vec{\nabla}\varphi + I\vec{T}_0^n \tag{3.54}$$

$$I\vec{\nabla}\times\vec{T}_0^n = \vec{j} \tag{3.55}$$

$$\vec{B} = \mu_0(\vec{H}+\vec{M}) \tag{3.56}$$

$$\vec{\nabla}\cdot\vec{B} = 0 \tag{3.57}$$

Combined with magnetic flux conservation rule (eq.3.57), the weak formulation is shown in (3.58), where $\Omega$ is the integration domain, $\upsilon$ is a test function, and $\nu_0$ is the vacuum reluctivity. With a given coil current $I$, the magnetic scalar potential $\varphi$ is deduced through the non-linear system resolution.

$$\begin{aligned}
\mathcal{F}_I(\varphi) &= \int_\Omega \vec{B}\cdot\vec{\nabla}\upsilon\,\mathrm{d}\Omega \\
&= \int_\Omega \mu_0\left(-\vec{\nabla}\varphi + I\vec{T}_0^n + \vec{M}\right)\cdot\vec{\nabla}\upsilon\,\mathrm{d}\Omega \\
&= 0
\end{aligned} \tag{3.58}$$

For the electrical devices containing multiple phases, such as three-phase power transformer, formulation (eq.3.58) is able to be easily adapted:

$$\begin{aligned}
\mathcal{F}_I(\varphi) &= \int_\Omega \vec{B}\cdot\vec{\nabla}\upsilon\,\mathrm{d}\Omega \\
&= \int_\Omega \mu_0\left(-\vec{\nabla}\varphi + I_1\vec{T}_{01}^n + I_2\vec{T}_{02}^n + I_3\vec{T}_{03}^n + \vec{M}\right)\cdot\vec{\nabla}\upsilon\,\mathrm{d}\Omega \\
&= 0
\end{aligned} \tag{3.59}$$

where $I_1$, $I_2$, and $I_3$ are current injected in phase 1, 2, and 3. $T_{01}^n$, $T_{02}^n$, and $T_{03}^n$ are the unit current potential vectors for each phase.

**Discretization and non-linear resolution**

The weak form of the magneto-static problem (eq.3.58) is then developed in first order Taylor series:

$$\mathcal{F}_I(\varphi+\Delta\varphi) = \mathcal{F}_I(\varphi) + \frac{\partial\mathcal{F}_I}{\partial\varphi}\Delta\varphi = 0 \tag{3.60}$$

This problem is then solved, using Newton-Raphson method. This leads to the iterative relation shown in (eq.3.61). $\boldsymbol{\mu}_{rd}^{p}$ is the differential relative magnetic permeability tensor for the $p^{th}$ iteration, obtained from $\chi_{d}^{p}$ (eq.3.62). $\Delta\varphi$ gives the difference between iterations (eq.3.63).

$$\int_{\Omega} \mu_0 \boldsymbol{\mu}_{rd}^{p} \cdot \vec{\nabla}\upsilon \cdot \vec{\nabla}(\Delta\varphi)\, \mathrm{d}\Omega = \int_{\Omega} \vec{B}^{p} \cdot \vec{\nabla}\upsilon\, \mathrm{d}\Omega \tag{3.61}$$

$$\boldsymbol{\mu}_{rd}^{p} = \chi_{d}^{p} + 1 \tag{3.62}$$

$$\Delta\varphi = \varphi^{p+1} - \varphi^{p} \tag{3.63}$$

This iterative relation is then discretized and solved using finite element method, leading to a linear system between iterations (eq.3.64), where $m$ is the number of degrees of freedom. $\boldsymbol{\varphi}$ is the vector gathering the magnetic scalar potential values at the nodes. Components in (eq.3.64) are defined in (3.65)-(3.66). $i$ and $j$ denote respectively the index of row and column of each component.

$$[\boldsymbol{A}]_{(m*m)}\,[\Delta\boldsymbol{\varphi}]_{(m*1)} = [\boldsymbol{D}]_{m*1} \tag{3.64}$$

$$a^{ij} = \iint_{\Omega} \mu_0 \boldsymbol{\mu}_{rd} \cdot \vec{\nabla}\varphi^{i} \cdot \vec{\nabla}\upsilon^{j}\, \mathrm{d}\Omega \tag{3.65}$$

$$d^{i} = \iint_{\Omega} \vec{\nabla}\upsilon^{i} \cdot \vec{B}^{i}\, \mathrm{d}\Omega \tag{3.66}$$

When this system converges, $\boldsymbol{\varphi}$ is obtained by accumulating $\Delta\boldsymbol{\varphi}$. Magnetic field $\vec{H}$ is then computed using (eq.3.54). $\vec{M}$ and $\boldsymbol{\epsilon}_{\mu}$ fields are the outputs of the SMSM at each time step.

### 3.4.2 Magnetic flux injection

#### Basic equations and weak formulation

Magnetic resolution with flux injection is built based on current injection. In magnetic resolution with current injection, coils current is given and the system solves the magnetic scalar potential, which leads to the computation of the magnetic field and induction. In magnetic resolution with flux injection, the magnetic flux in the core is imposed as the input of the problem, and one need to solve both the coils current and the magnetic scalar potential. The fact that the system has more unknown parameters needs the addition of another equation to solve the system. In addition to the classic magnetic scalar potential formulation described by (eq.3.54-3.57), the second equation is obtained from the total magnetic energy formulation shown in (eq.3.67) [Bouissou et Piriou, 1994].

$$\phi I = \int_{\Omega} I \vec{T}_{0}^{n} \cdot \vec{B}\, \mathrm{d}\Omega \tag{3.67}$$

where $\phi$ is the given magnetic flux. This formulation is rewriten in form of (eq.3.58). Combined with equation (eq.3.58), the magnetic resolution can be carried out with given applied magnetic flux, leading to the coil current value $I$ and magnetic scalar potential $\varphi$.

$$\begin{aligned}\mathcal{F}_{\phi}(\varphi, I) &= \int_{\Omega} \vec{T}_0^n \cdot \vec{B}\,\mathrm{d}\Omega - \phi \\ &= \int_{\Omega} \mu_0 \left(-\vec{\nabla}\varphi + I\vec{T}_0^n + \vec{M}\right) \cdot \vec{T}_0^n\,\mathrm{d}\Omega - \phi \\ &= 0\end{aligned} \tag{3.68}$$

This form described in (eq.3.68) can also be extended to multi-phase applications, where each phase corresponds to one formulation, shown in (eq.3.69).

$$\begin{aligned}\mathcal{F}_{\phi i}(\varphi, I_i) &= \int_{\Omega} \vec{T}_{0i}^n \cdot \vec{B}\,\mathrm{d}\Omega - \phi_i \\ &= \int_{\Omega} \mu_0 \left(-\vec{\nabla}\varphi + I_i\vec{T}_{0i}^n + \vec{M}\right) \cdot \vec{T}_{0i}^n\,\mathrm{d}\Omega - \phi_i \\ &= 0\end{aligned} \tag{3.69}$$

$\mathcal{F}_{\phi i}(\varphi, I_i)$ refers to equation in phase $i$. $\phi_i$ and $I_i$ are respectively the imposed magnetic flux and computed current in phase $i$.

### Discretization and non-linear resolution

At a given moment, this static non-linear magnetic problem is solved using the Newton-Raphson method. As a consequence, the problem defined by (eq.3.58) and (eq.3.68) is developed in first order Taylor series for both unknowns $\varphi$ and $I$:

$$\mathcal{F}_I(\varphi + \Delta\varphi, I + \Delta I) = \mathcal{F}_I(\varphi, I) + \frac{\partial \mathcal{F}_I}{\partial \varphi}\Delta\varphi + \frac{\partial \mathcal{F}_I}{\partial I}\Delta I = 0 \tag{3.70}$$

$$\mathcal{F}_{\phi}(\varphi + \Delta\varphi, I + \Delta I) = \mathcal{F}_{\phi}(\varphi, I) + \frac{\partial \mathcal{F}_{\phi}}{\partial \varphi}\Delta\varphi + \frac{\partial \mathcal{F}_{\phi}}{\partial I}\Delta I = 0 \tag{3.71}$$

The iterative relation of this problem is then described in (eq.3.72) and (eq.3.73). $\boldsymbol{\mu}_{rd}^p$ is the differential relative magnetic permeability tensor for the $p^{th}$ iteration. $\Delta\varphi$ and $\Delta I$ give respectively the difference between iterations.

$$\int_{\Omega} \mu_0 \boldsymbol{\mu}_{rd}^p \cdot \vec{\nabla}\upsilon \cdot \vec{\nabla}(\Delta\varphi)\,\mathrm{d}\Omega - \int_{\Omega} \mu_0 \boldsymbol{\mu}_{rd}^p \cdot \vec{T}_0^n \cdot \vec{\nabla}\upsilon(\Delta I)\,\mathrm{d}\Omega = \int_{\Omega} \vec{B}^p \cdot \vec{\nabla}\upsilon\,\mathrm{d}\Omega \tag{3.72}$$

$$-\int_{\Omega} \mu_0 \boldsymbol{\mu}_{rd}^p \cdot \vec{T}_0^n \cdot \vec{\nabla}(\Delta\varphi)\,\mathrm{d}\Omega + \int_{\Omega} \mu_0 \boldsymbol{\mu}_{rd}^p \cdot \vec{T}_0^n \cdot \vec{T}_0^n(\Delta I)\,\mathrm{d}\Omega = \phi - \int_{\Omega} \vec{B}^p \cdot \vec{T}_0^n\,\mathrm{d}\Omega \tag{3.73}$$

This iterative relation is then solved using a finite element method, leading to a linearized system of equation between iterations (eq.3.74). $\boldsymbol{\varphi}$ is the vector gathering the magnetic scalar potential values at the nodes. Components in (eq.3.74) are defined in (eq.3.75-3.79). $i$ and $j$ denote respectively the index of row and column of each component. $m$ indicates the number of degrees of freedom.

$$\left[\begin{array}{c:c} \boldsymbol{A}_{(m*m)} & \boldsymbol{B}_{(m*1)} \\ \hdashline \boldsymbol{B}^t_{(1*m)} & c \end{array}\right] \cdot \left[\begin{array}{c} \Delta\varphi_{(m*1)} \\ \hdashline \Delta I \end{array}\right] = \left[\begin{array}{c} \boldsymbol{D}_{(m*1)} \\ \hdashline e \end{array}\right] \tag{3.74}$$

$$a^{ij} = \iint_{\Omega} \mu_0 \boldsymbol{\mu}_{rd} \cdot \vec{\nabla}\varphi^i \cdot \vec{\nabla}\upsilon^j \,\mathrm{d}\Omega \tag{3.75}$$

$$b^i = -\iint_{\Omega} \mu_0 \boldsymbol{\mu}_{rd} \cdot \vec{\nabla}\upsilon^i \cdot \vec{T}^n_0 \,\mathrm{d}\Omega \tag{3.76}$$

$$c = \iint_{\Omega} \mu_0 \vec{T}^n_0 \cdot \vec{T}^n_0 \,\mathrm{d}\Omega \tag{3.77}$$

$$d^i = \iint_{\Omega} \vec{\nabla}\upsilon^i \cdot \vec{B}^i \,\mathrm{d}\Omega \tag{3.78}$$

$$e = \phi - \iint_{\Omega} \vec{B} \cdot \vec{T}^n_0 \,\mathrm{d}\Omega \tag{3.79}$$

### Multi-phase consideration and circuit coupling

The electromagnetic system is able to be extended to a three phase problem. The system described by (eq.3.58) and (eq.3.68) is then written in form of (eq.3.80) and (eq.3.81).

$$\begin{aligned} &\mathcal{F}_I\left(\varphi+\Delta\varphi, I_1+\Delta I_1, I_2+\Delta I_2, I_3+\Delta I_3\right) \\ =&\mathcal{F}_I\left(\varphi, I_1, I_2, I_3\right)+\frac{\partial \mathcal{F}_I}{\partial \varphi}\Delta\varphi+\frac{\partial \mathcal{F}_I}{\partial I_1}\Delta I_1+\frac{\partial \mathcal{F}_I}{\partial I_2}\Delta I_2+\frac{\partial \mathcal{F}_I}{\partial I_3}\Delta I_3 \\ =&0 \end{aligned} \tag{3.80}$$

$$\begin{aligned} &\mathcal{F}_{\phi i}\left(\varphi+\Delta\varphi, I_1+\Delta I_1, I_2+\Delta I_2, I_3+\Delta I_3\right) \\ =&\mathcal{F}_{\phi i}\left(\varphi, I_1, I_2, I_3\right)+\frac{\partial \mathcal{F}_{\phi i}}{\partial \varphi}\Delta\varphi+\frac{\partial \mathcal{F}_{\phi i}}{\partial I_1}\Delta I_1+\frac{\partial \mathcal{F}_{\phi i}}{\partial I_2}\Delta I_2+\frac{\partial \mathcal{F}_{\phi i}}{\partial I_3}\Delta I_3 \\ =&0 \quad (i=1,2,3) \end{aligned} \tag{3.81}$$

Considering a three phase transformer in star configuration without neutral, it is possible to add a closure equation for current: $I_1+I_2+I_3=0$. (eq.3.82) gives the new global weak formulation system of equations, where components are defined in (eq.3.83-3.87). $i$ and $j$ denote respectively the index of row and column of each component, and $k$ is the number of phases. Using an imposed magnetic flux computation at each phase $\phi_k$, two kinds of unknowns are solved at once: $\varphi$ is the vector gathering the magnetic scalar potential values at the nodes; $I_k$ is the $k^{th}$ phase current.

$$\left[\begin{array}{c:cc} \boldsymbol{A}_{(m*m)} & \boldsymbol{B}_{1(m*1)}-\boldsymbol{B}_{3(m*1)} & \boldsymbol{B}_{2(m*1)}-\boldsymbol{B}_{3(m*1)} \\ \hdashline \boldsymbol{B}^t_{1(1*m)}-\boldsymbol{B}^t_{3(1*m)} & c_1-c_3 & 0 \\ \boldsymbol{B}^t_{2(1*m)}-\boldsymbol{B}^t_{3(1*m)} & 0 & c_2-c_3 \end{array}\right] \cdot \left[\begin{array}{c} \Delta\varphi_{(m*1)} \\ \hdashline \Delta I_1-\Delta I_3 \\ \Delta I_2-\Delta I_3 \end{array}\right] = \left[\begin{array}{c} \boldsymbol{D}_{(m*1)} \\ \hdashline e_1-e_3 \\ e_2-e_3 \end{array}\right] \tag{3.82}$$

$$a^{ij} = \iint_{\Omega} \mu_0 \boldsymbol{\mu}_{rd} \cdot \vec{\nabla}\varphi^i \cdot \vec{\nabla}\upsilon^j \, \mathrm{d}\Omega \tag{3.83}$$

$$b_k^i = -\iint_{\Omega} \mu_0 \boldsymbol{\mu}_{rd} \cdot \vec{\nabla}\upsilon^i \cdot \vec{T}_{0(k)}^n \, \mathrm{d}\Omega \tag{3.84}$$

$$c_k = \iint_{\Omega} \mu_0 \, \vec{T}_{0(k)}^n \cdot \vec{T}_{0(k)}^n \, \mathrm{d}\Omega \tag{3.85}$$

$$d^i = \iint_{\Omega} \vec{\nabla}\upsilon^i \cdot \vec{B}^i \, \mathrm{d}\Omega \tag{3.86}$$

$$e_k = \phi_k - \iint_{\Omega} \vec{B} \cdot \vec{T}_{0(k)}^n \, \mathrm{d}\Omega \tag{3.87}$$

After resolution of this non-linear electro-magnetic system, $I_k$ and $\varphi$ are obtained by accumulating $\Delta I_k$ and $\Delta\varphi$. $\vec{M}$ and $\epsilon_\mu$ fields are the outputs of the SMSM at each time step.

### 3.4.3 Maxwell stress tensor

Maxwell stress tensor is developed from Maxwell equations, in order to compute the magnetic force in an easier way, compared to the Virtual Power Principle. The classical Maxwell stress tensor is noted as $\boldsymbol{T}^M$ (eq.3.88), where $\boldsymbol{\delta}$ stands for the second order identity tensor. This allows the computation of total magnetic force inside a surface $S$ by integrating the normal component of $\boldsymbol{T}^M$ over $S$. However, this is true when the surface $S$ lies entirely in a linear and isotropic material with a scalar magnetic permeability $\mu$, and this happens only in the air (or in an ideal infinite material). The application of classical Maxwell stress tensor allows an easy computation of the local magnetic force in air-gaps. When it comes to the computation of the distribution of magnetic force inside a magnetic material, or at the interface of two magnetic materials, the classical Maxwell stress tensor can not be applied.

$$\boldsymbol{T}^M = \vec{H} \otimes \vec{B} - \frac{1}{2}\vec{H} \cdot \vec{B}\boldsymbol{\delta} \tag{3.88}$$

We introduce in this modeling chain, a newly developed symmetric Maxwell stress tensor [Bossavit, 2015], which is able to deal with the nonlinearity and anisotropy of the material behavior (eq.3.89). The term $\varphi\left(\vec{H}\right)$ is the magnetic co-energy, which takes the material nonlinear behavior into account. The divergence of this newly developed Maxwell stress tensor is indeed the local force, supposing that the B-H law has no dependence on the local stress.

$$\boldsymbol{T}^{SM} = \frac{1}{2}\left(\vec{H} \otimes \vec{B} + \vec{B} \otimes \vec{H}\right) - \varphi\left(\vec{H}\right)\boldsymbol{\delta} \tag{3.89}$$

## 3.5 Force computation

Once the Maxwell stress tensor and the free magnetostriction strain tensor are computed, the next step consists in the calculation of the relating forces to obtain the mechanical loading of a pure vibrational problem.

Considering volume magnetic forces $\vec{f}_m$, the balance equation leads to:

$$\vec{\nabla} \cdot \boldsymbol{\sigma} + \vec{f}_m = \rho_m \frac{\partial^2 \vec{u}}{\partial t^2} \tag{3.90}$$

where $\vec{u}$ indicates the displacement field and $\rho_m$ the mass density. Using the decomposition of total strain $\boldsymbol{\epsilon}$ into elastic $\boldsymbol{\epsilon}_{el}$ and magnetostrictive strain $\boldsymbol{\epsilon}_\mu$, Hooke's law is expressed in (eq.3.91), under plane stress assumption.

$$\boldsymbol{\sigma} = \mathbb{C} : (\boldsymbol{\epsilon} - \boldsymbol{\epsilon}_\mu) \tag{3.91}$$

Equation (3.90) then becomes:

$$\vec{\nabla} \cdot \tilde{\boldsymbol{\sigma}} + \vec{f}_\mu + \vec{f}_m = \rho_m \frac{\partial^2 \vec{u}}{\partial t^2} \tag{3.92}$$

with:

$$\tilde{\boldsymbol{\sigma}} = \mathbb{C} : \boldsymbol{\epsilon} \qquad \text{and} \qquad \vec{f}_\mu = -\vec{\nabla} \cdot (\mathbb{C} : \boldsymbol{\epsilon}_\mu) \tag{3.93}$$

The magneto-elastic problem is transformed into a pure elastic problem where the material is submitted to a magnetostriction equivalent force $\vec{f}_\mu$ and a magnetic force $\vec{f}_m$. Magnetostriction equivalent force is a virtual force that creates the same quantity of strain on the material compared to the magnetostriction. These force densities are then transformed into weak forms, leading to corresponding nodal forces [Galopin *et al.*, 2008]. Nodal force is a fictive force, numerically concentrated on the nodes of the mesh. Weak formulations of magnetostriction equivalent nodal force and magnetic nodal force are given in (eq.3.94-3.95).

$$F_\mu^{v,i} = \int_\Omega (\boldsymbol{grad}_s(\vec{v}^i) : \mathbb{C} : \boldsymbol{\epsilon}_\mu) \, \mathrm{d}\Omega \tag{3.94}$$

$$F_m^{v,i} = \int_\Omega (\boldsymbol{grad}_s(\vec{v}^i) : \boldsymbol{T}) \, \mathrm{d}\Omega \tag{3.95}$$

where $\boldsymbol{grad}_s$ is the symetric gradient, defined as: $\boldsymbol{grad}_s(\vec{u}) = \frac{1}{2}(\vec{\nabla}\vec{u} + \vec{\nabla}\vec{u}^T)$. $\vec{v}^i$ is the vectorial test function at the node $i$, and $F_\mu^{v,i}$ ($F_m^{v,i}$) the magnetostriction equivalent nodal force (magnetic nodal force) at the node $i$ in the direction of $\vec{v}$. Then, nodal forces are used as loading for the mechanical resolution. A force profile over the time $\vec{F}_\mu(t)$ is obtained at each node.

## 3.6 Mechanical feedback loop

Magnetostriction and magnetic forces create stress fields that modify the magneto-mechanical behavior of materials. This influence is usually considered negligible in power transformers due to the low magnetostriction of the materials and weak level of magnetic forces in a core structure. The core deformation created by these two loadings is nevertheless not null, and can differ strongly from one layer to another at the same contact point. Because layers in the real transformer are assembled together, creating a uniform displacement and consequently a uniform deformation, the elastic deformation can strongly differ from one layer to another at the same point. The local stress can consequently be very strong through the layers, even if its average value remains small. To the author's knowledge, such kind of configuration has never been tested in the literature.

In this work, a mechanical feedback loop is introduced in the time domain, using static assumption. It is designed as an independent computation block in parallel with the magnetic loop. It can be activated in order to take the induced stress into consideration, or deactivated to economize computation time. In this mechanical feedback loop, the static mechanical resolution is carried out first, taking equivalent force densities as mechanical loadings (3.96). This leads to the total strain field $\boldsymbol{\epsilon}$, sum of the elastic and free magnetostriction strain (3.97), where $\boldsymbol{\epsilon}_{el1}$ ($\boldsymbol{\epsilon}_{el2}$) and $\boldsymbol{\epsilon}_{\mu 1}$ ($\boldsymbol{\epsilon}_{\mu 2}$) are respectively the elastic and free magnetostriction strain in layer family 1 (layer family 2).

$$\vec{f}_\mu = -\vec{\nabla} \cdot \tilde{\boldsymbol{\sigma}} \quad \text{with:} \quad \tilde{\boldsymbol{\sigma}} = \mathbb{C} : \boldsymbol{\epsilon} \tag{3.96}$$

$$\boldsymbol{\epsilon} = \boldsymbol{\epsilon}_{el1} + \boldsymbol{\epsilon}_{\mu 1} = \boldsymbol{\epsilon}_{el2} + \boldsymbol{\epsilon}_{\mu 2} \tag{3.97}$$

Magnetostriction induced stress at the structure level for each layer is finally obtained by a simple linear elastic relation (3.98).

$$\boldsymbol{\sigma}_1 = \mathbb{C} : \boldsymbol{\epsilon}_{el1} \quad \text{and} \quad \boldsymbol{\sigma}_2 = \mathbb{C} : \boldsymbol{\epsilon}_{el2} \tag{3.98}$$

This stress is injected as an input of the SMSM in the magnetic loop, leading to a fully coupled magneto-mechanical solution. Fig.3.6 gives the illustration of the strategy for mechanical feedback loop. In practice, the convergence procedure can be stabilized by the introduction of a relaxation coefficient.

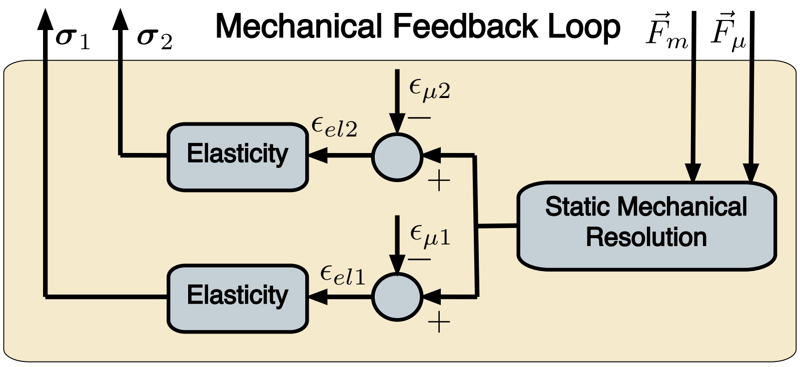


**Figure 3.6:** Modeling strategy for mechanical feedback loop.

## 3.7 Harmonic mechanical resolution

Once the equivalent force over time is calculated, a Fast Fourier Transformation (FFT) of equivalent force is performed. This helps to avoid transient calculation which takes more calculation time. The mechanical problem is then solved in the frequency domain. An Inverse Fast Fourier Transformation (IFFT) is then performed, which gives the displacement field of the transformer core in the time domain, as illustrated in Fig.3.7.

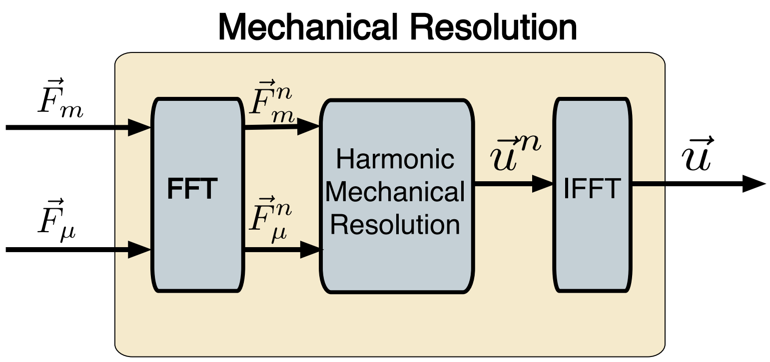


**Figure 3.7:** Modeling strategy for mechanical resolution.

Harmonic mechanical resolution is carried out for each harmonic $n$ of pulsation $\omega^n$ (3.99).

$$\vec{\nabla} \cdot \tilde{\sigma}^n + \vec{f}_\mu^n + \vec{f}_m^n = -\rho_m (\omega^n)^2 \vec{u}^n \tag{3.99}$$

where $\vec{f}_\mu^n$ is the density of the equivalent force of the n$^{th}$ harmonic. $\vec{u}^n$ is the displacement field of the n$^{th}$ harmonic. $\omega^n$ is the pulsation. After finite element discretization, the weak form of equation (3.99) can be written as:

$$\left([K] - (\omega^n)^2 [M]\right) [U^n] = [F_\mu^n] + [F_m^n] \tag{3.100}$$

where $[M]$ is the mass matrix, and $[K]$ corresponds to the stiffness matrix. Considering the damping coefficient $\beta$, equation (3.100) becomes:

$$\left([K] + 2j\beta\omega^n [K] - (\omega^n)^2 [M]\right) [U^n] = [F_\mu^n] + [F_m^n] \tag{3.101}$$

This equation is complemented by Dirichlet boundary conditions: one point is fixed and considered as the reference point; a neighbor point can only move along X direction (isostatic boundary condition). Displacement field $\vec{u}^n$ is obtained by solving equation (3.101). The time domain solution is obtained by an inverse Fourier transformation of the previous solution:

$$u_i(k\Delta t) = \sum_{n=1}^{N} U_i^n \, cos(\omega^n (k\Delta t) + \eta) \tag{3.102}$$

where $\eta$ is the phase delay, and $k$ an integer number starting from 0. The time discretization $\Delta t$ over a period $T$ gives the maximal number of harmonics that are considered in the calculation: $max(K) = T/2\Delta t - 1$.

Moreover it must be underlined that the constitutive equation of the material leads to an initial homogeneous non-null deformation (without electrical loading), due to $W^{\alpha}_{conf}$ (eq. 2.34). The actual displacement field is the difference between the displacement under loading and the no-load case:

$$u_i(k\Delta t)^{actual} = u_i(k\Delta t)^{loaded} - u_i(k\Delta t)^{unloaded} \tag{3.103}$$

Moreover a modal analysis can be implemented by solving the mechanical equation without applied force and damping:

$$[K][U] - \omega^2[M][U] = [0] \tag{3.104}$$

The solving of equation (3.104) allows the calculation of the main vibration modes of the transformer structure.

## 3.8 Acoustic estimation

The displacement field is obtained for each harmonic from the mechanical resolution, leading to the estimation of the vibration generation induced by the core deformation. A block of post-treatment is next added, calculating the acoustic power $P_{ac}$. Acoustic power is an integration of the sound intensity $\vec{I}_{ac}$ along the external oriented surface of the considered structure $\vec{s}$ (3.105). $\vec{I}^n_{ac}$ is the $n^{th}$ harmonic of sound intensity, which is the product of the $n^{th}$ sound pressure $P^n_{ac}$ with particule velocity $\vec{V}^n$ (effective value) (3.106).

$$P_{ac} = \int_s \vec{I}_{ac}\,\mathrm{d}\vec{s} = \int_s \sum_n \vec{I}^n_{ac}\,\mathrm{d}\vec{s} \tag{3.105}$$

$$\vec{I}^n_{ac} = P^n_{ac}\vec{V}^n = Z_0(V^n)^2\vec{n} \tag{3.106}$$

$\vec{n}$ is a unit vector of the particle velocity direction. $Z_0$ is the acoustic impedance, which equals 409.4 $Pa\,s/m$ at the room temperature in the free space. Sound pressure $P^n_{ac}$ is expressed as: $P^n_{ac} = Z_0\vec{V}^n$. A strong advantage of the formulation is that the acoustic power is neither room-dependent nor distance-dependent.

In this work, the acoustic power is estimated using a fictive 3D structure extruded from the 2D simulation. The total surface can be computed, once the thickness of the transformer core is given. Out of plane component of the total strain $\varepsilon_{zz}$ is obtained from the in-plane components (3.107). ($\nu$ is the Poisson ratio.)

$$\varepsilon_{zz} = \frac{1-2\nu}{1-\nu}\varepsilon^{\mu}_{zz} - \frac{\nu}{1-\nu}(\varepsilon_{xx} + \varepsilon_{yy}) \tag{3.107}$$

From $\varepsilon_{zz}$, the movement in direction $\vec{z}$ of the computation area is obtained. The contribution of this surface is then added to get the total acoustic power.

## 3.9 Summary of the assumptions and approximations

Although efforts are made to achieve an accurate numerical simulation, the modeling chain presented in this thesis uses several necessary assumptions and approximations whose objectives are mainly to reduce the computation time. Detailed explanations are given in the following chapters, while a summary of the assumptions is outlined as follows:

- Both magnetic resolution and mechanical feedback loop are carried out under quasi-static assumption.
- The entire modeling chain is carried out under 2D assumption by means of 2D finite element discretization.
- Layers are supposed to be thin enough and perfectly stacked together, leading to a homogenization law to deal with the 3D laminated structure in a 2D simulation.
- Magnetic hysteresis is not taken into consideration. Hysteresis effect is considered as a perspectives. Indeed, IMSM is too complex and needs further simplifications to be integrated into the FE modeling chain.
- Thermal aspects (especially associated with dilatation and stress) are not considered, so that the influences of the core loss and rising temperature on the material properties are not taken into consideration. (considered as perspectives)
- In order to reduce the size of the mesh, air-gaps between E-sheet and I-sheet are not considered. Thus, the E-I stacked core is mechanically equivalent to a '8' shaped core.
- The mechanical strength is supposed to be isotropic, defined only by Young's modulus and Poisson's ratio. The mechanical behavior is identical in all direction. (extension to the anisotropic situation is possible but not considered as crucial)
- Assumption of plane stress is applied for mechanical resolution.
- The damping coefficient is assumed to be a constant independent of the vibration frequency.

## 3.10 Conclusion

The detailed modeling chain is shown in Fig.3.8. This gives the possibility to the computation of the deformation and noise emission of the power transformer and synchronous electrical motor, with the consideration of Maxwell force and magnetostriction. It is adapted to a various ferromagnetic materials with magnetic and magnetostrictive anisotropy and stress-dependency. Most importantly, it offers the possibility to optimize the material and structure combination. The finite element problems are solved using FreeFem++

[Hecht, 2012] including the SMSM as a dynamically linked and parallelized function. Computation is processed on a personal computer of 8 cores with a 3.2GHz clock. In the following chapter, various measurements are carried out on prototypes and compared to the modeling results as a global validation of the modeling.

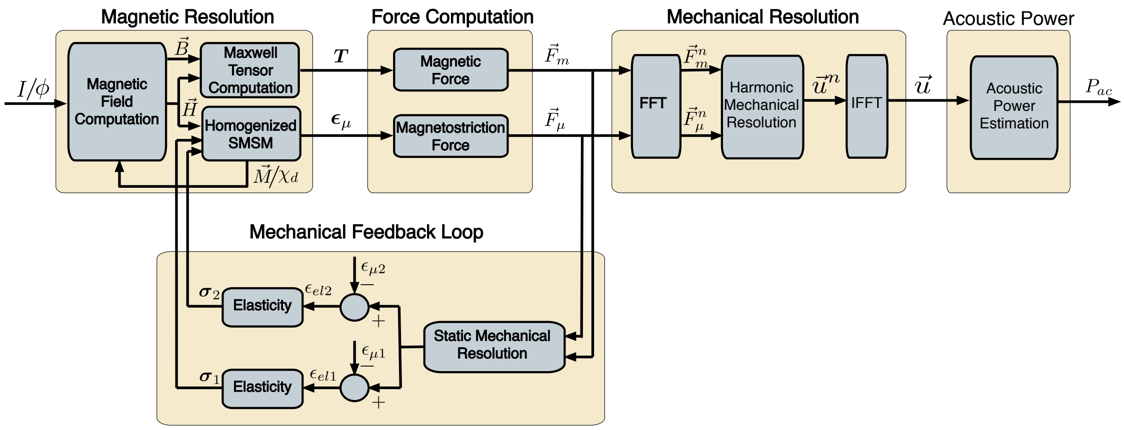


**Figure 3.8:** Detailed global modeling chain.

# Chapter 4

# Identification and Validation in Static Situation

## Contents

## 4.1 Summary of the material-structure configurations

The validation of the FE modeling chain requires the numeric estimations to be compared to experiments carried out on a real transformer: a three-phase three-limb core is chosen as usually used for on board applications. Different geometries of core are considered (design and sheet positioning) to test the robustness of the modeling chain. As explained in section 1.1.2, the core is made from interleaved stacks of 'E-shaped' steel sheets capped with 'I-shaped' pieces. This solution allows a low cost manufacturing and winding facility, 'E-shaped' and 'I-shaped' sheets are cut along the rolling direction of the lamination. They are positioned alternatively on top or on bottom of the transformer in order to dilute parasitic air-gaps and limit their effect [Weiser et Pfützner, 1998].

Four different materials are studied in the vibration measurement, including Grain-oriented (GO) FeSi, Non-oriented (NO) FeSi, FeNi Supra50, and FeCo Afk1. It is recalled that GO FeSi is famous for its high permeability and ultra-low magnetostriction in the rolling direction. In distribution power transformers, I-sheets are normally cut along RD to form the core. NO FeSi is probably the most common magnetic material in electrical machines. As it possesses relatively isotropic magnetic and magnetostrictive behavior, it is ideal for applications with rotational magnetization. FeNi Supra50 is a star product at Aperam Imphy. Its cubic texture design allows a theoretically low magnetostriction along RD and TD to be obtained. However, due to its high price and relatively low saturation magnetization, it is applied only for specific application. FeCo Afk1 is a material designed for high magnetization applications. A new forming process has recently been proposed by Aperam Imphy to use this material as a transformer core. Indeed, an ultra-low isotropic magnetostriction can be obtained over a large induction range. The ultra-low magnetostriction is discovered in strips directions. This might be the best candidate for low noise power transformer regardless of the price. Complementary studies are in progress to verify its performance in power transformer core.

| Material | Saturation magnetization | Magnetostriction in RD | Magnetostriction in TD | Stress depencency |
|---|---|---|---|---|
| NO FeSi | Medium | Medium | Medium | Medium |
| GO FeSi | Medium | Very low | high | Medium |
| FeNi Supra50 | Medium | Very low | Very low | High |
| FeCo Afk1 | High | Very low | Very low | Unknown (to be evaluated) |

**Table 4.1:** List of material used in the experimental part and main characteristics

A real power transformer core, more precisely E-I stacked core, is assembled from several hundred of electrical sheets. Fabrication of the power transformer prototype costs huge effort and money. Moreover, making experimental measurements on real power transformer necessitates large power supply, which is difficult to carry out in the laboratory. In this thesis, in order to validate the numerical simulation, simplified three-layer transformer core prototypes have been fabricated at LMT-Cachan, and experimental measurements have been carried out in the same condition. A precise description of the three-layer core is given in Section 4.3.

Five different configurations of the three-layer core have been considered. They are shown in Fig.4.1. Three-layer cores with configuration '8-x' and '8-y' are assembled by 8-shaped non-cut sheets, with RD oriented in horizontal and vertical directions respectively. These two geometries allow the texture effect to be evaluated. Three-layer cores with configuration 'EI-x' and 'EI-y' are assembled by E-shaped and I-shaped sheets, whose first and last layer are identical, with the E-shaped sheet on the bottom and I-shaped sheet on the top. The middle layer has the E-shaped sheet on the top and I-shaped sheet on the bottom. Rolling direction of all sheets for the configuration 'EI-x' ('EI-y') are oriented horizontally (vertically). Although real power transformer cores are never designed in this way, the comparison between configuration '8-x' and 'EI-x' ('8-y' and 'EI-y') allows a better understanding of the influence of the air-gap on core vibration. Three-layer cores with configuration 'EI' is the standard configuration for EI-core, where E-sheets and I-sheets are cut along RD to minimize the magnetostriction.

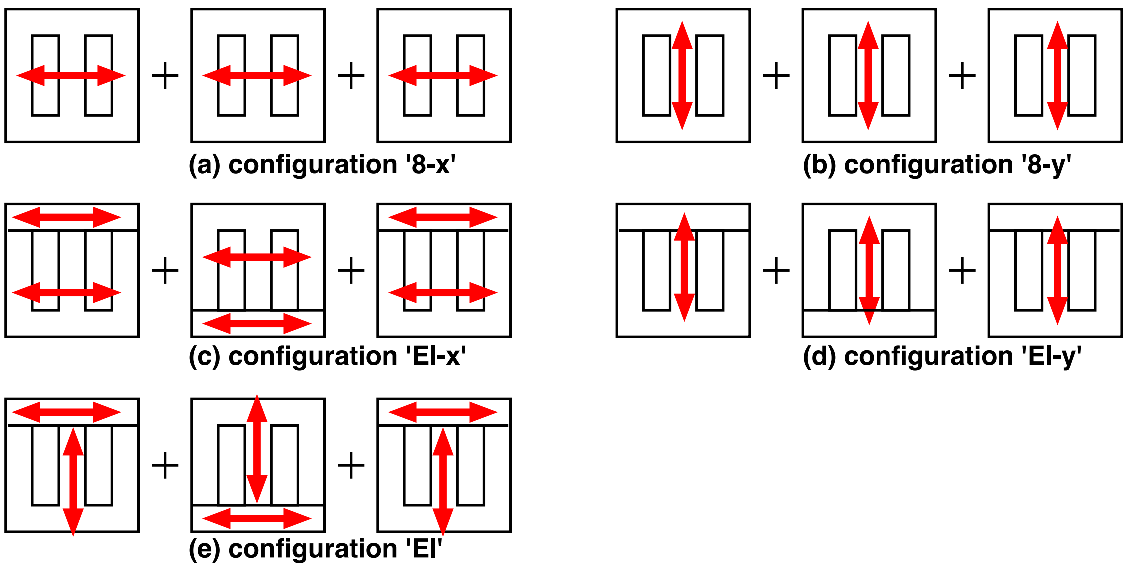


**Figure 4.1:** Illustration of different configurations of three-layer core, with red arrow indicating the rolling direction (RD).

All three-layer transformers have three phases and three limbs, in two different formats. The geometry of Format-A and Format-B are shown in Fig.4.2 and 4.3. Detailed geometry information is confidential and has been removed. The Format A has been used for an early study. It is only made of GO FeSi following a EI assembly. Recent studies are carried out on Format-B. Various material-configuration combinations are fabricated and studied in this format. There is no special link between the Format-A and Format-B. The surface, mass, shape, and coil section of the two formats are all different, so no comparison is proposed between them. The different material-configuration of all three-layer cores are listed in Table.4.2.

<table>
<tr><th>Configuration</th><th>Air-gap</th><th>Material</th><th>Format</th></tr>
<tr><td>8-x</td><td>NO</td><td>NO FeSi</td><td>B</td></tr>
<tr><td>8-y</td><td>NO</td><td>NO FeSi, FeNi Supra50</td><td>B</td></tr>
<tr><td>EI-x</td><td>YES</td><td>NO FeSi</td><td>B</td></tr>
<tr><td>EI-y</td><td>YES</td><td>NO FeSi</td><td>B</td></tr>
<tr><td rowspan="2">EI</td><td rowspan="2">YES</td><td>NO FeSi, FeNi Supra50, FeCo Afk1</td><td>B</td></tr>
<tr><td>GO FeSi</td><td>A</td></tr>
</table>

**Table 4.2:** List of configuration-material three-layer cores

### 4.1.1 Three-layer core prototype

Using three-layer prototypes brings several advantages, especially for E-I stacked core. E-sheet and I-sheet are usually cut along the rolling direction of the lamination as shown in Fig.4.4 (white arrows indicate the RD). As electrical sheets are assembled in a criss-cross way, they are positioned alternatively on the top or on the bottom of the transformer in order to dilute parasitic air-gaps and limit their effect. This forms two families of layer: family 1 with I-sheet on the top and E-sheet on the bottom; family 2 with E-sheet on the top and I-sheet on the bottom. Sectional views in different regions of this transformer are presented in Fig.4.4. For such configuration, the sectional surface of sheet in regions (a), (b) and (c) are composed of 2/3 RD + 1/3 TD, 1/1 RD and 1/3 RD + 2/3 TD respectively. This offers the $Y$-axis symmetry ($X$-axis is on the contrary not an axis of symmetry because upper and lower sections of the three-layer transformer exhibit two different volume fractions of 'E' and 'I' sheets, - i.e. $f_1 \neq f_2$), leading to some variations of the average behavior along the magnetic circuit and some in-plane dissymmetries of the structure. Such assembly is interesting because it leads to a heterogeneous situation, and allows to test the numerical model.

Three-layer prototype forms a sandwich-type structure: the layer in the middle is different from the layers on the boards. Compared to even-number-layer prototypes, three-layer prototype possesses a symmetry in the normal direction, which may be important. Indeed, this symmetry helps to reduce the out-of-plane displacements of the prototype. This point is essential to guarantee the accuracy of in-plane vibration measurements.

### 4.1.2 Preparation of the prototype

Unlike the real E-I stacked cores, where electrical sheets are usually assembled, welded, and clamped together, sheets of the three-layer core prototype are stuck together for simplicity. The fabrication process of this three-layer core prototype is briefly presented as follows:

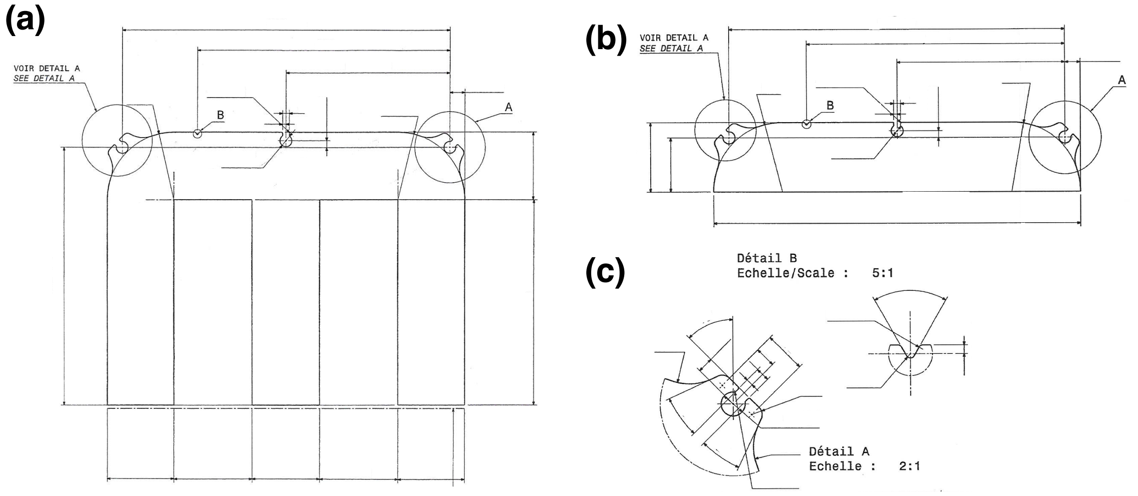


**Figure 4.2:** Geometry of electrical sheets of format A: (a) E-sheet; (b) I-sheet; (c) some detailes of format A

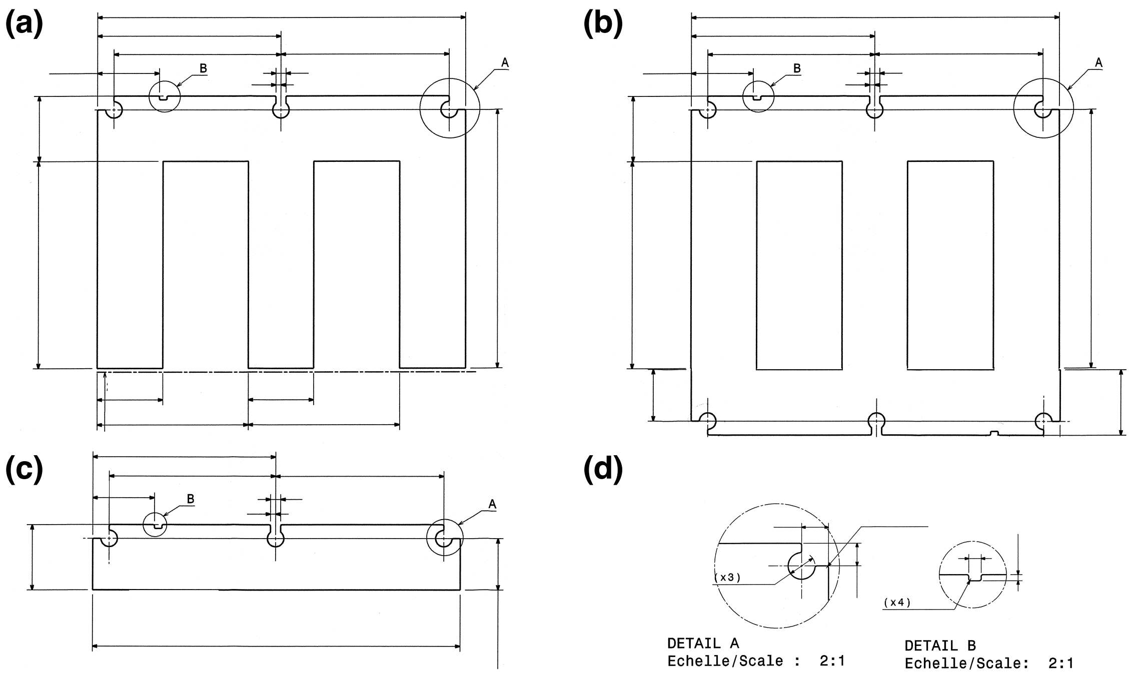


**Figure 4.3:** Geometry of electrical sheets of format B: (a) E-sheet; (b) I-sheet; (c) 8-sheet; (d) some details of format B

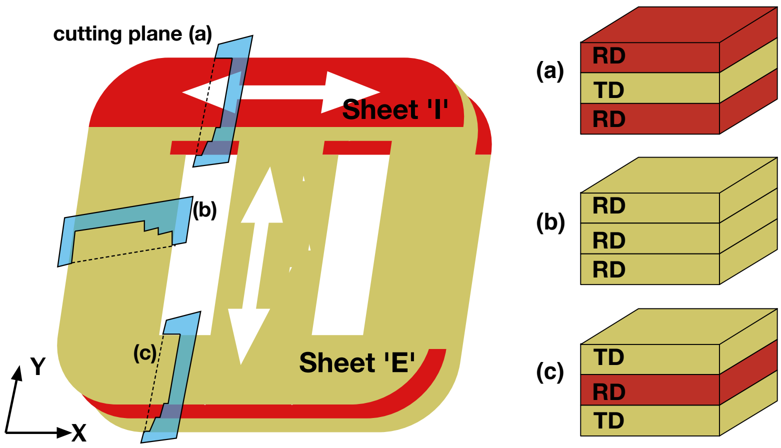


**Figure 4.4:** Transformer core structure : 'E-shaped' sheet (yellow region) + 'I- shaped' sheet (red region) with indication of RD (white arrows). RD of the 'E-shaped' sheet is vertical and RD of the 'I-shaped' sheet is horizontal. (a) sectional view of the top yoke; (b) sectional view of the limb; (c) sectional view of the bottom yoke.

1. Clean the surfaces of the electrical sheets with acetone.
2. Prepare and mix the glue epoxy ARALDITE 420A/B with pistol mixer until it's homogeneous.
3. Smear the glue on the electrical sheets of the bottom layer to get a uniform glue coating.
4. Put the sheets of the second layer on top of the bottom layer and then repeat step 3.
5. Put the sheets of the top layer on top of the second layer.
6. Adjust the position of the electrical sheets to minimize the air-gaps in the overlap region.
7. Apply a slight normal pressure to the sheet plane, in order to evacuate the extra glue and the air bubbles.
8. Clean and remove the extra glue.
9. Drying (24h).
10. Stick the strain gages on the point of measurements.
11. Add a 5-turn secondary coil to the central limb for the measurement of magnetic flux.
12. Add a 40-turn primary coil outside the secondary coil for electrical excitation.

## 4.2 Constitutive behavior identification

### 4.2.1 Experimental protocol

The measurement of the magnetic and magnetostrictive constitutive behavior are carried out using a set-up pre-developed at LMT-Cachan [Gourdin, 1998]. Samples are strips about 100mm long and 12mm wide (thickness depends on the material, about 0.2 to 0.5mm). They are placed between two 'U-shaped' yokes, forming a closed magnetic circuit. A $N$ turns winding is fixed around the electrical sheet sample, creating a quasi-uniform magnetic field. The magnetic field under the current $I$ is computed with Ampere's circuit law, considering the magnetic field inside the yokes strongly negligible comparing to the field in the sample:

$$H = \frac{N \cdot I}{L_{equi}} \tag{4.1}$$

$L_{equi}$ is the equivalent length which equals approximately the length of the sample between the yokes. This length is adjusted after calibration using an H-coil. The measurement of the magnetic induction is carried out using a $n$ turns B-coil:

$$B = -\frac{1}{n \cdot S} \int v(t)\, dt \tag{4.2}$$

where $S$ is the section of the sample, and $v(t)$ is induced voltage in the B-coil.

Local strain of the material is measured by the strain gauge. The strain gauge consists of an insulating flexible backing which supports a metallic foil pattern. The gauge is stuck to the surface of the core, the electrical resistance of the foil changes as it deforms. Although the strain gauge offers precise measurement and is easy to use, it is only used for static or low-frequency application because of its narrow bandwidth [Hubert *et al.*, 2003].

The set-up can be mounted inside an electro-hydraulic machine MTS, applying a tensile stress. This allows the study of the magnetic and magnetostrictive behavior of the material under stress. Here we take advantage of the previous measurement carried out by Z.Li at LMT-Cachan [Li, 2017]. The block diagram and photo of the whole set-up are given in Fig.4.5. More details of experimental protocols and experimental set up are introduced in the thesis work of Rekik [Rekik, 2014].

The measurement of the magnetic and magnetostrictive behavior can be hysteretic and/or anhysteretic. Typical anhysteretic magnetic and magnetostrictive curves are constructed point by point, by applying an alternative magnetic excitation with decreasing amplitude around a DC component $H_{an}$ (illustrated in Fig.4.6). This allows the magnetic domain walls to be unpinned from the pinning site, leading the microstructure of the magnetic material to an equilibrium state and allowing the magnetization to reach its anhysteretic value denoted $M_{an}$.

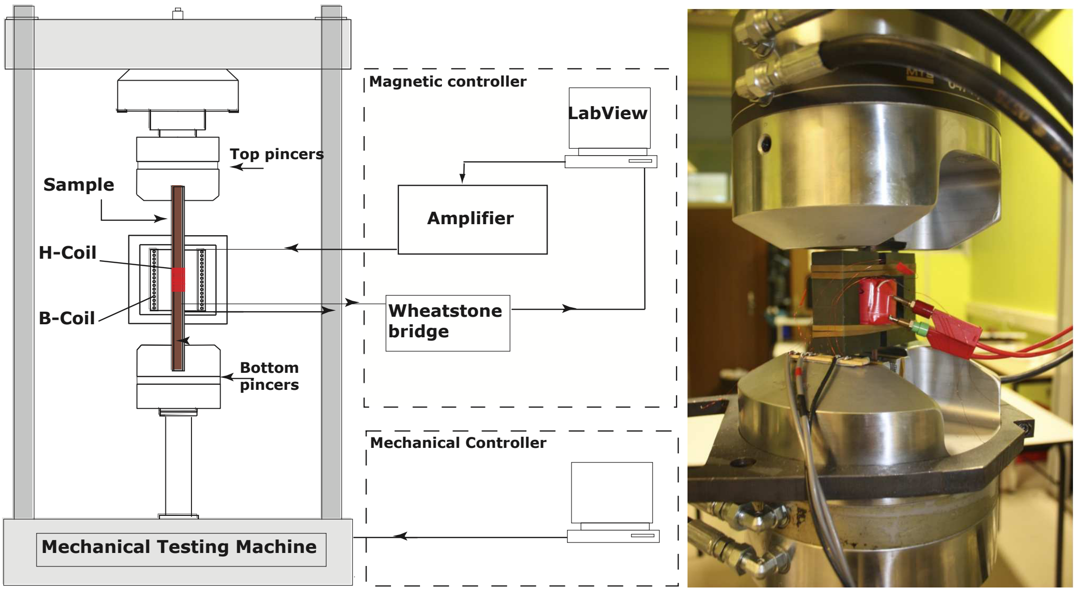


**Figure 4.5:** Block diagram and photo of the measuring set-up [Rekik, 2014].

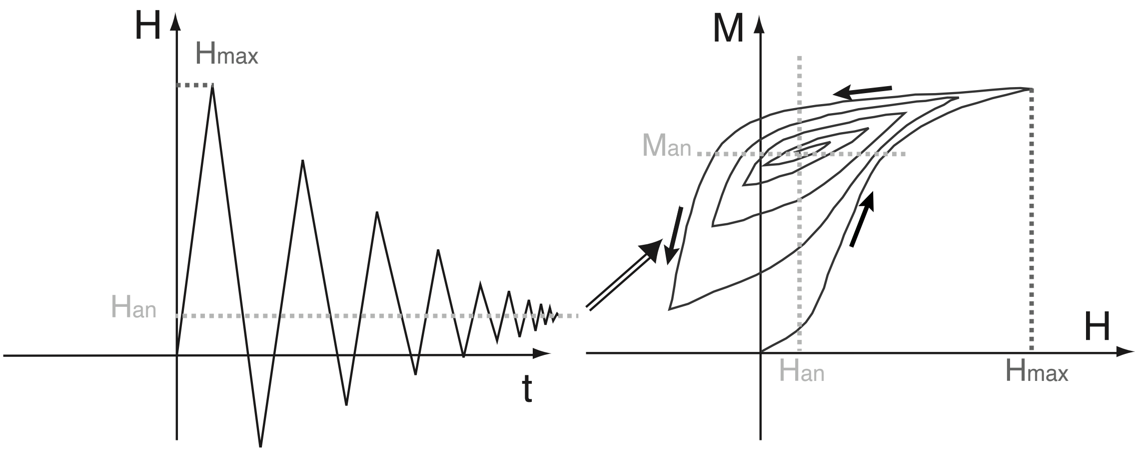


**Figure 4.6:** Illustration of anhysteretic measurement [Rekik, 2014].

### 4.2.2 Anhysteretic behavior

#### Grain Oriented FeSi

Grain Oriented (GO) FeSi, one of the most popular soft ferromagnetic materials, exhibits the so-called Goss texture ($\{110\} < 001 >$ along RD). This leads to a quasi-single-crystal behavior. The texture of a standard industrial GO 3% silicon–iron lamination (Hi-B from Nippon Steel) is shown in Fig.4.7 (left) and the corresponding pole figures are given in Fig.4.7 (right) [Buvat, 2000]. Associated with this texture, it is well known that GO FeSi exhibits a strong anisotropic magnetic and magnetostrictive behavior [Hubert et Daniel, 2008].

Experimental measurements of the magnetization and magnetostrictive strain along RD and TD are reported in Fig.4.8-4.9, illustrating the strong anisotropic behavior of this material. The magnetization reached at a magnetic field amplitude of $200A/m$ is about 40% higher along RD than along TD. Longitudinal and transversal strain measurements are shown in Fig.4.9. When a magnetic field is applied along RD, a very low magnetostriction magnitude is highlighted. When a magnetic field is applied along TD, the longitudinal magnetostriction strain reaches $18ppm$ in the direction of the magnetic field and about $-35ppm$ perpendicularly to the applied field. This anisotropy is explained by a much higher probability of the magnetic domains to be oriented along RD [Hubert et Daniel, 2008].

#### Non-oriented FeSi

Non-oriented (NO) FeSi is often used in the electrical devices, because of its low cost and relatively easy manufacturing process. Compared to GO FeSi, NO FeSi has a more complex texture characterized by a quasi isotropic distribution (isotropy is looked for). The texture of the NO FeSi obtained by Electron Backscatter Diffraction (EBSD) and the associated pole figures are shown in Fig.4.10. This leads to a macroscopic magnetic and magnetostrictive behavior that should be much more isotropic (compared to GO FeSi) [Petrovic, 2010]. It must be noticed that the texture may evolve from one manufacturer to another and from one thickness to another at a same composition. All experimental characterizations from micrographs to vibration measurement have been made using the same FeSi NO20 material from arcelormittal.

The measurements of magnetization and magnetostriction along RD, 45° and TD are reported in Fig.4.11 and Fig.4.12. NO FeSi possess the highest magnetic permeability along RD and the lowest one at 45° from RD. The difference between the highest and lowest permeability is less than 20%. The saturation is reached at a magnetic field of $300A/m$, with a difference between different directions lower than 20%. The magnetostriction is slightly anisotropic too: the longitudinal magnetostriction at saturation varies from $6ppm$ (TD) to $3.5ppm$ (45°).

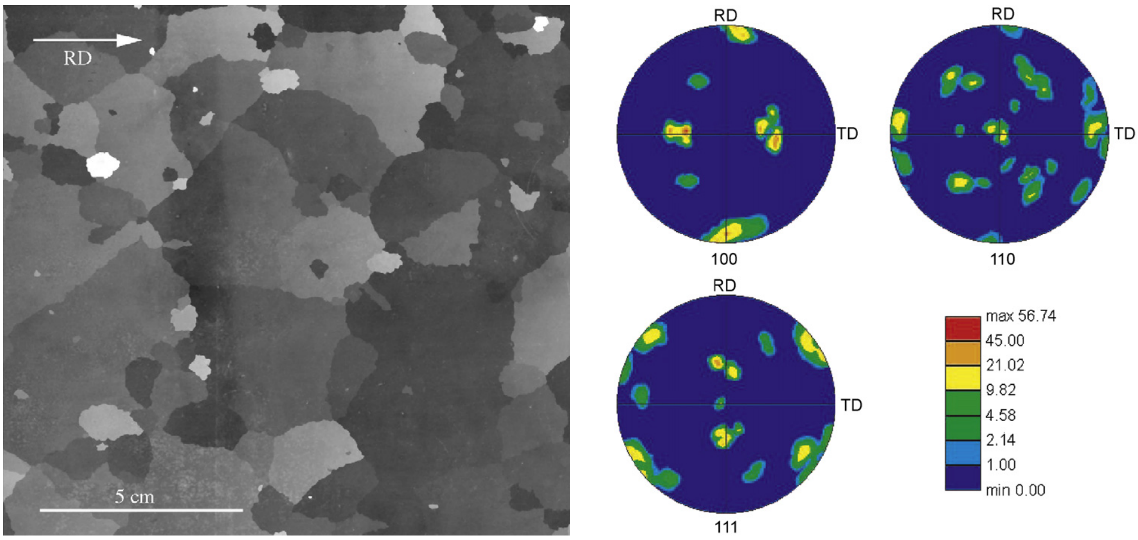


**Figure 4.7:** Macrograph picture of a standard industrial GO 3% silicon–iron lamination (Hi-B from Nippon Steel) (left); Pole figures of GO FeSi (right) [Buvat, 2000]

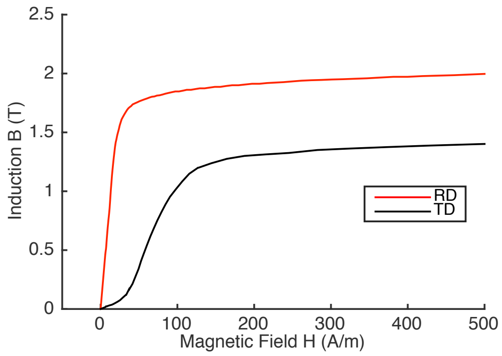


**Figure 4.8:** GO FeSi: Experimental measurement [Hubert et Daniel, 2008] - anhysteretic magnetization curves.

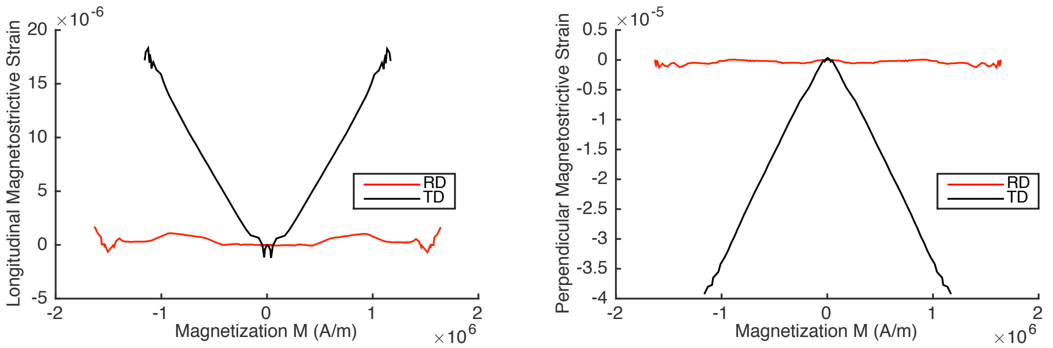


(a) longitudinal magnetostriction

(b) transversal magnetostriction

**Figure 4.9:** GO FeSi: Experimental measurement [Hubert et Daniel, 2008] - anhysteretic magnetostriction.

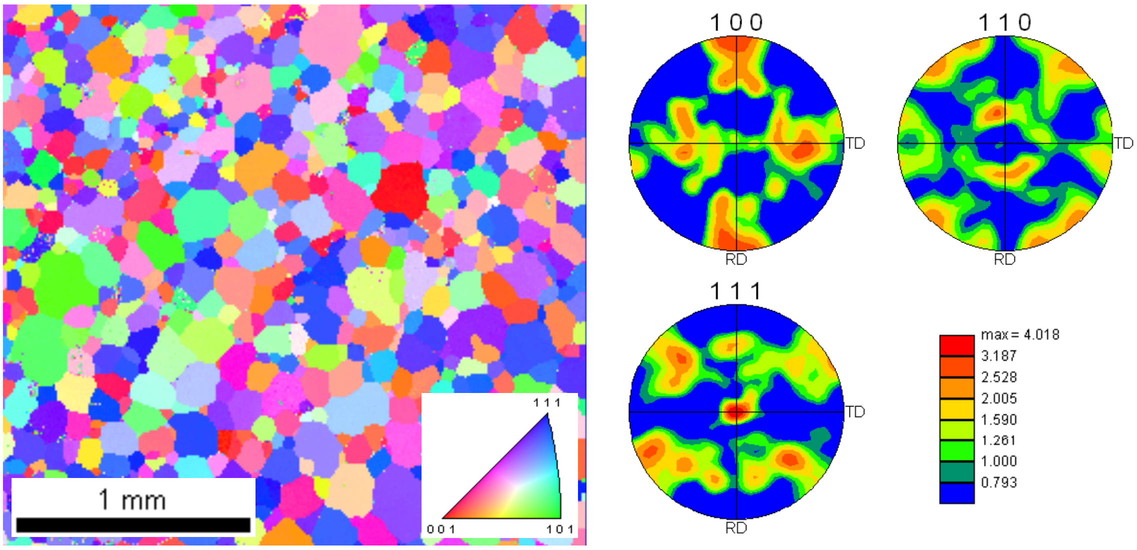


**Figure 4.10:** Texture of a NO FeSi lamination (left); Pole figures of NO FeSi (right)

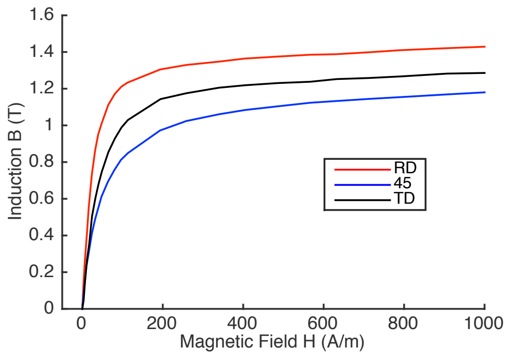


**Figure 4.11:** NO FeSi: Experimental measurement - anhysteretic magnetization curves.

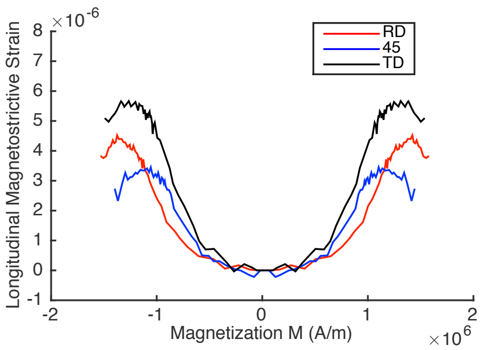


(a) longitudinal magnetostriction

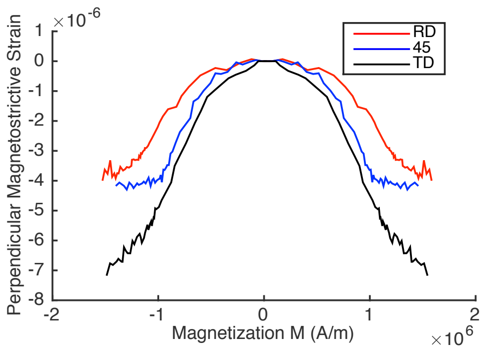


(b) transversal magnetostriction

**Figure 4.12:** NO FeSi: Experimental measurement - anhysteretic magnetostriction.

### FeNi Supra50

FeNi Supra50 is an iron-nickel alloy with a composition of 50% iron and 50% nickel. In terms of microstructure, FeNi Supra50 is a quasi-single-crystal exhibiting a cubic texture {001}<100> with axis <100> along RD and <010> along TD. This creates two easy axes in the sheet plane. The related poles figure is shown in Fig.4.13.

The measurements of magnetization and magnetostrictive strain are carried out along different directions, RD, TD, and 45°, reported in Fig.4.14-4.15. Along RD and TD, magnetic and magnetostrictive behavior are as expected: the magnetization reaches $1.2\times 10^6 A/m$ at $H = 500A/m$ and the magnetostriction strain remains very low with a maximum of $2ppm$ for $M = 1.5\times 10^6 A/m$. The magnetostriction begins nevertheless to increase for magnetization higher than $M = 1.5\times 10^6 A/m$ denoting the beginning of magnetization rotation mechanism. For the sample cut at 45° from RD, a small magnetostrictive strain is observed until the magnetization reaches $1.0\times 10^6 A/m$, and reaches $23ppm$ at saturation, much higher than the other two directions. The magnetostriction strain increases up to $23ppm$ at the magnetization saturation $(1.5\times 10^6 A/m)$. Indeed the magnetization rotation occurs at 45° from RD at a much smaller magnetic field level. The deformation appears finally strongly anisotropic for this material, in accordance with the cubic anisotropy observed by EBSD. The magnetostriction behaves opposite in the transverse direction compared to the longitudinal direction, highlighting the same anisotropy.

### FeCo Afk1

FeCo Afk1 is an iron-cobalt alloy composed of 74.5% iron, 25% cobalt, and 0.5% chromium. Cobalt helps to increase the magnetization saturation. Chromium is able to increase the electrical resistivity, resulting in lower eddy currents. FeCo Afk1 exhibits the highest magnetization at saturation of all ferromagnetic materials $(1.91\times 10^6 A/m)$. Because of its high magnetic saturation, FeCo Afk1 is ideal for high power density applications. However, the standard FeCo Afk1 exhibits at the same time very high magnetostriction, causing some vibration issue of the devices. Moreover, because of it's high price, this kind of alloy is usually used in small quantities.

An innovative fabrication process is developed and patented by Aperam S.A, using a special thermal treatment [Waeckerle *et al.*, 2017]. This forms a bi-domain structure preferentially oriented in the sheet plane, without changing the chemical composition nor the texture. The corresponding texture and the pole figures are given in Fig.4.16.

Some typical magnetic and magnetostrictive behavior of this material [Savary et Hubert, 2017, Savary *et al.*, 2018] is reported in Fig.4.17-4.18. Similar magnetic and magnetostrictive behavior are observed along RD, TD, and at 45° from RD. The magnetostriction remains smaller than $1ppm$ until the magnetization reaches $10^6 A/m$, that corresponds to a magnetic induction equals $1.5T$. For higher magnetization, the longitudinal magnetostriction increases dramatically until reaching $15ppm$. The difference of magnetostrictive strain between different directions is about $4ppm$ at the saturation. Although this

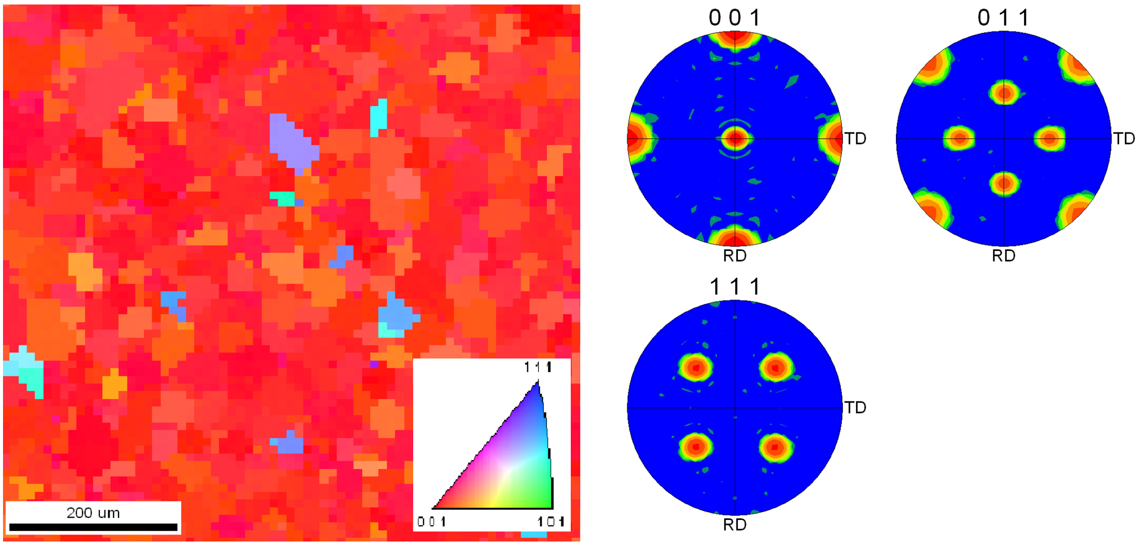


**Figure 4.13:** Texture of FeNi Supra50 (left); Pole figures of FeNi Supra50 (right) [Cetin, 2014]

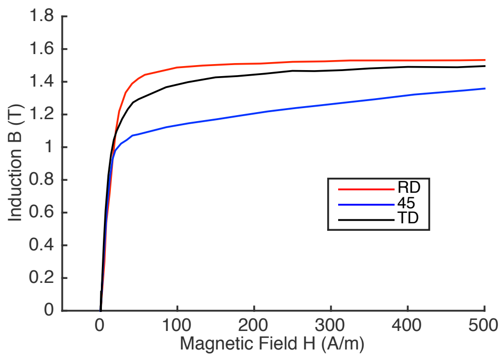


**Figure 4.14:** FeNi Supra50: Experimental measurement [Cetin, 2014] - anhysteretic magnetization curves.

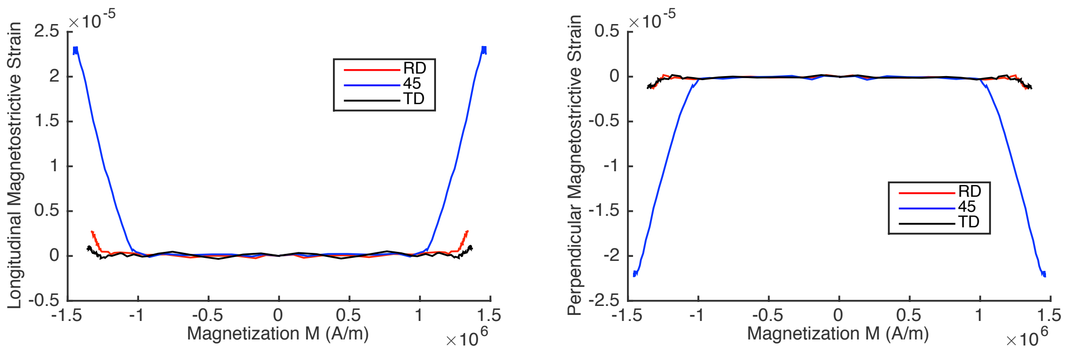


(a) longitudinal magnetostriction

(b) transversal magnetostriction

**Figure 4.15:** FeNi Supra50: Experimental measurement [Cetin, 2014] - anhysteretic magnetostriction.

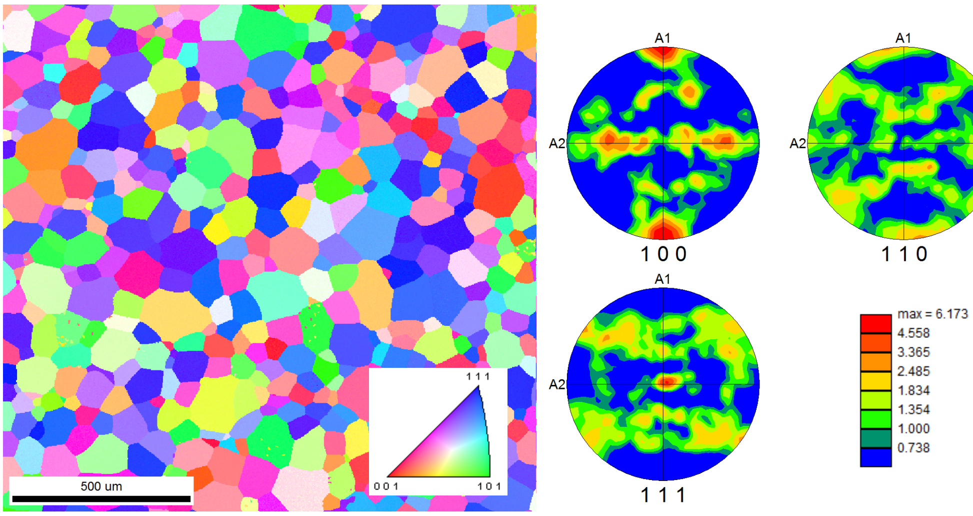


**Figure 4.16:** Texture of FeCo Afk1 (left); Pole figures of FeCo Afk1 (right) [Savary *et al.*, 2018]

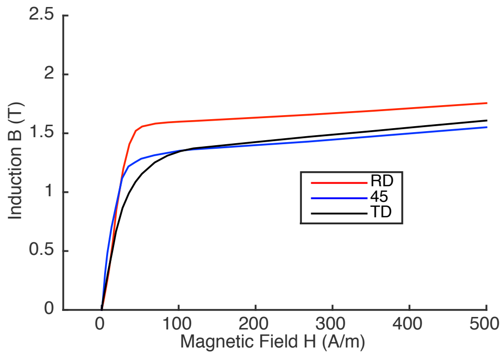


**Figure 4.17:** FeCo Afk1: Experimental measurement [Savary et Hubert, 2017] - anhysteretic magnetization curves.

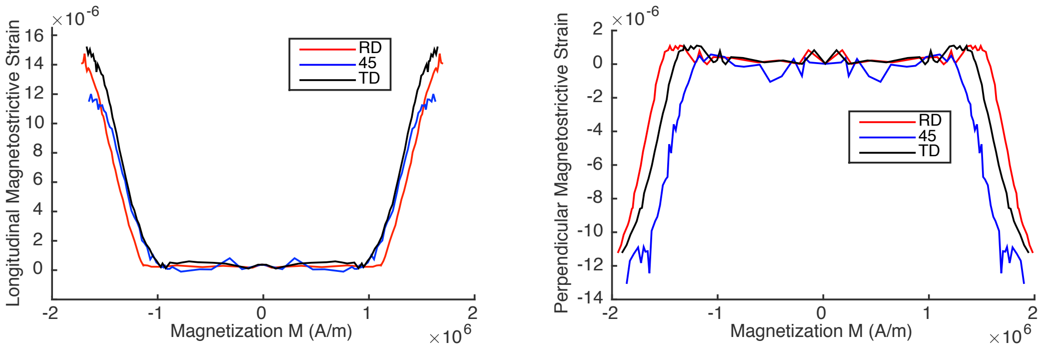


(a) longitudinal magnetostriction

(b) transversal magnetostriction

**Figure 4.18:** FeCo Afk1: Experimental measurement [Savary et Hubert, 2017] - anhysteretic magnetostriction.

material is still under development, it seems to be a good candidate for the low-noise power transformer, regardless of the price.

Pole figures reported in figure 4.16 show no preferential orientation in accordance with the apparent isotropic behavior of material. This crystallographic map is generally associated to non-oriented electrical steel which induces normally a quadratic shape of magnetostriction vs induction for this kind of material [Hubert *et al.*, 2005]. The forming process developed at APERAM-IMPHY allows to avoid this behavior despite the isotropic grain distribution.

### 4.2.3 Parameter identification

In this subsection, RD is supposed in the direction of X in the sample frame (SF) for simplification. The artificial anisotropic energy $W^{\alpha}_{an2}$ becomes eq.4.3, with the rotation matrix $\boldsymbol{P}$ shown in eq.4.4.

$$W^{\alpha}_{an2} = K_{11}\gamma_1^2 + K_{12}\gamma_2^2 + K_{13}\gamma_3^2 \tag{4.3}$$

$$\boldsymbol{P} = \begin{pmatrix} 1 & 0 & 0 \\ 0 & 1 & 0 \\ 0 & 0 & 1 \end{pmatrix} \tag{4.4}$$

In terms of constitutive behavior modeling via SMSM, the difference between the four different alloys mentioned above is the magneto-crystalline energy $W^{\alpha}_{an1}$ (eq.2.26). The expression of this magneto-crystalline energy varies from one material to another, depending on their texture and anisotropy.

#### Identification process of SMSM parameters

The identification of the SMSM parameters is the most challenging part of this work. It necessitates a good understanding of both the material and the SMSM. A general process of parameters identification is given as follows, however, this process may vary from one material to another.

- The saturation magnetization $M_s$ is first fixed according to the measurement. This value may not necessarily be the real saturation magnetization at an extremely high magnetic field. Depending on the range of applied magnetic field, $M_s$ can be adjusted to better fit the magnetization curve.
- $A_s$ is then fixed according to the initial magnetic permeability. A higher magnetic permeability needs a higher $A_s$. An optimization is nevertheless possible to account for the global magnetization and magnetostriction behavior.
- The magneto-crystalline energy $W^{\alpha}_{an1}$ is described based on the texture. According to the orientation of the crystalline, magneto-crystalline tensor is re-oriented using the rotation matrix $\boldsymbol{P}$. $K_1$ is a physical constant, which vary from material to material.

- Next, the artificial anisotropic energy $W^{\alpha}_{an2}$ may have to be proposed and adjusted in the way to privilege some higher or lower domain family densities in the certain directions. This time $K_{11}$, $K_{12}$ and $K_{13}$ control the energy in RD, TD and in the out of plane direction. The lower the energy is, the higher the magnetic domain density is, leading to a higher permeability in that direction compared to the others.

- Configuration energy $W_{conf}$ has similar effects as the artificial anisotropic energy. It gives an initial configuration of the non-random distribution of the magnetic domains. Add more anisotropic energy in a given direction is equivalent to apply a compression stress in that direction (for a 'positive' magnetostrictive material), leading to a lower magnetic susceptibility and a higher magnetostriction amplitude in that direction.

- $\lambda_{100}$ and $\lambda_{111}$ are physical constants which can be found in the literature. Materials close to single crystals (strong texture) may be described by $\lambda_{100}$ and $\lambda_{111}$ identified for the single crystal. However, a simplification is possible to describe the quasi-isotropic polycrystal, by artificially using $\lambda_{100} = \lambda_{111} = \lambda_s$ and adjust $\lambda_s$ to the measurement.

### Grain Oriented FeSi

As GO FeSi possess a Goss texture, an example of the magneto-crystalline energy is given in eq.4.5, considering RD oriented in the direction X in SF. The related transformation matrix $\boldsymbol{Q}$ in accordance with the Goss texture is defined in 4.6. From eq.2.31, free magnetostriction strain of the GO FeSi (RD in direction X of SF) is deduced, reported in eq.4.7.

$$W^{\alpha}_{an1} = K_1 \left( \gamma_1^2\gamma_2^2 + \gamma_1^2\gamma_3^2 + \frac{1}{4}(\gamma_2^4 + \gamma_3^4) - \frac{1}{2}\gamma_2^2\gamma_3^2 \right) \tag{4.5}$$

$$\boldsymbol{Q} = \begin{pmatrix} 1 & 0 & 0 \\ 0 & \sqrt{2}/2 & \sqrt{2}/2 \\ 0 & -\sqrt{2}/2 & \sqrt{2}/2 \end{pmatrix} \tag{4.6}$$

$$\epsilon^{\alpha}_{\mu} = \frac{3}{2} \begin{pmatrix} \lambda_{100}\left(\gamma_1^2 - \frac{1}{3}\right) & \sqrt{2}\lambda_{111}\left(\gamma_3 + \gamma_2\right)\gamma_1 & \sqrt{2}\lambda_{111}\left(\gamma_3 - \gamma_2\right)\gamma_1 \\ \sqrt{2}\lambda_{111}\left(\gamma_3 + \gamma_2\right)\gamma_1 & \lambda_{100}\left(\frac{1}{2}(\gamma_2^2 + \gamma_3^2)^2 - \frac{1}{3}\right) & \frac{1}{2}\lambda_{111}\left(\gamma_3 - \gamma_2\right)\left(\gamma_3 + \gamma_2\right) \\ \sqrt{2}\lambda_{111}\left(\gamma_3 - \gamma_2\right)\gamma_1 & \frac{1}{2}\lambda_{111}\left(\gamma_3 - \gamma_2\right)\left(\gamma_3 + \gamma_2\right) & \lambda_{100}\left(\frac{1}{2}(\gamma_2^2 - \gamma_3^2)^2 - \frac{1}{3}\right) \end{pmatrix} \tag{4.7}$$

Several physical constants from literature and two optimized parameters $A_s$ and $C$ used for the modeling are given in Table 4.3 (for the configuration energy associated with the demagnetizing surface effect). Optimization of $A_s$ and $C$ parameters is performed thanks to the minimization of a quadratic function, using differences between experimental and modeled magnetization and magnetostriction (least square method). The two magnetostrictive constants $\lambda_{100}$ and $\lambda_{111}$ are the real constants of the single crystal.

Comparisons between SMSM and experimental measurement are plotted in Fig.4.19-4.20. Very good agreements with experimental results are obtained allowing a great confidence to use this simplified model as the constitutive behavior in the numerical calculation of the transformer structure.

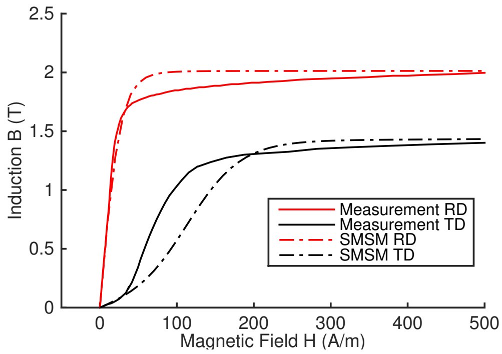


**Figure 4.19:** GO FeSi: Comparison between SMSM results (dots) and experimental measurement (lines) [Hubert et Daniel, 2008] - anhysteretic magnetization curves.

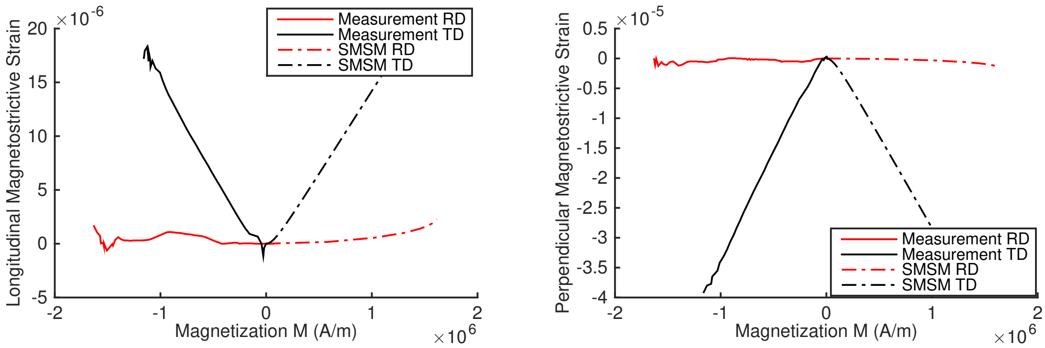


(a) longitudinal magnetostriction

(b) transversal magnetostriction

**Figure 4.20:** GO FeSi: Comparison between SMSM results (dots) and experimental measurement (lines) [Hubert et Daniel, 2008] - anhysteretic magnetostriction curves.

### Non-oriented FeSi

The modeling of this kind of material is more difficult, because of its complex texture. Both magneto-crystalline energy $W^{\alpha}_{an1}$, artificial anisotropic energy $W^{\alpha}_{an2}$ and configuration energy are engaged to describe correctly the macroscopic anisotropy.

As shown in Fig.4.21, the permeability along RD is slightly higher than along TD. This means that the initial distribution of magnetic domains is more concentrated along RD than along TD. In order to reproduce the initial distribution of the magnetic domains, a configuration energy is applied, using a tensile pre-stress of $8MPa$ along RD. As sheets are very thin, demagnetization energy forces magnetic domains to stay in the plane. This leads to a positive value of $K_{13}$, defined in artificial anisotropic energy $W^{\alpha}_{an2}$ (representative of the so-called demagnetizing surface effect [Hubert et Daniel, 2008]). Next step comes to the description of the behavior along the direction at 45° from RD. As shown in Fig.4.21, the permeability along the 45° direction is lower than that along TD. The anisotropic energy in this direction should be higher than in TD. We use here a cubic like formulation for the magneto-crystalline energy $W^{\alpha}_{an1}$ with negative $K_1$, rotated at 45° in the sheet plane (eq.4.8). Corresponding rotation matrix $\boldsymbol{Q}$ is given in eq.4.9. Free magnetostriction strain of the NO FeSi is given in eq.4.10, with $\lambda_{100} = \lambda_{111}$. All parameters used in SMSM for NO FeSi are summarized in Table 4.3.

$$W^{\alpha}_{an1} = K_1 \left( \gamma_1^2\gamma_3^2 + \gamma_2^2\gamma_3^2 + \frac{1}{4}(\gamma_1^4 + \gamma_2^4) - \frac{1}{2}\gamma_1^2\gamma_2^2 \right) \tag{4.8}$$

$$\boldsymbol{Q} = \begin{pmatrix} \sqrt{2}/2 & \sqrt{2}/2 & 0 \\ -\sqrt{2}/2 & \sqrt{2}/2 & 0 \\ 0 & 0 & 1 \end{pmatrix} \tag{4.9}$$

$$\epsilon^{\alpha}_{\mu} = \frac{3}{2} \begin{pmatrix} \lambda_{100}(\gamma_1^2 - \frac{1}{3}) & \lambda_{111}\gamma_1\gamma_2 & \lambda_{111}\gamma_1\gamma_3 \\ \lambda_{111}\gamma_1\gamma_2 & \lambda_{100}(\gamma_2^2 - \frac{1}{3}) & \lambda_{111}\gamma_2\gamma_3 \\ \lambda_{111}\gamma_1\gamma_3 & \lambda_{111}\gamma_2\gamma_3 & \lambda_{100}(\gamma_3^2 - \frac{1}{3}) \end{pmatrix} \tag{4.10}$$

Comparisons between SMSM and measurement of magnetic and magnetostrictive behaviors are shown in Fig.4.21-4.21. A general good agreement is observed and anisotropies are well reproduced. However, the magnetostrictive strain at saturation is not accurate. The rotation of the magnetostriction at saturation is not represented by SMSM. Indeed the SMSM is a simplified version of MSM, where only an equivalent single crystal is considered. The decrease of magnetostriction at high field is due to a combination of magnetization rotation and anisotropic magnetostrictive constants. Reproducing this effect with a SMSM would require to identify two equivalent magnetostrictive constants instead of one.

### FeNi Supra50

Modeling of the magnetic and magnetostrictive behavior of FeNi Supra50 is relatively easy, because of its regular texture. It is a quasi-single-crystal with axis <100> along RD and <010> along TD. Obviously a first order cubic anisotropy is used for the magneto-crystalline energy and the magnetostriction tensor. The corresponding magneto-crystalline energy and related rotation matrix are given in eq.4.11 and eq.4.12. The magnetostrictive strain is given by eq.4.13.

$$W^{\alpha}_{an1} = K_1 \left( \gamma_1^2\gamma_2^2 + \gamma_1^2\gamma_3^2 + \gamma_2^2\gamma_3^2 \right) \tag{4.11}$$

$$\boldsymbol{Q} = \begin{pmatrix} 1 & 0 & 0 \\ 0 & 1 & 0 \\ 0 & 0 & 1 \end{pmatrix} \tag{4.12}$$

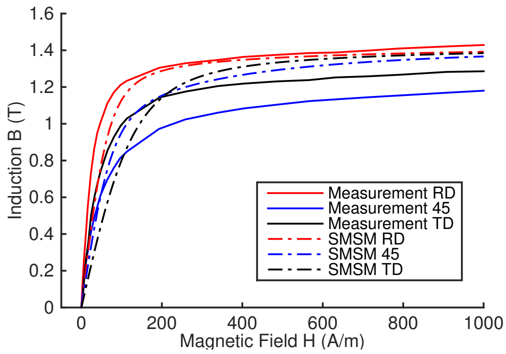


**Figure 4.21:** Non-oriented FeSi: Comparison between SMSM results (dots) and experimental measurement (lines) - anhysteretic magnetization curves.

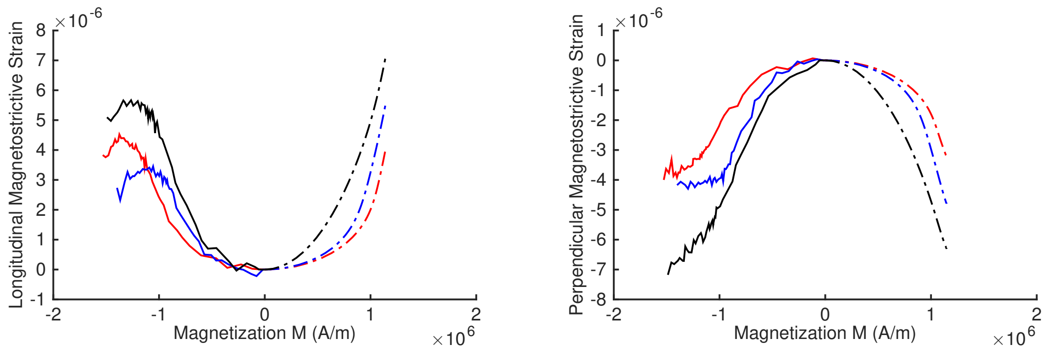


(a) longitudinal magnetostriction (b) transversal magnetostriction

**Figure 4.22:** Non-oriented FeSi: Comparison between SMSM results (dots) and experimental measurement (lines) - anhysteretic magnetostriction curves.

$$\epsilon_\mu^\alpha = \frac{3}{2}\begin{pmatrix} \lambda_{100}(\gamma_1^2-\frac{1}{3}) & \lambda_{111}\gamma_1\gamma_2 & \lambda_{111}\gamma_1\gamma_3 \\ \lambda_{111}\gamma_1\gamma_2 & \lambda_{100}(\gamma_2^2-\frac{1}{3}) & \lambda_{111}\gamma_2\gamma_3 \\ \lambda_{111}\gamma_1\gamma_3 & \lambda_{111}\gamma_2\gamma_3 & \lambda_{100}(\gamma_3^2-\frac{1}{3}) \end{pmatrix} \tag{4.13}$$

This classic strategy is not enough to correctly describe the behavior of FeNi Supra50. As the SMSM is based on a cubic texture, the magnetostriction strain along RD and TD are quadratic curves. In order to reproduce the ultra-low magnetostriction along RD and TD, a hypothesis is made: the origin of the low magnetostriction comes from the orientation of the domains dictated by the demagnetization effect. This structure-related effect influences the local magnetic and magnetostrictive behavior. A configuration energy as a function of the structure is added to the total internal energy, where the domains are oriented by the structure along the boundary. In the case of a power transformer where the direction of the magnetic field is generally along the boundary of the sheets, this structure-dependent configuration energy can be simply described as a function of the direction of the magnetic field. This structure configuration energy (defined in eq.4.14) is recalled here:

$$W_{struc}^\alpha = -C\,|\vec{\gamma}^\alpha \cdot \vec{h}| \tag{4.14}$$

The comparison between SMSM and experimental measurement of magnetic and magnetostrictive behaviors are shown in Fig.4.23-4.24. A good agreement is observed as expected. With the help of the structure energy, the SMSM reproduces correctly the ultra-low magnetostriction along RD and TD. At 45° from RD, the magnetostrictive strain remains less than $1ppm$ and increases up to $23ppm$ at saturation. In terms of finite element implementation, some numerical difficulties are observed: anisotropy is partially given by the direction of applied field. The numerical convergence is strongly braked to avoid numerical instabilities.

### FeCo Afk1

As explained in the paragraphs dedicated to the presentation of materials behavior, the low magnetostriction magnitude of FeCo AFK1 over a wide induction range seems to indicate that the magnetization mainly proceeds with 180° domains wall displacement. The magnetization rotation at higher induction (in accordance with the high magnetocrystalline constant $K_1$ for this material) would lead to a strong second step (and more classical) increasing of magnetostriction. On the other hand, due to a high demagnetizing surface effect, the bi-domains direction is oriented along the $< 100 >$ axis the closest to the sheet plane. As shown by Savary [Savary *et al.*, 2018], a multiscale approach close to the MSM is able to reproduce the complex magnetomechanical behavior of this material (see Fig.4.25). It is possible to propose a simplified approach by considering the material as a 2D uniaxial anisotropic material (simulating the in-plane bi-domain structure) disoriented from an initial angle $\psi$ from the direction of the applied field $\vec{h}$.

Uniaxial anisotropy energy field along axis-X in SF is usually given by:

$$W_{an2}^\alpha = K_{11}\gamma_1^2$$

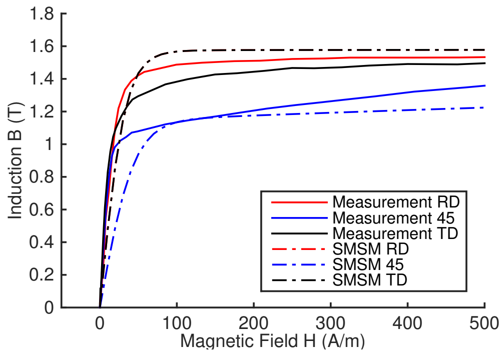


**Figure 4.23:** FeNi Supra50: Comparison of SMSM results (dots) to experimental measurement (lines) - anhysteretic magnetization curve.

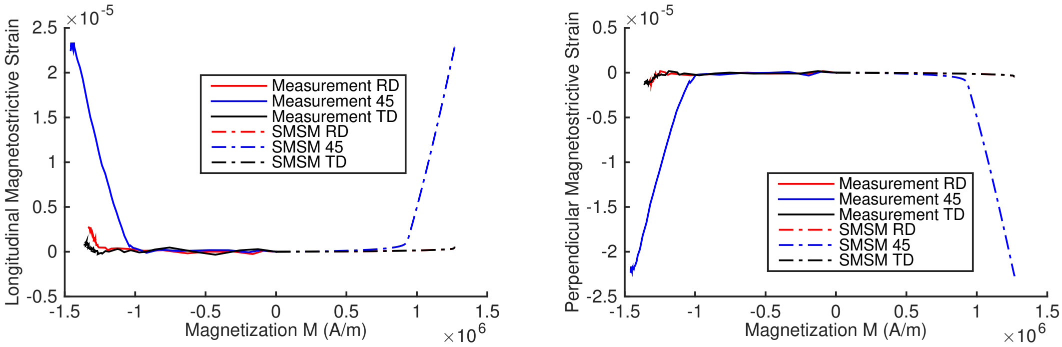


(a) longitudinal magnetostriction

(b) transversal magnetostriction

**Figure 4.24:** FeNi Supra50: Comparison of SMSM results (dots) to experimental measurement (lines) - anhysteretic magnetostriction.

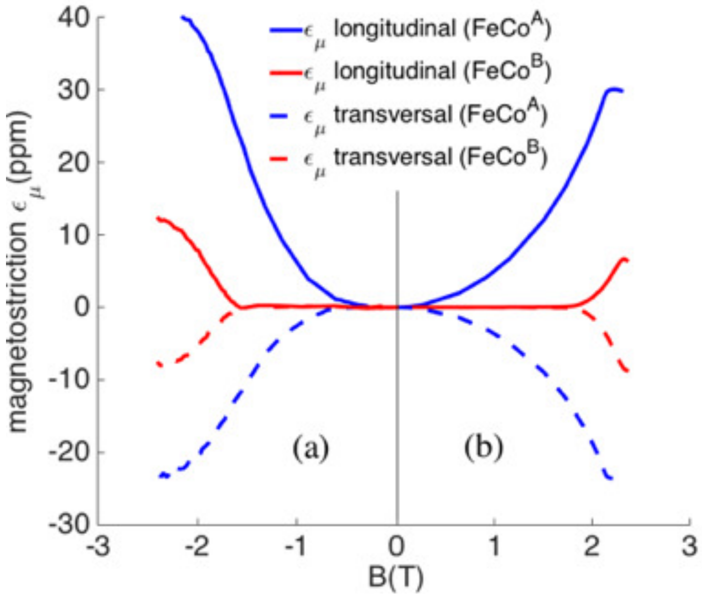


**Figure 4.25:** Magnetostrictive curve of $FeCo^A$AFK1 and $FeCo^B$AFK1 (a) experimental data (b) numerical results [Savary *et al.*, 2018]. $FeCo^A$AFK1 and $FeCo^B$AFK1 have been annealed at different temperatures allowing to enhance or remove the bi-domains structure. $FeCo^B$AFK1 corresponds to the material considered in the work.

When this is oriented along the direction of the applied field, this expression in a 2D plane ($\gamma_3 = 0$) becomes:

$$W^{\alpha}_{an2} = K_{11}\left(\gamma_1^2 h_1^2 + \gamma_2^2 h_2^2 + 2\gamma_1\gamma_2 h_1 h_2\right)$$

where $h_1$ and $h_2$ are the direction cosine of the applied field direction in the SF. When a disorientation angle $\psi$ from the applied field direction $\vec{h}$ is considered, the anisotropy energy becomes:

$$W^{\alpha}_{an2} = K_{11}\left(\gamma_1^2 (h_1^{\psi})^2 + \gamma_2^2 (h_2^{\psi})^2 + 2\gamma_1\gamma_2 h_1^{\psi} h_2^{\psi}\right)$$

where $h_1^{\psi}$ and $h_2^{\psi}$ are the direction cosine of the applied field direction disoriented an angle of $\psi$ in the 2D plane in the SF. They are expressed as follows:

$$h_1^{\psi} = h_1 cos(\psi) + h_2 sin(\psi)$$

$$h_2^{\psi} = h_1 cos(\psi) - h_2 sin(\psi)$$

Using a high value for $K_{11}$ the SMSM separates practically the equivalent single-crystal into two main opposite domain families. The rotation matrix $\mathbf{Q}$ and the magnetostriction tensor of the single crystal are for the same reason given by:

$$\mathbf{Q} = \begin{pmatrix} cos(h+\psi) & sin(h+\psi) & 0 \\ -sin(h+\psi) & cos(h+\psi) & 0 \\ 0 & 0 & 1 \end{pmatrix}$$

where $h$ is the angle of the applied field in the SF.

$$\epsilon_{\mu}^{\alpha} = \frac{3}{2}\begin{pmatrix} \lambda_{100}(\gamma_1^2 - \frac{1}{3}) & \lambda_{111}\gamma_1\gamma_2 & \lambda_{111}\gamma_1\gamma_3 \\ \lambda_{111}\gamma_1\gamma_2 & \lambda_{100}(\gamma_2^2 - \frac{1}{3}) & \lambda_{111}\gamma_2\gamma_3 \\ \lambda_{111}\gamma_1\gamma_3 & \lambda_{111}\gamma_2\gamma_3 & \lambda_{100}(\gamma_3^2 - \frac{1}{3}) \end{pmatrix} \tag{4.15}$$

The constants used for the modeling are the physical constants of the material except for $\lambda_{100}$, $\lambda_{111}$ and $\psi$ angle that must be accurately optimized ($\lambda_{100} = \lambda_{111} = \lambda_s$). It is fixed at $\psi = 30°$ that allows acceptable accordance between experiments and modeling to be obtained as illustrated in Fig.4.26-4.27. In the finite element implementation, we meet here a harder numerical difficulty than for FeNi material: anisotropy is fully (partially in case of FeNi) given by the direction of the applied field and not by a global reference vector. The problem of numerical instabilities is not totally solved at this moment.

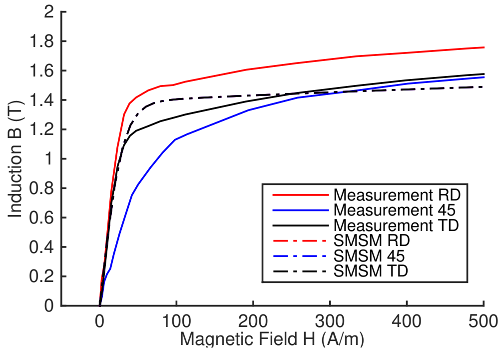


**Figure 4.26:** FeCo Afk1: Comparison of SMSM results (dots) to experimental measurement (lines) - anhysteretic magnetization curve.

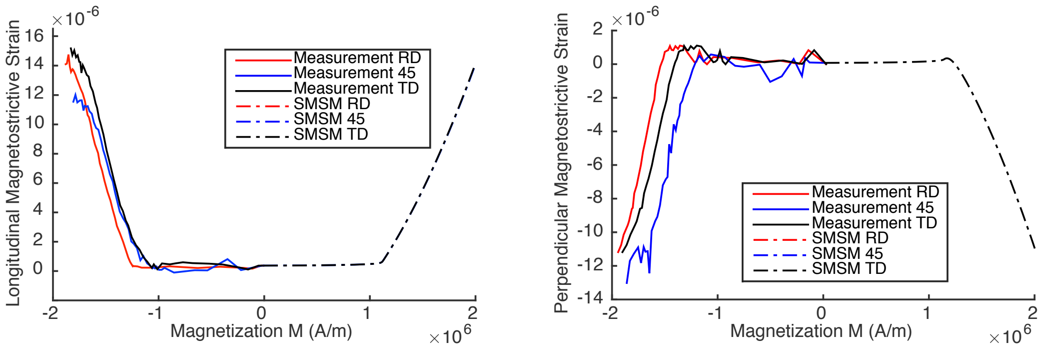


(a) longitudinal magnetostriction (b) transversal magnetostriction

**Figure 4.27:** FeCo Afk1: Comparison of SMSM results (dots) to experimental measurement (lines) - anhysteretic magnetostriction.

**Summary**

SMSM generally achieves to represent the magnetic and magnetostrictive behavior of the studied materials with good agreement. For materials such as GO FeSi, FeNi Supra50 and FeCo Afk1, the excellent prediction of SMSM should be highlighted. For more materials such as NO FeSi, SMSM gives an acceptable prediction at low fields but usually fails at high field when the magnetization rotation occurs. Consequently, structure modeling at low field may lead to more accurate results than when local saturation is reached. This is due to the simplification made in SMSM, which does not take into consideration the magnetic domain rotation. Parameters used in SMSM for all studied materials are summarized in Table 4.3.

**Table 4.3:** Physical constants used for SMSM.

| Param. | GO FeSi | NO FeSi | FeNi Supra50 | FeCo Afk1 | Unit |
|---|---|---|---|---|---|
| $M_s$ | $1.61\times10^6$ | $1.15\times10^6$ | $1.27\times10^6$ | $2.3\times10^6$ | $A/m$ |
| $K_1$ | 38 | 0.2 | 3.4 | 0 | kJ.m$^{-3}$ |
| $K_{11}$ | 0 | 0 | 0 | 20 | kJ.m$^{-3}$ |
| $K_{12}$ | 0 | 0 | 0 | 0 | kJ.m$^{-3}$ |
| $K_{13}$ | 0.3 | 0.4 | 0.2 | 0.3 | kJ.m$^{-3}$ |
| $\lambda_{100};\lambda_{111}$ | 23.5 ; -4.5 | 7 ; 7 | 10 ; 32 | 16 ; 16 | ppm |
| $\Sigma^c_{xx}$ | 0 | 8 | 0 | 0 | MPa |
| $C$ | 0 | 0 | 200 | 0 | J.m$^{-3}$ |
| $A_s$ | $20\times10^{-3}$ | $15\times10^{-3}$ | $20\times10^{-3}$ | $25\times10^{-3}$ | $m^3/J$ |

### 4.2.4 Behavior under stress

The magnetic and magnetostrictive behavior depends on the mechanical stress applied to the material. In this subsection, numerical simulations are carried out under various mechanical loadings (tension and compression) for all materials using SMSM. Simulated magnetization and longitudinal magnetostriction curves in certain directions are chosen to illustrate the capability and potential of the SMSM, for the prediction of the behavior under stress, shown in Fig.4.28-4.31. The application of an external stress modifies the internal energy of the material, leading to a redistribution of the magnetic domain. When a tensile stress is applied along certain directions, the internal energy decreases. This allows a larger portion of magnetic domains to be oriented in this direction, which increases the magnetic permeability and decreases the magnetostriction. When a compression stress is applied, the SMSM behaves in the opposite way.

By the use of the setup and method presented in section 4.2.1, experimental measurements have been carried out in LMT-Cachan by other researchers on the following materials: GO FeSi [Rizzo *et al.*, 2010], NO FeSi [Li, 2017], FeNi Supra50 [Cetin, 2014, Li, 2017], and FeCo Afk1 [Li, 2017]. Qualitative agreements between the experimental measurements and the SMSM simulation are achieved. Model adjustments are still under work for the purposes of quantitative comparison.

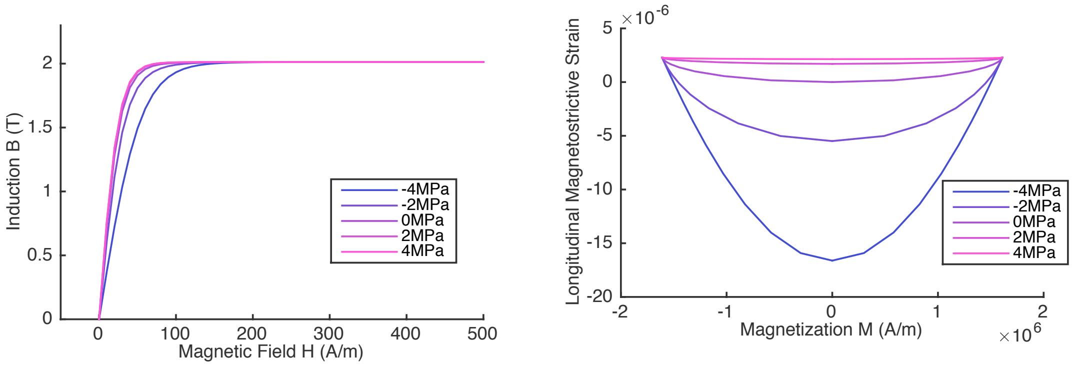


**Figure 4.28:** Simulated magnetic (a) and magnetostrictive (b) behaviors under stress of GO FeSi along RD.

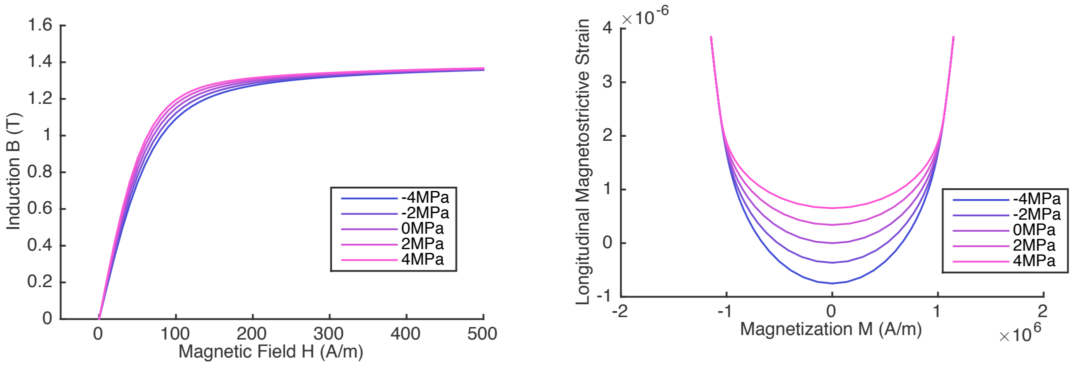


**Figure 4.29:** Simulated magnetic (a) and magnetostrictive (b) behaviors under stress of NO FeSi along RD.

## 4.3 Static structural behavior

Static measurement of a transformer core is carried out to study the anhysteretic material behavior combined with the structure effect. Although power transformers never work under this condition, it is important to measure the local strain of transformer core to validate both material model and the structural computation.

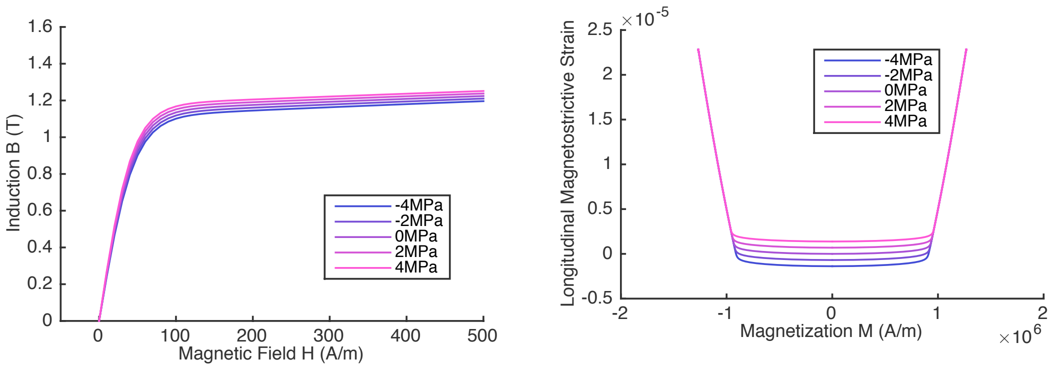


**Figure 4.30:** Simulated magnetic (a) and magnetostrictive (b) behaviors under stress of FeNi Supra50 along 45° from RD.

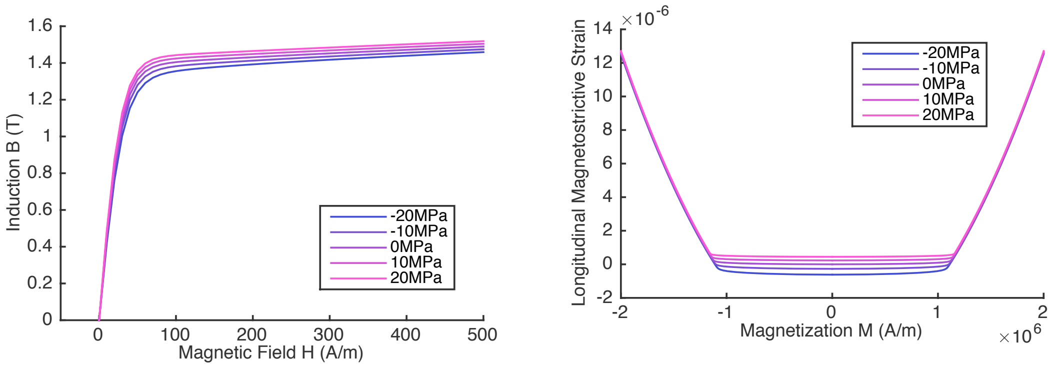


**Figure 4.31:** Simulated magnetic (a) and magnetostrictive (b) behaviors under stress of FeCo Afk1 along RD.

### 4.3.1 Experimental protocol

The central coil is fed with excitation current, creating the magnetic field inside the core. Strain gauges are stuck on several measuring points for local strain measurements. A typical anhysteretic procedure is then applied. The experimental set up shares the same control unit, power supply, and measurement equipment as the one used for magnetic and magnetostrictive constitutive behavior characterization.

Fig.4.32 shows the selected points for the local strain measurements. The example is an '8-shaped' non-cut three-layer core, with RD in the direction Y. Points P1, P2, and P3 are chosen where the magnetic field lies along RD, TD, and at 45° from RD. The red (black) flash indicates the longitudinal (transversal) direction of the strain gauge. Strain gauges are stuck on the two sides of the three-layer core, in order to obtain an average local strain.

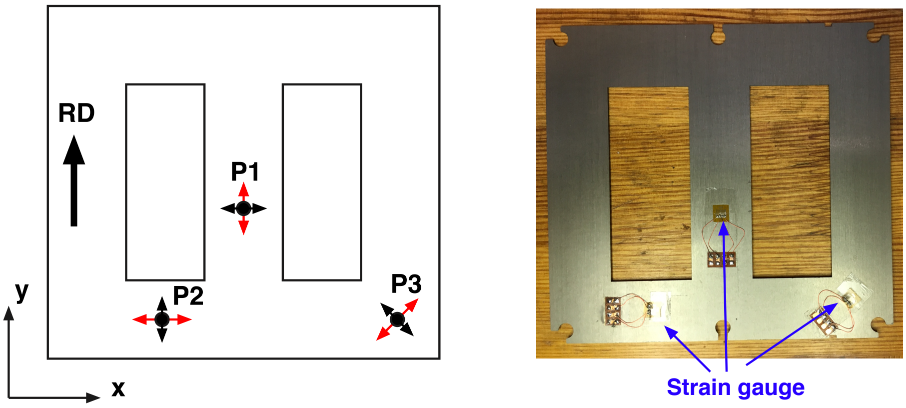


**Figure 4.32:** Selected points for local strain measurements.

### 4.3.2 Measurement/simulation comparison

Measurement of anhysteretic behavior is carried out on three-layer cores. These three-layer cores are made of NO FeSi, FeNi Supra50, and FeCo Afk1. A precise description of the three-layer core is given in Section 4.1. Numerical simulations are carried out under the same condition as the experimental ones. Comparisons are then possible between the experimental measurements and the numerical simulations.

#### Non-oriented FeSi

A three-layer NO FeSi core with configuration '8-y' is used for the measurements. The local magnetostriction strain obtained on this core during the anhysteretic procedure is shown in Fig.4.33(a). The longitudinal (transversal) strain at the three measured points is positive (negative). According to the material behavior measured on the strips, the magnetostrictive strain along RD is smaller that the strain along TD. However, the magnetostrictive strain at point P1 (magnetic field along RD) is greater than the strain at P2 (magnetic field along TD) and P3 (magnetic field applied at 45° from RD). This can be explained by the fact that the excitation coil is positioned around the central limb, so that the magnetic field amplitude at P2 and P3 is always half of the magnetic field amplitude at P1. It must also be noticed that the so-called 'rotation' of the magnetostriction is found at P1, where magnetostriction increases at low excitation current and decreases at high excitation current.

Numerical simulation is carried out under the same condition. Longitudinal and transversal magnetostrictive strain is plotted as a function of the excitation current is shown in Fig.4.33(b), using the same scale as the measurement. Similar to the measurement, the simulated magnetostriction increases rapidly as the excitation current increases till 50 Ampere-turns(At). The magnetostriction then becomes stable when the central limb reaches the saturation. As the SMSM is not able to reproduce the 'rotation' of the magnetostriction strain, the simulated magnetostriction on the transformer core does not decrease at the saturation. The amplitudes of the magnetostriction at P1 and P2 show good agreement between the measurement and the simulation. However, unlike the measurement, the simulated magnetostriction at P3 remains nearly zero. This is probably due to the difference between the measurement of a 3D (even thin) structure and a 2D plane stress simulation. In the 2D structural simulation, the positive longitudinal magnetostrictive strain is compensated by the induced stress at P3. While in the measurement, the three-layer core has some out-of-plane flexibility and a out-plane stress state can be created between sheets.

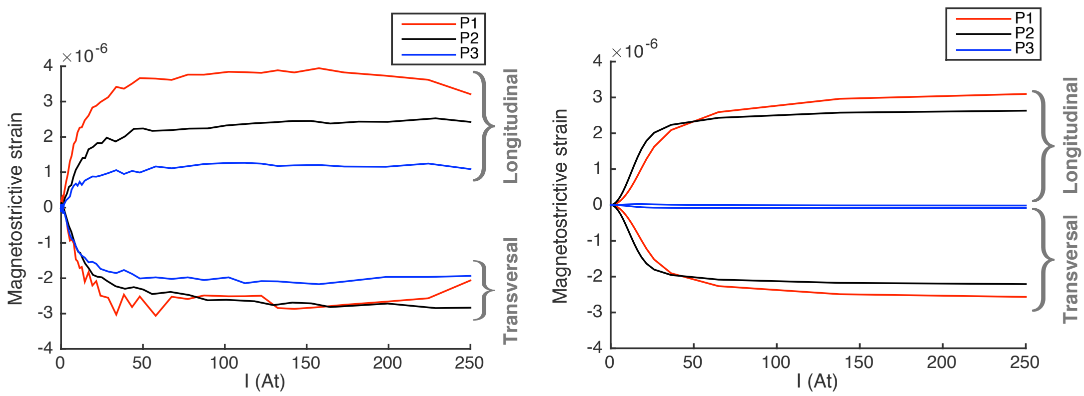


(a) measurement (b) simulation

**Figure 4.33:** NO FeSi three-layer core: comparison measurement/simulation of the local magnetostriction during anhysteretic procedure.

### FeNi Supra50

A three-layer FeNi Supra50 core with configuration '8-y' is used for the measurements. The local magnetostriction strain obtained on this core during the anhysteretic procedure is shown in Fig.4.34(a). The amplitude of magnetostriction measured at the three points is less than $\pm 1 ppm$, in accordance with the magnetostriction measured on the strips. Although the magnetostriction rises rapidly near saturation when the magnetic field is applied at 45° from RD, the magnetic field at P3 (magnetic field at 45° from RD) is half the magnetic field amplitude at P1, so that the magnetization at P3 never reaches its saturation and the magnetostriction always remains small.

Numerical simulation is carried out under the same condition. Magnetostrictive strain as a function of the excitation current is shown in Fig.4.34(b), using a different scale. The simulation gives the same order of the magnetostriction amplitude than the experiment (i.e. P1>P2>P3). However, the amplitude of the magnetostriction in the simulation is less than $\pm 0.5 ppm$. The difference between the experimental measurement and the numerical simulation can be explained in two points. On one hand, the magnetostriction strain on FeNi core is very small, which almost reach the limit of the strain gauge resolution and introduce strong measurement errors. On the other hand, some additional shape effects of FeNi might be presented in this complex core structure (e.g. does the domain structure in the corner remain parallel to the applied field?).

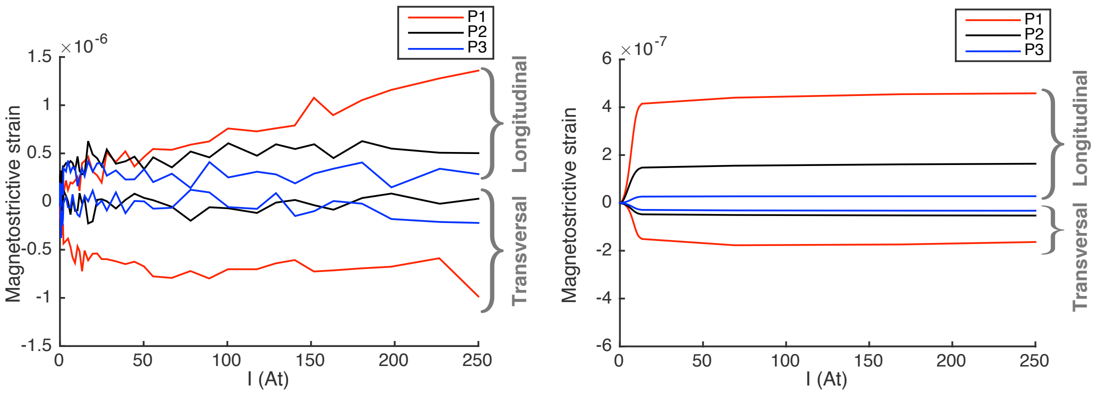


(a) measurement (b) simulation

**Figure 4.34:** FeNi Supra50 three-layer core: comparison measurement/simulation of the local magnetostriction during anhysteretic procedure.

### FeCo Afk1

A three-layer FeCo$^B$Afk1 core with configuration 'EI-y' is used for the measurements. The local magnetostriction strain obtained by the anhysteretic procedure shown in Fig.4.35(a). The magnetostriction at P2 and P3 is less than $\pm 2 ppm$. At P1, the magnetostriction strain rises linearly as the excitation current increases. It reaches $\pm 15ppm$ at a 250 Amper-turns(At) excitation current. Unlike the behavior measured on the strips where magnetostriction remains very small till the magnetization reaches $10^6$ A/m, the structural magnetostrictive behavior is more close to the FeCo$^A$Afk1. Some investigations show that the heat treatment of E and I sheets may be the origin of the discrepancies. Indeed, E and I sheets have been annealed at the appropriate temperature (see §4.2.3 to appreciate this point) but stacked together (hundred of sheets), while strips had been annealed one by one. The stacking is well known to reduce the demagnetizing surface effect. The consequence is a strong decrease of the in-plane bi-domain selection and so an increase of magnetostriction strain amplitude.

Numerical simulation has been carried out using a SMSM identified by FeCo$^A$Afk1, with the modification of parameter $\lambda_{100} = \lambda_{111} = 40$ppm, $K_{11} = K_{13} = 0$ and $M_s = 1.6 \times 10^6 A/m$. Magnetostrictive strain as a function of the excitation current is shown in Fig.4.35(b). The simulation gives the same order of the magnetostriction amplitude than the experiment (i.e. P1>P2>P3). Although the simulation tends to overestimate the magnetostriction in P2, general good agreements are observed between the experimental measurements and numerical simulation. This verifies the assumptions that the structural magnetostriction of the core is similar to the magnetostrictive behavior of FeCo$^A$Afk1.

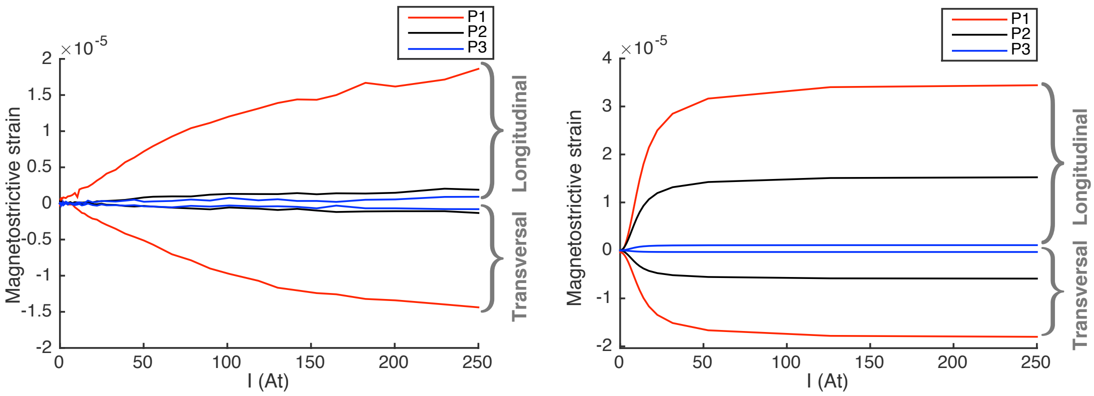


(a) measurement

(b) simulation

**Figure 4.35:** FeCo Afk1 three-layer core: comparison measurement/simulation of the local magnetostriction during anhysteretic procedure.

## 4.4 Conclusion

Four different iron-based electrical sheets are introduced in this chapter. Detailed explanations are given from microscopic energy descriptions to the macroscopic behaviors. This is followed by the parameter identification of SMSM, allowing the SMSM adapted to each material under study to be defined. Good agreements of the magnetic and magnetostrictive behavior between the measurements and the modeling are highlighted. The ability of SMSM to model the magnetostrictive behavior under stress has also been illustrated, while quantitative identifications are still missing at this stage. Static measurements of a transformer core have also been carried out to study the anhysteretic material behavior combined with the structure effect. Comparisons between the measurements and simulations show good agreements, allowing the validation of both simulation chain and SMSM.

# Chapter 5

# Comparison Modeling/Experiment in Dynamic Situation

## Contents

# 5.1 Dynamic structural behavior

## 5.1.1 Experimental protocol

### Measurement set up

The vibration measuring bench is built up, consisting of a power supply with current/-voltage command, three mono-phase accelerometers, a sonometer, a current probe, a data acquisition card, and a PC equipped with LMS Test.lab (Fig.5.1). The PC controls the power supply to generate sinusoidal current/voltage with various amplitude at $400Hz$. The current/voltage is then measured forming a feedback loop for accurate control. The current/voltage acts as excitation of the three-layer core prototype, creating vibration and noise. The three-layer transformer prototype is hung up with two ropes to remove high-frequency perturbations and fill the force-free boundary condition. Several accelerometers are then positioned to record the acceleration over hundred of excitation periods. Both the secondary coil and the accelerometers are connected to the acquisition card.

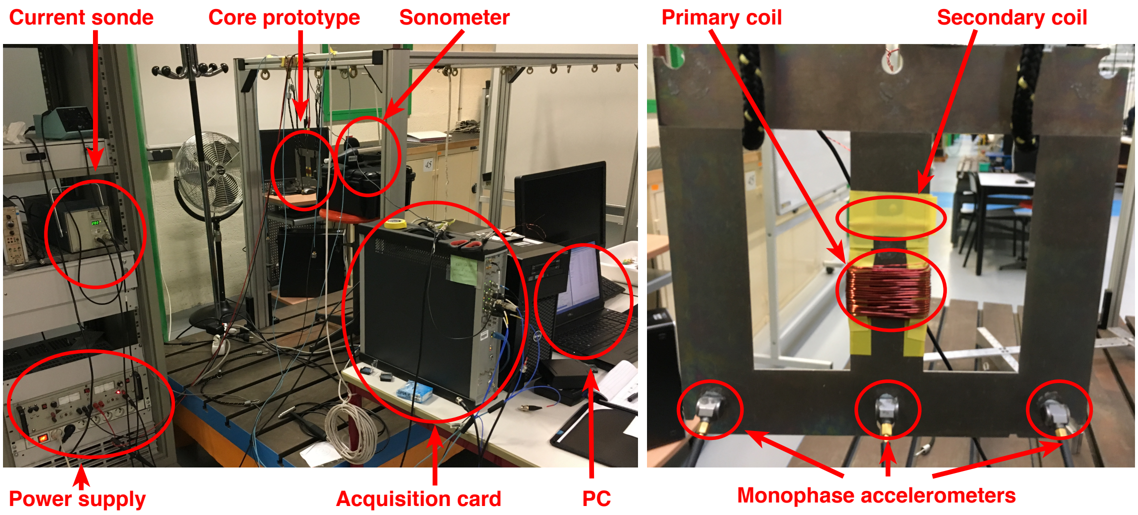


**Figure 5.1:** Experimental set up for prototype testing.

### Local vibration measurement

Vibration can be measured in terms of displacement, velocity, and acceleration. The measurement of velocity can be made using a laser doppler vibrometer, which is the most accurate, wide-frequency-range, and non-intrusive method. This technique, however, is very expensive and takes a lot effort for the mounting and adjustment. In this thesis, we choose piezoelectric accelerometers (Bruel & Kjaer - type 4519) to measure the local acceleration of the core prototype. These single channel, low weight (1.5g) piezoelectric accelerometers have a frequency range up to $20kHz$. As an adhesive mounting is used, the positioning and manipulation of the accelerometers are easy.

As shown in Fig.5.2, the central point of the transformer is set as a reference point to correct rigid body displacements. An average operation has been made among some measuring points (points 3-5 and 4-6) thanks to the $Y$-axis symmetry to remove the rigid body in-plane rotation. Typically, at points 3 and 5 (the same for points 4 and 6), the common mode of displacements in direction Y and differential mode of displacements in direction X are drawn from this operation. Low-frequency perturbations (associated to rigid body movements) have been removed by signal post-processing using a low-pass filtering. Once the acceleration of the chosen points are measured, corrected, and filtered, associated velocity and displacement are obtained by integration. The instant velocity $v(t)$ and displacement $d(t)$ are given by eq.5.1-5.2.

$$v(t) = \int a(t)\mathrm{d}t + c_1 \tag{5.1}$$

$$d(t) = \iint a(t)\mathrm{d}t + c_1 t + c_2 \tag{5.2}$$

where $c_1$ and $c_2$ are two unknown constants. $c_1$ can be set to make the average velocity null. However, it is difficult to compute or measure the constant $c_2$. In this measurement, we suppose that the displacement of all area on the three-layer core is zero when the excitation current is set at zero. This is not true because the displacement is known for a constant, only variations are really significant. Constant $c_2$ can be adjusted a posteriori after a comparison to experimental data.

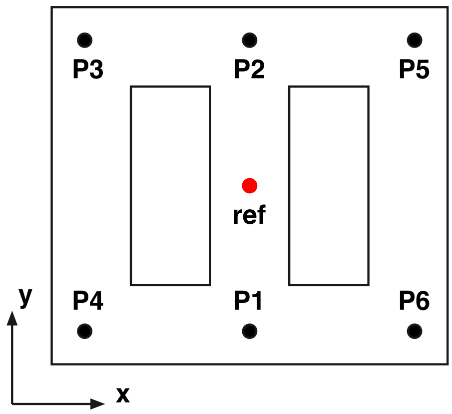


**Figure 5.2:** Selected points for acceleration measurements.

### Global noise measurement

There are several international standards for the measurement of sound level, such as IEC 60551:1993 and IEC 60076-10. To follow these standards, the measurement has to be carried out in an anechoic chamber whose ceiling and walls are covered by a highly absorptive material to eliminate reflections. Moreover, an array of microphones is often positioned around the measured object. The signal processing is normally achieved by a professional software.

As the measurement of the noise is not essential in this study and only relative comparisons have been investigated, we have not invested in a professional equipment nor an anechoic chamber. Our measurements are carried out using one sonometer, type 01dB fusion. This sonometer comes with a microphone (40CE GRAS) and a built-in preamplifier. It is placed in at the level of three-layer transformer core, $3cm$ away from it for each test to get a comparable measurement. Measurements are carried out at night in order to be less influenced by background noise.

### 5.1.2 Measurement/simulation comparison

The validation of the modeling chain is an important step in this thesis. Both numerical simulations and experimental measurements are carried out on a three-layer EI-core. Three-layer EI-cores are especially chosen to test the homogenization rule in the modeling chain. Numerical simulations are achieved under the same condition as the experimental measurements.

#### GO FeSi EI-core

GO FeSi is processed in such a way that it offers better magnetic properties in its easy magnetization direction (RD), due to a dominant quantity of domains oriented along this direction because of its very strong anisotropic behavior. On one hand, this material is the best example to verify the homogenization law and the correct implementation of the SMSM in the modeling chain. On the other hand, it may be a good candidate for this transformer application if the advantages brought by the RD are higher than the drawbacks brought by the TD.

A $400Hz$ sinusoidal excitation current of $200At$ is injected in the central coil. Displacements within one period of the injection current are shown in Fig.5.3 (it must be noticed that the four sub-figures are plotted using the same scale and that results reported are averaging results over five periods), with full lines representing the measured displacement and dotted lines representing the simulated displacement. For better readibility, displacements along $X$ and $Y$ directions are presented separately in red and blue. We observe that the vibration frequency is two times higher than the current frequency in accordance with the even variation of magnetostriction strain with magnetization. The displacement along $Y$ axis of point 2 that is positioned at the corner above the reference point exhibits the highest magnitude. Its displacement along $X$ axis is much lower in accordance with theory (theoretically null due to $Y$-axis symmetry). A double fundamental frequency of mechanical vibration (1600Hz) occurs in this signal (red line) that may be associated to a non-perfect symmetry of the transformer amplified by some resonance phenomenon. The $X$ axis displacements of points 3 and 4 are clearly not the same underlining the dissymmetry of anisotropy axis distribution in the transformer. This may also be the reason why displacements of points 3 and 4 along axis Y are not opposite.

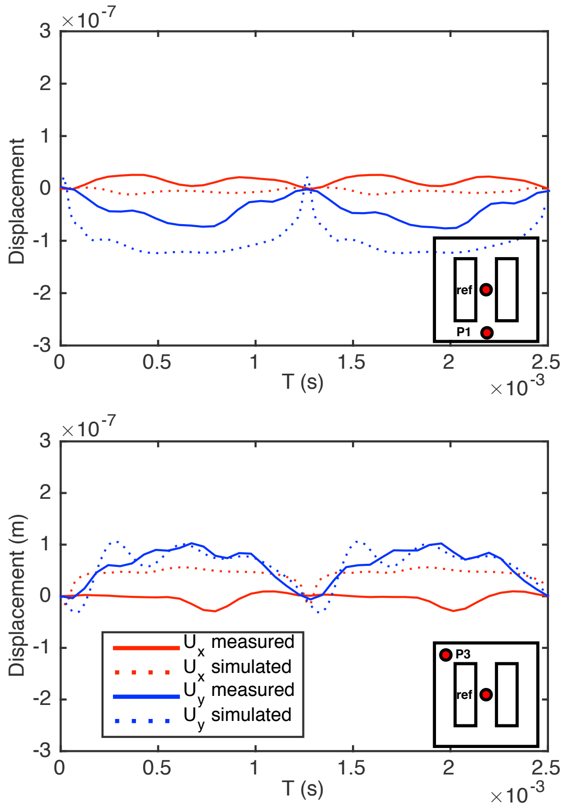


**Figure 5.3:** Comparison between modeled and measured displacements at some selected points

The numerical results reported in the same figures allow the main experimental trends to be predicted. A good agreement between measurements and simulation is obtained for the displacement period and the order of magnitude. The numerical model accurately predicts displacements along Y direction better than along X direction: point 2 displacement should be theoretically null as already underlined; the simulated and experimental displacement of point 3 along X are of opposite sign. A modal analysis has been carried out for the entire structure 'E+I' and for I-sheet and E-sheet separately. The main vibration modes of the structure are presented in Table 5.1. Mode 2 corresponding to 1515Hz frequency for sheet 'E' is plotted in Appendix A. This mode could be associated with the unexpected measured displacement along X-axis at the point 2. Indeed such variations cannot be given by the model since the parasite air-gap is not considered. It can be noticed on the other hand that the measured displacement along Y direction at point 3 is larger than predicted displacement. This can be explained by the existing air-gaps, that are not considered in the present model. Indeed air-gaps weaken the mechanical stiffness along the Y direction. Another significant discrepancy concerns the *sharpness* of modeling comparing to experiments: displacement rates are clearly overestimated by the modeling. This discrepancy is associated to the anhysteretic character of the modeling. Experiments are hysteretic and obtained at 400Hz frequency. Dissipative phenomena, characterized by a delay between magnetic field and magnetic induction, do influence global rates and especially displacement rates. Despite these defects, the results presented above constitute a significant advance in the field. A complete modeling involving hysteretic behavior may be required to improve further the prediction of vibrations.

| mode number | E | I | E+I |
|---|---|---|---|
| 1 | 1007Hz | 4839Hz | 3717Hz |
| 2 | 1515Hz | 12707Hz | 5457Hz |
| 3 | 2984Hz | 13271Hz | 5867Hz |
| 4 | 4406Hz | 21264Hz | 5928Hz |

**Table 5.1:** Resonance mode of structure 'E', 'I', 'E+I'

### Comparison between FeCo Afk1, NO FeSi and FeNi Supra50

Measurements are carried out on three-layer EI-cores in Format-B, made of different materials including FeCo Afk1, NO FeSi, and FeNi Supra50. All measurements are carried out under the same condition: $400Hz$ electrical voltage excitation in the central limb. Sinusoidal voltage electrical excitation creates a quasi-sinusoidal magnetic flux in the central limb. The magnetic flux is measured by a secondary coil positioned in the central limb. Due to the nonlinearity of the magnetic permeability, the current in the primary coil exhibits certainly some distortions and harmonics. Fig.5.4(a) and Fig.5.4(b) show respectively the measured (left figures) amplitude and the total harmonic distortion (THD) of the current in the central coil as a function of the amplitude of magnetic induction. The THD describing the harmonic distortion is defined as the ratio of the sum of the amplitude of all harmonic components to the amplitude of the fundamental frequency:

$$THD = \frac{\sqrt{I_{2nd}^2 + I_{3rd}^2 + I_{4th}^2 + \ldots}}{I_{1st}} \tag{5.3}$$

THD tends to zero when the signal is perfectly sinusoidal. For all three tested three-layer EI-cores, the amplitude and THD of the current increase with increasing amplitude of magnetic induction. The three-layer EI-core made of FeCo Afk1 exhibits the highest saturation level and the lowest current harmonic distortion. Meanwhile, FeCo Afk1 leads to the highest magnetization current because of its relatively low magnetic permeability (compared to the others). Remark: this fact is another element that confirms a probable mistake during the heat treatment of E and I sheets. The permeability of strips (in FeCo$^B$ Afk1) exhibited on the contrary a high permeability level.

Numerical simulations are carried out under the same conditions using the imposed magnetic flux method introduced in §3.4.2. Numerical predictions of the current amplitude and THD are given in Fig.5.4(a) and Fig.5.4(b) on the right side. Figures showing

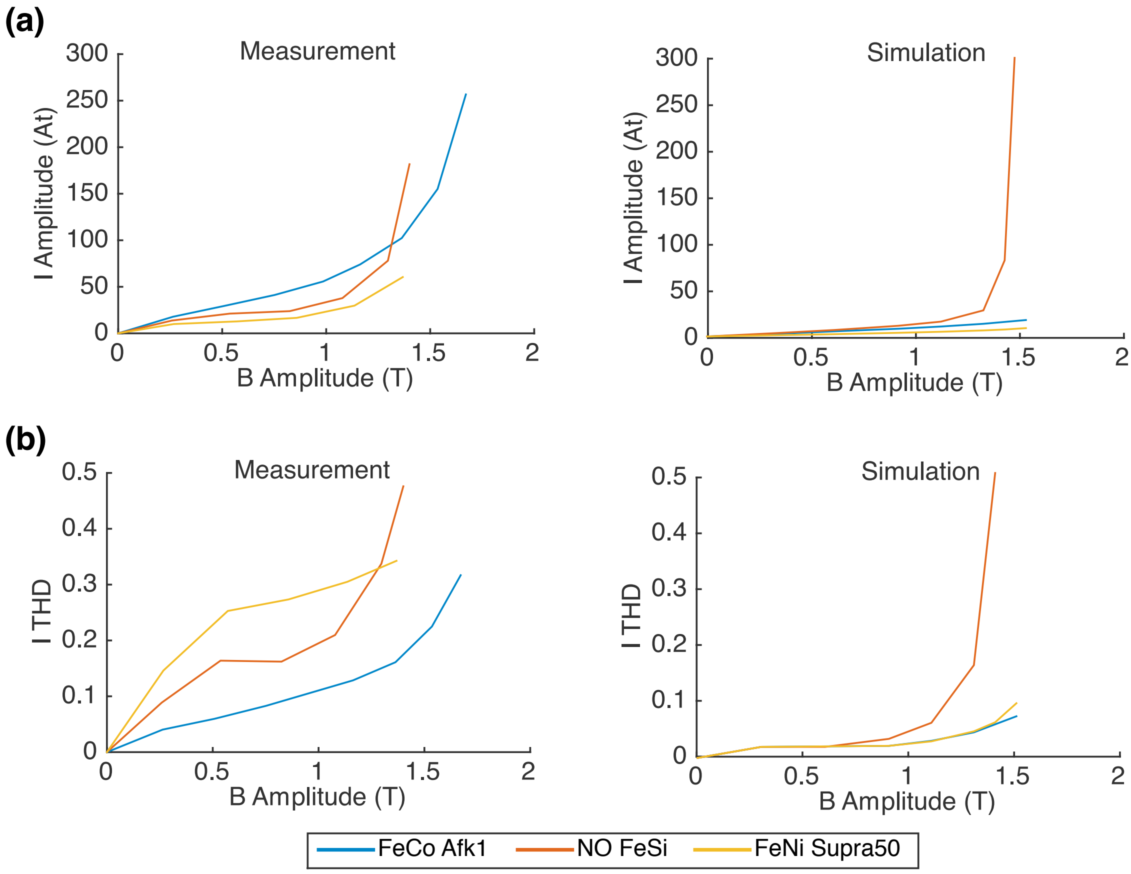


**Figure 5.4:** (a) Amplitude of the excitation current as function of magnetic induction in the central limb; (b) THD of the excitation current as function of magnetic induction amplitude in the central limb.

the simulated and measured results are plotted using the same scale. It is highlighted that the numerical simulation gives a relatively accurate prediction of the excitation current amplitude and THD for the NO FeSi core, while the current amplitude and THD are underestimated for the FeCo Afk1 and FeNi Supra50 cores. This is probably due to the inaccurate setting of the initial permeability in SMSM for these two materials. Indeed, optimization of both magnetization and magnetostriction is not perfect. For these two materials, an acceptable magnetostriction modeling is obtained by sacrificing the initial slope of the magnetization curve. As the initial permeabilities of FeCo Afk1 and FeNi Supra50 are lower in the simulation, the computed excitation currents are smaller as a consequence when magnetic flux is imposed.

Vibration measurements are carried out at the same time. Fig.5.5 gives the amplitude of relative displacement between different measuring points. Similar to the measured static structural behavior, FeCo Afk1 three-layer core exhibits the largest displacement between different pairs of points, while the FeNi exhibits the smallest. The amplitude of the displacement for NO FeSi and FeNi Supra50 increases when magnetic induction increases in the central limb. The existence of an inflection for the FeCo Afk1 should be highlighted. A local minimum of the displacement is located at about $B = 1.5T$ in the central limb. No clear explanation is available at present for this reduction in the displacement amplitude. The amplitude of the displacement is mainly related to the fundamental frequency of the vibration ($800Hz$), while the noise emission is largely associated with the higher order harmonics. However, a power transformer which generates less displacement on its board is still beneficial, because the mechanical power transmitted from the power transformer to the fixing parts is lower. Therefore, the local minimum discovered on FeCo Afk1 may be interesting to be set as an operating point.

Dynamic behavior of the transformer core is also computed by numerical simulations, as shown in Fig.5.5. The results of measured and simulated displacement are plotted using the same scale. Unsurprisingly, the numerical simulation using a behavior of FeCo$^A$Afk1 shows that the displacement is monotonically increasing as a function of excitation current. Unlike the static local magnetostriction, numerical simulation tends to underestimate the dynamic behavior (vibration) of the power transformer. This may be related to the hysteresis effect which is not taken into consideration in the simulation. Overall, the numerical simulation gives a relatively good prediction for all three materials.

Fig.5.6 gives the measured noise level and simulated acoustic power as a function of magnetic induction in the central limb for all three materials. As the noise level and the acoustic power are not really comparable, the simulated acoustic power is given here as a complementary information. As no anechoic chamber is available, the ambient noise reaches $40dB$. A general agreement is observed between the noise level and the relative displacement. However, two differences have to be underlined. They are listed below:

- Unlike the previous experiment, where NO FeSi displacement is clearly about two times greater than FeNi Supra50 displacement, the noise level of NO FeSi and FeNi Supra50 cores is very close to each other.

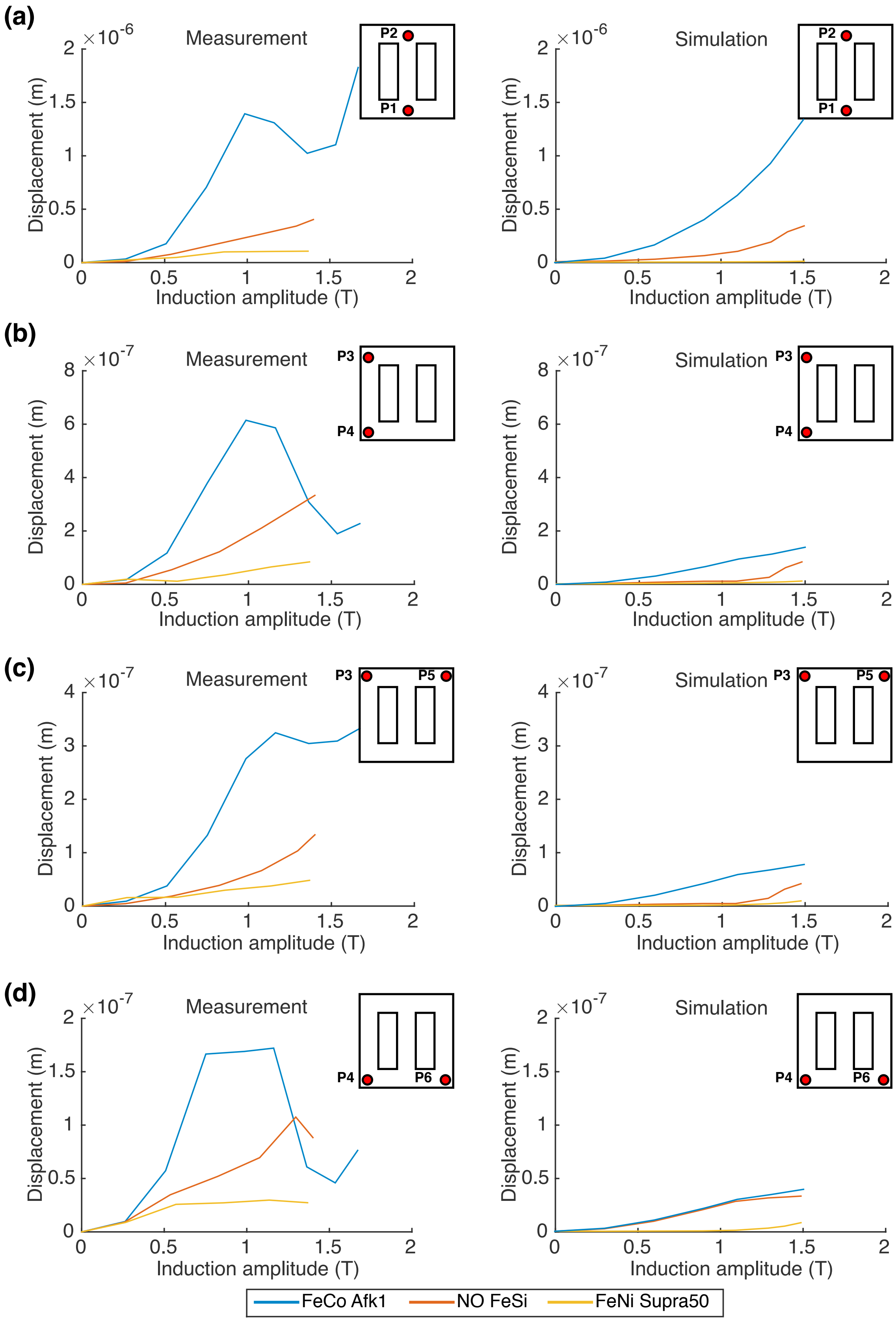


**Figure 5.5:** Measured and simulated amplitude of the relative displacement between several pairs of points on three-layer EI cores: (a)P1-P2; (b)P3-P4; (c)P3-P5; (d)P4-P6.

- The noise level of FeCo Afk1 increases when magnetic induction in central limb increases. Unlike the displacement measurement, no local minimum of the measured sound level is observed at $B = 1.5T$.

The difference between the noise level and the relative displacement can be explained in many ways. The measured noise level has different contributions including the in-plane core vibration, out-of-plane core vibration, vibration at the core joints (air-gaps), background noise, and coil noise. Moreover, the noise level is directly related to the outer surface velocity of the core, which has a spectrum composition different from the relative displacement spectrum composition.

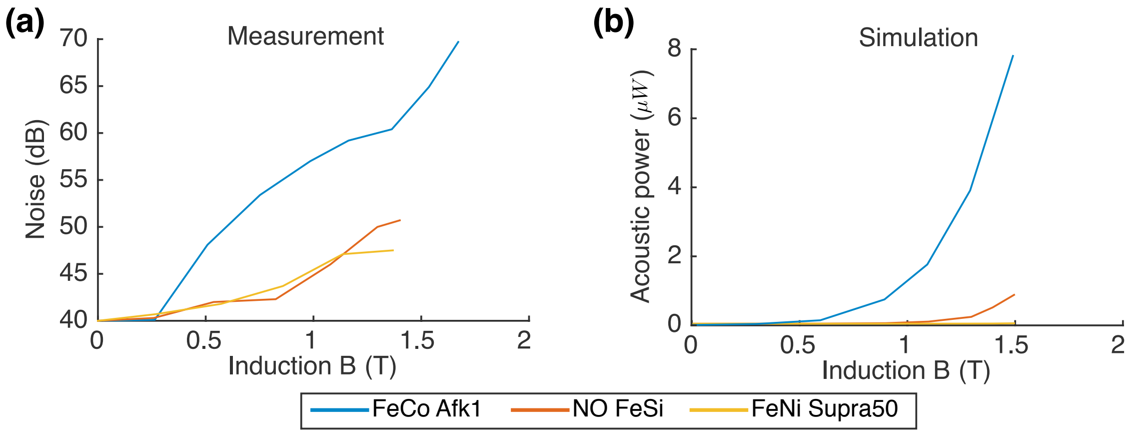


**Figure 5.6:** (a) Measured noise level; (b) Simulated acoustic power

Further studies of noise emission in the frequency domain have also been carried out. Fig.5.7 shows the frequency spectrum of noise level for the three-layer EI cores. The red line gives the outline of the background noise. Magnetic induction for all tested cores is set at about $B = 1.4T$. It is clear that the noise emission is mainly related to the high-frequency harmonics. A large portion of noise emission is found beyond $3kHz$ for all tested cores. One big contribution of the component at $800Hz$ (fundamental harmonic of the vibration/magnetostriction) is observed with the three-layer core made of FeCo Afk1 and NO FeSi, but this component has no contribution in the FeNi Supra50 noise. The noise of the FeNi Supra50 core is consequently not related to the first order magnetostriction, but related to the higher order magnetostriction, appearing for example near the magnetic saturation in the limbs or at lower induction in the corner of the core where the magnetic flux lies at 45° from RD.

Fig.5.8 shows the frequency spectrum of the relative displacement and velocity between two measuring points in the FeCo Afk1 three-layer EI core, under various magnetic induction levels. From the spectrum of relative displacement, the fundamental harmonic at $800Hz$ is discovered as the dominant component. In terms of velocity spectrum, contributions of higher order harmonics within $4kHz$ are observed.

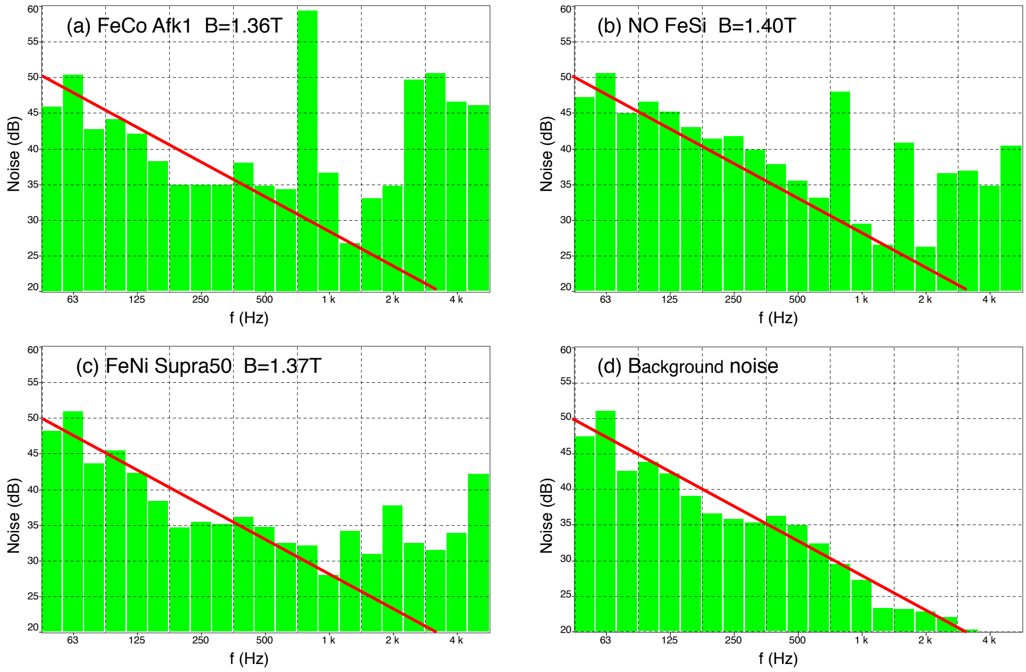


**Figure 5.7:** Frequency spectrum of noise level on three-layer EI core with different materials: (a)FeCo Afk1; (b)NO FeSi; (c)FeNi Supra50; (d) background noise

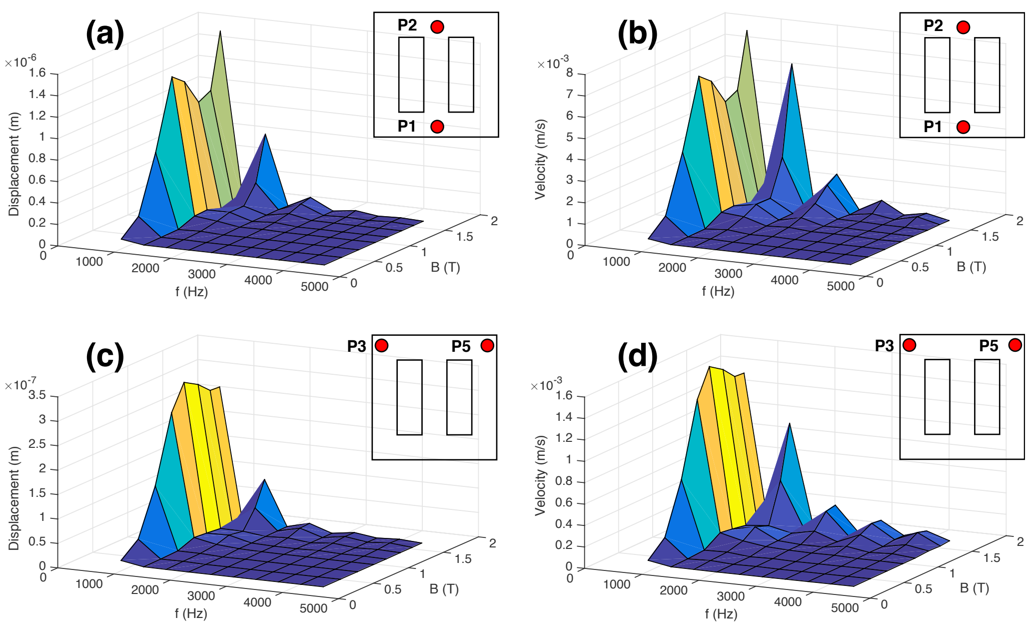


**Figure 5.8:** Frequency spectrum of the relative displacement and velocity between two measuring points on FeCo Afk1 three-layer EI core: (a)displacement P1-P2; (b)velocity P1-P2; (c)displacement P3-P5; (d)velocity P3-P5.

### 5.1.3 Other experimental study: air-gap sensibility

EI-cores are assembled with hundreds of E-sheets and I-sheets. This leads to air-gaps at the junction region. Considering the complexity of this region, the study of the air-gap influence in overlap regions by numeric simulation seems difficult and inaccurate. A series of measurements on the three-layer core with and without air-gap are prepared and tested, to appreciate the influence of the air-gap on the EI core noise emission.

Noise and vibration measurements are carried out on the three-layer cores made of NO FeSi, assembled following the five different configurations listed in Fig.4.1. The RD of all electrical sheets of configuration 'EI-x' and '8-x' ('EI-y' and '8-y') are oriented horizontally (vertically). The only difference between 'EI-x' and '8-x' ('EI-y' and '8-y') is the existence of air-gap on 'EI-x' ('EI-y'). Comparison between configuration 'EI-x' and '8-x' ('EI-y' and '8-y') allows the influence of the air-gap on the core noise and vibration to be studied. Fig.5.9 gives the noise level of these five configurations at two different magnetization levels. As expected, the standard configuration 'EI' emits the lowest noise level. However, configuration 'EI-x' ('EI-y') leads to a lower noise level than '8-x' (8-y), leading to an opposite conclusion that the noise level on the configuration with air-gap is lower than that without air-gap.

In terms of magnetic behavior, the air-gap increases the reluctance, creates magnetic flux leakage, and possibly disorients the magnetic flux from one layer to another. In terms of mechanical behavior, this air-gap weakens the global stiffness of the core that enhances the low frequency magnetic deformations and reduces the high frequency components. It is consequently possible that air-gap introduces a mechanical relaxation effect, which reduces the total noise and vibration of the core. Another observation is that the configuration '8-x' emits a lower noise than '8-y', while configurations 'EI-x' and 'EI-y' give similar results. It is extremely difficult to give a precise analysis of these results because of the competitive and sometimes opposite effects of structure, non-monotonous magnetostriction, and the interaction between magnetic force and magnetostriction. A more precise analysis would require a full 3D numerical analysis of the problem.

Fig.5.10 gives finally the amplitude of relative displacement of the five configurations at different positions. A general agreement between the relative displacement and the noise level is observed. It is important to recall that the noise is not only due to the core displacement, but also to excitation coils. It can be supposed that the latter contributions are relatively the same for all configurations.

## 5.2 Simulation and optimization of three-phase power transformer

Coils are fed with a sinusoidal current. The discrete-time expression of current function is given hereafter:

$$I(k) = I_{max} \cos\left(\frac{2\pi k}{K}\right) \tag{5.4}$$

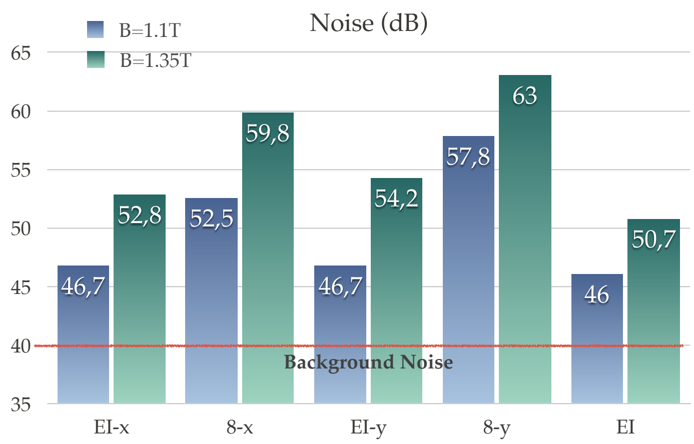


**Figure 5.9:** Noise level of the NO FeSi three-layer core with different configurations.

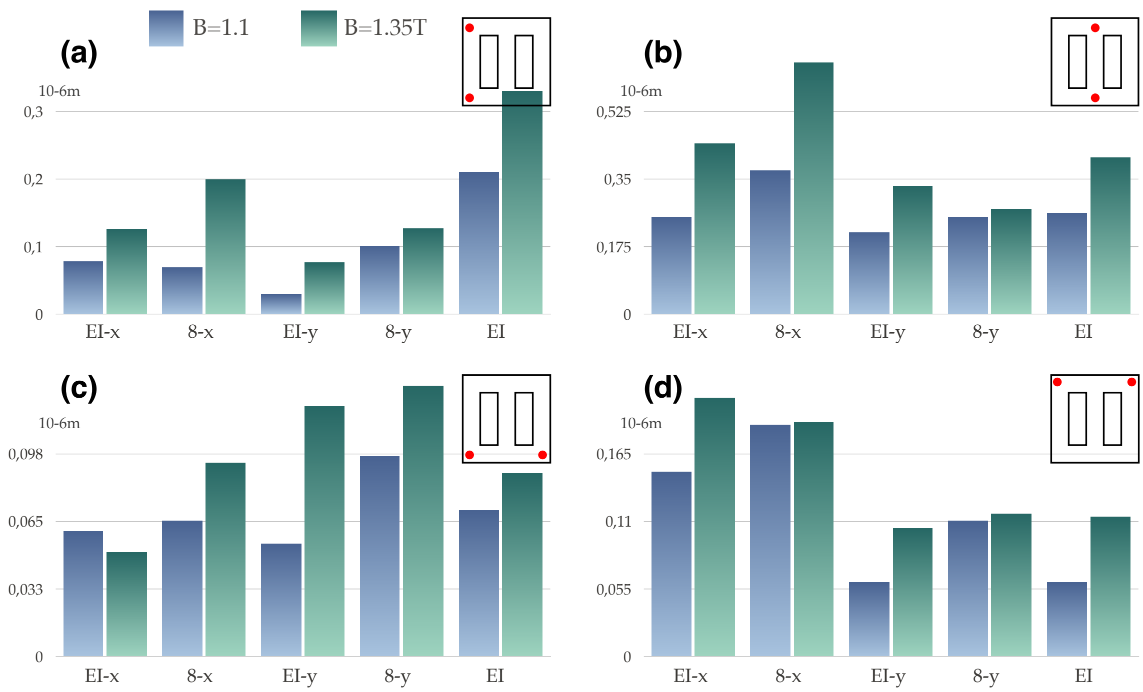


**Figure 5.10:** Amplitude of relative displacement measured on different configurations of NO FeSi three-layer cores.

where $I_{max}$ is the current amplitude, $K$ is the total number of steps in one period, and $k$ represents the time index integer ($k \in [1..K]$). The mesh used is made of triangular T3 elements. Regions where saturation appears have been refined leading to a total number of elements of 5046. Moreover the mechanical behavior is considered isotropic and homogeneous (extension to anisotropic elastic behavior is possible). Some complementary numerical and physical parameters used in the modeling are gathered in table 5.2.

| Param. | $I_{max}$ | $f$ | $\beta$ | $N$ | $E$ | $\nu$ |
|---|---|---|---|---|---|---|
| Value | 200 | 400 | 0.02 | 40 | 210 | 0.3 |
| Unit | Amper-turn | Hz | - | - | GPa | - |

**Table 5.2:** Numerical parameters and elastic constants used for transformer 2D modeling.

In this section, numeric simulation is carried out to estimate the behavior of a real GO FeSi EI-core (in Format-A) with hundreds of layers. This leads to an equal volume fraction of layer family 1 and 2 equal to each other ($f_1 = f_2 = 0.5$), with its reference dimensions $213mm \times 202mm$. A $40mm$ transformer core thickness is supposed for the computation of the acoustic power at the border. All three phases are excited by sinusoidal magnetic flux, with a phase-shift of $\frac{2\pi}{3}$ from each other. The working frequency is set at $400Hz$, which is a good balance between the power efficiency and the power density of onboard electrical transmission system. Current in each phase is then computed as a result of the magnetic resolution.

### 5.2.1 Numerical simulation

Fig.5.11 shows the current in the three phases as function of time for a magnetic flux excitation corresponding to a maximal induction of $B_{max} = 1.2T$. The displacement field is shown in Fig.5.12 at instants $t_1$ and $t_2$ (indicated in Fig.5.11) as examples. $t_1$ is the initial computation step, $t_2$ corresponds to $\frac{1}{8}$ period. The deformed core shape is shown with a scale factor of 20000 for better visibility.

The constitutive behavior of materials is fully coupled. It means that some stress fields do exist and that they influence the overall behavior of the structure. Stress components of layer family 1 ($\boldsymbol{\sigma}_{1xx}$, $\boldsymbol{\sigma}_{1yy}$ and $\boldsymbol{\sigma}_{1xy}$) and layer family 2 ($\boldsymbol{\sigma}_{2xx}$, $\boldsymbol{\sigma}_{2yy}$ and $\boldsymbol{\sigma}_{2xy}$) are shown respectively in Fig.5.13 and Fig.5.14. In this example, they are given at instant $t_2$. We observe first that the stress levels reached for the two layer families are the same but extremal values are positioned symmetrically with respect to the x axis. Indeed the two-layer families are geometrically symmetric with respect to this axis and they are considered at the same volume fraction for the calculation. We observe secondly that the stress level is relatively small in most of the areas except for some specific regions:

1. regions of connections between the 'E-shaped' and 'I-shaped' sheets present some stress concentrations especially for components $\boldsymbol{\sigma}_{1xx}$ and $\boldsymbol{\sigma}_{2xx}$ (up to $1.3MPa$).

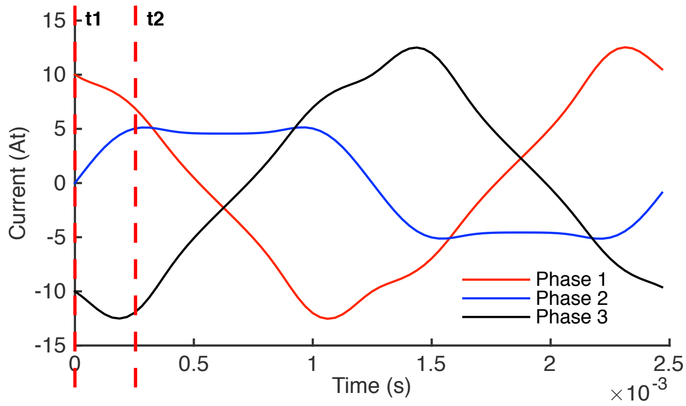


**Figure 5.11:** Current in the three phases of one period of time.


**Figure 5.12:** Displacement field described by color density at $t_1$ (left) and $t_2$ (right). Deformed core shape is shown with a scale factor of 20000

These stress concentrations are associated with the 90 degrees rotation of the easy direction, creating large magnetostriction variations.

2. some parts of the yokes undergo homogeneous stress along Y direction ($\boldsymbol{\sigma}_{1yy}$ and $\boldsymbol{\sigma}_{2yy}$) reaching about $2.4MPa$ of magnitude. These stresses are due to the difference in magneto-mechanical properties between TD and RD layers deposited alternately.

3. shear stresses are especially significant at the internal corners of the structure (reaching $\pm 0.3MPa$).

It must be, on the other hand, underlined that this stress distribution is changing during an excitation period. Plots are given at time $t_2$ and are different at other times. Moreover even if the stress level is not high, previous works have demonstrated that the magnetic and magnetostrictive behavior of GO materials are strongly stress sensitive even at a low level [Rizzo *et al.*, 2010]. The shear stress concentration at the internal corners could finally have a significant effect because it is positioned where the highest values of the magnetic flux densities are located. The numerical calculation will allow the global effect of stress to be appreciated. It must be noticed that the calculation of a magneto-mechanical equivalent stress would be possible following [Hubert et Daniel, 2011] in order to appreciate the global effect of the stress field without any huge numerical implementation.

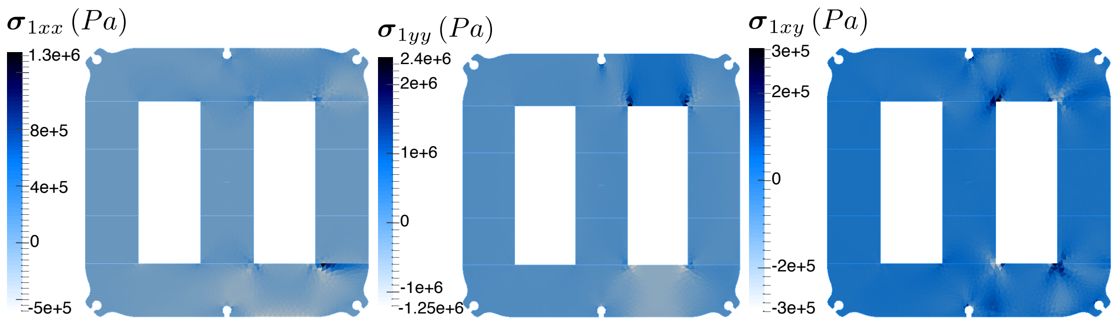


**Figure 5.13:** Induced stress in-plane components for layer family 1 at instant $t_2$

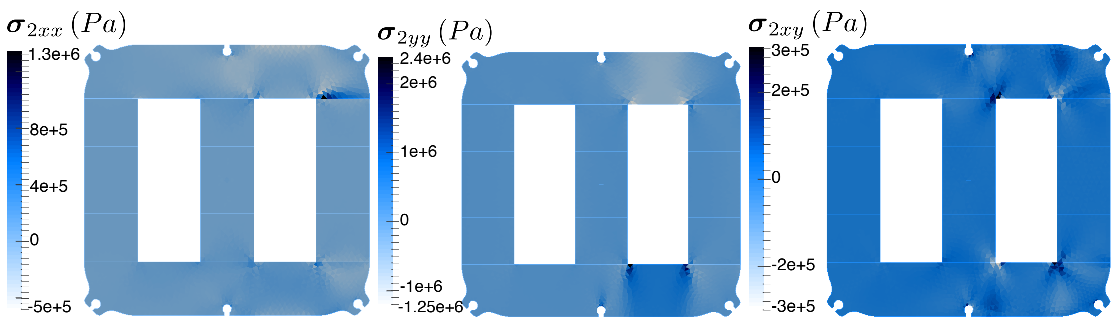


**Figure 5.14:** Induced stress in-plane components for layer family 2 at instant $t_2$

The root mean square (RMS) of the current in phase 1, 2 and 3 is respectively 7.98, 4.29 and 7.98 Ampere-turn, under no-load condition. This current is non-balanced because the magnetic reluctance in each phase is different from each other. Average RMS of three phases is 6.97 Ampere-turn, defined as $I_{RMS(avg)} = \sqrt{(I_{RMS1}^2 + I_{RMS2}^2 + I_{RMS3}^2)/3}$ which directly relates to energy loss by Joule effect. The shape of the current is deformed comparing to an ideal sinusoidal form. This is due to the non-linear permeability. THD of phases 1st, 2nd and 3rd are respectively 10%, 28% and 10%.

### 5.2.2 Comparison of fully/weakly coupled modeling chain

To study the effect of mechanical feedback loop, a test computation is carried out using the weakly coupled model (mechanical feedback loop deactivated) as comparison, with the magnetic flux excitation discretized in 80 steps. The comparison is summed up in table 5.3. Fully coupled model leads to more current, higher current distortion and more acoustic power (about 10% higher) compared to weakly coupled model, showing clearly that the stresses degrade the material properties.

| | Fully coupled | Weakly coupled | Unit |
|---|---|---|---|
| $I_{RMS(avg)}$ | 6.97 | 6.66 | $At$ |
| $THD$ phase 1,3 | 10.1 | 8.3 | % |
| $THD$ phase 2 | 27.9 | 23.7 | % |
| $P_{ac}$ | 1.63 | 1.56 | $\mu W$ |
| Computation time | 3.30 | 1.45 | hrs |

**Table 5.3:** Comparison of fully coupled and weakly coupled model.

### 5.2.3 Optimization of core geometry

The optimization process presented in this subsection is carried out using the weakly coupled model instead of fully coupled one to reduce the computation time. It has been verified that the use of fully coupled version improve the accuracy of results without changing the major tendencies. As shown in Fig.5.12, core deformation is mainly concentrated at the yokes where the magnetic field goes from the rolling direction to the transversal direction (mixed zone), leading to a huge magnetostriction induced deformation.

Intuitively, one might think that increasing the width of the yokes and decreasing the width of the limbs in order to keep a constant mass would lead to an interesting solution to reduce the noise. Indeed, such transformation allows a new distribution of flux density: flux density is increased for parts along RD that exhibit a low magnetostriction; flux density is decreased for parts along TD that exhibit a high magnetostriction, leading to the reduction of the global deformation of the system. The initial width of yokes and limbs is $W$. In order to verify this pre-considered idea, the new width of the yokes is defined by: $W_1 = \alpha W$, with $\alpha$ a geometry coefficient. The width of the limbs is recalculated, in order to keep the mass and window area constant. Some examples of modified geometries are illustrated in Fig.5.15 for various $\alpha$.

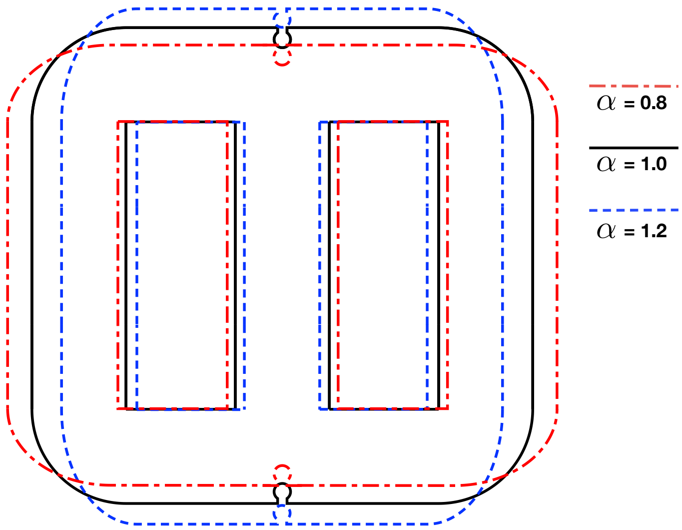


**Figure 5.15:** Examples of modified geometries

A series of simulations is carried out with imposed maximum magnetic flux density from $1.2T$ to $1.5T$ (averaged over the central section), for $\alpha$ varying from 0.8 to 1.2. In the case of excitation $1.5T$ at $\alpha = 1.0$, the magnetic saturation is reached in limbs. No numerical solution exists for thinner limbs, because of the saturation of the material. Indeed, it is not possible to impose magnetic flux density higher than saturation. Current in three phases are given in Fig.5.16. As the magnetic flux is imposed with a sine waveform, non-linearity and saturation of the material influence directly the amplitude and distortion of excitation current. The magnetic saturation is clearly observed with $\alpha$ lower than 1, where the current in the windings come with very high distortion. Average RMS and THD of current are shown in Fig.5.17 and Fig.5.18. At low magnetic flux excitation, a smaller current is enough to magnetize the transformer core. At high magnetic flux excitation, average RMS and THD increase rapidly with the flux excitation. By decreasing the geometry coefficient $\alpha$ (limbs wider and yokes thinner), average RMS and THD of the current increase dramatically because of the saturation in yokes. From an electric point of view, the optimized design of transformer core is obtained for a geometry coefficient close to $\alpha = 1.05$ at high magnetic excitation, where average RMS and THD of current are both minimum. At low magnetic excitation, the average RMS and THD of current continue to decrease as $\alpha$ increases. Optimum point for low magnetic excitation may be higher than $\alpha = 1.2$. This leads to the lowest joule losses. The acoustic power is shown in Fig.5.19. The acoustic power is an interesting indicator of global deformation level, that may be related to the sound emission. At a given maximum flux density, the acoustic power varies with the geometry coefficient $\alpha$.

For high $\alpha$, the width of the yokes is larger than that of the limbs, leading to low flux

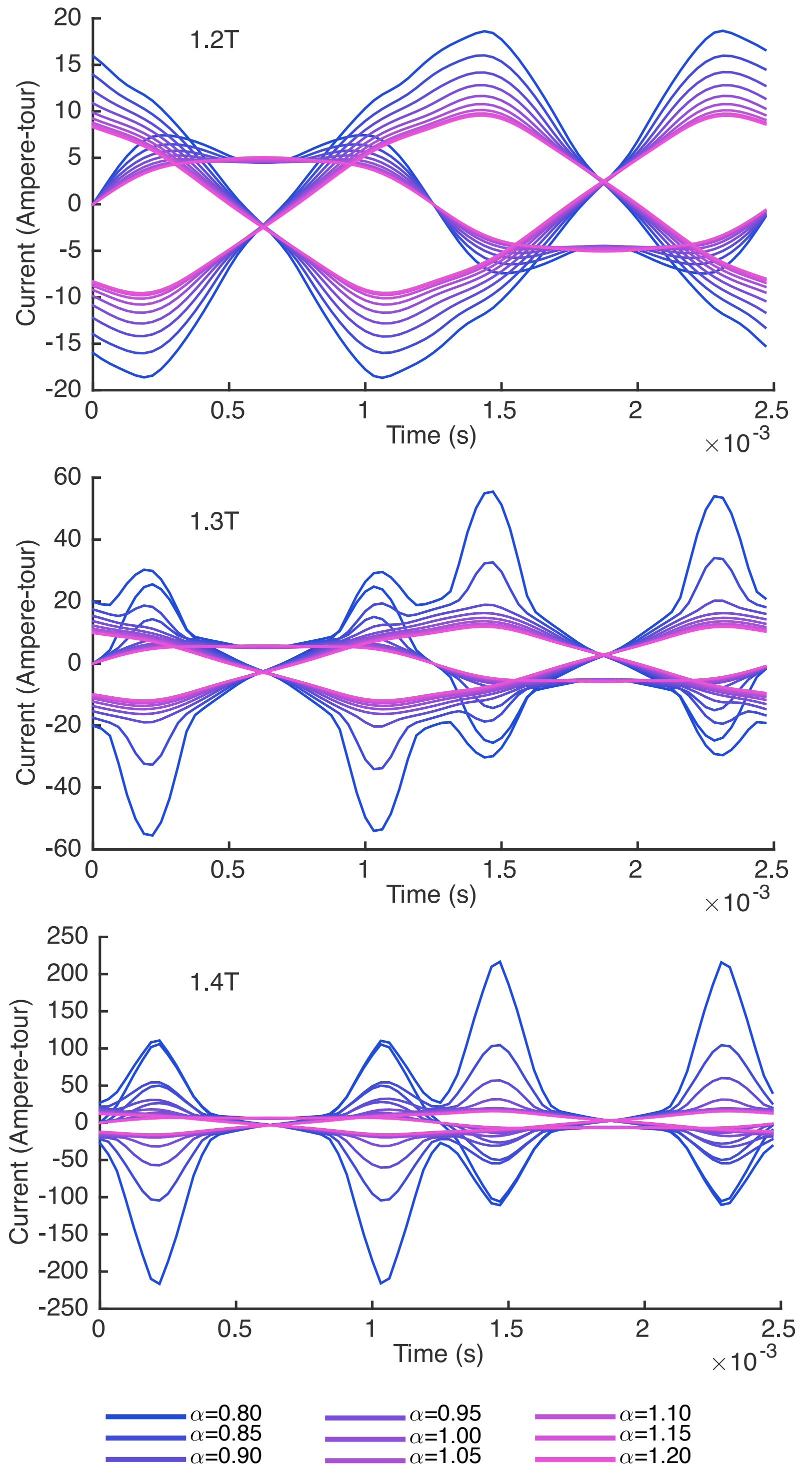


**Figure 5.16:** Current of three phases with maximum induction of $1.2T$ (top), $1.3T$ (middle) and $1.4T$ (bottom) on different geometries.

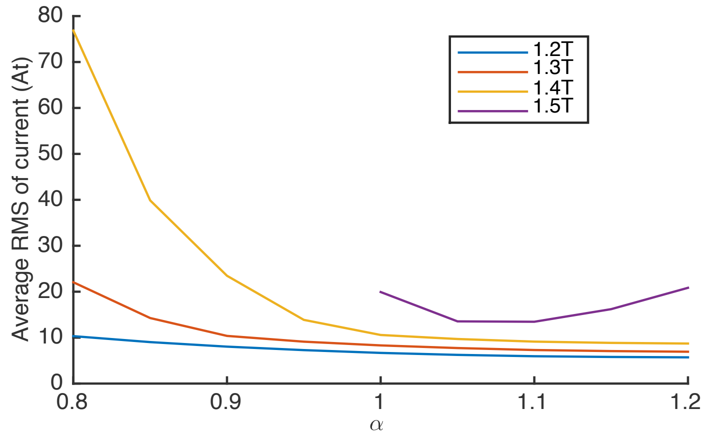


**Figure 5.17:** Average RMS of current of three phases with different maximum inductions and geometries.

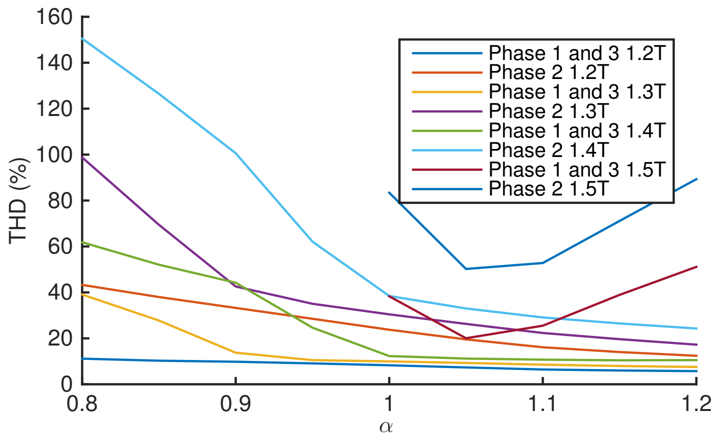


**Figure 5.18:** THD with different maximum inductions and geometries.

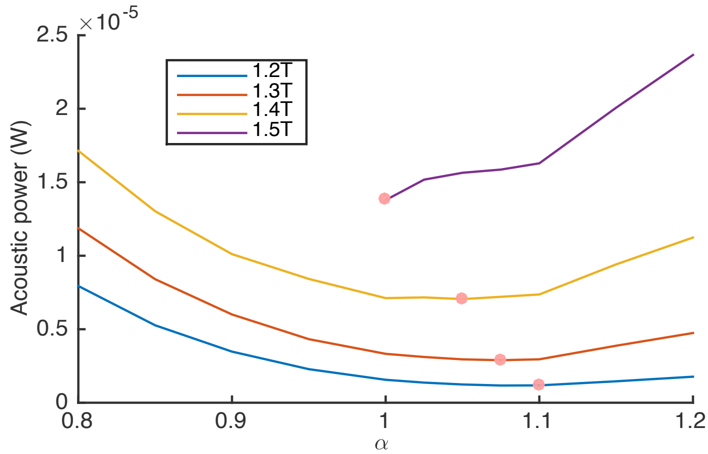


**Figure 5.19:** Acoustic power with different maximum flux density and geometries.

density and then low deformation in yokes, where magnetic flux lines up to TD and normally creates large deformation. As the $\alpha$ goes extremely high, the deformation in limbs becomes larger because of the saturation. For low $\alpha$, the width of the yokes is smaller than that of the limbs, so that saturation appears first in the yokes, leading to a huge deformation. On the other hand, the optimum $\alpha$ corresponding to the minimum acoustic power changes with the magnetic induction. For $B = 1.2T$, optimum $\alpha$ locates at 1.1, which means yokes wider than limbs. This verifies the speculation made previously that by increasing the width of yokes and decreasing the induction in the transversal direction of the lamination, the noise can be reduced. As the magnetic flux increases, the optimum $\alpha$ decreases. It reaches 1.0 at $B = 1.5T$. At this high level of excitation, where all areas of the transformer core are almost saturated, acoustic power is no more sensitive to the geometry variations. Other mechanisms coming from assembly precision and air gaps may also influence the sound emission but are not considered in this simulation. It has been verified that the optimized geometry remains roughly the same when the fully coupled SMSM is used.

## 5.3 Conclusion

A vibration measuring bench has been build up, allowing the measurement of the dynamic structural behavior of the transformer core, including local acceleration and noise emission. Measurements are carried out on a series of material-structure configurations, under different external loadings (current excitation, voltage excitation). Comparisons are made between transformers fabricated in different materials. Analyses in both time domain and frequency domain are achieved for better comprehension of the transformer dynamic behavior. The validation of the modeling chain is an important step in this thesis. Simulations are carried out under the same condition as the experimental measurements. Good agreements are obtained between the simulation and measurements. A geometry optimization process is finally carried out, leading to lower noise emission at constant mass.

# Conclusions and Perspectives

In the context of 'More Electric' or 'All Electric', manufacturers of land and air vehicles seek to increase the on-board power to equal mass. One of the solutions considered is to increase the magnetic flux density in the magnetic materials constitutive of electrical machines. However, materials with the highest flux densities have the disadvantage of deforming under the effect of the magnetic field. This deformation leads to a significant increase in vibration, which causes undesirable acoustic noise. The main origin of these deformations is the phenomenon of magnetostriction. The magnetostriction results from the rearrangement under magnetic field of the microstructure into magnetic domains. The paths explored to reduce this noise without adversely affecting the performance of the systems are numerous. We are interested here in the development of a complete modeling chain, from the local behavior of the material to the calculation of the total deformation of the structure, using a multi-scale approach combining a local constitutive behavior, an analytical homogenization for the description of the multilayer medium, and a finite element modeling for the resolution of the mechanical and magnetic structure problem.

## 5.4 Modeling strategies

The aim is to solve a coupled magneto-mechanical problem (a 2D numerical model is preferred). A sequential and quasi-static approach is first applied: the solving of the magnetic problem is carried out first, followed by the resolution of the mechanical problem. The induced stress in the transformer structure is generally low; it nevertheless influences the magnetic and magnetostrictive behavior of the material. A strong coupling has been implemented within the multilayer model. This method of calculation is suitable for materials whose behavior is considered sensitive to stress.

Two methods of iterative resolution (modified fixed point and Newton-Raphson) have been implemented to solve the non-linear magnetic problem. By sending a sinusoidal current in the coils (or a magnetic flux in the core) discretized in time, at convergence, we have obtained a series of solutions constituted by magnetic fields (field, induction, flux, magnetization) and the free magnetostriction deformation fields. The next operation consists in defining a volume force, which should be equivalent to the magnetostriction deformation from the mechanical equilibrium equation. The calculation is performed at each time step over an excitation period and then decomposed into Fourier series. Each harmonic is considered as the excitation of the mechanical problem for different frequencies. The total displacement of the structure as a function of time is obtained by summing the harmonics of displacements (superposition principle). The mechanical problem is solved in the frequency domain to avoid transient calculations and thus save time. An acoustic post-processing block is developed, which gives the acoustic power. It is considered as an overall indicator of the acoustic behavior of transformers.

A first optimization of the geometry with equal mass is carried out, with three-phase magnetic flux directly imposed in the core of the transformer. Optimization of the geometry in order to reduce the noise and the losses at given power is thus made possible. This procedure is applied to identify the ideal shape factor of a three-phase grain-oriented iron-silicon transformer at given power.

## 5.5 Development of constitutive behaviors laws

Considering the complexity of the magnetic and magnetostrictive behavior of materials (non-linearity, anisotropy, stress sensitivity, hysteresis ...), a simplified multi-scale model is integrated into the finite element chain. In this model, the macroscopic behavior of the magnetic material is represented by an equivalent single crystal. We are looking for the probability of existence of a magnetic domain in different directions from its local energy, sum of different contributions: field energy, magnetocrystalline anisotropy, elastic (magneto-mechanical), and configuration energy. Several extensions and improvements (configuration energy, anisotropic energy, crystal rotation…) of this model are proposed to adapt it to different materials, in particular, highly anisotropic grain-oriented iron-silicon, non-oriented grain iron-silicon, iron-cobalt afk1, iron-nickel supra50.

A complete multi-scale model with hysteresis is then proposed. This model is able to account for rotating magnetic field loading, and to estimate associated iron losses. The rotational magnetic loading is often found in electrical machines and at the T-joints of the power transformers. A hysteresis model with rotational magnetic field is a key point for accurate loss and vibration calculations. Note that this multi-scale model has not yet been proposed in a simplified version and is therefore not implemented in the finite element chain.

A transformer generally consists of a stack of metal sheets cut in the form of E and I (in order to close the magnetic circuit). Sheets are stacked head-to-tail which leads to a mixture of the behaviors of each sheet. The 2D resolution requires defining the average behavior of the sheet stack. A law of mixtures is applied: it uses a hypothesis of homogeneous magnetic field and total deformation in different layers, with the consideration of the conventional tangential continuity of the magnetic field and the displacement.

## 5.6 Identification and experimental validation

A first series of experiments makes it possible to identify the anhysteretic behavior of materials. The strips are cut following the rolling direction, transverse and at 45° from the rolling direction. Materials are characterized in a magnetic and magnetostrictive measuring bench, developed at LMT-Cachan. The parameters of the simplified multiscale model are identified from the measured behaviors.

Validation of the structural computation uses a three-layer transformer (for simplicity reason) in the form of '8' made up of different materials. Strain gauges are glued at different measuring points of some structures,. The same procedure for characterizing anhysteretic behavior is then applied. Numerical simulations are carried out using the same loading conditions and boundary conditions as the measurements. The numerical results are in general in good agreement with the experimental measurements which allow a first validation of the complete model.

A second series of experiments carried out on transformers allows a measurement of the vibration of the transformer and an estimation of the emitted noise. Several 'EI' tri-layer transformers are made of different materials. The central winding is fed with a sinusoidal excitation current (or voltage). Accelerometers placed at different points of the sheet lead to the measurement of the local displacement by integration. The measurement points are chosen so as to identify and eliminate solid body displacement components. The displacement of the measuring points as a function of time is obtained by means of a post-treatment. The vibrations of the transformer and the noise emission are also compared with the numerical simulation. This model makes it possible to reconstruct the main trends of the measured behavior. In particular, the prediction of the amplitude and form of the displacement are well predicted at high field. Discrepancies that remain are discussed.

## 5.7 Perspectives

The main perspectives of this work are to improve the accuracy of the vibration and noise prediction of the numerical tool.

In terms of constitutive behavior, on one hand, the simplification of IMSM and its finite element implementation are strongly required, so as to consider the static hysteresis effect (irreversible behavior) under complex magnetic (rotational) and mechanical (biaxial) loadings. On the other hand, the SMSM still needs to be improved, in order to achieve higher accuracy and better stability (numerical convergence) in a structural computation under complex mechanical loadings. In terms of modeling chain, extension from 2D to 3D is definitely essential, which allows the consideration of out-of-plane magnetic field and vibration, the non-homogeneous magnetic field through the thickness because of the eddy currents, and acoustic radiation in the free space. For better accuracy of the simulation, one needs to add shell element for the consideration of air-gaps while keeping an acceptable mesh size. As the power transformer is always fixed in a supporting structure introducing non-negligible external stresses, the simulation of the transformer together with the mechanical connection and/or the supporting structure should be achieved. Other numerical improvements should include: GPU computing for extensive vector computation and packaging of the source code into a user-friendly software. In terms of experimental aspects, measurements on a real power transformer are strongly required. This needs a more powerful power supply and several three-axes accelerometers and/or laser Doppler velocity sensors.

This SMSM together with the modeling chain is a powerful tool for the noise and vibration simulation of all kinds of low-frequency electromagnetic devices, including electrical motors, generators, power transformers and inductors. Moreover, this tool is able to consider several materials with complex magnetic and magnetostrictive behavior. It is able to consider anisotropy and stress dependency too. We see huge potentials of the applications of this numerical tool.

# Appendix A

# Vibration mode

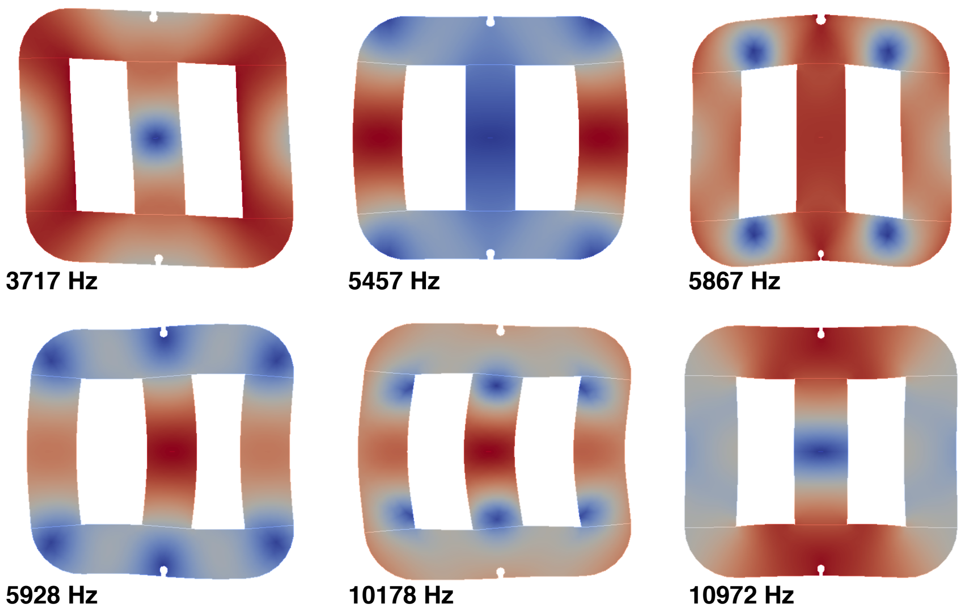


**Figure A.1:** In-plane vibration mode for 8-shaped sheet (Format-A).

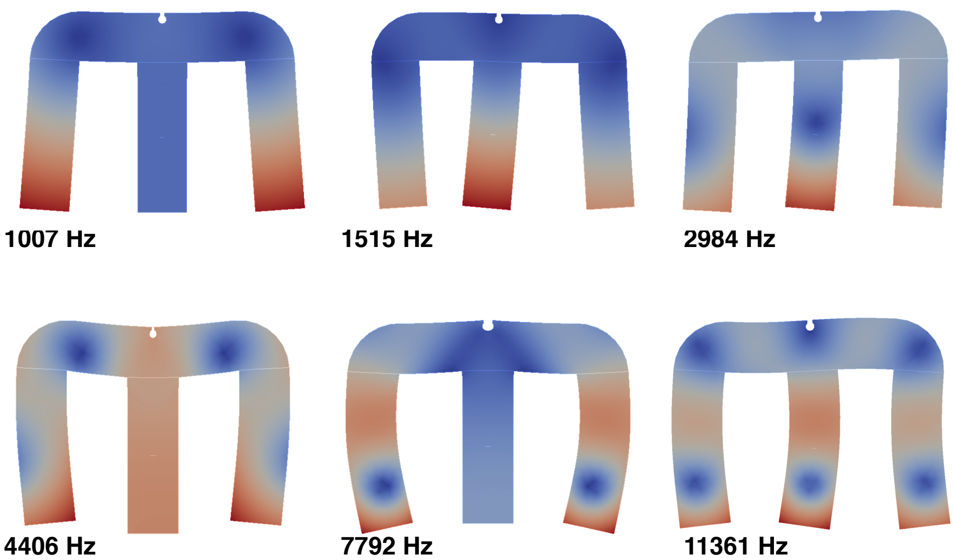


**Figure A.2:** In-plane vibration mode for E-shaped sheet (Format-A).

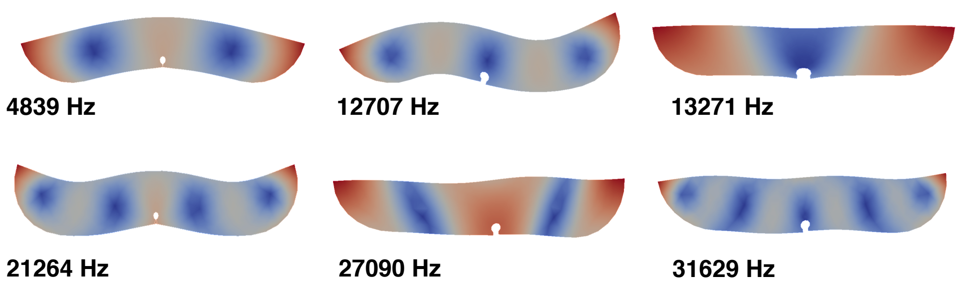


**Figure A.3:** In-plane vibration mode for I-shaped sheet (Format-A).

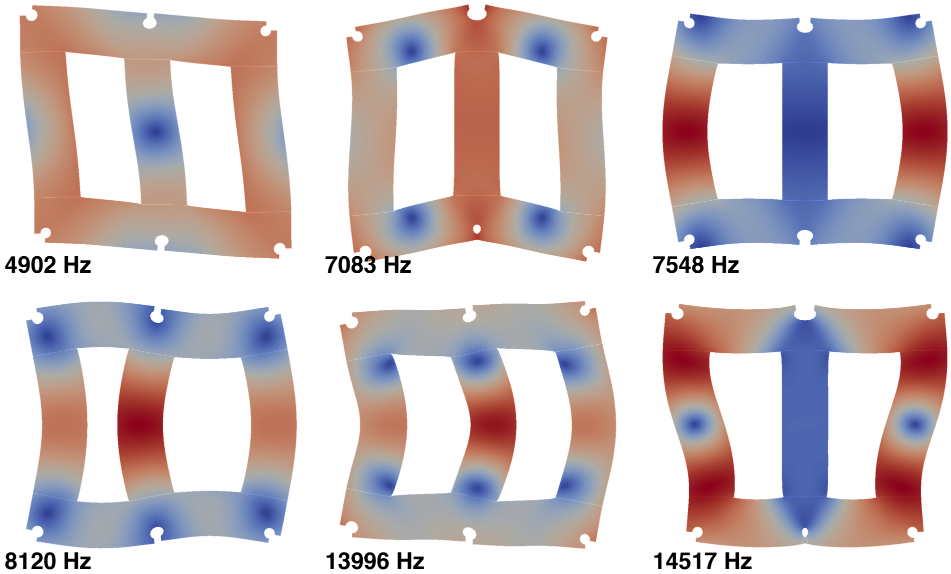


**Figure A.4:** In-plane vibration mode for 8-shaped sheet (Format-B).

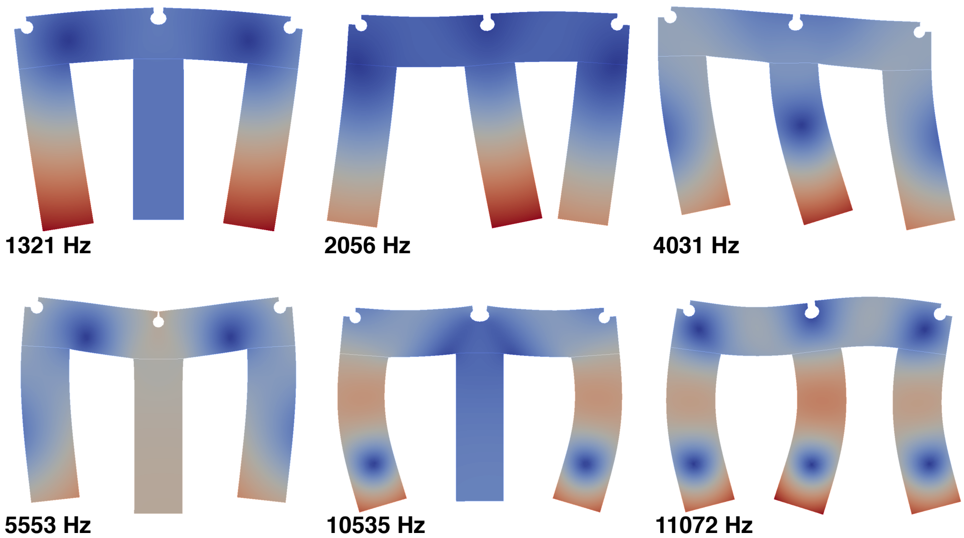


**Figure A.5:** In-plane vibration mode for E-shaped sheet (Format-B).

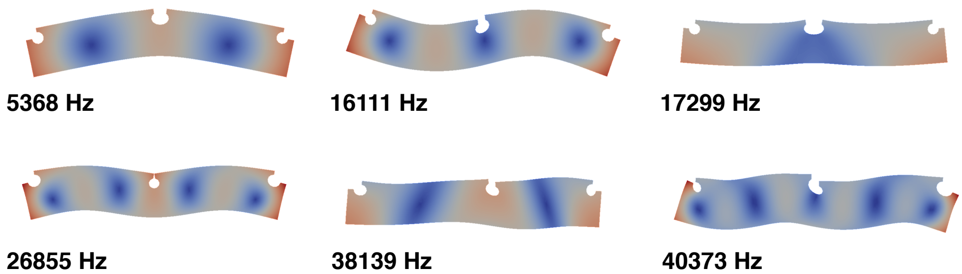


**Figure A.6:** In-plane vibration mode for I-shaped sheet (Format-B).

# Appendix B

# Core simulation with mono-phase excitation

Numerical simulations are carried out on four different material-structure configurations including GO FeSi (three-layer 'EI'), NO FeSi ('8-y'), FeNi Supra50 ('8-y'), and FeCo Afk1 ('8-y'). GO FeSi core is fed with a coil current of $200At$, while the other three cores are fed with a magnetic induction of $1.5T$ at the central limb.

### Three-layer GO FeSi EI-core

Fig.B.1 shows the distribution of magnetic induction (left) and nodal equivalent force (right). As illustrated in Fig.4.4, axis X is not an axis of symmetry of the three-layer EI-core, so that the distribution of the equivalent force is different on the top and bottom yokes. This, on one hand, helped to compare with the vibration measurement on three-layer transformer prototype. On the other hand, the asymmetry of the force verifies the functionality of the homogenization rule. Fig.B.2 shows the components of total strain when excitation current reaches its maximum. The points where strains are the strongest are positioned exactly where the magnetic field is aligned with TD. This result seems in accordance with the material behavior. A shape scale factor of 20000 is used for better visibility of the small total displacements in Fig.B.3. The reference point for mechanical computation is not chosen in the center (shifted towards to the bottom) of the core. This is where the reference point was set for the vibration measurement. Local displacements obtained are lower than $1\mu m$.

### 8-shaped NO FeSi core

Fig.B.4-B.6 give the distribution of magnetic induction, nodal equivalent force, total strain and the displacement field of the 8-shaped NO FeSi core. As the magnetic induction is only imposed in the central limb, the magnetic flux in the lateral limbs is half of that in the central limb. This makes the central limb elongates more than the lateral limbs and pushes the top and bottom yokes. Displacements obtained are lower than $0.2\mu m$. A shape scale factor of 20000 is used for better visibility.

### 8-shaped FeNi Supra50 core

The distribution of magnetic induction and nodal equivalent force on FeNi Supra50 core are given in Fig.B.7. Fig.B.8 shows the components of total strain when excitation current reaches its maximum. The displacement field and the distorted core shape is shown in Fig.B.9 with a shape scale factor of 200000. It is noticed that the equivalent force is mainly concentrated on the inner corner of the central limb, where the directions of the force are not regular. On other words, neighbor forces are found pointing to the opposite directions. The direction of the magnetic field changes rapidly from one element to another at the corner, leading to the change of structure energy in SMSM and the material behavior. This causes numerical errors closely related to the discretization of the mesh. It also explains the fact that the simulated local displacement and strain are always smaller than the measured ones. Displacements obtained by simulation are lower than $0.01\mu m$.

### 8-shaped FeCo Afk1 core

Fig.B.10-B.12 give the distribution of magnetic induction, nodal equivalent force, total strain and the displacement field of the 8-shaped FeCo Afk1 core. Similar to NO FeSi, FeCo Afk1 exhibits a behavior that is relatively isotropic. This leads to a similar distribution of the force, strain, and the displacement of the core. A shape scale factor of 60000 is used for better visibility. As already observed, the numerical simulation on the FeCo Afk1 core is far from the experimental measurement. Further investigations are necessary for this material.

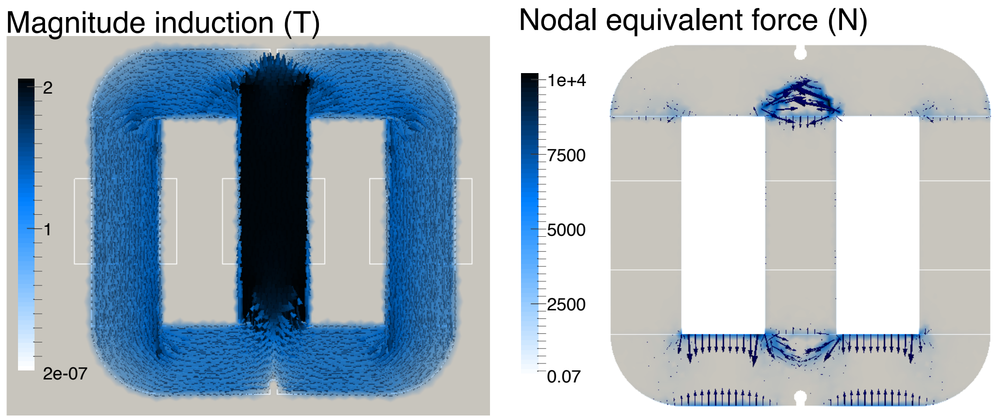


**Figure B.1:** Distribution of the magnetic induction (left) and nodal equivalent force (right) for three-layer GO FeSi EI-core

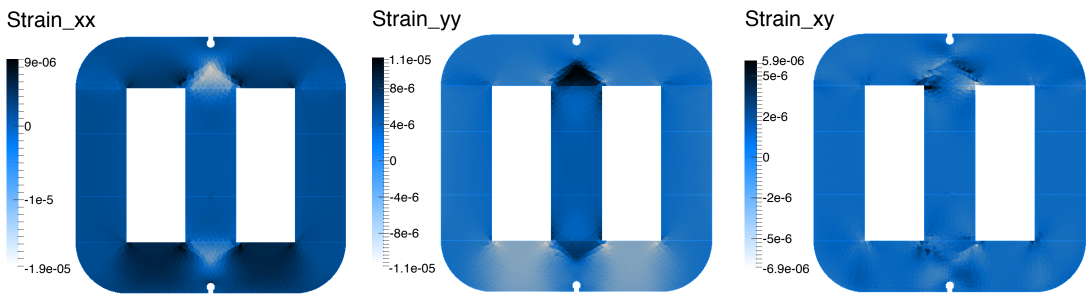


**Figure B.2:** Distribution of the induced stress in-plane components for three-layer GO FeSi EI-core

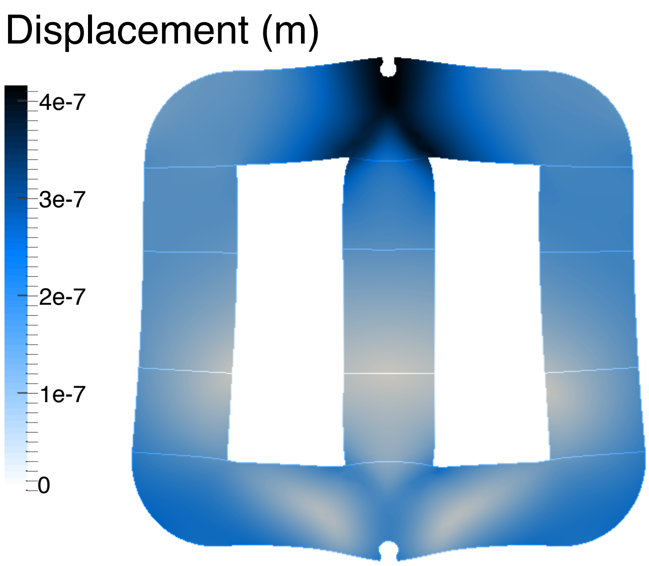


**Figure B.3:** Distribution of the local displacement for three-layer GO FeSi EI-core, with a shape scale factor of 20000

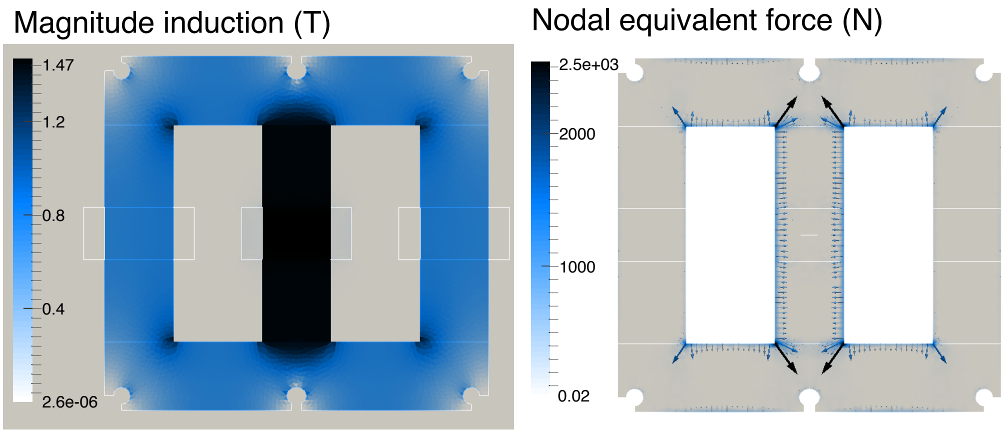


**Figure B.4:** Distribution of the magnetic induction (left) and nodal equivalent force (right) for NO FeSi 8-shaped core

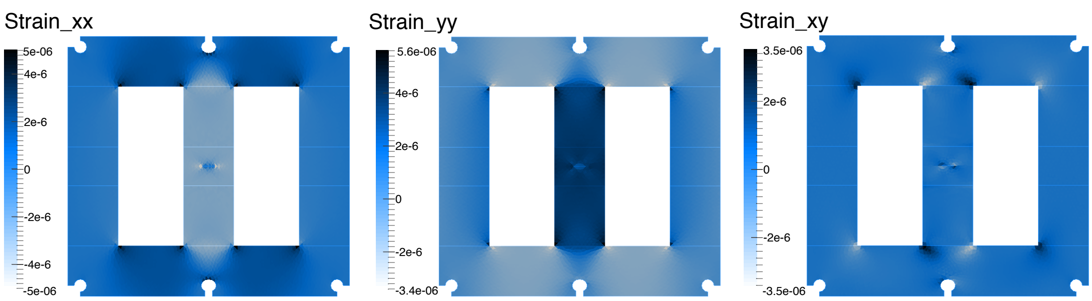


**Figure B.5:** Distribution of the induced stress in-plane components for NO FeSi 8-shaped core

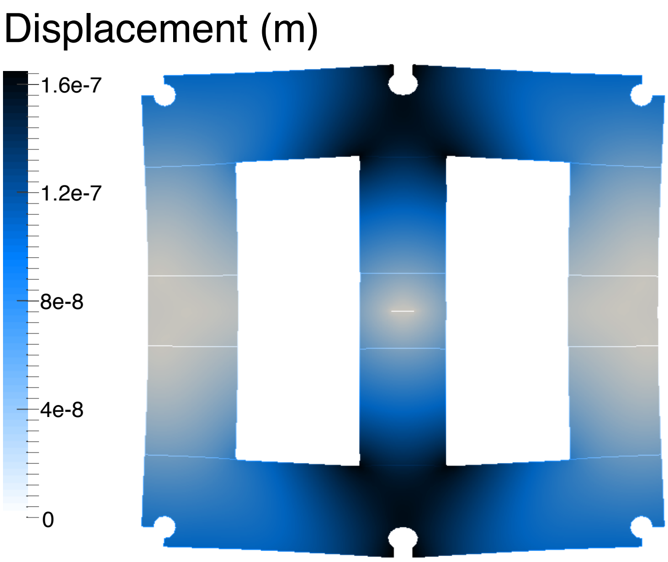


**Figure B.6:** Distribution of the local displacement for NO FeSi 8-shaped core, with a shape scale factor of 20000

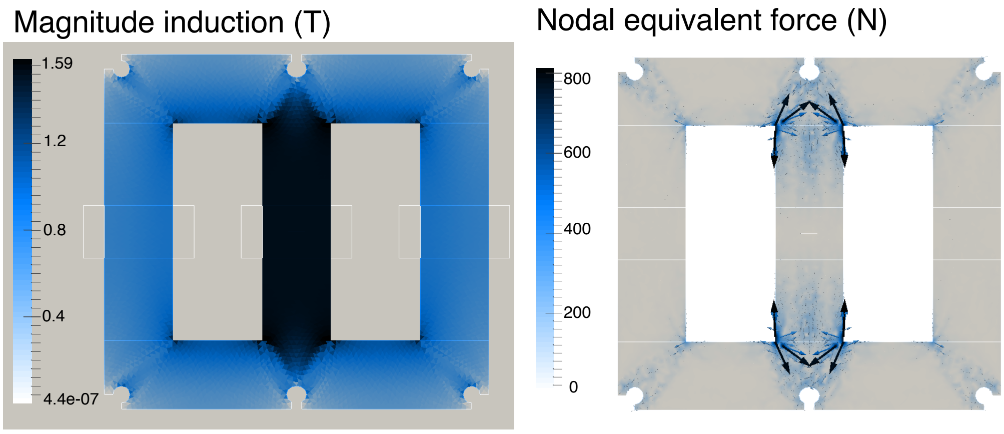


**Figure B.7:** Distribution of the magnetic induction (left) and nodal equivalent force (right) for FeNi Supra50 8-shaped core

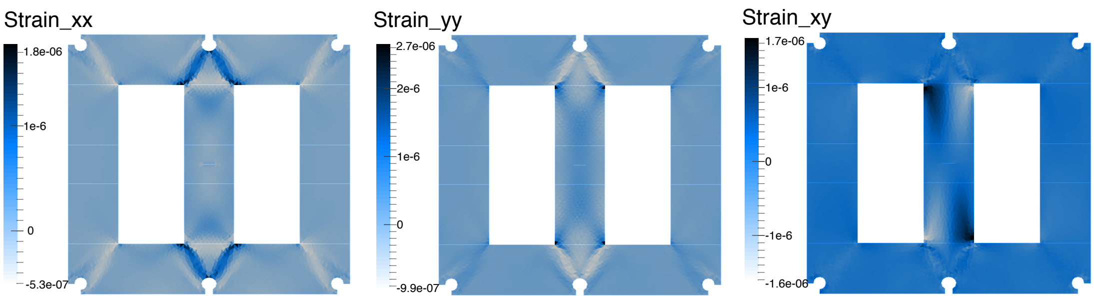


**Figure B.8:** Distribution of the induced stress in-plane components for FeNi Supra50 8-shaped core

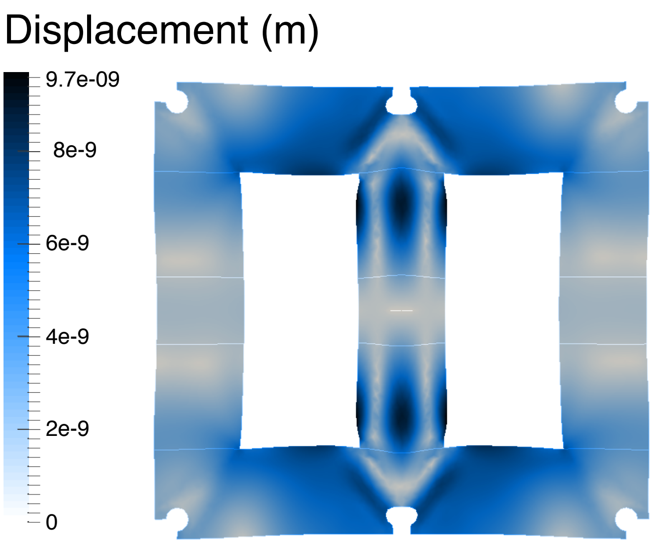


**Figure B.9:** Distribution of the local displacement for FeNi Supra50 8-shaped core, with a shape scale factor of 200000

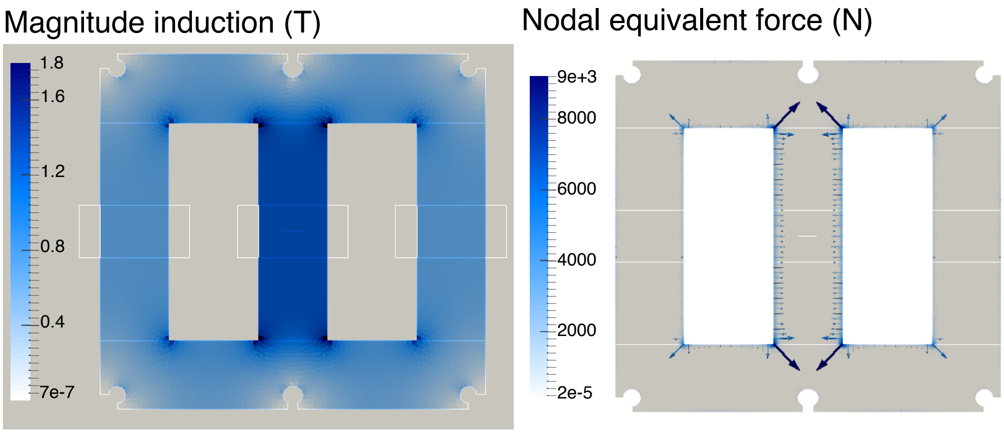


**Figure B.10:** Distribution of the magnetic induction (left) and nodal equivalent force (right) for FeCo Afk1 8-shaped core

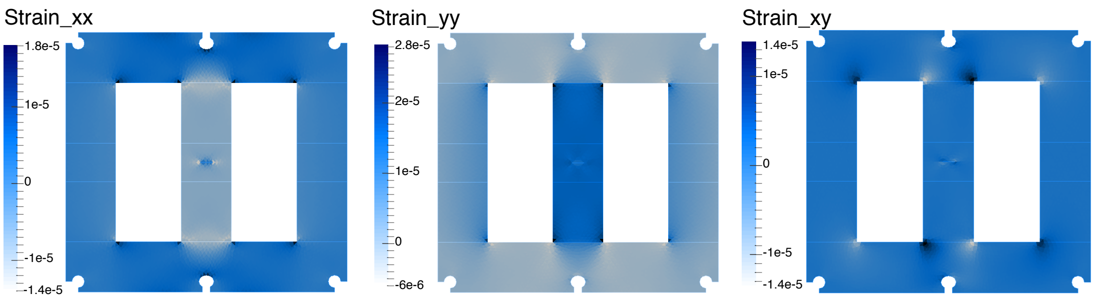


**Figure B.11:** Distribution of the induced stress in-plane components for FeCo Afk1 8-shaped core

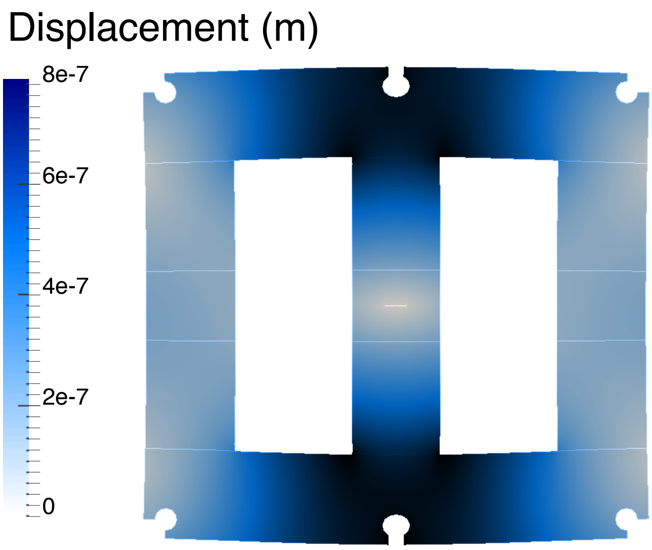


**Figure B.12:** Distribution of the local displacement for FeCo Afk1 8-shaped core, with a shape scale factor of 2000

# Appendix C

# Study of mesh-to-mesh projection

### C.0.1 Introduction and state of the art

Magneto-elastic coupled problem is usually solved by dividing it into two sub-problems: magnetic part and mechanic part [Mininger *et al.*, 2009, Bernard *et al.*, 2011]. The magnetic resolution gives the distribution of magnetic field, leading to the computation of magnetic force and magnetostriction induced force. These forces are used as loadings of mechanical problem, leading to structure deformations and vibrations. Each sub-problem can be solved on its own mesh with adapted support and optimized discretization. Such a modeling process requires the data projection from one mesh to another, making mesh-to-mesh date transfer crucial in these high accuracy multiphysics modelings.

Mesh-to-mesh projection can be performed through an explicit interpolation or Galerkin method [Geuzaine *et al.*, 1999, Ciarlet, 1988]. The latter has the advantage of great overall precision. For magneto-elastic coupled problems, Galerkin projections can be carried out at different stages. Wang *et al.* compare the magnetic field projection in different spaces [Wang *et al.*, 2013], and propose energetic Galerkin projection [Wang *et al.*, 2014] to minimize the errors of magnetic energy while projecting magnetic field. Journeaux *et al.* [Journeaux *et al.*, 2013] demonstrate that, for a magneto-elastic coupled modeling chain, projection of magnetic force density offers better accuracy than projection of magnetic field.

However, for most of mechanical computation softwares, only the source tensor (strain/stress) and the force density are considered as source term. Projections of magnetic field or magnetic potential will be hard to achieve. Moreover, data transfer of magnetostriction induced force and deformation have never been studied in the literature. To tackle these issues, computation process of the magnetostriction and magnetic force induced deformation are first unified by involving the modified Maxwell tensor (equivalent to magnetostriction strain tensor), which is able to deal with nonlinear and anisotropic material magnetic behaviour. The modeling chain can be then summarised as magnetic resolution, source tensor computation, nodal force computation and finally mechanical resolution. Source tensor projection is first time introduced in magneto-elastic coupled problems, including both magnetic force and magnetostriction. It is then compared with classical force density projection, in termes of accuracy, for an isotropic ferromagnetic piece.

### C.0.2 Theoretical consideration

Let us consider $\mathcal{D} \subset \mathbb{R}^2$ the studied domain. $L^2(\mathcal{D})$ is a space of square integrable vectorial or tensorial functions, depending on the context. Two function spaces are defined: $V_1 \subset L^2(\mathcal{D})$ in the source mesh; $V_2 \subset L^2(\mathcal{D})$ in the target mesh. The aim of the mesh-to-mesh projection is to find the fields in target mesh $u^t \in V_2$, that possess the minimum errors compared to the fields in source mesh $u^s \in V_1$.

By defining a test function in the target space $u' \in V_2$, Galerkin method gives the formulation to solve $u^t$ in weak form. Equation (C.1) and (C.2) are adapted respectively to vectorial field and tensorial field ($2^{nd}$-order).

$$\int_{\mathcal{D}} u^s \cdot u' \, \mathrm{d}\tau = \int_{\mathcal{D}} u^t \cdot u' \, \mathrm{d}\tau \tag{C.1}$$

$$\int_{\mathcal{D}} u^s : u' \, \mathrm{d}\tau = \int_{\mathcal{D}} u^t : u' \, \mathrm{d}\tau \tag{C.2}$$

In discrete domain, $u^s$ and $u^t$ are usually defined as (C.3)

$$u^s = \sum_{i=1}^{N_s} u_i^s \omega_i^s \quad \text{and} \quad u^t = \sum_{i=1}^{N_t} u_i^t \omega_i^t \tag{C.3}$$

Source tensors and nodal force densities are associated respectively to each element and node. $N_s$ and $N_t$ are the number of elements or nodes in 2D case. $u_i^s$ and $u_i^t$ are the degrees of freedom associated with the $i^{th}$ node or element. $\omega_i^s$ and $\omega_i^t$ are the shape functions on $i^{th}$ node or element. By applying the classical Ritz-Galerkin method, the test function $u'$ is naturally chosen to be the same as the shape function in the target mesh $u' = \{\omega_i^t\}_{i=1}^{N_t}$. This leads to a linear system as follows:

$$[A][U^s] = [B][U^t] \tag{C.4}$$

where $[U^s]$ and $[U^t]$ are degrees of freedom vectors in source and target meshes. $[A]_{N_t \times N_s}$ and $[B]_{N_t \times N_t}$ are two matrices with their elements defined in (C.5).

$$A_{i,j} = \int_{\mathcal{D}} \omega_i^t \omega_j^s \, \mathrm{d}\tau \quad \text{and} \quad B_{i,j} = \int_{\mathcal{D}} \omega_i^t \omega_j^t \, \mathrm{d}\tau \tag{C.5}$$

### C.0.3 Integration of projection to the modeling chain

The weakly coupled magneto-elastic problem is solved using a sequential approach: magnetic resolution is followed by mechanical resolution. The domain of magnetic problem is noted as $\mathcal{D}_{mag}$, including air and iron areas. $\mathcal{D}_{mec}$ is defined as a subdomain of $\mathcal{D}_{mag}$ ($\mathcal{D}_{mec} \subset \mathcal{D}_{mag}$), containing only the iron part, dedicated to the mechanical resolution.

### Source tensor projection

The idea is to unify the computation process of magnetostriction and magnetic force induced deformation into a single modeling chain, from magnetic resolution, source tensor computation, nodal force computation and finally to the mechanical resolution. Magnetostriction strain tensor is deduced from SMSM. Magnetic force is first expressed in its tensorial form, Maxwell tensor. These source tensors can be then both transformed into nodal forces. If any mesh to mesh projection is needed from magnetic part to mechanical part, choices are the projection of source tensors and projection of force densities.

In 2D modeling, source tensors contain four components (three components if the tensor is symmetric), while force density vector contains only two. It is believed that these source tensors contain more information than their associated force density vectors. Data projections carried out at the source tensor stage is introduced as follows. Given $\boldsymbol{\epsilon}_\mu^s, \boldsymbol{T}^s \in V_1$, to find $\boldsymbol{\epsilon}_\mu^t, \boldsymbol{T}^t \in V_2$, such that:

$$\int_{\mathcal{D}_{mec}} \boldsymbol{\epsilon}_\mu^s : \boldsymbol{\epsilon}_\mu{}' \,\mathrm{d}\tau = \int_{\mathcal{D}_{mec}} \boldsymbol{\epsilon}_\mu^t : \boldsymbol{\epsilon}_\mu{}' \,\mathrm{d}\tau, \quad \forall \boldsymbol{\epsilon}_\mu{}' \in V_2. \tag{C.6}$$

$$\int_{\mathcal{D}_{mag}} \boldsymbol{T}^s : \boldsymbol{T}' \,\mathrm{d}\tau = \int_{\mathcal{D}_{mag}} \boldsymbol{T}^t : \boldsymbol{T}' \,\mathrm{d}\tau, \quad \forall \boldsymbol{T}' \in V_2. \tag{C.7}$$

Projections of free magnetostriction strain tensor and Maxwell tensor are carried out using the formulation (C.2). As Maxwell tensor is non-null in the air, the integration domain for (C.7) is carried out in $\mathcal{D}_{mag}$. This is different from the free magnetostriction strain, which exists only in the iron part. Force densities are then computed in the target mesh. The main procedure is summarised in Fig.C.1.

### Force density projection

Magnetic forces are often computed through virtual power principle (VPP) [Ren et Razek, 1992]. In this technique, nodal forces are directly derive from the magnetic energy.

Projections of force density in magneto-elastic coupled problems are also carried out for comparison reasons. Nodal forces are computed in the source mesh for both magnetostriction and magnetic forces. As nodal forces are concentrated only at the nodes, these forces are first transformed into a field of force density before projection, using the following formulation:

$$[S][f] = [F] \quad \text{with} \quad S_{i,j} = \int_{\mathcal{D}_{mec}} \omega_i^s \omega_j^s \,\mathrm{d}\tau \tag{C.8}$$

where $[F]$ and $[f]$ are respectively the array of nodal force and the degrees of freedom of the force density. As the matrix $[S]$ is diagonal, force density is obtained by dividing the nodal force by its associated surface of each node. Projection of force density is then carried out using formulation (C.1). Given $\vec{f}^s \in V_1$, to find $\vec{f}^t \in V_2$, such that:

$$\int_{\mathcal{D}_{mec}} \vec{f}^s \cdot \vec{f}' \,\mathrm{d}\tau = \int_{\mathcal{D}_{mec}} \vec{f}^t \cdot \vec{f}' \,\mathrm{d}\tau, \quad \forall \vec{f}' \in V_2. \tag{C.9}$$

The main procedure is summarised in Fig.C.2.

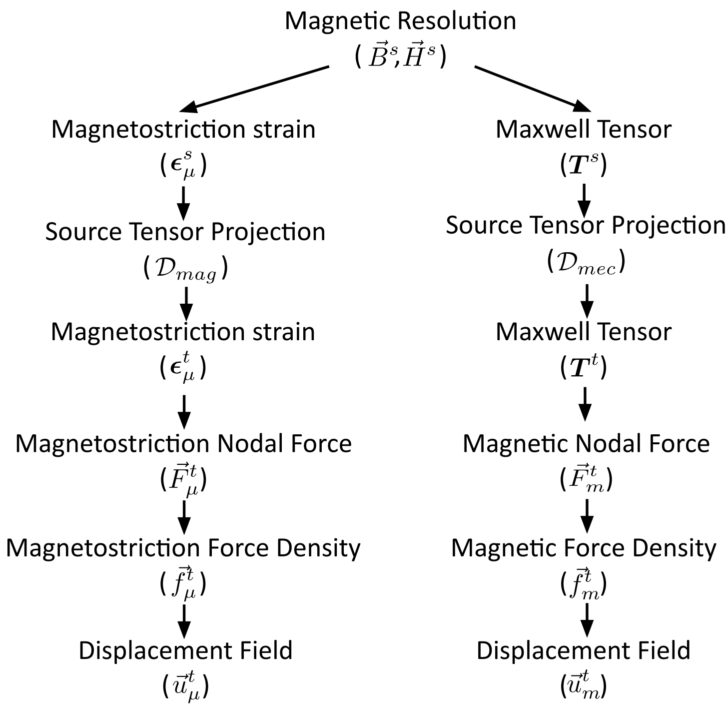


**Figure C.1:** Strategy of source tensor projection

### C.0.4 Application and results

#### Academic example

The proposed projection formulations are first applied on an academic example, in order to compare source tensor and force density projections. A ferromagnetic ring made of FeSi is submitted to a horizontal magnetic field defined by magnetic potential $\phi$ boundary conditions.

Parameters of SMSM are chosen to reproduce the ideal isotropic FeSi behaviors defined in [Liu *et al.*, 2015a]. Fig.C.3 gives the distribution of the magnetic force density and magnetostriction equivalent force density computed on a reference well refined mesh. Source tensors and force densities are then computed in source mesh and projected to the target mesh, leading to static mechanical resolution. The fields of displacement due to magnetostriction and magnetic force are finally obtained.

Two meshes are considered: a well-refined mesh M1 (144 K elements) and a relatively coarser mesh M2 (36 K elements). M1 and M2 are used respectively as source mesh and target mesh. In order to eliminate the influence of mesh sensitivity, tests are carried out using the same mesh (M1 or M2) without data projection. Similar magnetic and mechanical field are observed on the two meshes.

Displacements of the outer border on the right side of the FeSi ring are shown in Fig.C.4-C.5. Fig.C.4 and Fig.C.5 are dedicated respectively to magnetostriction and magnetic force induced displacements.

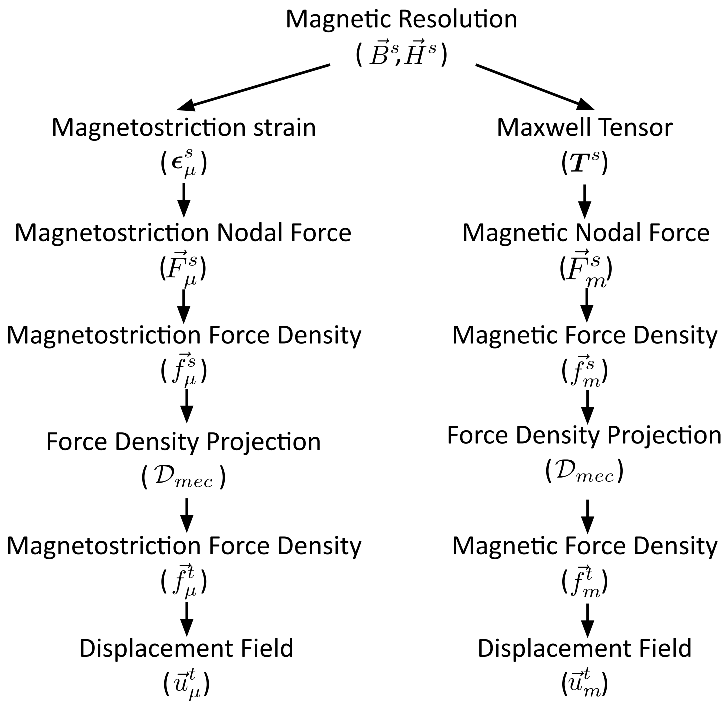


**Figure C.2:** Strategy of force density projection

Comparisons are made between three different approaches: the reference, a coarser mesh M2 for the mechanical resolution with the source tensor projection, as well as the classical force density projection. The reference is defined using the same well-refined mesh M1 without projections, in order to minimize the discretization error and to eliminate projection error. For magnetostriction induced displacement, source tensor projection shows great efficiency over force density projection. For displacements due to magnetic forces, source tensor projection gives slightly better projection results.

The efficiency of the source tensor projection is different for forces of different physical natures. This can possibly be explained as follows: Free magnetostriction strain exists only in the ferromagnetic material, and is null in the air. However, Maxwell tensor exists both in the air and ferromagnetic material. Magnetic force mainly depends on the discontinuity of the Maxwell tensor on the air-iron interface. This makes magnetic force extremely sensitive to the change of mesh (data projection), which modifies the discontinuity on the interface.

### Multi-layer power transformer

In order to verify the efficiency of the source tensor projection, another example is proposed: multi-layer ($f_1 = f_2 = 0.5$) GO FeSi EI-core, under Format-A. In this case, the effect of magnetic forces is negligible because there is no air-gap in the modeling. The efficiency of source tensor projection is only verified for magnetostriction.

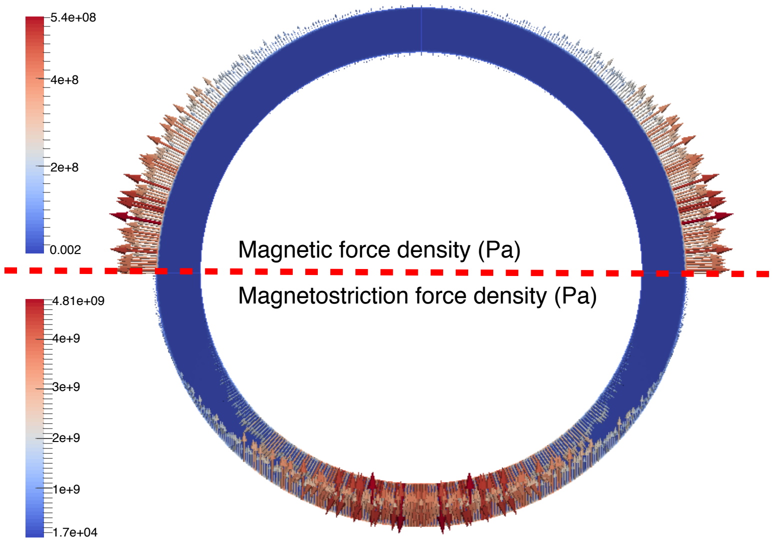


**Figure C.3:** Magnetic force density (top); Magnetostriction induced force density (bottom)

Sinusoidal current excitation is set in central limb of the power transformer. Free magnetostriction strain tensor or magnetostriction induced forces are then projected to the target mesh for dynamic mechanical resolution. Displacements at three representative locations are plotted as function of time (Fig.C.6-C.7).

Excitation current is set in the center coil to 400Hz and 200At. By imposing the boundary condition, a fixed point is set as reference in the center of the transformer. P1, P2 and P3 are selected as measurement points. The same comparison procedure as in previous example is applied with M1 (56 K elements) and M2 (14 K elements). Displacements in directions X and Y of the point P1, P2 and P3 are shown in Fig.C.6-C.7. This numerical example shows better performance of source tensor projection over force density projection in case of magnetostriction induced displacement. This may be explained by the richer information that source tensor contains then the force density.

As a conclusion: for magnetostriction, great efficiency of source tensor projection over force density projection is proved in both static and dynamic magneto-elastic problems; for magnetic force, overall better results are observed using source tensor projection. This may be explained by the fact that the magnetostriction nodal force naturally makes the force density appear from the tensor $\nabla\vec{u}\cdot(\mathbb{C}:\epsilon_\mu)$, which is deduced from $\vec{u}\cdot(\vec{\nabla}\cdot(\mathbb{C}:\epsilon_\mu))$. ($\vec{u}$ is a test function)

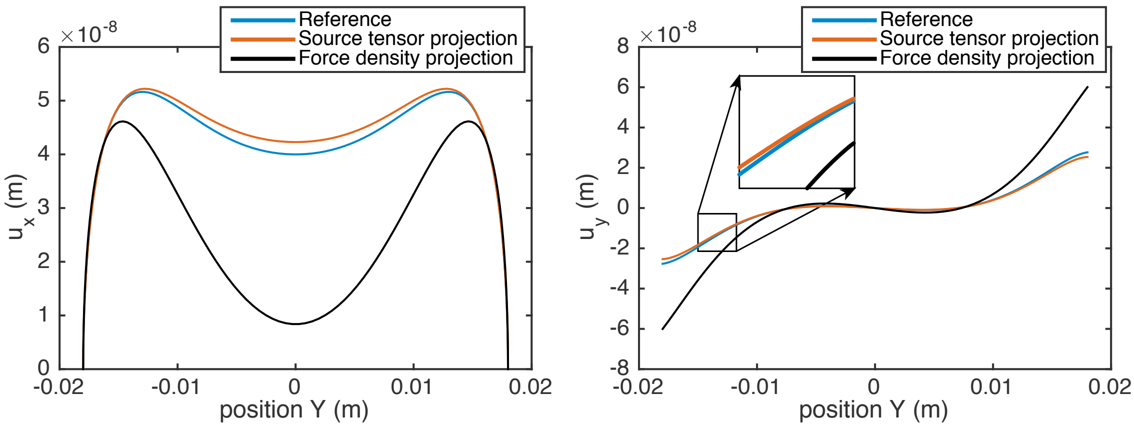


**Figure C.4:** Displacements due to magnetostriction in direction X (left) and Y (right).

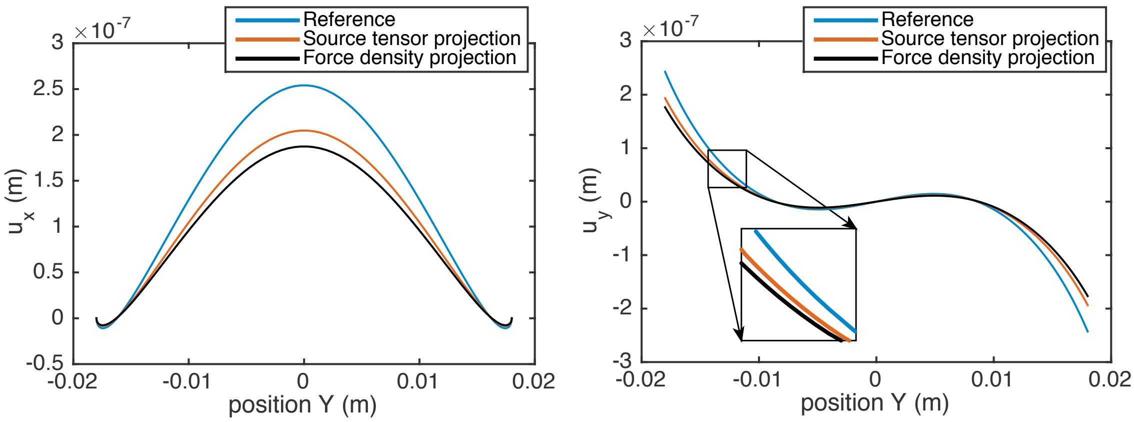


**Figure C.5:** Displacements due to magnetic force in direction X (left) and Y (right).

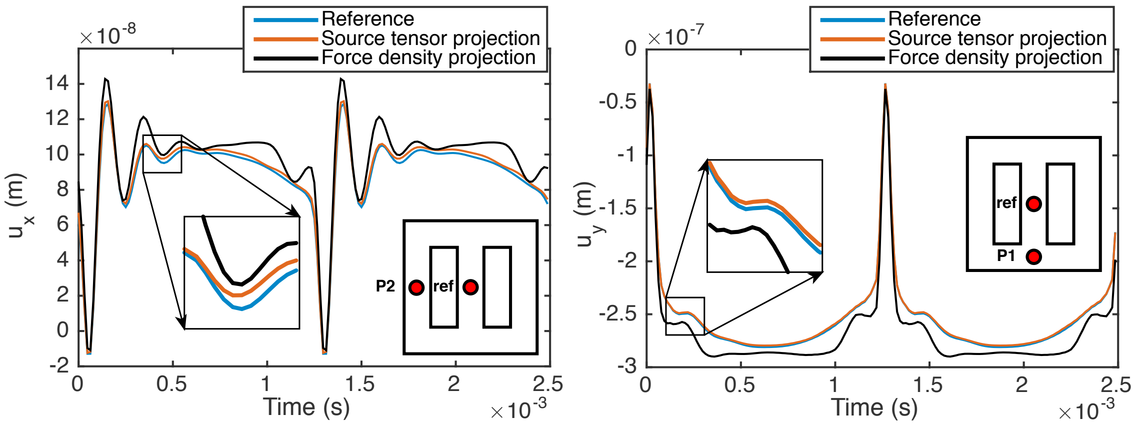


**Figure C.6:** Displacements in direction X as a function of time at P2 (left); Displacements in direction Y as a function of time at P1 (right)

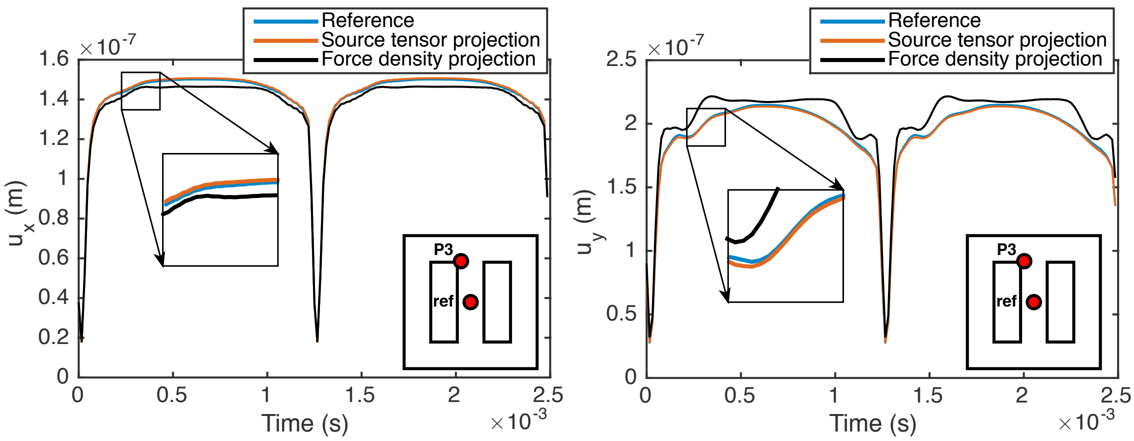


**Figure C.7:** Displacements in direction X (left) and Y (right) as a function of time at P3

# Appendix D

# Core vibration under DC bias

Although power transformers are normally designed to operate under sinusoidal excitation, in reality, a direct current (DC) component may be superposed in primary or secondary windings. For example, the equipment failure or conventional maintenance may lead to a DC component in the electrical power transmission system [Jiayin *et al.*, 2013]. In other cases, if a power transformer is connected with an AC/DC converter as the loading, the secondary coils or the power transformer contain a DC component which can not be found in the primary coils. This DC component leads to half-cycle saturation, which increases the losses, creates more harmonics, and generates more vibrations and noise [Li *et al.*, 2013]. These effects need to be taken into consideration for the power transformer design. Therefore, a good comprehension of power transformer behavior under DC bias becomes crustial for its optimized design.

Here we chose an '8' core made of NO FeSi. For simplification reasons, the three-phase power transformer is excited here only by a central coil imposing a sinusoidal flux which leads to a maximum induction of $B = 1.4$T. Amplitude of the current in central coils and core displacement as a function of time are then solved. A series of simulations are carried out with a DC component, in addition to the sinusoidal flux. DC component of the magnetic flux is set as 0%, 10%, 20% and 30% of the maximum flux. With the finite element resolution, this corresponds respectively to DC current bias of 0At, 18 At, 26 At and 108 At in the secondary coils. Excitation current in primary coils and spectrum of displacement amplitude at particular point of the core are given in Fig.D.1-D.2.

With the presence of DC component, the transformer core is highly saturated in the first half period. As the DC component rises, the current in coils becomes more distorted with harmonics. With a DC bias at $108At$, the excitation current rises dramatically in amplitude. In terms of core distortion, magnetic saturation of the first half period creates relatively large magnetostriction, which generally rises the amplitude of displacements of all harmonics. Core distortion is much higher in the the half period than it in the second half period, which induces odd harmonics of the vibration. Harmonics at higher frequency are found with the increase of DC bias, which may be close to resonance.

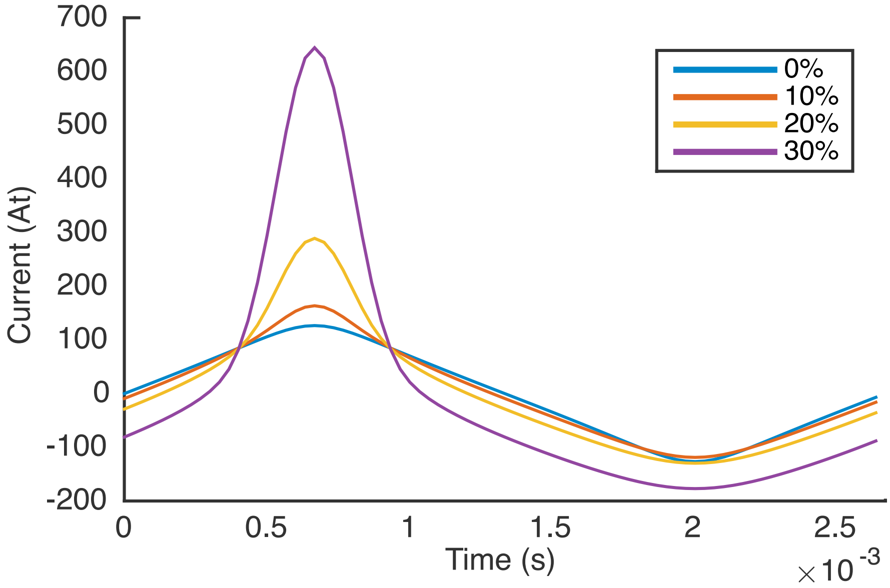


**Figure D.1:** Excitation current in primary coils

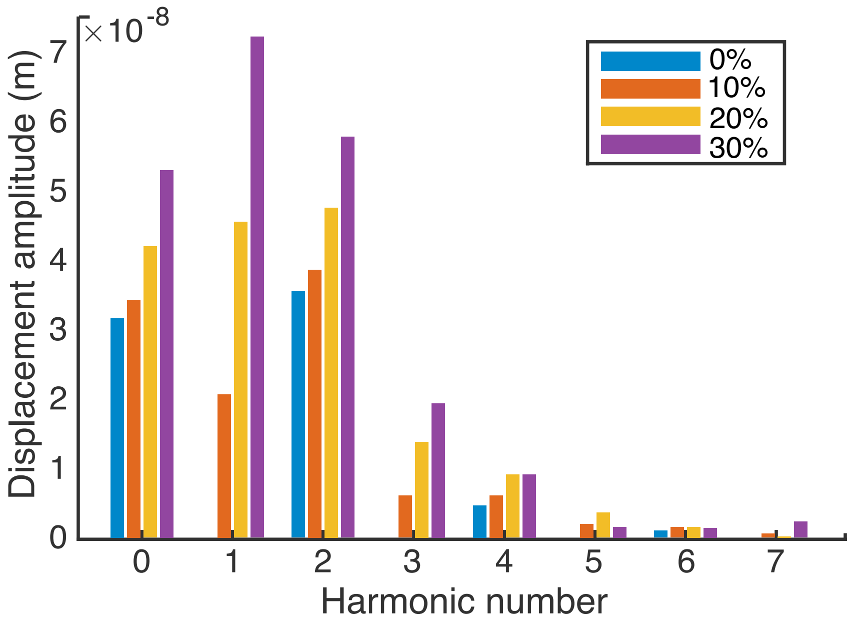


**Figure D.2:** Spectrum of displacement amplitude at particular point of the core

# Bibliography


[Adly et Mayergoyz, 1996] ADLY, A. et MAYERGOYZ, I. (1996). Magnetostriction simulation using anisotropic vector Preisach-type models. *IEEE Transactions on Magnetics*, 32(5):4773–4775.

[Anjanappa et Bi, 1917] ANJANAPPA, M. et BI, J. (1917). Modelling, design and control of embedded terfenol-d actuator. *In Proc. SPIE*, volume 2, page 908.

[Annakkage *et al.*, 2000] ANNAKKAGE, U., MCLAREN, P., DIRKS, E., JAYASINGHE, R. et PARKER, A. (2000). A current transformer model based on the Jiles-Atherton theory of ferromagnetic hysteresis. *IEEE Transactions on Power Delivery*, 15(1):57–61.

[Appino *et al.*, 2016] APPINO, C., KHAN, M., DE LA BARRIERE, O., RAGUSA, C. et FIORILLO, F. (2016). Alternating and rotational losses up to magnetic saturation in non-oriented steel sheets. *IEEE Transactions on Magnetics*, 52(5):1–4.

[Atherton et D.L., 1990] ATHERTON, D. J. et D.L. (1990). Theory of ferromagnetic hysteresis erratum. *Journal of Magnetism and Magnetic Materials*, 92(2):289.

[Aydin *et al.*, 2017] AYDIN, U., RASILO, P., MARTIN, F., SINGH, D., DANIEL, L., BELAHCEN, A., REKIK, M., HUBERT, O., KOUHIA, R. et ARKKIO, A. (2017). Magneto-mechanical modeling of electrical steel sheets. *Journal of Magnetism and Magnetic Materials*, 439:82–90.

[Aydin *et al.*, 2016] AYDIN, U., RASILO, P., SINGH, D., LEHIKOINEN, A., BELAHCEN, A. et ARKKIO, A. (2016). Coupled magneto-mechanical analysis of iron sheets under biaxial stress. *IEEE Transactions on Magnetics*, 52(3):1–4.

[Azuma et Hasegawa, 2008] AZUMA, D. et HASEGAWA, R. (2008). Audible noise from amorphous metal and silicon steel-based transformer core. *IEEE Transactions on Magnetics*, 44(11):4104–4106.

[Baghel *et al.*, 2015] BAGHEL, A., GUPTA, A., CHWASTEK, K. et KULKARNI, S. (2015). Comprehensive modelling of dynamic hysteresis loops in the rolling and transverse directions for transformer laminations. *Physica B: Condensed Matter*, 462:86–92.

[Baghel *et al.*, 2016] BAGHEL, A., SAI RAM, B., CHWASTEK, K., DANIEL, L. et KULKARNI, S. (2016). Hysteresis modelling of GO laminations for arbitrary in-plane directions taking into account the dynamics of orthogonal domain walls. *Journal of Magnetism and Magnetic Materials*, pages 1–7.

[Balehosur *et al.*, 2010] BALEHOSUR, M. B., MARKETOS, P., MOSES, A. J. et VINCENT, J. N. (2010). Packet-to-packet variation of flux density in a three-phase, three-limb power transformer core. *IEEE Transactions on Magnetics*, 46(2):642–645.

[Barre *et al.*, 2006] BARRE, O., BROCHET, P. et HECQUET, M. (2006). Experimental validation of magnetic and electric local force formulations associated to energy principle. *IEEE Transactions on Magnetics*, 42(4):1475–1478.

[Belahcen, 2005] BELAHCEN, A. (2005). Magnetoelastic coupling in rotating electrical machines. *IEEE Transactions on Magnetics*, 41(5):1624–1627.

[Belahcen *et al.*, 2015] BELAHCEN, A., SINGH, D., RASILO, P., MARTIN, F., GHALAMESTANI, S. G. et VANDEVELDE, L. (2015). Anisotropic and strain-dependent model of magnetostriction in electrical steel sheets. *IEEE Transactions on Magnetics*, 51(3):1–4.

[Bergqvist, 1996] BERGQVIST, A. (1996). A simple vector generalization of the Jiles-Atherton model of hysteresis. *IEEE Transactions on Magnetics*, 32(5):4213–4215.

[Bernard et Daniel, 2015] BERNARD, L. et DANIEL, L. (2015). Effect of stress on magnetic hysteresis losses in a switched reluctance motor: application to stator and rotor shrink-fitting. *IEEE Transactions on Magnetics*, 51(9):1–1.

[Bernard *et al.*, 2011] BERNARD, L., MININGER, X., DANIEL, L., KREBS, G., BOUILLAULT, F. et GABSI, M. (2011). Effect of stress on switched reluctance motors: a magneto-elastic finite-element approach based on multiscale constitutive laws. *IEEE Transactions on Magnetics*, 47(9):2171–2178.

[Besbes *et al.*, 1996] BESBES, M., REN, Z. et RAZEK, A. (1996). Finite element analysis of magneto-mechanical coupled phenomena in magnetostrictive materials. *IEEE Transactions on Magnetics*, 32(3):2–5.

[Betanda et Olivier, 2015] BETANDA, A. et OLIVIER, Y. B. (2015). *Formation de la l'hypertexture Cube {100}< 001> dans les alliages cubiques à faces centrées*. Thèse de doctorat, Paris Saclay.

[Bitter, 1932] BITTER, F. (1932). Experiments on the nature of ferromagnetism. *Physical Review*, 41(4):507.

[Bossavit, 1988] BOSSAVIT, A. (1988). Whitney forms: a class of finite elements for three-dimensional computations in electromagnetism. *IEE Proceedings A Physical*

*Science, Measurement and Instrumentation, Management and Education, Reviews*, 135:493.

[Bossavit, 2015] BOSSAVIT, A. (2015). Un tenseur de maxwell non-linéaire et symétrique. *NUMELEC 2015, Actes, 8e Conférence Européenne sur les méthodes numériques en Électromagnétisme (3-5 Juin, Saint-Nazaire), IUT de Saint-Nazaire*, pages 3–4.

[Bouillault, 1991] BOUILLAULT, F. (1991). Contribution à la modélisation numérique de systèmes électromagnétiques régis par les équations de la mgnétodynamique. *Habilitation à diriger les recherches*.

[Bouissou et Piriou, 1994] BOUISSOU, S. et PIRIOU, F. (1994). Study of 3D formulations to model electromagnetic devices. *IEEE Transactions on Magnetics*, 30(5):3228–3231.

[Bozorth, 1993] BOZORTH, R. M. (1993). Ferromagnetism. *Ferromagnetism, by Richard M. Bozorth, pp. 992. ISBN 0-7803-1032-2. Wiley-VCH, August 1993.*, 1.

[Brailsford, 1939] BRAILSFORD, F. (1939). Alternating hysteresis loss in electrical sheet steels. *Journal of the Institution of Electrical Engineers*, 84(507):399–407.

[Buiron *et al.*, 1999] BUIRON, N., HIRSINGER, L. et BILLARDON, R. (1999). A multi-scale model for magneto-elastic couplings. *Le Journal de Physique IV*, 9(PR9):Pr9–187.

[Burkert *et al.*, 2004] BURKERT, T., NORDSTRÖM, L., ERIKSSON, O. et HEINONEN, O. (2004). Giant magnetic anisotropy in tetragonal FeCo alloys. *Physical review letters*, 93(2):27203.

[Buvat, 2000] BUVAT, C. (2000). *thesis*. Thèse de doctorat, University Paris 6.

[Cetin, 2014] CETIN, G. (2014). Etude d'une nouvelle solution de feni pour les transformateurs embarqués. Mémoire de D.E.A., LMT-Cachan, France.

[Chang *et al.*, 2011] CHANG, Y.-H., HSU, C.-H., CHU, H.-L. et TSENG, C.-P. (2011). Magnetomechanical vibrations of three-phase three-leg transformer with different amorphous-cored structures. *IEEE Transactions on Magnetics*, 47(10):2780–2783.

[Cheng *et al.*, 2015] CHENG, S.-J., LIU, J.-J., CHANG, Y.-H., FU, C.-M., HSU, C.-H., LEE, C.-Y. et CHANG, C.-W. (2015). Correlation of magnetostriction variation on magnetic loss and noise for power transformer. *Journal of Applied Physics*, 117(17): 17E716.

[Ciarlet, 1988] CIARLET, P. G. (1988). Mathematical elasticity. Vol. I, volume 20 of Studies in Mathematics and its Applications.

[COUDERCHON, 1994] COUDERCHON, G. (1994). Alliages fer-nickel et fer-cobalt: Propriétés magnétiques. *Techniques de l'ingénieur. Génie électrique*, 2(D2130):2130–1.

[Coulomb, 1983] COULOMB, J. L. (1983). A methodology for the determination of global electromechanical quantities from a finite element analysis and its application to the evaluation of magnetic forces, torques and stiffness. *IEEE Transactions on Magnetics*, 19(19):2514.

[Cullity et Graham, 2009] CULLITY, B. D. et GRAHAM, C. D. (2009). Magnetostriction and the Effects of Stress. *In Introduction to Magnetic Materials*, pages 241–273. John Wiley & Sons, Inc., Hoboken, NJ, USA.

[Daniel, 2003] DANIEL, L. (2003). *Modélisation multi-échelle du comportement magnéto-mécanique des matériaux ferromagnétiques texturés*. Thèse de doctorat, École normale supérieure de Cachan-ENS Cachan.

[Daniel, 2013] DANIEL, L. (2013). An analytical model for the effect of multiaxial stress on the magnetic susceptibility of ferromagnetic materials. *IEEE Transactions on Magnetics*, 49(5):2037–2040.

[Daniel *et al.*, 2008] DANIEL, L., HUBERT, O., BUIRON, N. et BILLARDON, R. (2008). Reversible magneto-elastic behavior: a multiscale approach. *Journal of the Mechanics and Physics of Solids*, 56(3):1018–1042.

[Daniel *et al.*, 2015] DANIEL, L., HUBERT, O. et REKIK, M. (2015). A simplified 3D constitutive law for magnetomechanical behavior. *IEEE Transactions on Magnetics*, 51(3):1–4.

[Daniel *et al.*, 2014] DANIEL, L., REKIK, M. et HUBERT, O. (2014). A multiscale model for magneto-elastic behaviour including hysteresis effects. *Archive of Applied Mechanics*, 84(9-11):1307–1323.

[Delaere *et al.*, 2000] DELAERE, K., HEYLEN, W., HAMEYER, K. et BELMANS, R. (2000). Local magnetostriction forces for finite element analysis. *IEEE Transactions on Magnetics*, 36(5):3115–3118.

[Della Torre *et al.*, 2006a] DELLA TORRE, E., PINZAGLIA, E. et CARDELLI, E. (2006a). Vector modeling - Part I: Generalized hysteresis model. *Physica B: Condensed Matter*, 372(1-2):111–114.

[Della Torre *et al.*, 2006b] DELLA TORRE, E., PINZAGLIA, E. et CARDELLI, E. (2006b). Vector modeling—Part II: Ellipsoidal vector hysteresis model. Numerical application to a 2D case. *Physica B: Condensed Matter*, 372(1-2):115–119.

[Demian *et al.*, 2012] DEMIAN, C., CASSORET, B., BRUDNY, J.-f. et BELGRAND, T. (2012). Electrical steel sheets : impact on induction machine magnetic noise. *IEEE Transactions on Magnetics*, 48(4):1409–1412.

[Dlala *et al.*, 2010] DLALA, E., BELAHCEN, A., FONTEYN, K. et BELKASIM, M. (2010). Improving loss properties of the mayergoyz vector hysteresis model. *IEEE Transactions on Magnetics*, 46(3):918–924.

[Du et Liu, 2014] DU, B. et LIU, D. (2014). Dynamic behavior of magnetostriction-induced vibration and noise of amorphous alloy cores. *IEEE Transactions on Magnetics*, 9464(c):1–1.

[Du Trémolet de Lacheisserie, 1993a] Du Trémolet de LACHEISSERIE, E. (1993a). *Magnetostriction: theory and applications of magnetoelasticity*. CRC press.

[Du Trémolet de Lacheisserie, 1993b] Du Trémolet de LACHEISSERIE, E. (1993b). *Magnetostriction, Theory and Applications of Magnetoelasticity*. CRC Press.

[Du Trémolet de Lacheisserie, 2002] Du Trémolet de LACHEISSERIE, E. (2002). *Magnetism - Fundamentals, Materials and Applications*. Springer.

[Ebrahimi et Moses, 1991] EBRAHIMI, a. et MOSES, a. J. (1991). Correlation between normal flux transfer from lamination to lamination during the magnetization process with static domain structures in grain oriented 3% silicon iron. *Journal of Applied Physics*, 70:6265.

[Enokizono *et al.*, 1993] ENOKIZONO, M., TODAKA, T., KANAO, S., SIEVERT, J., ENOKIMM, M., TODAKA, T., KANAO, S., OITA, D. et SIEVERT, J. (1993). Two-dimensional magnetic properties of silicon steel sheet subjected to a rotating field. *IEEE Transactions on Magnetics*, 29(6):3550–3552.

[Ertl et Landes, 2007] ERTL, M. et LANDES, H. (2007). Investigation of load noise generation of large power transformer by means of coupled 3D FEM analysis. *COMPEL*, 26(3):788 – 799.

[Fall, 2017] FALL, M. D. (2017). *Mesure et modélisation multiéchelle du comportement thermo-magnéto-mécanique des alliages à mémoire de forme*. Thèse de doctorat, LMT-Cachan, France.

[Fiorillo et Rietto, 1990] FIORILLO, F. et RIETTO, A. (1990). Rotational and alternating energy loss vs. magnetizing frequency in sife laminations. *Journal of Magnetism and Magnetic Materials*, 83(1-3):402–404.

[Flemisch *et al.*, 2004] FLEMISCH, B., MADAY, Y., RAPETTI, F. et WOHLMUTH, B. I. (2004). Coupling scalar and vector potentials on nonmatching grids for eddy currents in a moving conductor. *Journal of Computational and Applied Mathematics*, 168(1-2):191–205.

[Fonteyn *et al.*, 2010] FONTEYN, K., BELAHCEN, A., KOUHIA, R., RASILO, P. et ARKKIO, A. (2010). FEM for directly coupled magneto-mechanical phenomena in electrical machines. *IEEE Transactions on Magnetics*, 46(8):2923–2926.

[Frank et Ferman, 1965] FRANK, R. C. et FERMAN, J. W. (1965). Magnetomechanical damping in iron-silicon alloys. *Journal of Applied Physics*, 36(7):2235.

[Galopin *et al.*, 2008] GALOPIN, N., MININGER, X., BOUILLAULT, F. et DANIEL, L. (2008). Finite element modeling of magnetoelectric sensors. *IEEE Transactions on Magnetics*, 44(6):834–837.

[Ganet *et al.*, 2013] GANET, F., HUBERT, O., MININGER, X., BOUILLAULT, F. et BERNARD, L. (2013). Application of the magneto-mechanical coupling to the prediction of deformation of non-oriented FeSi based transformers. *Proceedings of the Conference on the Computation of Electromagnetic Fields*, 1(1):2–5.

[Gao *et al.*, 2011a] GAO, Y., MURAMATSU, K., HATIM, M. J. et NAGATA, M. (2011a). The effect of laminated structure on coupled magnetic field and mechanical analyses of iron core and its homogenization technique. volume 47, pages 1358–1361. IEEE.

[Gao *et al.*, 2011b] GAO, Y., NAGATA, M., MURAMATSU, K., FUJIWARA, K., ISHIHARA, Y. et FUKUCHI, S. (2011b). Noise reduction of a three-phase reactor by optimization of gaps between cores considering electromagnetism and magnetostriction. *IEEE Transactions on Magnetics*, 47(10):2772–2775.

[Geuzaine *et al.*, 1999] GEUZAINE, C., MEYS, B., HENROTTE, F., DULAR, P. et LEGROS, W. (1999). A Galerkin projection method for mixed finite elements. *IEEE Transactions on Magnetics*, 35(3).

[Ghalamestani *et al.*, 2014] GHALAMESTANI, S. G., VANDEVELDE, L. et MELKEBEEK, J. (2014). Identification of transformer core vibrations and the effect of third harmonic in the electricity grid. *International Journal of Electrical, Computer, Energetic, Electronic and Communication Engineering*, 8(6):871–874.

[Goto *et al.*, 1983] GOTO, M., TANGE, H., KAMIMORI, T. et OKUMA, K. (1983). Saturation magnetostriction of some (FeCo)-metalloid-compounds and -amorphous alloys. *Journal of Magnetism and Magnetic Materials*, 31-34(PART 3):1601–1602.

[Gourdin, 1998] GOURDIN, C. (1998). *Identification et modélisation du comportement électromagnétique de structures ferromagnétiques*. Thèse de doctorat, Université Pierre et Marie Curie, France.

[Gourdin *et al.*, 1998] GOURDIN, C., HIRSINGER, L., BARBIER, G. et BILLARDON, R. (1998). Experimental identification of the coupling between the anhysteretic magnetic and magnetostrictive behaviours. *Journal of Magnetism and Magnetic Materials*, 177: 201–202.

[Hantila *et al.*, 2000] HANTILA, F., PREDA, G. et VASILIU, M. (2000). Polarization method for static fields. *IEEE Transactions on Magnetics*, 36(4):672–675.

[Hauser, 1994] HAUSER, H. (1994). Energetic model of ferromagnetic hysteresis. *Journal of Applied Physics*, 75(5):2584–2597.

[Hauser *et al.*, 2009] HAUSER, H., MELIKHOV, Y. et JILES, D. C. (2009). Examination of the equivalence of ferromagnetic hysteresis models describing the dependence of magnetization on magnetic field and stress. *IEEE Transactions on Magnetics*, 45(4): 1940–1949.

[Hecht, 2012] HECHT, F. (2012). New development in freefem ++. *Journal of Numerical Mathematics*, 20(3):251–265.

[Henrotte, 2004] HENROTTE, F. (2004). Technical article handbook for the computation of electromagnetic forces in a continuous medium. *Int. Compumag Society Newsletter*, 24(2):3–9.

[Hihat *et al.*, 2011] HIHAT, N., NAPIERALSKA-JUSZCZAK, E., LECOINTE, J. P., SYKULSKI, J. K. et KOMEZA, K. (2011). Equivalent permeability of step-lap joints of transformer cores: Computational and experimental considerations. *IEEE Transactions on Magnetics*, 47(1 PART 2):244–251.

[Hilgert *et al.*, 2007] HILGERT, T., VANDEVELDE, L. et MELKEBEEK, J. (2007). Neural-network-based model for dynamic hysteresis in the magnetostriction of electrical steel under sinusoidal induction. *IEEE Transactions on Magnetics*, 43(8):3462–3466.

[Hilgert *et al.*, 2008] HILGERT, T., VANDEVELDE, L. et MELKEBEEK, J. (2008). Comparison of magnetostriction models for use in calculations of vibrations in magnetic cores. *IEEE Transactions on Magnetics*, 44(6):874–877.

[Hirsinger et Billardon, 1995] HIRSINGER, L. et BILLARDON, R. (1995). Magneto-elastic finite element analysis including magnetic forces and magnetostriction effects. *IEEE Transactions on Magnetics*, 31(3).

[Hong *et al.*, 1994] HONG, S., KIM, D., JUNG, H. et WON, J. (1994). Vector hysteresis model for unoriented magnetic materials. *IEEE Transactions on Magnetics*, 30(5): 3371–3374.

[Hsu *et al.*, 2012] HSU, C.-H., CHANG, Y.-H., LEE, C.-Y., YAO, C.-S., HE, Y.-L., CHU, H.-L., CHANG, C.-W. et CHAN, W.-S. (2012). Effects of magnetomechanical vibrations and bending stresses on three-phase three-leg transformers with amorphous cores. *Journal of Applied Physics*, 111(7).

[Hsu *et al.*, 2015a] HSU, C. H., HSIEH, M. F., FU, C. M. et HUANG, Y. M. (2015a). Effects of Multicore Structure on Magnetic Losses and Magnetomechanical Vibration at High Frequencies. *IEEE Transactions on Magnetics*, 51(11):3–6.

[Hsu *et al.*, 2014] HSU, C.-H., LEE, C.-Y., CHENG, S.-J., FU, C.-M. et CHANG, C.-W. (2014). Effects of magnetostriction and magnetic reluctances on magnetic properties of distribution transformers. *Journal of Applied Physics*, 115(17):17E718.

[Hsu *et al.*, 2015b] HSU, C.-h., LEE, S.-l., LIN, C.-c., LIU, C.-s., CHANG, S.-y., HSIEH, M.-f., HUANG, Y.-m. et FU, C.-m. (2015b). Reduction of vibration and sound-level for a single-phase power transformer with Large capacity. *IEEE Transactions on Magnetics*, 51(11):1–4.

[Hsu *et al.*, 2015c] HSU, C. H., LIU, J. J., FU, C. M., HUANG, Y. M., CHANG, C. W. et CHENG, S. J. (2015c). Suppressing magneto-mechanical vibrations and noise in magnetostriction variation for three-phase power transformers. *Journal of Applied Physics*, 117(17).

[Hubert et Schäfer, 1998] HUBERT, A. et SCHÄFER, R. (1998). Magnetic domains: the analysis of magnetic microstructure. *Magnetic domains: the analysis of magnetic microestructure*.

[Hubert et Schäfer, 2008] HUBERT, A. et SCHÄFER, R. (2008). *Magnetic domains: the analysis of magnetic microstructures*. Springer Science & Business Media.

[Hubert *et al.*, 2005] HUBERT, O., CHAABANE, M., JUMEL, J., MAUREL, V., ALVES, F., BENSALAH, A., BESBES, M., AZOUM, K., DANIEL, L. et BOUILLAULT, F. (2005). A new experimental set-up for the characterisation of magneto-mechanical behaviour of materials submitted to biaxial stresses. application to fe-co alloys. *Przeglad Elektrotechniczny*, 81:19 – 23.

[Hubert et Daniel, 2006] HUBERT, O. et DANIEL, L. (2006). Effect of plastic straining on magnetostriction of ferromagnetic polycrystals experiments and multiscale modeling. *Journal of Magnetism and Magnetic Materials*, 304:489–491.

[Hubert et Daniel, 2008] HUBERT, O. et DANIEL, L. (2008). Multiscale modeling of the magneto-mechanical behavior of grain-oriented silicon steels. *Journal of Magnetism and Magnetic Materials*, 320(7):1412–1422.

[Hubert et Daniel, 2011] HUBERT, O. et DANIEL, L. (2011). Energetical and multiscale approaches for the definition of an equivalent stress for magneto-elastic couplings. *Journal of Magnetism and Magnetic Materials*, 323(13):1766–1781.

[Hubert *et al.*, 2003] HUBERT, O., DANIEL, L. et BILLARDON, R. (2003). Experimental analysis of the magnetoelastic anisotropy of a non-oriented silicon iron alloy. *Journal of Magnetism and Magnetic Materials*, 254:352 – 354.

[Hubert et Rizzo, 2008] HUBERT, O. et RIZZO, K.-J. (2008). Anhysteretic and dynamic piezomagnetic behavior of a low carbon steel. *Journal of Magnetism and Magnetic Materials*, 320(20):979–982.

[Jang et Choi, 2012] JANG, P. et CHOI, G. (2012). Acoustic noise characteristics and magnetostriction of Fe-Si powder cores. *IEEE Transactions on Magnetics*, 48(4): 1549–1552.

[Javorski *et al.*, 2013] JAVORSKI, M., CEPON, G., SLAVIC, J. et BOLTEZAR, M. (2013). A generalized magnetostrictive-forces approach to the computation of the magnetostriction-induced vibration of laminated steel structures. *IEEE Transactions on Magnetics*, 49(11):5446–5453.

[Jiayin *et al.*, 2013] JIAYIN, W., BAODONG, B., HONGLIANG, L. et CHUANG, M. (2013). Research on vibration and noise of transformer under dc bias based on magnetostriction. *In Electrical Machines and Systems (ICEMS), 2013 International Conference on*, pages 2225–2228. IEEE.

[Jiles, 1994] JILES, D. C. (1994). Modelling the effects of eddy current losses on frequency dependent hysteresis in electrically conducting media. *IEEE Transactions on Magnetics*, 30(6):4326–4328.

[Jiles et Atherton, 1986a] JILES, D. C. et ATHERTON, D. L. (1986a). Theory of ferromagnetic hysteresis. *Journal of magnetism and magnetic materials*, 61(1-2):48–60.

[Jiles et Atherton, 1986b] JILES, D. C. et ATHERTON, D. L. (1986b). Theory of ferromagnetic hysteresis. *Journal of Magnetism and Magnetic Materials*, 61(1-2):48–60.

[Jillek et Hubert, 1980] JILLEK, W. et HUBERT, A. (1980). The influence of mechanical stresses on losses and domains of oriented transformer steel. *Journal of Magnetism and Magnetic Materials*, 19:365–368.

[Journeaux *et al.*, 2013] JOURNEAUX, A. A., BOUILLAULT, F. et ROGER, J.-Y. (2013). Multi-physics problems computation using numerically adapted meshes: application to magneto-thermo-mechanical systems. *The European Physical Journal Applied Physics*, 61(3):30001.

[Kaltenbacher *et al.*, 1997] KALTENBACHER, M., LANDES, H. et LERCH, R. (1997). An efficient calculation scheme for the numerical simulation of coupled magnetomechanical systems. *IEEE Transactions on Magnetics*, 33(2):0–3.

[Krell *et al.*, 2000] KRELL, C., BAUMGARTINGER, N. et KRISMANIC, G. (2000). Relevance of multidirectional magnetostriction for the noise generation of transformer cores. *Journal of Magnetism and Magnetic Materials*, 216:634–636.

[Kulkarni et Khaparde, 2016] KULKARNI, S. V. et KHAPARDE, S. A. (2016). *Transformer engineering: design, technology, and diagnostics*. CRC Press.

[Landau et Lifshitz, 1935] LANDAU, L. et LIFSHITZ, E. (1935). On the theory of the dispersion of magnetic permeability in ferromagnetic bodies. *Phys. Z. Sowjetunion*, 8(153):101–114.

[Lazreg et Hubert, 2011] LAZREG, S. et HUBERT, O. (2011). A multidomain modeling of the magnetoelastic behavior for nondestructive evaluation. *Journal of Applied Physics*, 109(7):07E508.

[Leite *et al.*, 2004] LEITE, J., SADOWSKI, N., KUO-PENG, P., BATISTELA, N., BASTOS, J. et DEESPINDOLA, A. (2004). Inverse Jiles–Atherton vector hysteresis model. *IEEE Transactions on Magnetics*, 40(4):1769–1775.

[Li *et al.*, 2012] LI, Q., WANG, X., ZHANG, L., LOU, J. et ZOU, L. (2012). Modelling methodology for transformer core vibrations based on the magnetostrictive properties. *IET Electric Power Applications*, 6(May):604.

[Li *et al.*, 2013] LI, Y., GAO, Y., LI, L., ZHANG, D. et HAN, F. (2013). Effects of DC magnetic bias on the magnetic and sound fields of transformer. *Energy and Power Engineering*, 05(04):1097–1100.

[Li, 2017] LI, Z. (2017). Mesure et modélisation du comportement magnéto-mécanique et du bruit des transformateurs embraqués. Mémoire de D.E.A., Université Paris-Sud, France.

[Liu *et al.*, 2015a] LIU, M., HUBERT, O., MININGER, X., BOUILLAULT, F. et BERNARD, L. (2015a). Calculation of magnetostriction induced deformations in grain oriented and non-oriented silicon iron transformer cores thanks to an imposed magnetic flux method. *In COMPUMAG 2015*.

[Liu *et al.*, 2016] LIU, M., HUBERT, O., MININGER, X., BOUILLAULT, F. et BERNARD, L. (2016). Homogenized magneto-elastic behavior model for the computation of strain due to magnetostriction in transformers. *IEEE Transactions on Magnetics*, 52(2):1–12.

[Liu *et al.*, 2015b] LIU, M., HUBERT, O., MININGER, X., BOUILLAUT, F. et BERNARD, L. (2015b). Calculation of magnetostriction induced deformations in grain oriented and non-oriented silicon iron transformer cores thanks to an imposed magnetic flux method. *Compumag*.

[Lollioz *et al.*, 2006] LOLLIOZ, L., PATTOFATTO, S. et HUBERT, O. (2006). Application of piezo-magnetism for the measurement of stress during an impact. *Journal of electrical engineering*, 57(8):10–15.

[Lopez *et al.*, 2009] LOPEZ, S., CASSORET, B., BRUDNY, J. F., LEFEBVRE, L. et VINCENT, J. N. (2009). Grain oriented steel assembly characterization for the development of high efficiency AC rotating electrical machines. *IEEE Transactions on Magnetics*, 45(10):4161–4164.

[Lundgren, 1999] LUNDGREN, A. (1999). On measurement and modelling of 2d magnetization and magnetostriction of sife sheets. *KTH Reprocental, Stockholm*.

[Mayergoyz, 2003] MAYERGOYZ, I. D. (2003). *Mathematical models of hysteresis and their applications*. Academic Press.

[Mballa-Mballa *et al.*, 2014] MBALLA-MBALLA, F. S., HUBERT, O., HE, S., DEPEYRE, S. et MEILLAND, P. (2014). Micromagnetic modeling of magneto-mechanical behavior. *IEEE Transactions on Magnetics*, 50(4):1–4.

[Mbengue *et al.*, 2016] MBENGUE, S., BUIRON, N. et LANFRANCHI, V. (2016). An anisotropic model for magnetostriction and magnetization computing for noise generation in electric devices. *Sensors*, 16(4):553.

[Mechler et Girgis, 2000] MECHLER, G. et GIRGIS, R. (2000). Magnetic flux distributions in transformer core joints. *IEEE Transactions on Power Delivery*, 15(1):198–203.

[Mininger *et al.*, 2009] MININGER, X., GALOPIN, N., OJEDA, X., BOUILLAULT, F. et GABSI, M. (2009). Modeling of magnetoelastic and piezoelectric coupling: Application to srm noise damping. *IEEE Transactions on Magnetics*, 45(3):1218–1221.

[Mizokami et Kurosaki, 2015] MIZOKAMI, M. et KUROSAKI, Y. (2015). Noise variation by compressive stress on the model core of power transformers. *Journal of Magnetism and Magnetic Materials*, 381:208–214.

[Moses *et al.*, 2015] MOSES, A. J., ANDERSON, P. I. et SOMKUN, S. (2015). Modeling 2-D magnetostriction in nonoriented electrical steels using a simple magnetic domain model. *IEEE Transactions on Magnetics*, 51(5):1–7.

[Nachtergaele *et al.*, 2010] NACHTERGAELE, P., RIXEN, D. J. et STEENHOEK, A. M. (2010). Efficient weakly coupled projection basis for the reduction of thermomechanical models. *Journal of Computational and Applied Mathematics*, 234(7): 2272–2278.

[Ossart *et al.*, 1995] OSSART, F., DAVIDSON, R. et CHARAP, S. (1995). A 3D moving vector Preisach hysteresis model. *IEEE Transactions on Magnetics*, 31(3):1785–1788.

[Parent *et al.*, 2008] PARENT, G., DULAR, P., DUCREUX, J. P. et PIRIOU, F. (2008). Using a galerkin projection method for coupled problems. *IEEE Transactions on Magnetics*, 44(6):830–833.

[Parent *et al.*, 2013] PARENT, G., PENIN, R., LECOINTE, J. P., BRUDNY, J. F. et BELGRAND, T. (2013). Analysis of the magnetic flux distribution in a new shifted non-segmented grain oriented AC motor magnetic circuit. *IEEE Transactions on Magnetics*, 49(5):1977–1980.

[Payen et Bathe, 2011] PAYEN, D. J. et BATHE, K. J. (2011). The use of nodal point forces to improve element stresses. *Computers and Structures*, 89(5-6):485–495.

[Penin *et al.*, 2014a] PENIN, R., LECOINTE, J.-p., PARENT, G., BRUDNY, J.-f., MEMBER, S. et BELGRAND, T. (2014a). Grain oriented steel sings for an experimental comparison of relative magnetostriction and maxwell's forces effects. *IEEE Transactions on Industrial Electronics*, 61(8):1–8.

[Penin *et al.*, 2014b] PENIN, R., PARENT, G., LECOINTE, J.-P., BRUDNY, J. et BELGRAND, T. (2014b). Impact of mechanical deformations of transformer corners on core losses. *IEEE Transactions on Magnetics*, 51(4).

[Petrovic, 2010] PETROVIC, D. S. (2010). Non-oriented electrical steel sheets. *Materiali in tehnologije*, 44(6):317–325.

[Pfützner *et al.*, 2011] PFÜTZNER, H., MULASALIHOVIC, E., YAMAGUCHI, H., SABIC, D., SHILYASHKI, G. et HOFBAUER, F. (2011). Rotational magnetization in transformer cores - a review. *IEEE Transactions on Magnetics*, 47(11):4523–4533.

[Phophongviwat, 2013] PHOPHONGVIWAT, T. (2013). *Investigation of the influence of magnetostriction and magnetic forces on transformer core noise and vibration*. Thèse de doctorat, Cardiff University.

[Preisach, 1935] PREISACH, F. (1935). {Ü}ber die magnetische Nachwirkung. *Zeitschrift f{ü}r Physik A Hadrons and Nuclei*, 94(5):277–302.

[Ramesh *et al.*, 1996] RAMESH, A., JILES, D. C. et RODERICK, J. M. (1996). A model of anisotropic anhysteretic magnetization. *IEEE Transactions on Magnetics*, 32(5):4234–4236.

[Rasilo *et al.*, 2016] RASILO, P., SINGH, D., AYDIN, U., MARTIN, F., KOUHIA, R., BELAHCEN, A. et ARKKIO, A. (2016). Modeling of hysteresis losses in ferromagnetic laminations under mechanical stress. *IEEE Transactions on Magnetics*, 52(3):1–4.

[Rasilo *et al.*, 2013] RASILO, P., SINGH, D., BELAHCEN, A. et ARKKIO, A. (2013). Iron losses, magnetoelasticity and magnetostriction in ferromagnetic steel laminations. *IEEE Transactions on Magnetics*, 49(5):2041–2044.

[Rausch *et al.*, 2002] RAUSCH, M., KALTENBACHER, M., LANDES, H., LERCH, R., ANGER, J., GERTH, J. et BOSS, P. (2002). Combination of finite and boundary element methods in investigation and prediction of load-controlled noise of power transformers. *Journal of Sound and Vibration*, 250(2):323–338.

[Rekik, 2014] REKIK, M. (2014). *Mesure et modélisation du comportement magnéto-mécanique dissipatif des matériaux ferromagnétiques à haute limite élastique souschargement multiaxial: application aux gératrices à grandes vitesses pour l'aéronautique*. Thèse de doctorat, Ecole normale supérieure de Cachan-ENS Cachan.

[Ren et Ionescu, 1995] REN, Z. et IONESCU, B. (1995). Calculation of mechanical deformation of magnetic materials in electromagnetic. *IEEE Transactions on Magnetics*, 31(3):4–7.

[Ren et Razek, 1992] REN, Z. et RAZEK, A. (1992). Local force computation in deformable bodies using edge elements. *IEEE Transactions on Magnetics*, 28(2):1212–1215.

[Rezaei-Zare *et al.*, 2009] REZAEI-ZARE, A., IRAVANI, R. et SANAYE-PASAND, M. (2009). Impacts of transformer core hysteresis formation on stability domain of ferroresonance modes. *IEEE Transactions on Power Delivery*, 24(1):177–186.

[Ribbenfjärd et Engdahl, 2007] RIBBENFJÄRD, D. et ENGDAHL, G. (2007). Hysteresis modeling including asymmetric domain rotation. *IEEE Transactions on Magnetics*, 43(4):1385–1388.

[Rivera, 2000] RIVERA, H. (2000). Measurements of mechanical vibrations at magnetic cores of power transformers with fiber-optic interferometric intrinsic sensor. *Selected Topics in Quantum Electronics, IEEE Journal of*, 6(5):788–797.

[Rizzo, 2012] RIZZO, K.-j. (2012). *Modélisation multi-échelle du comportement magnéto-mécanique dissipatif*. phdthesis.

[Rizzo *et al.*, 2010] RIZZO, K. J., HUBERT, O. et DANIEL, L. (2010). Magnetic and magnetostrictive behavior of iron-silicon single crystals under uniaxial stress. *IEEE Transactions on Magnetics*, 46(2):270–273.

[Rossi et Le Besnerais, 2015] ROSSI, M. et LE BESNERAIS, J. (2015). Vibration reduction of inductors under magnetostrictive and Maxwell forces excitation. *IEEE Transactions on Magnetics*, 51(12):1–6.

[Rowley *et al.*, 2004] ROWLEY, C. W., COLONIUS, T. et MURRAY, R. M. (2004). Model reduction for compressible flows using POD and Galerkin projection. *Physica D: Nonlinear Phenomena*, 189(1-2):115–129.

[Sablik et Jiles, 1993] SABLIK, M. J. et JILES, D. C. (1993). Coupled magnetoelastic theory of magnetic and magnetostrictive hysteresis. *IEEE transactions on magnetics*, 29(4):2113–2123.

[Savary et Hubert, 2017] SAVARY, M. et HUBERT, O. (28 aout-1er septembre 2017). Influence des conditions de refroidissement sur le comportement magnétostrictif des matériaux ferromagnétiques – approche par modèle biphasé. *In CFM2017 - 23ème Congès Français de Mécanique*.

[Savary *et al.*, 2018] SAVARY, M., HUBERT, O., HELBERT, A., BAUDIN, T. et WAECKERLÉ, T. (2018). Magnetostrictive and magnetic effects in fe-27%co laminations (submitted). *In AIP Proceedings, 23rd Soft Magnetic Materials conference*.

[Schinnerl et Schoberl, 2002] SCHINNERL, M. et SCHOBERL, J. (2002). Multigrid Methods for the 3D Simulation of Nonlinear Magneto-Mechanical Systems. 38(Sfb 013):1497–1511.

[Shahaj et Garvey, 2011] SHAHAJ, A. et GARVEY, S. D. (2011). A possible method for magnetostrictive reduction of vibration in large electrical machines. *IEEE Transactions on Magnetics*, 47(2):374–385.

[Shao *et al.*, 2012] SHAO, P., LUO, L., LI, Y. et REHTANZ, C. (2012). Electromagnetic vibration analysis of the winding of a new HVDC converter transformer. *IEEE Transactions on Power Delivery*, 27(1):123–130.

[Shilyashki *et al.*, 2014a] SHILYASHKI, G., PFUTZNER, H., ANGER, J., GRAMM, K., HOFBAUER, F., GALABOV, V. et MULASALIHOVIC, E. (2014a). Magnetostriction of transformer core steel considering rotational magnetization. *IEEE Transactions on Magnetics*, 50(1).

[Shilyashki *et al.*, 2014b] SHILYASHKI, G., PFÜTZNER, H., HAMBERGER, P., AIGNER, M., HOFBAUER, F., MATKOVIC, I. et KENOV, A. (2014b). The impact of off-plane flux on losses and magnetostriction of transformer core steel. *IEEE Transactions on Magnetics*, 50(11):1–4.

[Shilyashki *et al.*, 2015] SHILYASHKI, G., PFUTZNER, H., PALKOVITS, M., HAMBERGER, P. et AIGNER, M. (2015). A Tangential induction sensor for 3-d analyses of peripheral flux distributions in transformer cores. *IEEE Transactions on Magnetics*, 51(6):1–1.

[Shuai et Biela, 2014] SHUAI, P. et BIELA, J. (2014). Investigation of acoustic noise sources in medium frequency, medium voltage transformers. *In 2014 16th European Conference on Power Electronics and Applications*, pages 1–11.

[Shuai et Biela, 2015] SHUAI, P. et BIELA, J. (2015). Impact of core shape and material on the acoustic noise emission of medium frequency, medium voltage transformers. *In 2015 17th European Conference on Power Electronics and Applications (EPE'15 ECCE-Europe)*, pages 1–11. IEEE.

[Siemens, ] SIEMENS. Siemens high voltage power transformer. https://www.siemens.com/global/en/home/products/energy/high-voltage/transformers.html.

[Somkun *et al.*, 2012] SOMKUN, S., MOSES, A. J. et ANDERSON, P. I. (2012). Measurement and modeling of 2-d magnetostriction of nonoriented electrical steel. *IEEE Transactions on Magnetics*, 48(2):711–714.

[Somkun *et al.*, 2010] SOMKUN, S., MOSES, A. J., ANDERSON, P. I. et KLIMCZYK, P. (2010). Magnetostriction anisotropy and rotational magnetostriction of a nonoriented electrical steel. *IEEE Transactions on Magnetics*, 46(2):302–305.

[Sourmail, 2005] SOURMAIL, T. (2005). Near equiatomic FeCo alloys: Constitution, mechanical and magnetic properties.

[Szewczyk, 2014] SZEWCZYK, R. (2014). Validation of the anhysteretic magnetization model for soft magnetic materials with perpendicular anisotropy. *Materials*, 7(7):5109–5116.

[Szymański et Waszak, 2004] SZYMAŃSKI, G. et WASZAK, M. (2004). Vectorized Jiles–Atherton hysteresis model. *Physica B: Condensed Matter*, 343(1):26–29.

[Tegopoulos, 1992] TEGOPOULOS, A. (1992). A new scalar potential formulation for 3-D magnetostatics necessitating no source field calculation. *IEEE Transactions on Magnetics*, 28(March).

[Thales, ] THALES. Thales Avionics Electrical Systems Catalog. https://customeronline.thalesgroup.com/sites/default/files/asset/document/thales_avionics_electrical_systems_catalog.pdf.

[Valkovic, 1998] VALKOVIC, Z. (1998). Effects of transformer core design on noise level. *Le Journal de Physique IV*, pages 11–14.

[Vanoost *et al.*, 2015] VANOOST, D., STEENTJES, S., DE GERSEM, H., PEUTEMAN, J., GIELEN, G., PISSOORT, D. et HAMEYER, K. (2015). Embedding a magnetoelastic material model in a coupled magnetomechanical finite-element solver. *IEEE Transactions on Magnetics*, 51(11):1–4.

[Vanoost *et al.*, 2016] VANOOST, D., STEENTJES, S., PEUTEMAN, J., GIELEN, G., DE GERSEM, H., PISSOORT, D. et HAMEYER, K. (2016). Magnetic hysteresis at the domain scale of a multi-scale material model for magneto-elastic behaviour. *Journal of Magnetism and Magnetic Materials*, 414:168–179.

[Waeckerle *et al.*, 2017] WAECKERLE, T., BAUDIN, T., HELBERT, A. et HUBERT, O. (2017). Tôle ou bande en alliage feco ou fesi ou en fe et son procédé de fabrication, noyau magnétique de transformateur réalisé à partir d'elle et transformateur le comportant. WO Patent App. PCT/EP2015/067,443.

[Wang *et al.*, 2015] WANG, J., GAO, C., DUAN, X. et MAO, K. (2015). Multi-field coupling simulation and experimental study on transformer vibration caused by DC bias. *Journal of Electrical Engineering and Technology*, 10(1):176–187.

[Wang et Pan, 2015] WANG, Y. et PAN, J. (2015). Comparison of mechanically and electrically excited vibration frequency responses of a small distribution transformer. *IEEE Transactions on Power Delivery*, PP(99):1–1.

[Wang *et al.*, 2011] WANG, Y., PAN, J. et JIN, M. (2011). Finite element modelling of the vibration of a power transformer. *Proceedings of ACOUSTICS*, (34):1–7.

[Wang *et al.*, 2013] WANG, Z., HENNERON, T., NEMITZ, N., MIPO, J. C. et PIRIOU, F. (2013). Electromagnetic field projection on finite element overlapping domains. *IEEE Transactions on Magnetics*, 49(4):1290–1298.

[Wang *et al.*, 2014] WANG, Z., TANG, Z., HENNERON, T., PIRIOU, F. et MIPO, J.-C. (2014). Energetic Galerkin Projection of Electromagnetic Fields Between Different Meshes. *IEEE Transactions on Magnetics*, 50(2):613–616.

[Weiser et Pfützner, 1998] WEISER, B. et PFÜTZNER, H. (1998). Relevance of magnetostatic forces for transformer core vibrations. *Le Journal de Physique IV*, 8(1 998):8–11.

[Weiser *et al.*, 2000] WEISER, B., PFÜTZNER, H., ANGER, J., PFUTZNER, H. et ANGER, J. (2000). Relevance of magnetostriction and forces for the generation of audible noise of transformer cores. *In IEEE Transactions on Magnetics*, volume 36, pages 3759–3777.

[Williams et Shockley, 1949] WILLIAMS, H. J. et SHOCKLEY, W. (1949). A simple domain structure in an iron crystal showing a direct correlation with the magnetization. *Physical Review*, 75(1):178.

[Witczak, 2014] WITCZAK, P. (2014). Magnetostriction force spectrum in power transformer. *Electrical Machines (ICEM), 2014 International Conference*, (3):2246–2251.

[Xian *et al.*, 2014] XIAN, Z., PENGCHENG, Z., QINGXIN, Y., LIHUA, Z. et XIN, Z. (2014). Numerical estimation and optimization of vibration noise due to magnetostriction and magnetic forces for laminated core structure. *In Electrical Machines and Systems (ICEMS), 2014 17th International Conference on*, numéro 51307120, pages 1548–1551. IEEE.

[Yang *et al.*, 2016] YANG, Y., QINGFEN, L., DICHEN, L., SHANSHAN, L. et JINGZHU, H. (2016). Electromagnetic vibration noise analysis of transformer windings and core. *IET Electric Power Applications*, 10(4):251–257.

[Yang et Zhang, 2006] YANG, Y. et ZHANG, X. (2006). Study on noise reduce for equipment at UHVDC converter station. *Gaodianya Jishu/ High Voltage Engineering*, 32(9):149–152.

[Zagrai et Çakan, 2010] ZAGRAI, A. N. et ÇAKAN, H. (2010). Magneto-mechanical impedance identification and diagnosis of metallic structures. *International Journal of Engineering Science*, 48(10):888–908.

[Zheng *et al.*, 2015] ZHENG, J., PAN, J. et HUANG, H. (2015). An experimental study of winding vibration of a single-phase power transformer using a laser Doppler vibrometer. *Applied Acoustics*, 87:30–37.

[Zhu et Ramsden, 1998] ZHU, J. G. et RAMSDEN, V. S. (1998). Improved formulations for rotational core losses in rotating electrical machines. *IEEE Transactions on Magnetics*, 34(4):2234–2242.

[Zhu *et al.*, 2016] ZHU, L., WANG, B., YAN, R., YANG, Q., YANG, Y. et ZHANG, X. (2016). Electromagnetic Vibration of Motor Core Including Magnetostriction Under Different Rotation Speeds. *IEEE Transactions on Magnetics*, 52(3):1–4.

[Zhu *et al.*, 2012] ZHU, L., YANG, Q. et YAN, R. (2012). Numerical analysis of vibration due to magnetostriction of three phase transformer core. *2012 6th International Conference on Electromagnetic Field Problems and Applications, ICEF'2012*, pages 3–6.

[Zhu *et al.*, 2013] ZHU, L., YANG, Q., YAN, R., LI, Y., ZHANG, X., YAN, W. et ZHU, J. (2013). Numerical computation for a new way to reduce vibration and noise due to magnetostriction and magnetic forces of transformer cores. *Journal of Applied Physics*, 113(17):2014–2017.

université PARIS-SACLAY

ÉCOLE DOCTORALE
Sciences mécaniques et énergétiques, matériaux et géosciences (SMEMAG)

**Titre:** Optimisation des performances électromagnétiques et acoustiques des transformateurs

**Mots-clés:** Magnétostriction, Homogénéisation, Transformateur de puissance, Vibration/bruit, Modèle multiéchelle, Matériau ferromagnétique, Méthode des éléments finis

**Résumé:** Le travail présenté dans ce mémoire s'intéresse à la prédiction des vibrations d'un noyau de transformateur multicouche, constitué d'un assemblage de tôles ferromagnétiques. Le problème couplé magnéto-mécanique est résolu par une approche séquentielle progressive : la résolution magnétique est suivie d'une résolution mécanique. Un modèle multi-échelle simplifié 3D décrivant les anisotropies magnétiques et magnétostrictives, et considérant les non-linéarités magnétiques et de magnétostriction, est utilisé comme loi de comportement du matériau. La structure du noyau du transformateur est modélisée en 2D. Une technique d'homogénéisation permet de tenir compte du comportement anisotrope de chaque couche afin de définir un comportement moyen pour chaque élément du maillage éléments finis.. Des mesures expérimentales sont ensuite effectuées, permettant d'une part la validation des lois de comportement matériau utilisées, et d'autres part des modèles de comportement structurel statique, du comportement structurel dynamique et de l'estimation du bruit. Différents matériaux et différentes géométries de prototypes de transformateurs sont considérés pour ce travail. Des optimisations structurelles sont finalement proposées grâce à des simulations numériques s'appuyant sur le modèle développé, afin de réduire les vibrations et les émissions de bruit du noyau du transformateur.

Title: Optimization of electromagnetic and acoustic performances of power transformers

**Keywords:** Magnetostriction, Homogenization, Power transformers, Vibration/noise, Multiscale modeling, Ferromagnetic materials, Finite element method.

**Abstract:** This thesis deals with the prediction of the vibration of a multi-layer transformer core made of an assembly of electrical sheets. This magneto-mechanical coupled problem is solved by a stepping finite element method sequential approach: magnetic resolution is followed by mechanical resolution. A 3D Simplified Multi-Scale Model (SMSM) describing both magnetic and magnetostrictive anisotropies is used as the constitutive law of the material. The transformer core structure is modeled in 2D and a homogenization technique is implemented to take the anisotropic behavior of each layer into consideration and define an average behavior at each element of the finite element mesh. Experimental measurements are then carried out, allowing the validation of the material constitutive law, static structural behavior, dynamic structural behavior, and the noise estimation. Different materials geometries are considered for this workStructural optimizations are finally achieved by numerical simulation for lower vibration and noise emission of the transformer cores.

Université Paris-Saclay
Espace Technologique / Immeuble Discovery
Route de l'Orme aux Merisiers RD 128 / 91190 Saint-Aubin, France